Arnold Schwarzenegger
Governor

UTILIZATION OF WASTE RENEWABLE FUELS IN BOILERS WITH MINIMIZATION OF POLLUTANT EMISSIONS

LABORATORY SCALE GASIFICATION SCREENING EXPERIMENTS

PIER TECHNICIAL REPORT

Prepared For:
California Energy Commission
Public Interest Energy Research Program

Prepared By:
UNIVERSITY OF CALIFORNIA,
DEPARTMENT OF BIOLOGICAL AND AGRICULTURAL ENGINEERING

December 2005
CEC-500-2005-134

Prepared By:
B.C. Meister, R.B. Williams, B.M. Jenkins
UNIVERSITY OF CALIFORNIA,
DEPARTMENT OF BIOLOGICAL AND
AGRICULTURAL ENGINEERING
Davis, CA 95616-5294
Contract No.500-99-013

Prepared For:

California Energy Commission
Public Interest Energy Research (PIER)
Program

Valentino Tiangco, Ph.D.
Contract Manager

Elaine Sison-Lebrilla, P.E.
Manager, Energy Generation Research Office

Martha Krebs, Ph. D.
Deputy Director
ENERGY RESEARCH AND
DEVELOPMENT DIVISION

B.B. Blevins
Executive Director

SUMMARY

Biomass fuels were gasified in a bench scale atmospheric fluidized bed reactor. Fuels were gasified over a range of substoichiometric conditions to determine gas compositions and fuel conversion effects to acquire data for design applications in close-coupled boiler-gasifier systems providing boiler NOx reductions through producer gas fuel reburning.

Reported here are data and results obtained from the bench-scale experiments for almond shell, walnut prunings, rice straw, whole tree wood chips, sludge, and non-recyclable waste paper. These results include bed and disengagement temperature profiles, bed differential pressures, overall mass balances, overall power balances, concentration of solids and condensibles, producer gas concentrations, gas phase ammonia, hydrogen cyanide, chloride and potassium concentrations, agglomeration tendencies, particle distributions and hot and cold gas efficiencies.

Higher heating values (HHV) of producer gas ranged from 3.6 to 6.9 MJ m^{-3}, hot gas efficiencies ranged from 26 to 55 %, cold gas efficiencies ranged from 25 to 54 %, gas phase ammonia concentrations ranged from 70 ppmv to 3.99 % by volume dry gas basis and showed good correlation (r^2=0.66) with fuel nitrogen content. Gas phase hydrogen cyanide ranged from 2.4 to 23.0 ppmv, potassium ranged from 2 to 61 ppmv and gas phase chlorine ranged from 9 ppmv to 810 ppmv. Closures for power balances were in the range of 55 to 92 %. Closing the carbon and nitrogen balances to account for possible experimental error suggests that gas flow rates and gasifier efficiencies were in general higher than reported. For fuels other than rice straw, no agglomeration of the bed was detected over the course of the tests and operation was largely stable. For rice straw, the normal alumina-silica bed was replaced with a largely MgO bed in order to avoid agglomeration. The amount of initial fuel potassium and sodium leaving the stack in the particle phase ranged from 0.1 % for almond shell to 0.2 % for rice straw and < 0.1% for almond shell to 0.1 % for rice straw respectively.

Laboratory data generated during the gasification tests were compared to predictions from a commercially available bubbling fluidized bed model, Comprehensive Simulator for Fluidized Bed Equipment (CSFB, Technologix Corporation, Chicago, Il. (de Souza-Santos, 2001)) and also compared against equilibrium gas phase concentrations computed via STANJAN (Reynolds, 1986). The model predictions from CSFB, when compared to experimental gas phase concentrations, were consistently low for energy carrier gases of interest at the same temperature. Using higher temperatures and increased inert size with the CSFB model improved predictions but the predictions were still poor. A later modification to CSFB predicted slightly higher concentrations of H2, CO and CH4 but predictions are still poor. The CSFB model would need further modification to make it useful for design purposes. STANJAN predictions were more closely aligned with experimental results but were notably higher for most gas species of interest at the same

temperature. Adjustments to STANJAN atom populations, to account for the remaining carbon, hydrogen, oxygen and nitrogen left in the bed, horizontal pass dropout and cyclone dropouts, provided predictions that were somewhat closer to experimental results. In general, equilibrium predictions at temperatures that were lower than experimental temperatures by mean values of 213 K, 279 K and 190 K for gas constituents CO, H2, and CH4, respectively, more closely matched the experimental results (some results were higher). These lower equilibrium temperatures corresponded to those in the disengagement region of the fluidized bed.

All fuels tested are potential candidates for close-coupled boiler-gasifier systems, potentially providing boiler NO_x reductions through producer gas fuel reburning. These fuels are abundant in California as well as many other parts of the country and world and can potentially augment current fuel resources.

TABLE OF CONTENTS

LIST OF FIGURES

LIST OF TABLES

NOMENCLATURE

A	cross sectional area of the bed	[m^2]
A_1	cross sectional area of frontal fuel feed on feed belt	[mm^2]
$AF_{gasification}$	gasification air to fuel ratio	-
$AF_{stoichiometric}$	stoichiometric air to fuel ratio	-
ASF	almond shell fuel	-
c	constant	-
c_1	constant 1	-
c_2	constant 2	-
Cp	specific heat	[kJ $kmol^{-1}$ K^{-1} or kJ kg^{-1} K^{-1}]
C(s)	carbon in solid form	[g]
db	dry basis	-
e	excess air fraction	-
FN	fuel nitrogen	-
g	gravitational acceleration	[m s^{-2}]
$\bar{g}_j$	gibbs free energy	J
GC	gas chromatograph	-
GMD	geometric mean diameter	[mm]
H	bed height	[m]
h_a	enthalpy of dry air	[kJ kg^{-1}]
HHV	higher heating value at constant volume (either wet or dry basis as stated)	[MJ kg^{-1}]
h_w	enthalpy of water steam in air	[kJ kg^{-1}]
I	atoms in system	-
j	species	-
LHV	lower heating value at constant volume	[MJ kg^{-1}]
$\dot{m}_{a(db)}$	mass flow rate of air (dry basis)	[g s^{-1}]
$\dot{m}_a$	mass flow rate of air including moisture	[g s^{-1}]
$\dot{m}_{f(db)}$	mass flow rate of fuel (dry basis)	[g s^{-1}]
m_{air}	mass of supplied air including humidity	[g]
$m_{air\ dry}$	mass of supplied dry air	[g]
$m_{air\ wet}$	humidity in air	[g]
m_{ash}	total weight of ash in ash dropouts	[g]
$m_{ash\ c}$	total weight of ash in cyclone ash dropout	[g]
$m_{ash\ h}$	total weight of ash in horizontal ash dropout	[g]
$m_{bed\ fresh}$	total weight of fresh bed material placed in the furnace	[g]
$m_{bed\ out}$	total weight of spent bed material removed after test	[g]
$m_{fuel\ dry}$	total dry weight of burned fuel	[g]
$m_{fuel\ wet}$	total water present in fuel as moisture	[g]
m_{stack}	total particle and gas mass leaving the stack	[g]
$m_{gas\ phase}$	mass of gas (or vapor) leaving the system at the stack	[g]

$m_{particle\ phase}$	mass of particle phase leaving the system at the stack	[g]
n_{ij}	number of i atoms in molecule j	-
ND	not detected	-
NPF	non-recyclable waste paper	-
Q	power	[kW]
$\dot{q}_{fuel}$	power represented by the fuel input	[kW]
$\dot{q}_{heater}$	supplied power from the external electric heater	[kW]
$\dot{q}_{air}$	power of preheated supplied air	[kW]
$\dot{q}_{ash}$	power of ash (sensible and chemical)	[kW]
$\dot{q}_{stack}$	power of stack gas (sensible and chemical)	[kW]
$\dot{q}_{system}$	power lost as heat to the environment	[kW]
r^2	correlation coefficient	-
R	universal gas constant	[kJ $kmol^{-1}$ K^{-1}]
RSF	rice straw fuel	-
SLF	sludge	-
T	absolute temperature	[K]
$T_{furnace}$	surface temperature of furnace	[°C]
$T_{reactor}$	average gas temperature inside reactor	[°C]
T_1	ambient temperature	[°C]
T_2	preheat air temperature	[°C]
T_{2c}	average gas temperatures at the exit of the cyclone	[°C]
$t_{burn\ time}$	time associated with burning of a fuel	[s]
TC	thermocouple	-
U	heat transfer coefficient	[W K^{-1}]
V	velocity of feed belt	[mm min^{-1}]
w	mass fraction of water in dry air	-
wb	wet basis	-
w_d	condensed water in desiccant	[g]
WPF	walnut prunings fuel, wood “p”	-
WWF	whole tree wood chips, wood “w”	-
X_i	weighted component of geometric mean	-
z	height above bottom of bed	m

Greek Symbols

$\delta\psi$	uncertainty of result	-
λ_I	Lagrange multiplier	-
θ_I	uncertainty of measured parameter	-
$\delta\theta_I$	differential of uncertainty of measured parameter	-
ρ_g	density of gas	[g cm^{-3}]
ρ_p	particle density	[g cm^{-3}]
ρ_{da}	density of dry air	[g cm^{-3}]

ρ	density of fuel	[g cm^{-3}]
Δ	difference (delta)	-
$\eta_{\text{hot gas}}$	hot gas efficiency	[%]
$\eta_{\text{cold gas}}$	cold gas efficiency	[%]

INTRODUCTION

Biomass originates from a variety of sources and is a term used to describe all biologically produced matter. In a fuels context, biomass refers to mostly plant materials and their derivatives produced through photosynthesis. Included in this definition are agricultural, industrial and municipal wastes and residues derived therefrom. Worldwide, biomass ranks fourth as an energy resource, providing approximately 14% of the world's energy needs. Biomass is the most important source of energy in many developing nations, providing approximately 35% of their energy, particularly in rural areas where it is often the only accessible and affordable source of energy (Bain et al., 1998).

There is a wide diversity of thermal methods for converting biomass into a more valuable form of energy. The most common thermal conversion methods are direct combustion (an energy conversion process usually carried out under at least stoichiometric conditions) and gasification (an energy conversion process carried out at substoichiometric conditions). Currently, there are over 350 biomass-fired power plants in the U.S. that deliver 7,000 MWe to the utility grid. The typical Rankine cycle power plant employs combustion to produce high pressure superheated steam. This steam is then expanded through an impulse turbine driving an electric generator that supplies electricity to the grid. Another 650 biomass-fired installations are operated by industries that generate electricity for their own use. The vast majority of these facilities are based on direct combustion of a variety of low-cost wood wastes, including forest and wood manufacturing residues (Bain et al., 1996).
The direct combustion of many biomass fuels is sometimes inefficient or in some cases unacceptable because of poor combustion characteristics. When compared to natural gas and petroleum, biomass and waste fuels have a heterogeneous composition, are sometimes high in ash or moisture content, have low heating value, can contain substantial alkali, chlorine and, in some instances, trace heavy metals including lead, mercury and cadmium.

Currently, biomass boilers are limited in their efficiency and suffer undesirable consequences of fuel ash fouling (sticky deposits on the convective heat transfer surfaces of the boiler) and also ash slagging (larger molten ash deposits in the furnace) when certain fuels are burned. Evidence of problems relating to the combustion of straw fuel, for example, has been illustrated by full-scale and laboratory combustion tests (Jenkins, et al., 1994). Even small fractions of straw fuels blended with woody biomass can result in serious fouling and slagging, causing boiler system shutdown and subsequent reduced availability (Miles et al., 1993). As an example, one grate-fired boiler in California was fired on a fuel blend of 80% wood and 20% wheat straw. After just five days of firing this blend (three days on partial load and two days on full load), the boiler was shut down due to severe slagging on the grate and failure of the ash handling equipment (Bakker et al., 2000). Laboratory combustion experiments with rice straw in a 4.2 m long electrically heated furnace resulted in the production of heavy deposits on furnace walls that impeded the normal completion of the tests. Combustion of rice straw in a

laboratory atmospheric fluidized bed combustor caused rapid bed agglomeration within 30 minutes of testing (Salour et al., 1993). Although the energy industry in Denmark has introduced boiler systems that can handle straw more successfully than in California, wheat straw combustion leads to substantial slagging, fouling and corrosion, thereby increasing the cost of producing energy from straw fuels (Jorgensen and Sander, 1997). Cereal straws in general have a high total ash concentration and are high in silica.

Even though the melting point of silica is comparatively high (>1700°C), alkaline silicate minerals melt at lower temperatures. Chlorine and sulfur present in straw fuels facilitate the volatilization of alkali or otherwise participate in ash deposition. The fluxing of silica, due to alkali, in addition to the enhanced alkali volatilization lead to the rapid formation of heavily sintered and fused glassy deposits at normal furnace operating conditions (800 to 1000° C) (Bakker et al., 2000).

Currently, there are a number of strategies to overcome both fouling and slagging problems that occur with combustion of straw and other herbaceous biomass. Some researchers are investigating controlling the furnace exit gas temperature in order to lower the average temperature in the convective heat transfer section. Changing boiler design by placing heat transfer sections further downstream to reduce temperature was accomplished in Denmark, and is also utilized in solid waste combustors, however this strategy mitigates fouling problems only partially, and has economic constraints. Additives to reduce fouling are used on a limited scale; however, they appear to be only effective in systems where complete mixing is accomplished (Jenkins et al, 1994). Other methods involve pretreatment steps of high fouling fuels such as fermentation (with subsequent combustion of gaseous and liquid products). Although these options certainly require consideration, they have not been demonstrated yet on a full-scale basis and therefore their potential for application is uncertain (Bakker et al., 2000).

Jenkins, et al. (1996) note, however, that simple water leaching leads to considerable changes in combustion properties and ash transformation in biomass. In general, leaching elevates the sintering and melting temperatures of biomass, improves ash fusibility and reduces the volatilization of inorganic species at ashing temperatures higher than 575° C. Leaching leads to a notable decline in the alkali index, which is a broad indicator of the fouling potential of a biomass fuel. However, technical and economic challenges that are inherent to leaching or to biomass utilization at large exist that affect the economic potential of fuel leaching (Bakker, 2000).

As an alternative to combustion, gasification can be used to provide a gaseous fuel. Gasification technology was developed more than two hundred years ago (Kaupp and Goss, 1984) and lately has been improved primarily for the purposes of providing solid fuels access to some of the same commercial markets as natural gas, propane, gasoline, and diesel fuel and to improve power generation efficiencies. Thermochemical gasification is the conversion, by partial oxidation at elevated temperatures, of a carbonaceous feedstock, such as biomass, into a gaseous energy carrier. The gaseous fuel can be used for cofiring and/or reburning, or advanced reburning applications in existing biomass boilers and can also be used directly in boilers and in engines with sufficient

cleaning. In cofiring, the producer gas from the gasifier is directed to the boiler burners and fired along with the principal fuel, or in the case of a solid fuel fired boiler, is fired through separate gas nozzles into the boiler. Reburning is essentially a staged-combustion technique for controlling nitrogen oxides. In the main combustion zone, 80% to 90% of the fuel is burned with a normal amount of air (about 10% to 15% excess). Then, in the second stage, the gasified fuel (known as the reburn fuel) is added into the secondary combustion zone to generate a fuel rich, reducing environment above the existing burner zone (Zamansky et al., 1999a). NO_x is reduced to molecular nitrogen (N_2) by reactions with the hydrocarbon fragments produced by the substoichiometric combustion of the reburn fuel. Overfire air is then added through specially designed over-fire air ports to complete the combustion process but at temperatures low enough to avoid much production of thermal NO_x. Advanced reburning techniques have been used to obtain even greater levels of NO_x control and to utilize alternative fuels (Zamansky, 1996a). An advanced reburning process has recently been patented (Ho et al., 1993; Seeker et al., 1998). In another study, (Zamansky 1996b) found that injection of small amounts of an alkali promoter species along with ammonia into the reburning zone can further improve the reburn process. Some researchers believe that the efficiency of reburning is higher when using waste fuels that already include volatile N-, Na- and K-containing compounds which promote the reburning process. In effect, the alkali serves as a catalyst and thus lowers the activation energy of the reaction. In one study, injection of 15 ppm Na_2CO_3 with a urea solution in advanced waste reburning resulted in 94 to 96 % NO_x reduction (Zamansky et al., 1996b).

A variety of waste products are currently underutilized in California and many parts of the world. Reasons include poor combustion characteristics of the fuel, high levels of pollutant emissions, costly controls to reduce pollutant emissions and adverse effects on boiler operation to include fouling and slagging.

The use of gasification technology offers the potential to convert low-grade feedstocks such as almond shells, walnut prunings, rice straw, sludge, and other materials into a valuable energy carrier and thus replace currently used fossil fuels. The gasification process also takes solid waste products and greatly improves their combustion characteristics and handleability, and simultaneously reduces harmful pollutant emissions such as NO_x. Diverting solid waste from landfills will create several benefits, such as reducing the risk of groundwater contamination, improving land usage and decreasing methane emissions. In addition to landfill diversion benefits, gasification technology may reduce pollutant emissions from direct combustion processes. Gasification reduces the volatilization of some fuel constituents relative to combustion and converts the low-grade fuels into a gaseous product with more stable combustion properties. Substitution of fossil fuels with renewable fuels will also result in a reduction of net CO_2 emissions. The close-coupled technique also provides a means for segregating ash from different fuels that is useful when attempting to recover valuable byproduct, such as high silica ash from rice straw. Such opportunities are largely lost when fuel is blended.

The combination of direct combustion and gasification can offer key advantages for widening the range of fuels for biomass boilers, decreasing maintenance costs while reducing harmful pollutant emissions.
This research is part of a much larger and comprehensive research project currently being pursued by the California Energy Commission and General Electric - Energy and Environmental Research Corporation (GE-EER). Their research efforts are ultimately focused on implementing and/or retrofitting close-coupled gasified boiler systems throughout California and the world.

As one aspect of this report, data related to temperature profiles and pressure drops across the fluidized bed were studied in order to assess the quality of fluidization and the uniformity of temperature obtained. Pressure drop is used as an indicator of bed, agglomeration, attrition and ash build-up. These parameters are useful diagnostics for reactor performance and to determine the appropriateness of a fuel for conversion purposes.

Because experiments are expensive to conduct, modeling was performed primarily to find a reliable predictive tool for examining the potential gasification characteristics over a broader range of conditions than possible experimentally and to assist in optimizing gas quality in future experiments of individual fuels or blended fuels.

OBJECTIVES

The overall objective of this study was to assess the fluidized bed gasification behavior for a range of different biomass fuels. In part, because of budget limitations, the number of individual experimental runs was limited and full replications were not performed. A variety of data on these individual runs was collected in order to meet the objectives of this study.

The specific objectives of this study were:

1. To investigate fluidized bed reactor performance including temperature profiles, bed differential pressures, overall mass balances, overall power balances, concentration of solids and condensibles, producer gas concentrations, gas phase ammonia, hydrogen cyanide, chloride, and potassium concentrations, and hot and cold gas efficiencies.

2. To examine the potential bed agglomeration associated with the different fuels.

3. To compare predictions from a commercial bubbling fluidized bed software model, Comprehensive Simulator for Fluidized Bed Equipment (CSFB) (de Souza-Santos, 2001) and equilibrium compositions (computed via the commercial STANJAN model) (Reynolds, 1986), to the experimental results.

4. To examine the appropriateness of the test fuels as potential candidates in close-coupled gasifier boiler reburn systems.

CHAPTER 1 REVIEW OF LITERATURE

1.1 Biomass Conversion

There are essentially three principal routes for converting biomass into a more useful form of energy. These conversion routes are: biochemical, physicochemical, and thermochemical. Frequently, two or more of these routes may be used in the generation of the final product or products.

Thermochemical conversion processes rely on combustion, pyrolysis and/or gasification to convert the biomass to heat, fuel gases, liquids and solids (chars). Thermochemical techniques tend to be non-selective for individual biomass components, in that the chemically complex biomass is substantially degraded into simple compounds (Chum and Bazier, 1985).

Although the most widely applied conversion method for biomass is combustion, gasification technology continues to be improved for the purposes of providing biomass fuels access to some of the same commercial markets as natural gas, propane, gasoline and diesel fuels. An integral part of the gasification process is pyrolysis (or devolatilization), which consists of a number of complex chemical reactions leading to the decomposition of the organic matter and the separation of different components into individual gases. Close-coupled gasification, an emerging hybrid technology, is a

synergistic combination of direct combustion and gasification that utilizes low-grade biomass and waste fuels to reduce pollutant emissions from furnaces and boilers.

1.2 Combustion

Combustion is the physical reaction of fuel with oxygen to release energy (Soffer, 1981) and involves simultaneous coupled heat and mass transfer with chemical reaction and fluid flow (Bamford et al., 1945). The term combustion refers to those reactions, which take place very rapidly with a large conversion of chemical energy in the fuel, to sensible energy (Borman et al., 1998). The combustion process usually requires at least stoichiometric oxygen and in practice, to obtain complete combustion of fuels, excess oxygen is required.

A global reaction for the combustion of a biomass fuel in air might take the following form, where the first reactant compound is a biomass fuel (Jenkins et al., 1998). This is shown below in equation [1.1], where the n_i indicates the number of moles of each species and e is the excess oxygen (or air):

$$C_{x1}H_{x2}O_{x3}N_{x4}S_{x5}Cl_{x6}Si_{x7}K_{x8}Ca_{x9}Mg_{x10}Na_{x11}P_{x12}Fe_{x13}Al_{x14}Ti_{x15} + n_1H_2O + n_2(1+e)(O_2 + 3.76\ N_2) = n_3CO_2 + n_4H_2O + n_5O_2 + n_6N_2 + n_7CO + n_8CH_4 + n_9NO + n_{10}NO_2 + n_{11}SO_2 + n_{12}HCl + n_{13}KCl + n_{14}K_2SO_4 + n_{15}C + \ldots \quad [1.1]$$

Equation [1.1] is by no means all inclusive. Other elements, such as heavy metals for example, have a strong influence on ash disposal and emissions, but are not included in the above relationship for simplicity. Jenkins et al. (1998) and the associated reference list in the subject paper, provide an extensive review of literature on the combustion properties of biomass.

When biomass materials convert under the influence of heat, the reaction gives rise to a volatile mixture of gases and carbonaceous char (fixed carbon and ash). Following ignition, the volatile matter burns with air in a visible flame while the carbonaceous char burns by a process known as glowing ignition. The release of volatile matter and the burning of the char have different chemical mechanisms and kinetics. Both modes are affected by the chemical composition of the fuel as well as by the characteristics of the combustion system (Borman, 1998).

A solid fuel particle in a combustion environment undergoes drying, devolatilization and char burning. As the fuel heats, pyrolysis starts releasing volatiles and forming char. According to Borman (1998), the rates of devolatilization and the pyrolysis depend on the temperature and the type of fuel. The pyrolysis products containing gases H_2, CH_4, CO, CO_2, H_2O, hydrocarbons and tars then ignite and form a flame around the surface if sufficient oxygen is present. The flame heats the fuel, causing enhanced devolatization. Borman (1998) notes that for wood, the hemicellulose pyrolyzes at 225 to 325° C, the cellulose at 275 - 375° C and the lignin at 300 - 500° C.

The final step in the solid fuel combustion process is char combustion. As the moisture and volatile release begins to decline, the char surface begins to react. Oxygen diffuses into the porous char and generates carbon monoxide (CO). The CO then reacts to form CO_2. Char is highly porous. The porosity of wood char is about 90%. When no more volatiles are escaping from the char, oxygen can diffuse through the external boundary layer and into the char particles (Borman, 1998). The burning rate of the char depends on both the chemical rate of the carbon-oxygen reaction at the surfaces and the rate of boundary layer and internal diffusion of oxygen. Finally, the mineral matter in the fuel is converted to a layer of ash on the char surface if not removed by mechanical abrasion.

The understanding of combustion has progressed considerably over the years. In the original works by Bamford et al. (1945), the combustion reactions were represented by a simple single global reaction scheme, which followed first-order kinetics and which had a fixed heat of reaction. The temperature profiles were determined by solving the equations of heat conduction and heat generation simultaneously, using the appropriate boundary conditions. Although there have been numerous independent experimental studies in the field of reaction kinetics that have collectively made considerable progress towards better understanding of biomass combustion, one fact remains very clear: the combustion of many biomass materials is still problematic and in some cases unacceptable because of the inherent characteristics of the fuel's inorganic constituents.

The presence of inorganic matter in solid fuels can create an environment that is detrimental to furnace grates, refractories, and waterwalls, as well as heat transfer surfaces downstream of the furnace (Levy et al., 1981; Raask, 1985; Jenkins et al., 1994). With regard to thermochemical conversion of biomass, inorganics affect the burning characteristics of the fuel as well as the ignition characteristics (Bakker, 2000). Bakker provides an excellent review of literature on the characteristics of inorganic constituents of biomass fuels as well as their impact on furnaces and boilers. These detrimental effects, coupled with the continued desire and need to lower NO_x emissions have, in part, provided the catalyst and driving force for new hybrid techniques, such as close-coupled gasification, which can provide an acceptable means for utilizing some of the more historically troublesome biomass fuels, like rice straw.

Power boilers utilize three principal types of combustors: grate burners, suspension burners and fluidized beds (Thorn et al., 1980). Grate burners utilize a perforated platform on which to burn the fuel. Fuel is usually but not always fed (or "stoked") onto the grate from overhead, sometimes into a pile and sometimes into a relatively uniform layer on the grate. Primary or "underfire" combustion air is delivered through the grate from underneath. Secondary, or "overfire" combustion air is delivered into the gas space above the grate, where it reacts with volatile fuel gases released by the heating, pyrolysis and partial oxidation of the fuel on the grate and fine particles entrained on the gas stream. Grates can be stationary or moving, flat or inclined and air cooled or water cooled.

Suspension burners burn the fuel particles while suspended in the air stream entering the boiler. In this sense, they are similar to fluid fuel combustors that employ one or more

burner nozzles on the side of the boiler. Small fuel particle sizes are required to ensure particle burnout and high heat release within the relatively short residence time in the flame. Fluidized bed combustors are discussed in more detail in section 1.6.

1.3 Gasification

Gasification technology was developed more than two hundred years ago (Kaupp and Goss, 1984). Gasification is a thermal process converting biomass feedstock into a mixture of gases that can be burned in boilers, internal combustion engines and gas turbines. The gasification process usually takes place in a reactor with a restricted supply of air. Gasification (pyrolysis) can also be done by indirect heating (no air). This process is sometimes known as gasification by partial combustion or partial oxidation and depending on reactor type may have a lower carbon conversion efficiency than combustion, producing a carbonaceous solid residue known as char.

Gasification takes place at elevated temperatures under substoichiometric conditions resulting in a typical equivalence ratio much greater than one. Because the gasification process takes place under substoichiometric conditions, the solid fuel is only partially oxidized and the thermochemical conversion yields a valuable energy carrier (known as a producer gas) that typically contains carbon monoxide, carbon dioxide, methane, hydrogen, nitrogen (especially if air is used as oxidant), other nitrogenous species, water, smaller amounts of lighter hydrocarbon gases, and varying amounts of tars, oils, acids, and other condensibles. The gas may also contain entrained char and ash particles.
Pyrolysis, which is the first step in gasification and solid fuel combustion, is the process of degrading or breaking down a material at elevated temperatures to produce oils, tars, char, and gases (e.g. CO, CO_2, H_2, H_2O, CH_4). A variety of oxidants can be used to complete the gasification process, including oxygen, air (Narvaez et al., 1996), steam (Herguido et al., 1992) or a combination of these.

An abbreviated gasification reaction for an organic fuel is as shown below in equation 1.2

$$C_xH_yO_z + n_1H_2O + n_2(1+e)(O_2 + 3.76\ N_2) = n_3CO_2 + n_4H_2O + n_5N_2 + n_6O_2 + n_7CO + n_8H_2 + n_9CH_4 + n_{10}C(s) + \text{other gases} + \text{tars, oils, acids} \quad [1.2]$$

1.4 Biomass Fuels

The components of biomass include cellulose, hemicellulose, lignin, lipids, proteins, simple sugars, starches, water, hydrocarbons, ash and other compounds. The concentration of each class of compound varies depending on species, type of plant tissue, stage of growth and growing conditions. Many elementary properties of biomass have been determined for a wide range of fuel types. Summaries of various types appear in the literature (Miles, 1995; Jenkins 1993, Domalski et al., 1987).

Miles et al. (1995) notes that biomass fuels can be subdivided into four major classes:

a) Wood and woody materials
b) Herbaceous and other annual growth materials such as straws, grasses and leaves
c) Agricultural by-products and residues including shells, hulls, pits, and animal manures
d) Refuse-derived fuels (RDF) and waste or non-recyclable papers often mixed with plastics

Inorganic elements include macronutrients, micronutrients and other beneficial nutrients and include the following elements: nitrogen, sulfur, phosphorus, magnesium, calcium, potassium, iron, manganese, copper, zinc, nickel, molybdenum, boron, chlorine, sodium, silicon and aluminum. These constituents can be divided into four groups of elements: refractory materials, alkali and alkaline earth elements, nonmetallic elements, and iron (Miles et al., 1995). Jenkins et al. (1996) points out that these four groups mainly differ in their degree of solubility and ion exchangeability, and whether they appear in the plant as an oxide, in ionic form, or as a constituent of larger more complex molecules. He also points out that the higher the degree of solubility or ion exchangeability of a certain element, the higher the likelihood of vaporization of that element during thermal conversion, and the higher the reactivity of the element.

With regard to biomass combustion systems, silica, which is contained in the refractory group of elements, is a major constituent of the inorganic fraction in many straws. Silica will form compounds that melt at low temperatures when in the presence of other elements, in particular the alkali metals potassium and sodium. Pure silica melts at around 1700°C, while a mixture of 32% K_2O and 68% SiO_2 will melt at 769°C (Raask, 1985).

Figure 1.1 is a binary phase diagram for both $Na_2O - SiO_2$ and $K_2O - SiO_2$ systems. This diagram shows how alkali influences the melting behavior of alkali-silicates. Note especially the depression in liquidus temperature for alkali concentrations in the 20 to 40% concentration range (60 – 80% SiO_2), characteristic of many cereal straws and other herbaceous materials.

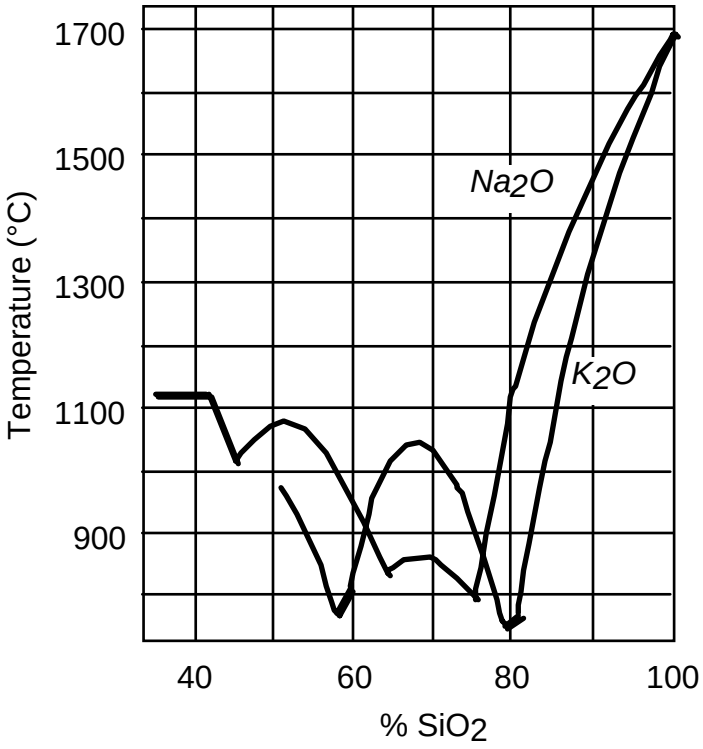

Figure 1.1 Binary phase diagram showing liquidus lines for Na_2O - and K_2O - SiO_2 systems. (Levin et al., 1956).

The second group of elements includes the alkali metals potassium and sodium and the alkaline earth metals calcium and magnesium. Jenkins (1996) notes that most of the potassium that is inherent to the fuel is volatile at typical boiler temperatures and will exist in vapor form as potassium chloride, KCl, or potassium hydroxide, KOH, if chlorine is absent. Both KCl and KOH are highly reactive compounds and will readily combine with sulfur oxides to form potassium sulfate.

The third group of nonmetallic materials includes chlorine, sulfur and phosphorous. Chlorine reacts with potassium and sodium to form relatively volatile and stable alkali chlorides (Miles et al., 1995). Direct observation of alkali vapor release during biomass fuel combustion by molecular beam/mass spectrometry (MBMS) showed that even at relatively low combustion temperatures (~ 800°C), significant amounts of alkali metals, along with chlorine, are released in the form of vapors (Dayton et al., 1995). Chlorine is corrosive to metallic surfaces and is also involved in the formation of acid gases (HCl) and toxic and hazardous air pollutants. Jenkins (1994) noted that almost all sulfur occurring in the fuel oxidizes during combustion to sulfur oxides, SO_2 and SO_3, and variable quantities of these gaseous species will react with potassium to form potassium sulfate, K_2SO_4 that condenses on fly ash or on furnace and tube walls and will subsequently promote ash agglomeration. Sulfur also reacts from the gas phase to replace Cl in existing deposits releasing it predominately as HCl. Chlorine is an inhibitor

of combustion. The presence of chlorine leads to depletion of radicals, highly reactive compounds that are essential in many combustion reaction mechanisms (Ho et al., 1992). The fourth group contains the transition elements and includes the element iron. Miles (1995) notes that although iron plays a major role in ash deposition in coal-fired boilers, there is very little iron in most biomass fuels, except for iron that is introduced from extraneous sources, such as soil. Sugar cane bagasse in Hawaii, for example, typically contains substantial amounts of iron from soil.

Metals present in biomass can influence the pyrolysis by either catalyzing or inhibiting thermal degradation (Williams and Horne, 1994). The major influence of inorganic metals on the pyrolysis of cellulose, one of the major organic components of biomass fuels, is to inhibit the formation of volatiles and increase the yield of char (Antal, 1983).

1.5 Close-Coupled Gasification

Close-coupled gasification is a combination of direct combustion and biomass gasification that can utilize low-grade biomass and waste fuels to reduce pollutant emissions in biomass boilers. The gaseous fuel produced in a gasifier can be used for cofiring and/or reburning applications in biomass boilers.

In cofiring, the producer gas from the gasifier is directed to the boiler's burners and co-fired with the principal fuel, or in the case of a solid fuel fired boiler, is fired through separate gas nozzles into the boiler. Gasification-based cofiring has been demonstrated in Lahti, Finland at the Lahden Lampovoima Oy's Kymijarvi power plant. The goal of this project is to demonstrate the direct gasification of wet biomass and the use of hot, low-BTU gas directly in the existing pulverized coal boiler (Palonen, 1998). There are problems in cofiring solid fuels, and gasification ameliorates these problems. Gasification based cofiring addresses several issues including accomplishing complete combustion in a furnace with a very short gas residence time (Tillman, 2000).

Reburning is essentially a staged-combustion technique for controlling nitrogen oxides. First tested in about 1950 and named in 1973, it has been commercially demonstrated in very large scale utility boilers (Hill et al, 1998). It is a process whereby a fuel is injected immediately downstream of the combustion zone to establish a fuel-rich zone which can convert nitric oxide to hydrogen cyanide, HCN and ultimately N_2 (Smoot et al., 1997). In the main combustion zone, 70% to 90% of the fuel is burned with a normal amount of air (about 10% to 15% excess). Then, in the second stage, the gasified fuel (known as the reburn fuel) is added into the secondary combustion zone to generate a fuel rich, reducing environment above the existing burner zone (Zamansky et al., 1999c). Typically, the amount of reburning fuel is 10 – 30% of the total fuel. NO_x is reduced to molecular nitrogen (N_2) by reactions with the hydrocarbon fragments produced by the substoichiometric combustion of the reburn fuel. Overfire air is then added through specially designed over-fire air ports to complete the combustion process. Laboratory experiments by Folsom et al (1991) showed that the NO_x and SO_2 emissions may be reduced up to 60% and 20%, respectively, by reburning.

1.6 Fluidized Bed Technology

In 1922, the development of the fluidized-bed technique started with the famous Winkler patent for the gasification of lignite. It took many years until this technique could be commercialized in power plant units. The first commercial plant in the United States, for example, with a circulating fluidized bed firing system was built at the University of Minnesota in 1979 (Jacobs, 1999). Due to the inherent advantages of low process temperatures, isothermal operating conditions and fuel flexibility, fluidized bed technology has been found to be one suitable approach to converting a wide range of biomass fuels into energy.

The fluidized bed is a set of solid particles, which are set into motion by blowing a gas stream upward through the bed at a sufficient velocity to locally suspend the particles, but yet not too great a velocity to blow the particles out of the bed. The circulating bed, however, does just this, with particles recirculating through disengagement from the flow. During overall circulation of the bed, there are transient streams of gas flowing upwards in channels containing few solids and clumps or masses of solids flowing downwards The fluidized bed looks like a boiling liquid and has many similarities in physical properties to a true fluid. In fluidized bed combustion of biomass, the gas is usually air and the bed is usually sand or limestone. The air acts as the fluidizing medium and is the oxidant for biomass combustion (Overend et al., 1998). While gaseous and liquid fuels may be burned in fluidized beds, the main applications for fluidized beds are combustion and gasification of solid fuels (Borman et al., 1998).

Bubbling Bed

The basic components of a bubbling fluidized bed are the air plenum, the air distributor, the bed material, disengagement zone and the freeboard as shown schematically in Figure 1.2. The disengagement zone (considered part of the freeboard) is the section above the expanded bed that is largely free of bed particles, is designed to disengage the bed material that travels out of the fluidized bed portion of the reactor.

After the material is disengaged, it falls by gravity back into the fluidized bed. The velocity of the air delivered through the distributor into the bed is at a sufficiently high velocity (1 to 3 m s^{-1}) to cause a bubble phase to form. If the air flow of a bubbling bed is increased beyond this range, the air bubbles become larger, forming large voids in the bed and entraining substantial amounts of solids. This type of bed is referred to as a turbulent bed (Kunii and Levenspiel, 1987; Babcock and Wilcox, 1992).

Circulating Bed

As with bubbling fluid beds, the primary driving force for development of circulating fluid beds in the United States is emissions (Overend et al., 1998). The uniform low temperature gives low thermal NO_x emissions. Circulating fluidized bed temperatures are maintained at about 870°C, which helps to optimize the limestone-sulfur reactions

(Tampella Power, 1992). The circulating bed operates at a higher gas velocity (3 to 10 m s^{-1}) than the bubbling bed, and employs a particle separation device (such as a cyclone) either within the primary reactor or external to it. At higher velocities, a greater fraction of the bed is entrained on the gas flow and exits the reactor. The larger particles, including the incompletely reacted fuel particles, are returned to the bed to increase fuel burn-up and combustion efficiency.

1.7 Bed Agglomeration

Agglomeration of bed media is a major ash-related problem encountered in fluidized bed boilers that can lead to severe defluidization of the bed, and possibly plant shut down (Salour et al., 1993; Natarajan et al., 1998).

The fluidized bed is rather homogeneously mixed, which creates a nearly uniform temperature distribution. Localized high temperature zones are largely eliminated, thus reducing slagging for certain types of fuels. However, volatiles released from the fuel can burn above the bed, creating a high temperature zone in the freeboard, and which may lead to bed agglomeration and eventual bed defluidization. Reactions between bed particles and elements in the fuel ash lead to bed agglomeration. Although agglomeration is not anticipated at most gasification temperatures with clean wood fuels, in the case of straw and other high ash, high alkali fuels, alkali reacting with the silica in the bed media can lead to rapid agglomeration. Transformation of the inorganic fraction may lead to severe bed agglomeration in fluidized bed combustors.

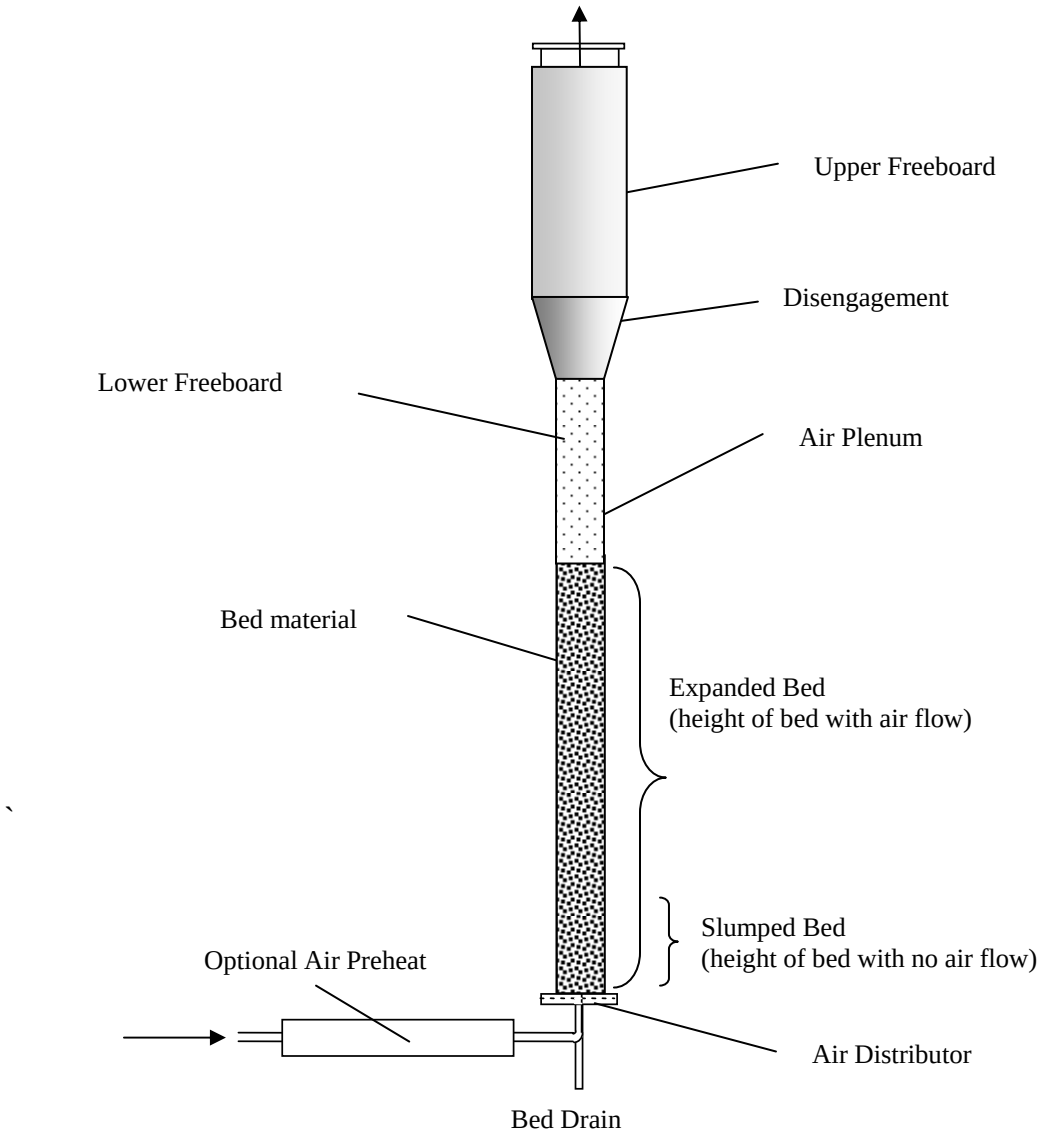

Figure 1.2 Components of a bubbling fluidized bed

Ohman (1997) points out that there are no reliable methods to determine bed agglomeration tendencies of different fuels, fuel combinations or fuels with additives. Standard ash fusion tests (e.g. ASTM D 1857 and DIN Prufung no. 51730) are often used to predict the behavior of the ash in different processes, but the methods have been extensively criticized in the literature (Wall et al., 1995; Coin et al., 1995). For example, it was shown by Stallman et al. (1980) that agglomeration often occurs at temperatures several hundred degrees below the initial deformation temperature of the ash, as determined by ASTM ash fusion test. Ohman (1997) notes that a more relevant method would be to use a fluidized bed for actual bed agglomeration studies and states that the most important individual parameter influencing the bed agglomeration is the actual bed or process temperature. He concludes by stating that the controlled fluidized bed agglomeration test seems to be a valuable and accurate method to determine agglomeration tendencies for different fuels and fuel and additive combinations.

Fluidized beds utilize a bed material to transfer heat to the fuel particles and to absorb unwanted constituents. Bed materials include silica and alumina-silicate sands and reactive materials include such products as limestone ($CaCO_3$) and magnesium oxide (MgO). Other materials like alumina-silicates are sometimes considered inert but are not truly inert, with silica reacting with alkali leading in some cases to agglomeration.

Fluidized bed technology offers a number of inherent advantages. Fluidized bed systems incorporate a substantial heat storage capacity, which insures ignition, and allow for a fast fuel load increase. Owing to the substantially longer residence time of fuel particles, the combustion or gasification reactions of fuel particles can be better controlled because of longer residence times in comparison to entrained flow firing systems (Jacobs, 1999). Generally because there are lower temperatures in the fluidized bed process, (815° C to 900° C) there is relatively lower thermal NO_x production, less volatilization of alkali metals and less erosion of in-bed boiler tube surfaces (Borman et al, 1998). Fuel flexibility is enhanced by allowing the use of a range of solid fuels with widely varying ash and moisture contents (Borman et al., 1998). Systematically higher heat transmission parameters can also allow for substantially smaller heat transfer surfaces. This can render the plant more compact, and possibly less expensive.

1.8 Fouling

Fireside fouling in solid fuel combustion is defined as the formation and accumulation of troublesome ash deposits on heat transfer surfaces in the furnace or the convection sections downstream of the furnace: superheaters, generating banks, reheaters, economizers and air heaters. In circulating fluidized bed boilers, fouling may also be encountered in particle separation devices (e.g. cyclones) that are situated directly downstream of the combustor (Jenkins et al., 1996). Fouling is responsible for a number of detrimental effects including: reduced heat transfer from convection pass tubes, an inability to achieve design superheat temperatures and increased gas-side pressure loss. Depending on combustion conditions and the type of inorganic matter in the solid fuel (i.e. inherent inorganic matter or inorganic matter added through fuel collection and

processing), ash produced during combustion is composed of varying amounts of vapors, fumes and larger particulate matter (Baxter, 1993).

1.9 Nitrogen Oxides and Reburn Chemistry

The formation of nitrogen oxides (NO_x) in combustion systems is a significant pollutant source in the environment. As the utilization of fossil fuels (natural gas, coal and fuel oil) continues to increase, the control of NO_x emissions will continue to be a world-wide concern.

NO_x reaction processes are very complex and comprehensive modeling of NO_x formation and reduction in turbulent reacting systems is difficult (Hill et al., 2000). Nitrogen oxides consist of nitric oxide (NO), nitrogen dioxide (NO_2) and nitrous oxide (N_2O). The combination of NO and NO_2 is commonly referred to as NO_x. From a health perspective, NO is a harmful pollutant causing direct respiratory injury and is the precursor for acid rain and ground-level ozone. N_2O is a very strong greenhouse gas and destroys ozone in the stratosphere (Winter et al., 1999).

During combustion, nitrogen from the air or fuel (fuel-bound nitrogen) is converted to nitrogen containing pollutants such as NO, NO_2, N_2O, NH_3 and HCN. In the combustion or gasification of biomass fuels, the primary source of nitrogen, for these species, is fuel nitrogen. The pollutant species formed depends principally on the temperature and fuel/oxygen ratio in the combustion zone (Hill et al., 2000). NO_2 typically makes up about 10% of NO_x released from methane/air flames, but it can rise to as high as 90% in low-temperature, low NO_x flames due to the high ratio of H to NO (Fiveland, et al., 1991). The amount of NO_2 formed is very sensitive to the fluid dynamics in the flame zone (Driscoll et al., 1992) and unexpectedly high levels of NO_2 have been measured in premixed flames (Hori, 1988). Note also that NO, once emitted, is oxidized to NO_2 in the atmosphere.

Nitrous oxide (N_2O) is a greenhouse gas and participates in ozone depletion in the stratosphere. Some N_2O does result from fluidized bed combustion due to the lower operating temperatures (Kramlich, 1994). N_2O can be formed by a number of reactions in gas reactors, but it rapidly reacts with H and OH radicals to form N_2.

NO from combustion systems results from three main processes: thermal NO, prompt NO and fuel NO. Published reviews including Bowman (1993), Kramlich (1994) and Pershing et al., (1979) document various details of one or more of these basic processes. The seminal contributions of Zeldovich (1946) on thermal NO_x, Fenimore (1979) on prompt NO_x and Pershing and Wendt (1979) on fuel NO_x are excellent references.

Thermal NO_x is formed from oxidation of atmospheric nitrogen at relatively high temperatures in fuel-lean environments, and has a strong temperature-dependence. This process is described by the widely accepted Zeldovich two-step mechanism shown in equations [1.3] and [1.4]:

$$N_2 + O = NO + N \quad [1.3]$$
$$N + O_2 = NO + O \quad [1.4]$$

The extended Zeldovich mechanism is used in some cases when NO from the Zeldovich mechanism is under-estimated. This extended Zeldovich mechanism is shown in equation [1.5].

$$N + OH = NO + H \quad [1.5]$$

Prompt NO is formed by the reaction of atmospheric nitrogen with hydrocarbon radicals in fuel rich regions of flames, which is subsequently oxidized to form NO. This was first reported by Fenimore (1976) who studied NO formation in Meker-type burners from gaseous pyridine and ammonia. He observed a higher NO formation rate in the fuel-rich regions of hydrocarbon flames. Prompt NO formation occurs in fuel-rich regions where hydrocarbon radicals increase the formation of HCN through the following reactions shown in equations [1.6] and [1.7]:

$$CH + N_2 = HCN + N \quad [1.6]$$
$$CH_2 + N_2 = HCN + NH \quad [1.7]$$

Fuel NO is formed from nitrogen bound in the fuel and is usually assumed to proceed through formation of HCN and/or NH_3 which are oxidized to NO while being competively reduced to N_2 according to the overall reactions shown in equations [1.8] and [1.9]:

$$HCN/NH_3 + O_2 \rightarrow NO + \ldots \quad [1.8]$$
$$NO + HCN/NH_3 \rightarrow N_2 + \ldots \quad [1.9]$$

The concept of reburning was originally introduced by John Zink Company (Reed, 1969) and Wendt (Wendt et al., 1973) and was based on the principle of Myerson (Myerson et al., 1957) that hydrocarbon fragments (CH) can react with NO_x. It is known that the emission of oxides of nitrogen (NO_x) from combustion processes can be reduced by the gas reburning process (Zamansky et al., 1997).

The reduction of NO_x occurs primarily in the reburn zone by reaction of NO with hydrocarbon fragments (CH, CH_2). These reactions typically produce hydrogen cyanide, which decays in the reburning zone along the chemical pathway in equation [1.10].

$$NO + CH_i \rightarrow HCN \rightarrow NCO \rightarrow NH \rightarrow N \rightarrow N_2 \quad [1.10]$$

The last step in this chemical pathway which converts the N to N_2 is called the reverse Zeldovich reaction, shown in equation [1.11], which is accepted as the primary route of NO formation and destruction in the thermal NO_x mechanism (Harding et al., 2000).

$$N + NO \rightarrow N_2 + O \quad [1.11]$$

The use of biomass to reduce NO_x is attractive for several reasons. First, biomass is a regenerable biofuel and when a fossil fuel is replaced by a biofuel, there is a net reduction in CO_2 emissions. In large scale systems, it is difficult to mix natural gas into the products of the primary combustion zone since the gas must be injected from the wall, at relatively low flows. Wood particles, which must be transported to the furnace by a carrier medium (flue gas in this case) have a ballistic effect upon entering the furnace that can enhance cross-stream mixing compared to the natural gas case (Harding et al., 2000). However, the use of producer gas from close coupled gasification will also pose mixing difficulties similar to natural gas reburning.

Many researchers including Glarborg and Hadvig (1991), Li et al (1993), Hura and Breent (1993) and Burch et al (1993), found for various reburning fuel types that two major kinetic pathways control the efficiency of reburning. These reactions are shown in equations [1.12] and [1.13].

$$C, CH, CH_2 + NO \rightarrow HCN + \ldots \quad [1.12]$$
$$HCN + O, OH \rightarrow N_2 + \ldots \quad [1.13]$$

Chagger et al. (1991) found experimentally that NO_x is slightly reduced by the presence of SO_2.

To provide higher levels of NO_x control, technologies are being developed based on hybrid schemes of reburning plus injection of a nitrogen agent (ammonia or urea) (Maly et al., 1998). This type of process is known as advanced reburning. Advanced reburning techniques have been used to obtain even greater levels of NO_x control and to utilize alternative fuels (Zamansky, 1996a). The advanced reburning process consists of three main processes: (1) injection of reburning fuel (e.g. biomass derived producer gas) to the products of the main burner; (2) the addition of N-agent, typically urea ($CO(NH_2)_2$), to the reburn zone or to the overfire air; and (3) the injection of overfire air which completes the process by burning out remaining combustibles. The advanced reburning process is identical to that of basic reburning except for the addition of the N-agent injection process (Zamansky et al., 1997). In close-coupled gasification systems using alkali-containing biomass, steps (2) and (3) above can be combined because the gasified biomass and/or waste fuel that is injected into the reburn zone already contains volatile species, including K and Na, which are known to promote the reburn process.

An advanced reburning process was recently patented (Ho et al., US Patent 5,270,025, 1993; Seeker et al., US Patent 5,756,059, 1998). In another study, Zamansky (1996b) found that injection of small amounts of an alkali promoter species along with ammonia into the reburning zone can further improve upon the advanced reburn process. The most effective promoter compounds were found to be alkalis, most notably sodium compounds (Maly et al., 1998).

Some researchers believe that the efficiency of waste reburning (i.e. using waste biomass fuels) is higher because waste fuels already include N-, Na- and K- containing compounds which promote the reburning process. In effect, the alkali serves as a catalyst

and thus lowers the activation energy of the reaction. In one study, injection of 15 ppm Na_2CO_3 with a urea solution in advanced waste reburning resulted in 94% to 96% NO_x reduction (Zamansky et al., 1996b).

More recently modeling was used in one study to determine the mechanism of the effect of Na-containing additives on NO_x reduction. The model combined a detailed description of the reburning chemistry with a simplified representation of the mixing. The modeling suggested that reduction of NO_x emissions in the presence of sodium-containing compounds was due to the inhibition of the combustion process by sodium. Because NO_x formation via thermal and fuel-NO mechanisms strongly depends on the local combustion environment, NO_x formation in the main combustion zone was inhibited because H, OH and O concentrations in the combustion zone decreased in the presence of Na (Lissianski et al., 2000).

One experimental study showed that injection of 100 ppm of K, Na, or Ca in the absence of reburning resulted in approximately 19%, 21% and 16% NO_x reduction respectively. Injection of 100 ppm K, Na or Ca (one at a time) with the main fuel in the presence of reburning, provided an additional 7%, 7% and 4% reduction respectively for each metal additive. The results also illustrate that both K- and Na-containing compounds are slightly more effective than Ca-containing compounds when added to the main fuel (Lissianski et al., 2000).

Also noteworthy was the determination that metal additives are much more effective than the compounds of the same metals present in fly ash. The flow rate of fly ash in one test was such that concentrations of iron, calcium, potassium and sodium from the fly ash in the flue gas (if all metals were released in atomic form) would be approximately 400 ppm, 90 ppm, 120 ppm and 60 ppm respectively. However, their effect on NO_x reduction is only 1 to 2 percentage points. The negligible effect of these metals can be explained by the difference in the chemical nature of metal compounds in the additives versus fly ash. Although traditional ash analyses present mineral composition in the form of metal oxides, the oxides are not the actual forms of the metals in fly ash. The metals are mainly present in the form of sulfides and silicate-alumino silicate matrices that are more stable than carbonates and acetates and thus are not effective in reactions with combustion radicals and therefore have minimal effect on NO_x reduction (Lissianski et al., 2000). The effect of alkali metals injection on NO_x reduction is less than the combined effect of N-agent and metal (Zamanski et al., 1996b; Zamanski et al., 1999a).

1.10 Modeling of Fluidized Beds

Scale-up and commercialization of any chemical process is an inexact science and the scale-up of fluidized bed processes is especially so (Matsen, 1996). With tests on large fluidized bed boilers being extremely expensive (Werther, 2000), one issue facing designers of fluidized bed systems is the applicability of laboratory-scale fluidized bed test data to the design of full-sized commercial fluidized beds.

Although much effort has gone into the modeling of fluidized bed gasification of coal (Wang et al. 1997; Huilin et al., 1999; Fang et al., 2000) there is limited information on mathematical models for fluidized bed gasification of biomass. Guo et al. (2000) notes that it is difficult to develop a simulation model for scale-up of biomass gasification because of a number of reasons: complexity of biomass gasification in a fluidized bed reactor, which involves gas-solid two phase flow, heat and mass transfer, pyrolysis of biomass material, cracking and subsequent steam reforming of tar vapor arising from the pyrolysis, heterogeneous gas-solid reactions and homogeneous gas-phase reactions. In addition, behavior of the gasification process is dependent on many factors including: type of material, operating temperature and pressure, residence time of solid and gas in the gasifier and feed rates of biomass and steam and/or air. Although considerable research in the biomass field has been done (Corella et al., 1989), actual studies involved in process modeling are few.

The studies that were found in the literature discuss both the basic bubbling fluidized bed and the circulating fluidized bed. Flow regimes include: bubbling, slug flow, turbulent fluidization including Type I and Type II as defined by Bi and Grace (1995) and fast fluidization. Geldart (Grace, 1984; Kunii and Levenspiel, 1987) observed the nature of particles fluidizing. He categorized his observations by particle diameter versus the relative density difference between the fluid phase and the solid particles. Geldart identified four regions in which the fluidization character can be distinctly defined.

Group A particles are characterized by a bubbling bed fluidization. The bed expands considerably before bubbling occurs and gas bubbles rise more rapidly than the rest of the gas. Bubbles spit and coalesce frequently through the bed and maximum bubble size is less than about 10 cm. Internal flow deflectors do not improve fluidization and gross circulation of solids occurs.

Group B particle beds are the most common. These beds are made of coarser particles than group A particles and are denser. They form small bubbles at the distributor that grow in size throughout the bed and have bubble sizes independent of the particle size and achieve gross circulation in the bed.

Group C particles are difficult to fluidize and tend to rise as a slug of solids and form channels in large beds with no fluidization, and tend to be cohesive.

Group D particles are very large, dense particles and form bubbles that coalesce rapidly and grow large, forming bubbles that rise slower than the rest of the gas phase. They form beds whose dense phase surrounding the bubbles has low voidage and cause slugs to form in beds when the bubble size approaches the bed diameter, and spout from the top of the bed easily.

In Type I, for Geldart group A solids, there is usually a relatively sharp transition from bubbling to a turbulent regime where small transient voids dart in a zig-zag manner up the bed, while particles are propelled obliquely upwards and also shower downwards. Type II turbulent behavior, encountered with Geldart group B and D solids, involves

intermittency. Periods of slug-flow-like behavior alternate with periods of fast-fluidization-like behavior, the latter becoming predominant as the fluidization velocity increases. While each of these flow regimes is encountered in industrial practice, reactor modeling has concentrated on bubbling beds (Grace, 1984; Kunii and Levenspiel, 1987). The lower and upper boundaries of these flow regimes have been delineated and predicted by various models and empirical correlations (Bi and Grace, 1995). Again, the majority of these models were developed for coal gasification instead of biomass gasification.

There is a significant difference between the fuel properties of biomass and coal (Ergudenler et al, 1992). The volatile content of biomass fuels is much higher (70 – 90%) than that of most coals (30 – 40%). This increases the importance of char gasification and the kinetics involved in gasification of coal, whereas for biomass fuels char gasification and its kinetics are not of the same importance due to the much higher reactivity of the fuel (Maniatis et al, 1988; Bacon et al, 1985; and Kosky and Floess, 1980). Jones et al. (2000) also notes that in comparison to a bitumous coal such as Pittsburgh No. 8, for example, straw burning involves extensive devolatilization and, as a consequence, the char burnout of the residue, which is a small quantity, does not play a significant part of the overall process. However, char burnout can be important for some biomass materials, such as rice hull.

Ergudenler et al. (1992) notes that in modeling any chemical reactor, the primary objective is to represent the key physical and hydrodynamic features of the system with reasonable accuracy, before inserting kinetic and other chemical parameters. The hydrodynamics of fluidized beds are far too complex to be used for deriving reaction kinetics (Grace, 1986). Grace (1986) recommended that the kinetic parameters should be obtained in reactors where the hydrodynamics can be described with confidence.

A comprehensive review of gasifier modeling was done by Buekens and Shoeters (1982, 1984). Models have been identified as being of five types. They are:

1) Equilibrium model – Reactor is considered to be lumped with known inputs of fuel and air. Exit gas composition determined by assuming a fixed reaction temperature and reaction equilibrium.
2) Kinetics free model – Reactor is divided into zones and each zone is assumed to be in chemical equilibrium with zone/reaction temperature determined by a separate energy balance.
3) Steady-state model – Model is based on governing equations for individual chemical species, energy of solid phase and energy of gas phase with transient terms neglected. Some models assume gas and solid temperature to be equivalent.
4) Semi-transient model – Transient terms in the governing equations are calculated using the pseudo-steady state assumption based on results from a steady state model.
5) Transient model – Governing equations are solved without simplification.

Additional model types found in the literature include: (a) thermodynamic models (Double et al., 1989; Bacon et al., 1985), (b) single phase models based on either a well

mixed reactor or a plug flow reactor (Prudy et al., 1981; Carman and Amudson, 1979), (c) two or three phase models featuring a distinct type of gas flow in the dense and the lean phase (van den Aaren et al., 1986) and (d) transient models (Weimer and Clough, 1981). Most of these are two-phase models in which the fluidized bed is divided into two regions: a solids-free bubble phase (also known as lower density or lean phase) and a solids-laden emulsion phase (also known as higher density or dense phase). Kulasekaran, et al. (1998) note that various assumptions have been employed to represent the motion of gas and solids within this framework. For fluidized bed models, however, these two-phase models are unable to predict the gas back mixing (Latham, 1970) and the recycle peak in solids mixing (Lim et al., 1993). Three phase models, which account for the presence of a cloud/wake phase, can predict the observed gas and solids mixing behavior. However, these models have been applied only for parametric studies on the combustion of char in fluidized beds operated under steady state conditions (Chen et al., 1977).

Single particle models have also been formulated for drying, volatile evolution and char combustion with the effect of the fluidized bed environment reflected in the boundary conditions of the particle problem. This approach has delivered considerable insight into the effect of various operating/design parameters on the dynamics of the individual processes (Agarwal, 1989; Prins, 1987).

Kaupp (1984) identifies six fuel properties, which affect producer gas quality. These are:

-Physical shape of particle and fuel bed structure
-Moisture content
-Volatile matter
-Ash content
-Ash composition
-Heating value

The importances of these fuel properties differ for different types of reactors. In addition, chemical composition has an overall bearing on gas composition and behavior of inorganic materials.

Turn (1994) notes that from a modeling perspective, the last five properties can be incorporated at a satisfactory level of sophistication relatively easily, however, the first property may be more challenging depending on fuel geometry.

Much research (Jones et al. 2000; Schiefelbein, 1989; Buekens and Schoeters, 1985; and Graboski and Bain, 1981) indicates that the volatile matter contained in biomass is released very rapidly as soon as the biomass is introduced into the reactor. This research suggests that the use of gas-phase reactions may be more appropriate than the gas-solid reactions commonly found in coal gasification.

Desrosiers (1981) notes that no hydrocarbon other than methane (CH_4) is thermodynamically stable under gasification conditions. Based on Desrosiers research, it

seems reasonable to only include CH_4 as the hydrocarbon to consider under equilibrium conditions in simple models.

With regard to equilibrium models, the STANJAN computer program (Reynolds, 1986), a FORTRAN based computer program in DOS developed by Reynolds at Stanford University, uses the Joint Army-Navy-Air Force (JANAF) (Stull and Prophet, 1971) thermochemical data in calculating equilibrium concentrations. In general, the program can calculate equilibrium between multiple phases, each containing multiple species. It provides an efficient algorithm for minimizing the Gibbs free energy of the mixture. A number of programs use the STANJAN engine in this manner, and a number of other equilibrium solvers exist.

Chemkin is another package of FORTRAN subroutines that are designed to facilitate simulations of reacting flows (Kee et al., 1980). Using Chemkin, chemical mechanisms may be specified in a problem-independent way, making them transportable between application codes and between users. Application codes call the Chemkin subroutines to calculate thermodynamic and chemical-kinetic quantities of interest for the particular application.

Another model, MFIX (Multiphase Flow with Interphase eXchanges) (Syamlal, 1994) is a general-purpose hydrodynamic model that describes chemical reactions and heat transfer in dense or dilute fluid-solids flow, flows typically occurring in energy conversion and chemical processing reactors. MFIX calculations give detailed information on pressure, temperature, composition and velocity distributions in the reactors.

Some modeling work has been done using ASPEN (Advanced System for Process ENgineering). ASPEN was developed at the Massachusetts Institute of Technology (MIT) under a United States Department of Energy project to simulate coal conversion processes. It has now become a tool modeling chemical, power generation and other processes (Sotudeh-Gharebaagh, 1997). ASPEN PLUS is widely accepted in the chemical industry as a design tool because of its ability to simulate a variety of steady-state processes ranging from single unit operation to complex processes involving many units.

The Comprehensive Simulator for Fluidized-Bed Equipment (CSFB) (de Souza-Santos, 2001) is a one-dimensional, steady state, gas-solid model. This model allows up to five physical phases and applies chemical reaction kinetics, fluid dynamics and heat and mass transfer in predicting reactor conditions and process states. Due to the specific and apparently comprehensive nature, this model was tested against experimental data as described later.

1.11 Summary

A variety of biomass and waste fuels are presently underutilized because of their poor combustion characteristics (fouling and slagging), high levels of pollutant emissions including NO_x and N_2O and adverse effects on boiler operation. Gasification, which takes place at elevated temperatures under substoichiometric conditions, results in only partially oxidized fuel and the thermochemical conversion of the fuel yields a valuable energy carrier.

Ammonia and the alkali metals of sodium and potassium have been shown to be effective promoters of NO_x reduction. Addition of alkali-containing compounds have been shown to increase NO_x reduction in combustion and reburning applications and increases reburning NO_x reduction when compared to straight reburning. Ammonia has been shown to be a dominant fuel nitrogen species, in some cases accounting for up to 60% of the fuel nitrogen. Hydrogen cyanide, although not a prominent species produced in gasification is important in controlling the efficiency of reburning.

A review of literature suggests that biomass fuels inherently containing alkali materials (mostly K) and fuel nitrogen that directly leads to the production of NH_3 and HCN can be potential candidates for use in the close-coupled gasification process leading to reduced NO_x levels.

CHAPTER 2 EXPERIMENTAL MATERIALS AND METHODS

2.1 Introduction

Fluidized bed gasification characteristics of a variety of biomass fuels were investigated for this study. Six fuels were selected: Almond shells (ASF), agricultural tree prunings, (WPF, also referred to as wood "p") from walnut orchards, rice straw (RSF), whole tree wood chips (WWF, also referred to as wood "w"), sewage sludge (SLF) and non-recyclable waste paper (NPF).

The fuels were gasified under a range of operating conditions including: air pre-heat temperature, bed wall temperature, bed gas temperature, stoichiometry, bed depth and type of bed material.

This section describes the gasification tests conducted, the equipment used and the data analysis.

2.2 Test fuels

Test fuels were procured through different sources and collected from various parts of California as shown in Table 2.1.

Table 2.1 Fuels used in experimental program

Fuel	Acronym	Description
Almond Shell*	ASF	By-product of the almond nut industry, Central and Sacramento Valleys, CA, USA
Orchard* Prunings	WPF	Walnut orchard tree prunings. Designated Wood "P" for experiments
Rice Straw	RSF	Rice straw (non-leached) from Sutter County, CA
Whole Tree* Chips	WWF	A mixture of coniferous and California Oak whole tree chips obtained from the western slopes of central Sierra Nevada Mountains. Designated Wood "W"
Sewage Sludge	SLF	Air-dried sewage sludge from anaerobic digesters at the East Bay Municipal Utility District Waste Water Treatment Plant, Oakland, CA.

Non Recyclable+ Paper	NPF	A mixture of approximately 80% cardboard (non-waxed) and 20% softwood (coniferous) from shredded cardboard and wooden crates.

*These fuels provided courtesy of Wheelabrator Shasta Energy Company, Anderson, Ca.
+ Non Recyclable Paper provided by GEER, Irvine, Ca.

Four of the fuels, ASF, RSF, SLF and NPF are problematic in conventional combustion boilers due to relatively large amounts of one or more of the following: alkali metals, chlorine, heavy metals and ash.

ASF can contain moderately high levels of chlorine. This chlorine can create an environment that fosters corrosion and also facilitates the volatilization of alkali (Na and K) leading to enhanced fouling of heat exchange equipment. WPF is a fuel with low ash, low sulfur, low nitrogen and moderate amounts of alkali. RSF has a high level of ash and the majority of this ash is in the form of silica (SiO_2) that is involved in a number of combustion/gasification related problems. The combination of potassium with silica in rice straw leads to high rates of slag formation and fouling due to the decrease in ash fusion temperature. The use of rice straw in biomass power plants is currently very limited (essentially non-existent) and would require leaching to be more suitable for combustion (Jenkins et al., 1999). WWF is a fuel with low ash, sulfur, alkali, and a relatively high heating value. SLF, which is available in large quantities, has very high contents of moisture, ash and nitrogen. NPF in general, is an abundant waste fuel with low ash but a moderate level of chlorine.

All test fuels, except SLF and NPF, were knife-milled through a 1 mm screen (Fritsch, Model P-19, Idar-Oberstein, Germany) for the purposes of feeding to the fluidized bed reactor. The NPF was milled through a 2 mm screen because it "fluffed" too much with the smaller screen (smaller screen created particles with a combined greater surface area making it very difficult to feed). The SLF was friable enough that only processing by hammer mill (Mix Mill Inc., Bluffton, IN) with a 13 mm screen was needed. The hammer mill was used primarily to break-up clumps of fuel formed during air drying. The sludge was otherwise present as particles. Fuels were fed to the reactor between 6% and 15% moisture content. Fuel conditions were fully determined at the time of each test. All fuels were analyzed for the following characteristics:

-Moisture content (% wet basis, air-oven method)
-Higher heating value at constant volume (MJ kg^{-1} dry basis, via adiabatic bomb calorimeter)
-Proximate analysis for ash, volatiles, and fixed carbon (% dry matter)
-Ultimate analysis for C, H, N, S, O (by difference), and Cl (% dry matter)
-Ash elemental analysis for Si, Al, Ti, Fe, Ca, Mg, Na, K, P, S, Cl, and CO_2 (% ash)
-As-fired bulk density (kg m^{-3}, dry basis)
-As-fired particle size distribution (% dry matter by size fraction via sieve analysis)

-Ash fusibility (initial deformation temperature, softening temperature, hemispherical temperature, fluid temperature), oxidizing and reducing conditions, via ASTM pyrometric cone determination.

Procedures used for these analyses are briefly summarized in Table 2.2 and further discussed below. Bulk fuel samples for analysis were collected and split for the various analyses.

2.3 Moisture content

Knowledge of fuel moisture was necessary in order to determine dry basis fuel flow for mass balance calculations and for setting the fuel feed belt speed (see reactor description below) to meet the target air:fuel ratio (AF). Samples of fuel were analyzed prior to each experiment for proper setting of the air and fuel flow rates, and samples were also collected from the feed belt at the start and conclusion of each test.

Moisture content was determined gravimetrically by the oven drying method (ASTM D 3173, ASTM E 871). Triplicate samples typically weighing 20 to 80 g each were obtained from the fuel container or feed belt and air-dried in a 104±3 °C air oven to constant weight, normally obtained within 24 h.

Table 2.2. Fuel sampling and analysis

Analysis	Method/Test Lab	Sampling
Moisture (% wet basis)	Air-oven (104±3°C) UCD Biomass Lab	Split batch, prior to tests Split batch, from fuel feed belt, start and end of test
Higher Heating Value (MJ kg^{-1})	Adiabatic Bomb Calorimeter UCD Biomass Lab	Split batch, prior to tests
Proximate Analysis (ash, volatiles, fixed carbon)	Muffle furnace UCD Biomass Lab	Split batch, prior to tests
Ash (% dry matter)	Muffle furnace, 575°C/2h UCD Biomass Lab	Split batch, prior to tests
Volatile matter (% dry matter)	Muffle furnace, 950°C, modified method for sparking fuels, UCD Biomass Lab	Split batch, prior to tests
Fixed carbon (% dry matter)	By difference on ash and volatile matter	
Ultimate Analysis (C, H, O, N, S, Cl) (% dry matter)	Hazen Research, Inc. (Golden, CO)	Split batch, prior to tests
Ash Elemental (Si, Al, Ti, Fe, Ca, Mg, Na, K, P, S, Cl, and CO_2 (% ash)	Hazen Research, Inc. Ashed at 575°C	Split batch, same sample as ultimate analysis
Bulk Density (kg m^{-3})	Volumetric, drop test	Batch, prior to tests

	UCD Biomass Lab	
Particle size distribution	Sieve UCD Biomass Lab	Split batch, prior to tests

2.4 Heating Value

Higher heating value at constant volume (HHV) was measured using an adiabatic oxygen bomb calorimeter (via the equivalent methods ASTM D 2015, ASTM E 711, or ASTM D 5468). These methods give the heat released by the combustion of the fuel in oxygen at constant volume. HHV includes the energy released by the condensation of the water. Most practical biomass energy systems do not recover the energy of condensation. The lower heating value, LHV, is defined for water product in the vapor state and can be computed from the HHV, the fuel hydrogen concentration, and the fuel moisture content.

Triplicate samples, approximately 1 g each, were split from batches prior to each test and analyzed using the bomb calorimeter (Parr, Model 1241, Moline, Illinois) with controller (Parr, Model 1720, Moline, Illinois) housed in the UC Davis Biomass Laboratory. Each determination was corrected for fuse consumption and nitric acid formation as set out in the standards. The instrument calibration was confirmed at each batch of samples against the standard heating value of benzoic acid (C_6H_5OOH): 26.453 MJ kg^{-1}.

Fuel was knife-milled to pass 40 mesh, sampled in 1 g amounts, pelleted in a hand press to 0.5 in (12.7 mm) diameter, and oven dried to constant weight at 104±3°C prior to analysis.

2.5 Proximate Analysis

Proximate analysis is an assay of moisture, ash, volatile matter, and fixed carbon as determined by prescribed methods (fixed carbon was calculated by difference from ash and volatiles determined as fractions of dry matter). Proximate determinations were made according to modified procedures from ASTM D 3172 through D 3175 (Standard Practice for Proximate Analysis of Coal and Coke); E 870 (Standard Methods for Analysis of Wood Fuels), E 871 (moisture in wood), D 1102 (ash in wood), and E 872 (volatile matter in wood); and the methods for refuse derived fuel (RDF)--E 830 (ash), and E 897 (volatile matter). For reporting purposes, moisture, which was normally part of the proximate analysis, is reported separately, and ash, volatiles, and fixed carbon are given as percent of dry matter.

Triplicate samples, approximately 1 g each, split from the main sample batch were knife-milled to pass 40 mesh, oven dried at 104±3°C, and analyzed. The amount of ash was determined at 575°C for 2 h in an atmospheric pressure air muffle furnace. This temperature was that specified by ASTM for RDF, and was slightly below the minimum temperature specified for wood (580°C). The ashing temperature specified for coal (750°C) is too high for biomass, resulting in loss of volatile alkali and decomposition of species. Volatile concentration was determined using a modified method for sparking

fuels in which samples in covered nichrome crucibles were placed in the front part of the open muffle furnace preheated to 950°C for 6 minutes to dispel volatiles over a period of more gradual heating, then brought to completion in the closed furnace during an additional 6 minutes, removed, and cooled under desiccant while still covered. Percent fixed carbon (dry basis) was computed by subtracting percent ash (dry basis) and percent volatile matter (dry basis) from 100 percent. All crucibles were first pre-fired at the test temperature (575 or 950°C) to remove any moisture or volatiles prior to each determination.

2.6 Ultimate Analysis

Ultimate analysis provides weight fractions by element of major constituents in biomass: C, H, S, N, ash, and O by difference. Cl was additionally analyzed due to its importance in thermal systems. For this analysis, fuel samples of approximately 100 g were sent to a commercial laboratory (Hazen Research, Inc., Golden, CO). Standard methods utilized by Hazen in their analyses are set out in their quality assurance report (Hazen Research, 1995).

2.7 Ash Elemental Analysis

Standard ash analysis including Si, Al, Ti, Fe, Ca, Mg, Na, K, P, S, Cl, and carbonate carbon as CO_2 (% ash, all except Cl normally reported on oxide basis) was performed by a commercial laboratory (Hazen Research, Inc., Golden, CO) on the same samples used for ultimate analysis. Fuel was pre-ashed in an air muffle furnace at 575°C for this analysis.

2.8 Bulk Density

Standard bulk densities of the as-fired fuel were measured. The volumetric drop test method of ASTM E 873 was used to obtain bulk density. This involves filling a fixed volume with fuel, and compacting by settling under given conditions to final weight at constant volume (obtained by adding fuel during settling).

2.9 Particle Size Distribution

Particle size distribution was determined on as-fired fuel samples following ASTM Manual 32 (supercedes STP447B) guidelines for sieve analysis and ASAE S424.1, method of determining and expressing particle size of chopped forage materials by screening. The methods use stacked sieves shaken or vibrated for a set length of time to separate particles into various size classes based on sieve dimension.

Mesh sizes 10 (2.00 mm), 14 (1.41 mm), 20 (0.841 mm), 40 (0.420 mm), 100 (0.149 mm), and the pan (<0.149 mm), were used to determine the distribution of particles.

2.10 Ash Fusibility (ASTM pyrometric cone test)

Fuel ash samples were analyzed for initial deformation, softening, hemispherical, and fluid temperatures via the standard ASTM pyrometric cone test (ASTM E 953, D 1857). This test monitors the shape of standard cones prepared from calcined fuel ash as the cones are heated in either reducing or oxidizing atmosphere. The test was partly subjective, and is known to overestimate initial liquid formation temperatures in biomass ash, sometimes by several hundred degrees. This test was conducted by a commercial laboratory (Hazen Research, Inc., Golden, CO) on ash samples prepared from the same fuel samples used for the ultimate analysis. Although the test was inadequate for determining initial fusibility states for biomass, it was useful for comparison with other fusibility tests and for comparison with other literature in which the method was widely utilized.

2.11 Fluidized Bed Reactor

The reactor used was an atmospheric pressure rig, with main reactor column measuring 73 mm inside diameter and 1 m in length. The main column discharges through a transition into a 127 mm square disengagement zone for internal recirculation of particles. The reactor is schematically shown in Figure 2.2.

Fuel was fed to the reactor at a controlled rate using a custom designed belt feeder driven by variable speed stepper motors. Fuel was injected in-bed using a high-speed stainless steel auger. Fuel metering was controlled by the speed of the belt, while the auger was used solely for fuel injection. The feed rate was typically controlled within the range of 0.3 to over 2 g s^{-1} (18 to 120 g min^{-1}) depending on fuel density, fuel bed height on the belt, and belt speed. The fuel feeder and hopper were lightly pressurized using a small amount of purge air (~5 L min^{-1}) to prevent back-flow of reaction products into the fuel feeder.

The reactor column was made from 321 stainless steel (2 mm wall thickness) and was surrounded by an electric furnace used to preheat the reactor. The maximum furnace temperature was 1200°C, but preheat temperature typically was set at 800°C or below. The electric furnace was automatically controlled using reactor wall temperature and maintains wall temperature at the set condition.
Fluidizing, or primary air was preheated through a series of parallel electric heaters to a maximum temperature of 400°C before being discharged through the distributor nozzles in the bottom of the bed. The bottom of the reactor terminates in a blind flange through which bed discharge, thermocouple, and pressure taps were inserted. The reactor was constructed in such a way that it could be rapidly disassembled for inspection and cleaning. Normal bed medium used was an Ione grain alumina-silicate from North American Refractories Co. (NARCO, Ione, CA), but any other medium including alumina, zirconia, and limestone can also be employed. For gasification tests, a NARCO Investocast 60 (sieved to 210 μm mean particle size) was standard, but a high MgO bed was used for rice straw.

Above the furnace the reactor expands into the disengagement section with four times the cross-sectional area as the main bed. Larger fuel and bed media particles were disengaged from the gas flow at this point and returned to the bed in the low velocity

boundary layer along the wall of the reactor column. Situated at the top of the disengagement section was a removable lid through which secondary air, temperature, pressure, and bed make-up taps were inserted.

Past the disengagement section the flow turns 90° and proceeds past a horizontal pass drop-out or settling section. A cyclone was situated past the horizontal pass, and discharges separated particles through the bottom. Gas was flared at the cyclone exit stack inside a refractory lined exhaust duct ported to receive sample inlets, deposition probes, and other instrumentation. Gas and fly-ash samples were drawn from the cyclone exit and post-flare. Gas and particle sampling equipment are described below. Parameters measured during operation are summarized in Table 2.3. Signals from thermocouples, pressure transducers, continuous gas analyzers and other electronic transducers were automatically recorded using a multi-channel datalogger communicating with a personal computer. A 10 s sampling interval was typically used.

For all gasification runs, the fuel was initially fed at a low rate to allow the thermal mass of the fluidized bed to heat up more uniformly. Figure 2.1 shows one example of feed flow for a run with ASF.

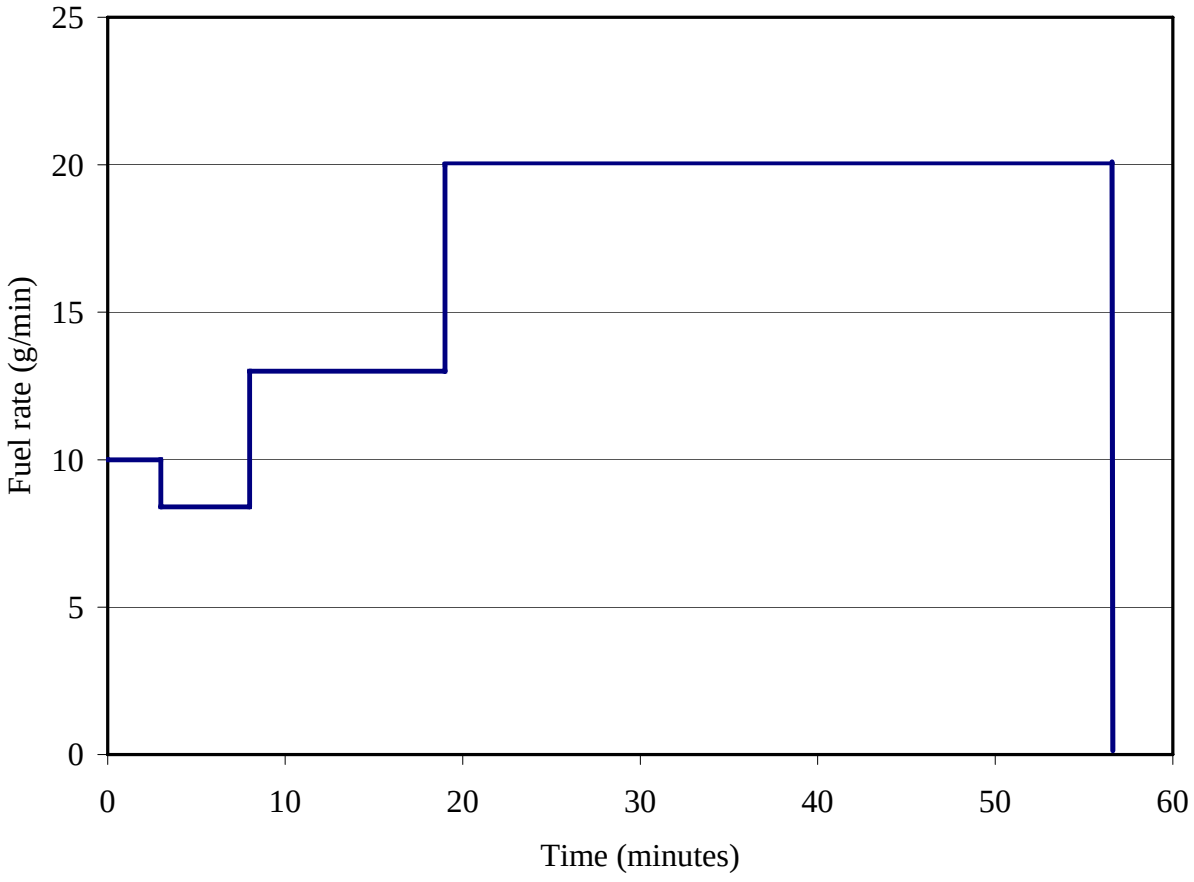

Figure 2.1 Example feed rate over the course of a test run with ASF g min^{-1}

Once the reactor was at the prescribed temperature, as fuel is being fed, (typically between approximately 700 °C and 825 °C), the fuel rate was then increased and the air supply was decreased to give the desired stoichiometry.

2.12 Generalized Test Procedures

Each fuel was tested under gasification conditions in the fluidized bed reactor. Milled fuel was injected into the preheated bed at a rate controlled by the speed of the belt on the fuel feeder. Fluidizing air was added up to a maximum of approximately 1 normal L s^{-1}. A flow of 1 L s^{-1} results in a superficial velocity of 0.85 m s^{-1} (at reactor temperature) and a gas residence time of 1.2 s in the main reactor column. However, superficial velocity increases and residence time decreases when fuel is fired due to the conversion of solids to gas. Fuel and air flow rates were adjusted, prior to the steady state run period, based on knowledge gained from prior research at UC Davis (Pfaff, 1999) with an objective to optimize gas quality as determined by the robustness of the gas combustion at the flare and gas analyses via gas chromatograph. Prior research with a wood-almond blend (Pfaff, 1999) showed typical values of CO, H_2 and CH_4 at levels of approximately 20%, 10% and 5% respectively at an air factor (actual AF divided by stoichiometric AF) of 0.17. Bed heating from the electric furnace around the reactor was controlled automatically following fuel injection. For the majority of runs, reactor heater, air inlet temperature, and the amount of bed material were fixed while some slight variations to air mass flow and fuel feed rate were made as described in Chapter 3. For highly fouling fuels,

Table 2.3 Sampling and measurements for fuel screening experiments.

Sample/Measurement	Method	Location
Fuel feed rate (kg s^{-1})	Feed belt speed/ Total gravimetric	Fuel feeder
Fluidizing air flow rate (L min^{-1})	Rotameter	Primary air inlet
Fuel feeder purge air (L min^{-1})	Rotameter	Purge air inlet
Fresh bed mass (g)	gravimetric at start	Media weighed prior to adding to clean reactor
Fresh bed addition (g)	gravimetric at time of addition	During operation, media was added through upper lid
Fresh bed chemical composition (%)	Hazen Research, Inc. NARCO	Batch sample submitted for analysis
Spent bed mass (g)	gravimetric during or at end of test	Bed dropped from lower flange and bed discharge
Spent bed chemical composition (%)	Hazen Research, Inc.	Split sample submitted for analysis
Residual fuel/carbon in bed (g)	loss on ignition at 575°C in air muffle furnace	Split sample
Ash	gravimetric at end of test	Ash collected from horizontal

(kg)		pass dropout and cyclone dropout
Ash chemical composition (%)	Hazen Research, Inc.	Split sample submitted for analysis incl. metals in some cases
Deposit mass on probes (g)	mass reconstructed from elemental composition of rinsate and gravimetric determination of filtered insoluble solids	Post-flare exhaust stack probe Filtered insoluble fraction Liquid filtrate
Deposit chemical composition (%)	Hazen Research, Inc.	Filtered insoluble fraction Liquid filtrate
Gas composition (%)	CO_2, CO, H_2, and O_2 by continuous analysis	Cyclone exit
Gas composition (%)	CO_2, CO, H_2, O_2, N_2, CH_4 by GC on grab samples	Cyclone exit
Ammonia in gas (ppm)	via absorption in dilute acid, analysis by ion-specific electrode (ISE)	Cyclone exit Post-flare
Hydrogen cyanide in gas (ppm)	via absorption in dilute acid, analysis by Hazen Research, Inc.	Cyclone exit

Table 2.3 (Continued)

Sample/Measurement	Method	Location
Alkali in fly-ash (ppm)	hot gas filtration, solid samples analyzed by Hazen Research, Inc., incl. metals (for SLF), soluble fraction of K, Cl by ISE	Cyclone exit
Alkali in gas (ppm)	via absorption in water, analysis by ISE for K, Cl	Cyclone exit
Tar (mg m^{-3})	gravimetric via water and dry-ice condensers, methanol solvent	Cyclone exit
Temperature (°C)	Type K thermocouples	Air inlet at distribution manifold Lower bed (89 mm and 178 mm above base) Mid-bed (356 mm above base) Upper bed (572 and 672 mm above base) Disengagement zone (954 and 1226 mm beyond base)

		Horizontal pass (1637 mm beyond base) Cyclone exit (2128 mm beyond base) Outside reactor wall at furnace center Sampling trains
Pressure (Pa)	Piezoelectric pressure transducer	Fluidizing air inlet Reactor bottom (10 mm above bed) Reactor top at transition to disengagement zone (940 mm) Bed differential Atmospheric
Total flow (L)	dry-test meter	Sampling trains

especially rice straw, bed temperature control was critical and temperature was adjusted in an attempt to identify regimes where slagging and agglomeration could be reduced to acceptable levels. In this case, bed media was also changed. A MgO enriched bed was utilized rather than the alumina-silicate only bed normally employed. Further adjustments were made as needed based on the extent of fouling, slagging, or agglomeration observed.

Once steady operation of the reactor was achieved (through monitoring reactor thermocouple temperatures), sampling for ammonia, alkali, and tars were initiated and continued for a minimum of 30 minutes. Additional runs on selected fuels were conducted to obtain data on HCN concentrations in the gas. The time was increased as possible to improve detection. Continuous gas sampling was initiated at start-up and continued throughout each test. Grab samples of gas for GC analysis were taken at frequent intervals throughout the steady operating period. Temperatures and pressures were monitored throughout each test. Total air and fuel flow rates were monitored, as were total flows through each of the sampling trains.

Post-test sampling occurred after the reactor cooled. The entire bed was recovered through the bottom reactor flange, and split as indicated in Table 2.2 for analysis of composition. Coarse ash/char collected from the horizontal pass and cyclone were submitted for analysis as indicated. Sampling lines were rinsed into the impingers and liquids analyzed for the intended species. Ammonia, hydrogen cyanide, chloride, and potassium were analyzed using ion-specific electrodes. Tar production was determined gravimetrically. Samples were air-dried under fume hood to obtain the moisture fraction.

Grab samples of gas were submitted to GC analysis as indicated in Table 2.3. Full mass and energy balances were completed for each test to assess quality of analysis and to provide information on the fate and partitioning of elements. Material and energy conversion efficiencies were derived and related to the test conditions.

The thermocouples that measure temperatures inside the fluidized bed are located at 89 mm, 178 mm, 356 mm, 572 mm and 672 mm measured upward from the bottom reactor flange. Figure 2.2 is a schematic of the reactor showing bed thermocouple locations (identified as TC1 through TC5).

The thermocouples in the disengagement section and horizontal pass of the reactor are noted in Figure 2.2 and shown as D1 through D3. The pressure ports for measuring static pressure inside the fluidized bed are located at just above the bottom of the bed (12 mm above the base of the bed) and at the top of the bed (940 mm vertically above the base of the bed). See Figure 2.2 for pressure port locations.

2.13 Fuel Feed Rate

As-fired fuel feed rate was calibrated against belt speed for each fuel prior to an experiment. Fuel feed rate was measured for each test by monitoring the metering belt speed and by weighing fuel in and out of the feeder at the start and end of each test and whenever fuel was added to the feeder during a test. Moist fuel feed rate calibration obtained for each of the six fuels is shown Figures 2.3 for as-fired milled material. The calibration was performed to span the range of belt speeds anticipated for each test. Bulk density was regressed against the slopes from the feed rate calibrations. The correlation is

Slope ($g\ s^{-1}\ mm^{-1}\ min$) = 5.3463*bulk density ($g\ cm^{-3}$) - 0.0168 $r^2 = 0.8746$

Table 2.4 shows the feed rate (slope), bulk density and moisture content of each tested fuel.

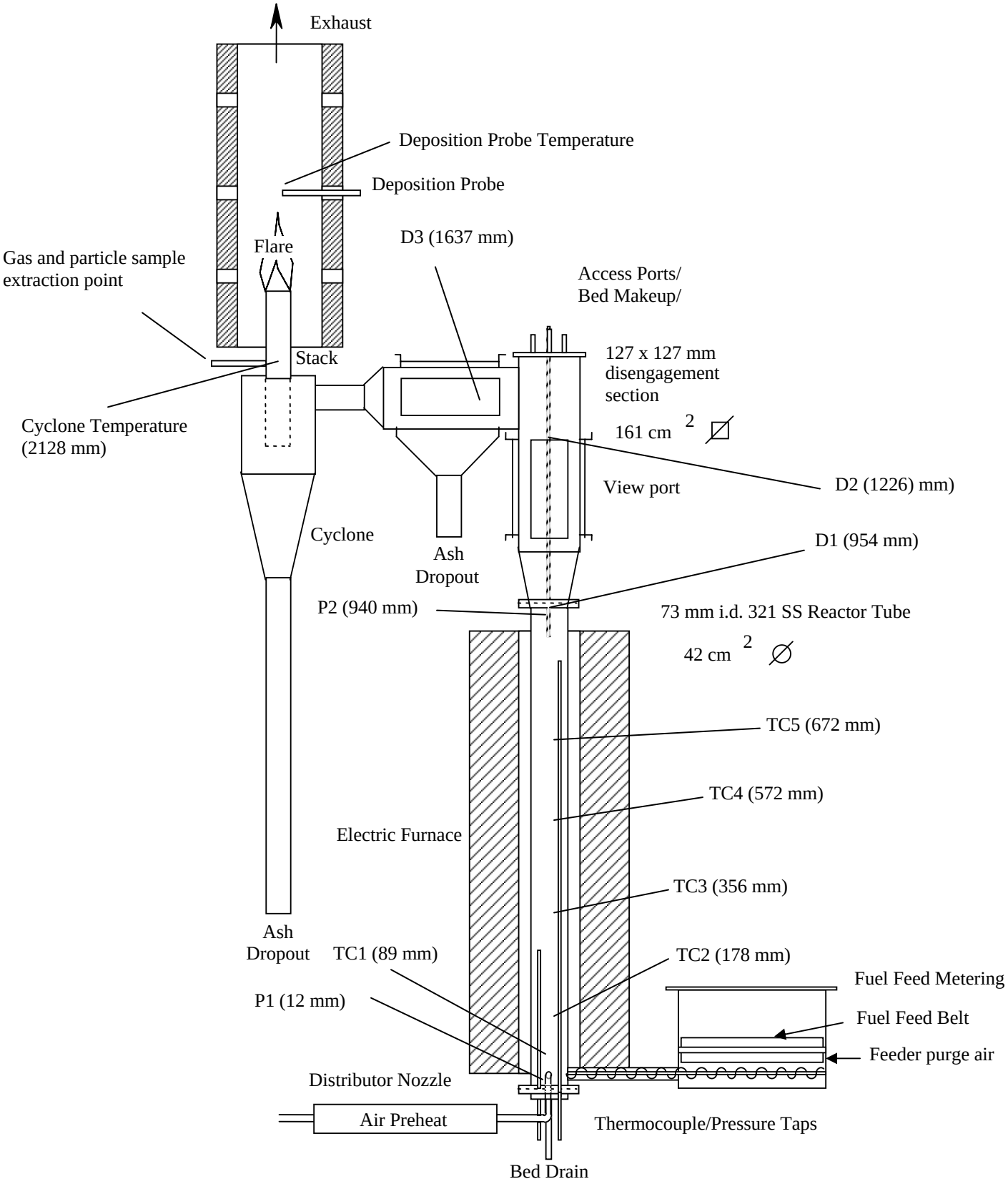

Figure 2.2. UC Davis fluidized bed reactor
TC = thermocouple, P= pressure tap, D= disengagement thermocouple

Table 2.4 Moist fuel feed parameters.

Fuel	Slope ($g\ s^{-1}\ mm^{-1}\ min$)	Bulk Density ($g\ cm^{-3}$)	Moisture (% wb)
ASF	0.0967	0.55	9.0
WPF	0.0540	0.31	14.3
RSF	0.0317	0.21	6.0
WWF	0.0316	0.19	7.5
SLF	0.1498	0.78	8.6
NPF	0.0137	0.09	6.3

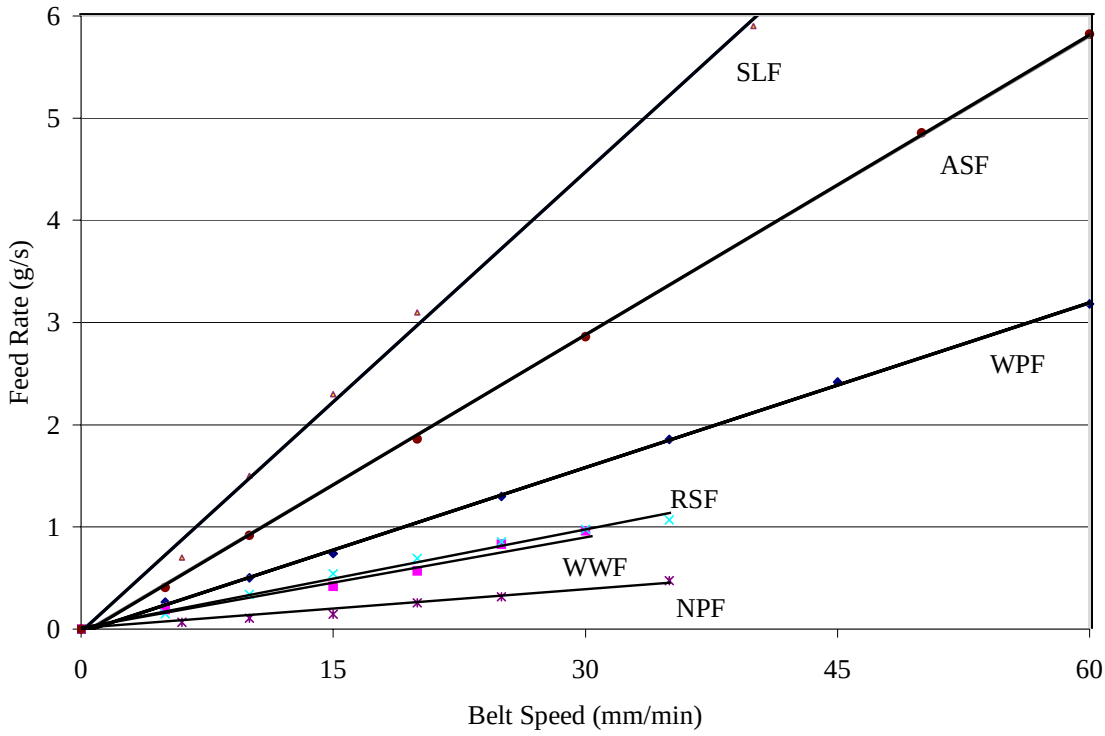

Figure 2.3 Individual measurements of moist fuel feed rates versus feeder belt speed

2.14 Bed Media

As noted above, a screened NARCO Investocast 60 grain (typically 433 g) was normally used in gasification. This grain had a mean particle size of 210 μm. Slumped bed depth was approximately 73 mm. Attrition and carry-over of fines leads to decreasing bed mass over time if ash retention in the bed or fuel ash addition rate is low. The fuel feed auger contributes to bed attrition by grinding particles against the feed tube wall at the bed entrance. To maintain bed mass, fresh media can be added through a top access port during operation. Bed mass was indicated by bed pressure drop during the run when the bed was not agglomerated. Bed pressure drop was also indicative of bed agglomeration, as a more rapid or sudden decline in pressure drop than that normally observed through elutriation implies agglomeration and channeling in the bed.

Fresh, screened bed material was used for each test. The initial mass of bed media was generally 433 g, however, some deep bed tests (866 g) were also run. In addition, some tests used a combination of alumina-silicate and MgO to prevent agglomeration. All additions during the run were weighed and recorded. After each test, spent bed was removed by dropping the lower flange plate and capturing the bed. Samples were submitted for elemental analysis. Any residual fuel or carbon in the bed was determined from loss on ignition in an air muffle furnace at 575°C.

2.15 Gas Analysis

Three independent extractive sampling trains were utilized (Figure 2.4). The three extraction points were located at the exit of the cyclone in the exhaust stack just below the base of the flare.

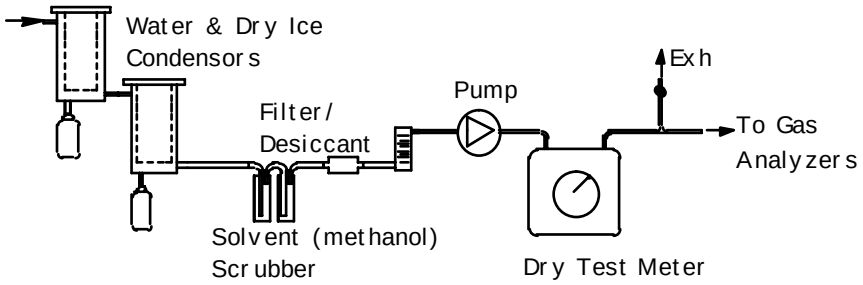

Tar Sampling and online Gas Analysis Train

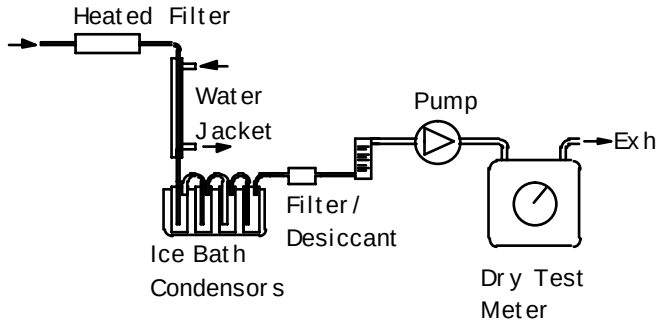

Alkali Sampling Train

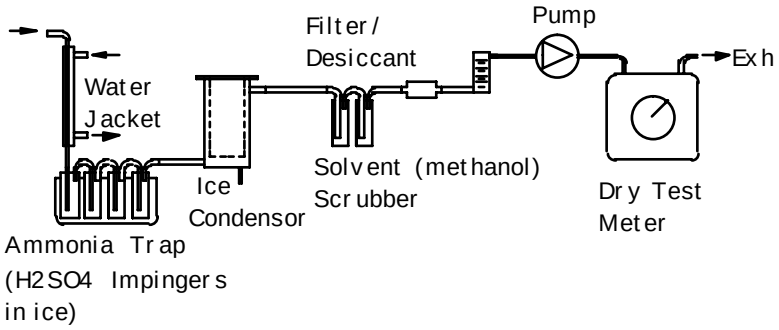

NH_3 Sampling Train

Figure 2.4 Extractive sampling train schematics

Continuous gas sampling/analysis was accomplished by a gas analyzer (Leeds & Northrup, Model 7865, North Wales, PA) indicating CO, CO_2, and H_2 concentration, and a O_2 analyzer (Panametrics, Model XM02, Waltham, MA).

Grab samples were collected in 250 mL glass flasks for GC analysis of permanent gases and CH_4. Primary sampling location for gases was from the cyclone exit as indicated in Figure 2.2.

2.16 Alkali Vapor Sampling

Samples for analysis of alkali in particle and vapor phases were extracted at the exit of the cyclone as indicated in Figure 2.2. The sample gas was extracted from the reactor isokinetically through a 7.8 mm i.d. (3/8 inch) 316 stainless steel buttonhook nozzle with a 0.028 wall thickness. The purpose of sampling isokinetically was to extract a representative sample of the particle-laden gas flow. This was accomplished by matching the velocity of the inlet sample to the gas stream in the sampling stack. Isokinetic probes are generally of two different designs: a button hook or elbow in accordance with EPA method #5. All tests utilized the button hook design.

After passing through the button hook, the flow was filtered through a heated stainless steel sintered (5 μm) porous filter to separate particulate matter from the gas without condensing alkali on the filter (See Figure 2.5). The stainless steel filter had an outside diameter of 12.7 mm (1/2 inch) and an effective length of 152 mm (6 inches). Filter temperature was automatically controlled from a type K thermocouple, mounted inside the filter body.

After passing through the filter, the gas stream was cooled in a water jacketed condenser consisting of a 3/8 in o.d. sample line within a 3/4 in o.d. x 600 mm long stainless steel tube containing flowing tap water for cooling.

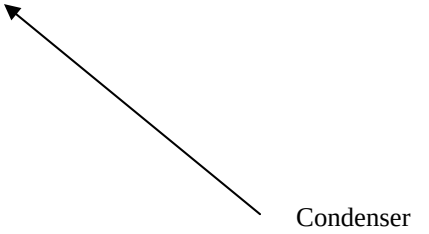

Figure 2.5 Heated alkali filter and cooling water jacket.

From the water-jacketed condenser, sample flowed through a set of 4 ice-bath cooled impingers (See Figure 2.6). The first two impingers were loaded with 200 mL each of distilled water, the third with 100 mL, and the forth was left empty.

Figure 2.6 Alkali impingers.

After passing through the impinger train, the gas flowed through a molecular sieve 3A desiccant, teflon coated glass fiber back-up filter, pump, rotameter and dry test meter to record total flow (See Figure 2.7 and 2.8).

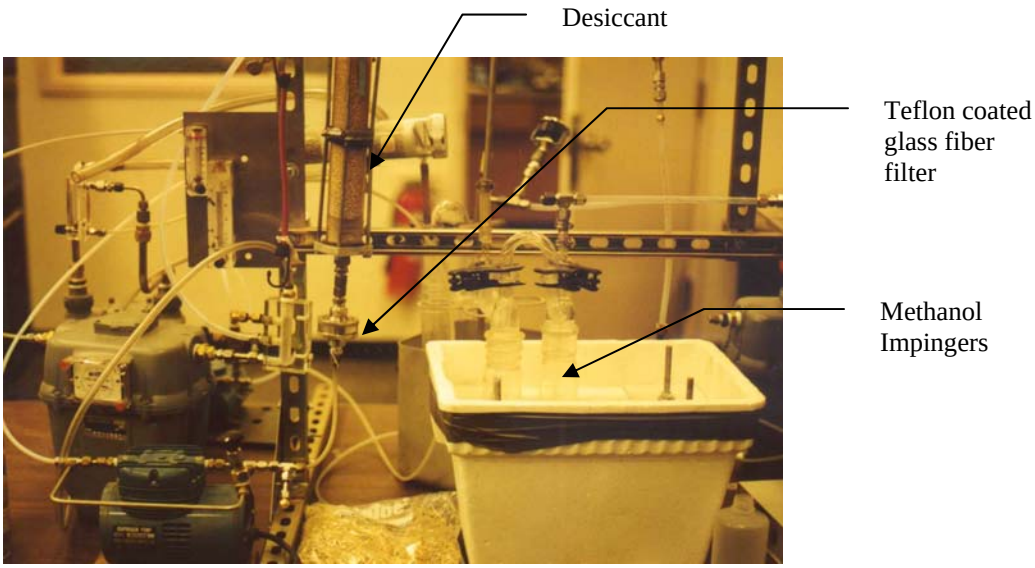

Figure 2.7 Desiccant and methanol impingers.

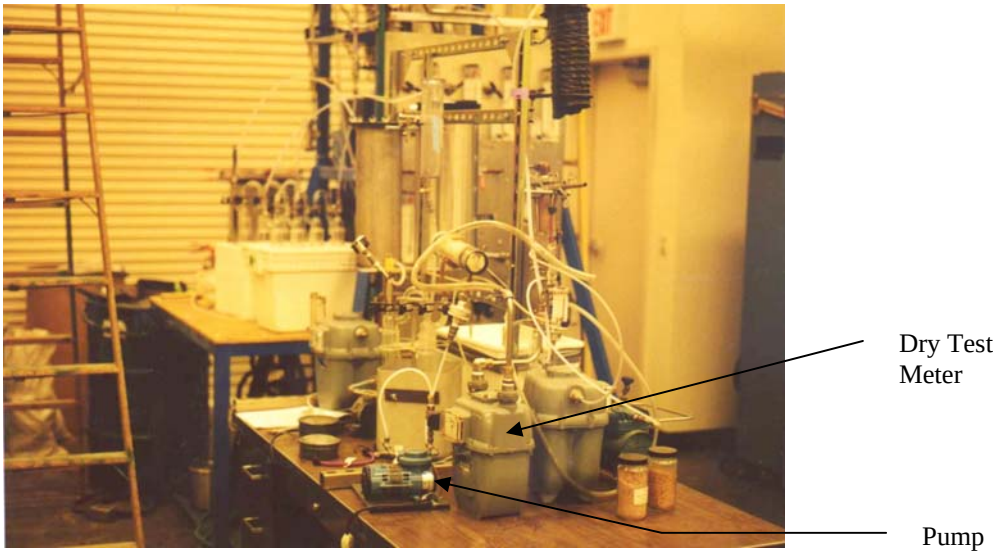

Figure 2.8 Dry test meter.

After a run, the sample line between the heated filter and the impinger set was rinsed and the rinsate added to the impinger liquid. The total liquid volume was recorded and a sample was analyzed for the species of interest (K and Cl). Filter cake was also analyzed to determine elemental partitioning between phases.

After each run, all sampling lines and the impingers were acetone rinsed in preparation for the next run.

2.17 Ammonia and hydrogen cyanide

Nitrogenous species other than NO_x (principally ammonia and smaller amounts of HCN), were measured via an absorption train similar to that used for alkali. Ammonia sampling was conducted using methods similar to those of Ishimura (1994), Furman et al. (1992), and Blair et al. (1976). Similar to the alkali sampling, the sample stream was drawn through a condenser and then through a set of ice bath impingers filled with a sulfuric acid (0.1 M H_2SO_4) solution. In the presence of the acid, ammonia reacts essentially to completion to form the ammonium ion (NH_4^+):

$$NH_3 + H_2O = NH_4^+ + OH^- \quad [2.1]$$

The net ionic reaction is:

$$NH_3 + H^+ = NH_4^+ \quad [2.2]$$

After the test, all sample lines were rinsed into the impingers and the liquid volume recorded. An ion selective electrode (sensitive to ammonium) was then used (Accumet, Model 13-620-505) to measure [NH_4^+] and hence ammonia. The same train with a different absorbing solution was used for HCN with almond shell and rice straw. Although this compound has previously been found to be present at much lower

concentrations compared with ammonia, two determinations were performed for HCN concentration to determine levels for experimental fuels.

2.18 Chloride and potassium

Both chloride and potassium are soluble in water. Ion selective electrodes (Accumet Model 13-620-527 and Accumet Model 13-620-532) were used to measure levels of chloride and potassium species respectively. Concentrations in the last impinger indicated no breakthrough of these species during sampling.

2.19 Tar

Tar, water vapor, other condensibles and particulate matter were captured in the tar train. The majority of the material was found in condenser #1. The first condenser is shown in Figure 2.13. The first condenser (condenser 1) was water/ice-bath cooled and located approximately 35 cm from the stack (See Figure 2.9). The second condenser (condenser 2) was located downstream of condenser 1 and was filled with dry ice in ethanol. The condensers were designed to condense as much tar as possible and to prevent downstream sample lines from clogging. Following the condensers, the gas flowed through a set of methanol solvent scrubbers, a molecular sieve 3A desiccant, teflon coated glass fiber back-up filter, pump, rotameter and dry test meter to record total flow. Figure 2.4 shows a schematic of the tar train.

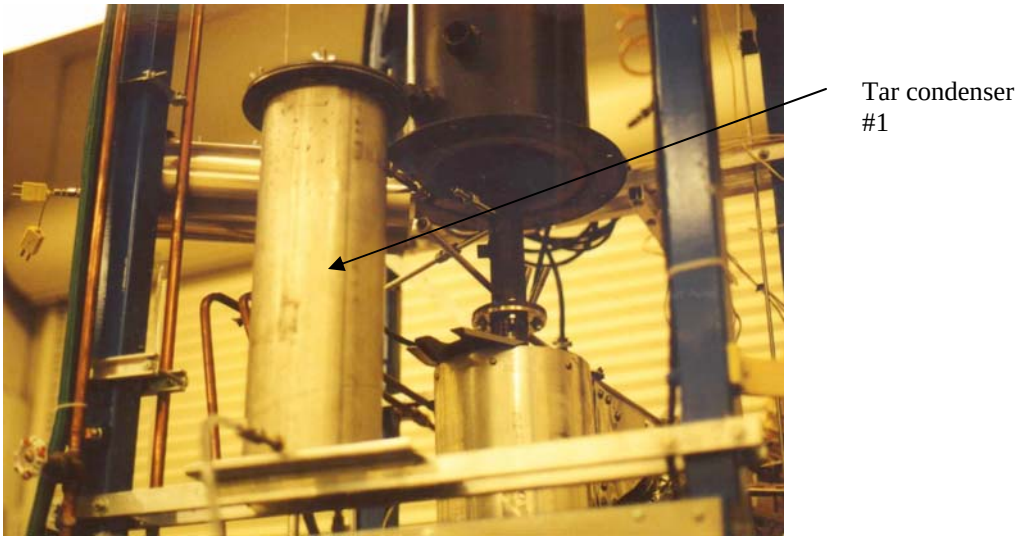

Figure 2.9 Tar condenser #1.

2.20 Gas Chromatography

Gas chromatography was used to determine the concentrations of CO, H_2, CO_2, CH_4, N_2 and O_2 present in grab samples of a gas periodically collected throughout a run. The GC (HP, Model 8590, Mountainview, CA) with TCD was calibrated on the composition shown in Table 2.5 and also calibrated with air (assumed 79 % v/v N_2 and 21 % v/v O_2). After each experiment, 100 μl samples were taken by syringe from 250 mL grab sample flasks and injected into the gas chromatograph. Comparisons were made of gas concentrations from the continuous analyzer with the gas chromatograph results.

Table 2.5 Composition of GC calibration gas

Component Gas	Percentage by volume (%)
H_2	15
N_2	40
CO	15
CH_4	15
CO_2	15

Continuous gas concentrations were obtained using a Leeds and Northrup gas analyzer capable of measuring CO, CO_2 and H_2. A comparison of the recorded values plotted against the values determined by use of gas chromatography (GC) is shown in Figures 2.10 to 2.12. Individual point measurements from continuous analyzer (taken at the same time as GC values) for ASF, WPF and RSF were used in the plots with GC data. In general, the continuous measurements are biased low relative to GC for CO and high for H_2. The reasons for this are not entirely clear as all analyzers were calibrated prior to use. To be consistent, GC data were used in mass and energy balances reported later.

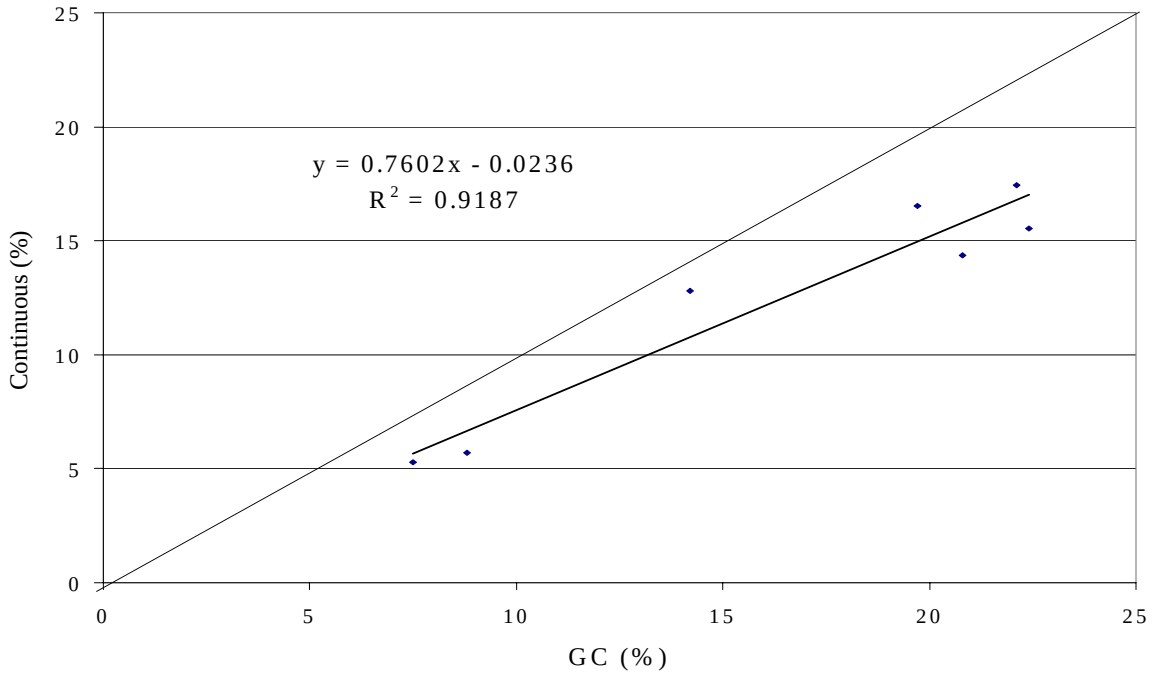

Figure 2.10 Comparison of continuous analyzer versus GC for CO for ASF, WPF and RSF.

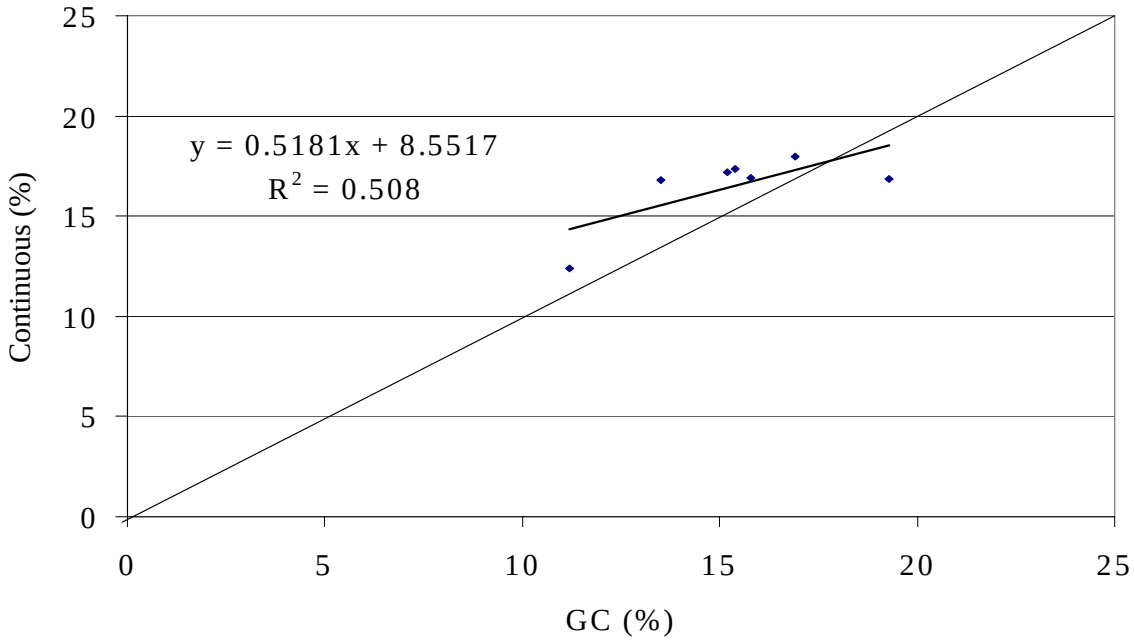

Figure 2.11 Comparison of continuous analyzer versus GC for CO_2 for ASF, WPF and RSF.

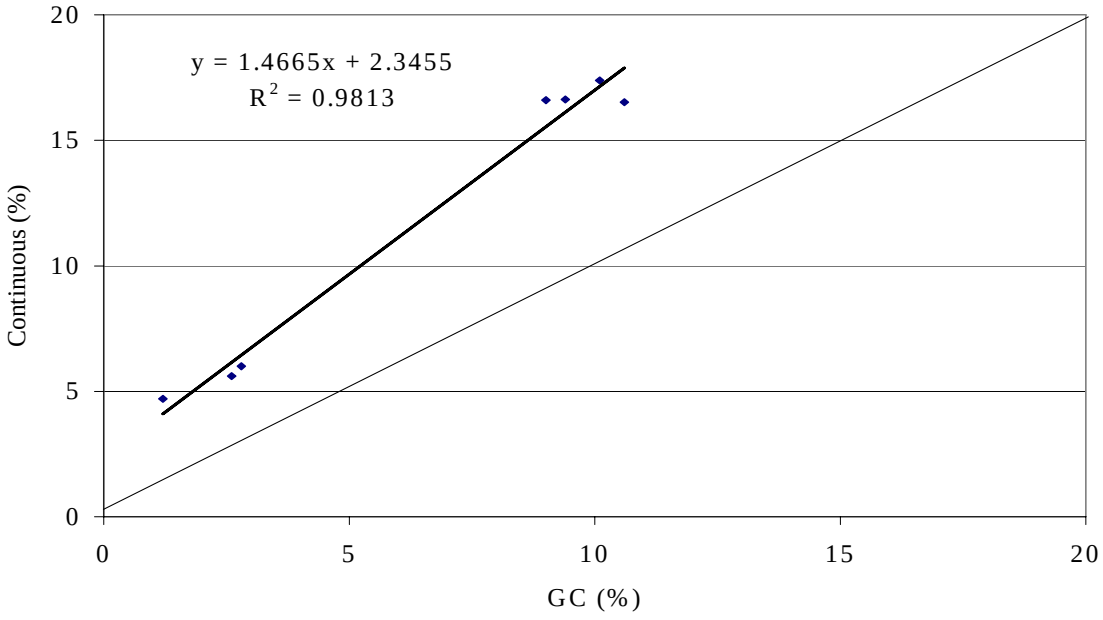

Figure 2.12 Comparison of continuous analyzer versus GC for H_2 for ASF, WPF and RSF.

CHAPTER 3 EXPERIMENTAL RESULTS

3.1 Introduction

Reported here are data and results obtained from the experiments for the six fuels. For each individual fuel, results are presented with operational parameters, a mass balance summary, concentration of solids and condensibles, stack gas grab sample average analysis by gas chromatograph, gas phase ammonia, hydrogen cyanide (where applicable), chloride and potassium species, a power balance summary, and hot and cold gas efficiencies (These specific test run data start in section 3.2).

Detailed results for an independent assessment of uncertainty analyses, including tables with individual component errors, are located in Appendix A. Uncertainty analyses were conducted for ASF 1 and SLF 2.

3.1.1 Proximate analysis and heating values

Proximate analysis and heating values for the six tested fuels are listed below in Table 3.1. The fuels had low to moderate moisture levels between 6 and 14 % wet basis. Ash for WPF, WWF and NPF was relatively low (≤ 3.5 %) while ASF, RSF and SLF had high levels of ash (≥ 20.8 %). Ash content is within expectations for all fuels except ASF. It is believed that ASF had a large amount of dirt in the fuel which is the likely reason this fuel had such a high ash content. The high volatile content of NPF reflects its low ash content. The opposite is true for sludge.

Table 3.1 Proximate analysis and heating values for each of the six fuels

Parameter	ASF	WPF	RSF	WWF	SLF	NPF
As-fired Moisture [% wb]	9.0	14.3	6.0	7.5	8.6	6.3
Ash [% db]	26.4	3.5	20.8	3.1	38.1	1.4
Volatiles [% db]	58.8	80.8	68.3	78.3	56.5	89.4
Fixed Carbon [% db]	14.8	15.8	10.9	18.6	5.4	9.2
Total	100	100	100	100	100	100
Higher Heating Value [MJ kg^{-1} db]	15.1	19.0	14.8	20.4	15.4	18.8
Moisture and Ash Free (maf) Basis						

Volatiles [% maf]	79.9	83.6	86.2	80.8	91.3	90.7
Fixed Carbon [% maf]	20.1	16.4	13.8	19.2	8.7	9.3
Higher Heating Value [MJ kg^{-1} db maf]	20.5	19.7	18.7	21.1	24.9	19.1

Similarity among the native biomass fuels are apparent when volatile and fixed carbon concentrations are determined on a moisture and ash free (maf) basis. SLF and NPF are modified substantially due to the processing involved in their production. The higher carbon concentration in the organic matter of SLF is apparent in its HHV (maf).

3.1.2 Stoichiometric and gasification AF ratios and air factors

Air Factor

The air factor (or lambda, λ, as air factor is sometimes referred to) is the ratio of the actual AF (for the achieved gasification condition) divided by the stoichiometric AF ratio for that fuel. The air factor is defined in equation [3.1], and is the reciprocal of the equivalence ratio.

$$\text{Air factor} = \frac{AF_{gasification}}{AF_{stoichiometric}} \qquad [3.1]$$

The stoichiometric AF ratios, gasification AF ratios and the operational air factors ($AF_{gasification}/AF_{stoichiometric}$) for the six test fuels are summarized in Table 3.2.

Table 3.2 As-fired stoichiometric AF ratios (kg air/kg fuel), gasification AF ratios (kg air/kg fuel) and air factors (kg air/kg fuel gasification)/(kg air/kg fuel stoichiometric) achieved under gasification conditions.

Parameter	ASF		WPF		RSF		WWF		SLF		NPF	
Test	1	2	1	2	1	2	1	2	1	2	1	2
Stoichiometric AF ratio	3.73		4.38		3.81		4.80		4.63		5.09	

Gasification AF ratio	0.25	0.37	0.48	0.42	0.71	0.74	1.44	1.09	0.32	0.27	1.51	1.31
Gasification Air Factor	0.07	0.10	0.11	0.10	0.19	0.19	0.30	0.22	0.07	0.06	0.30	0.26

The gasification AF and air factor are reported on an as-measured basis. As noted later, carbon and nitrogen balances suggest these were in many cases higher than shown here.

3.1.3 Particle size distribution

One measurement for determining mean size of the fuel particles is the geometric mean shown in equation 3.2.

$$\text{Geometric Mean} = \left(\prod_{i=1}^{n} X_i \right)^{\frac{1}{n}} \qquad [3.2]$$

X_i represents the particle distribution terms. The geometric mean was computed using ASAE standard S319, Method of determining and expressing fineness of feed materials by sieving. Table 3.3 summarizes the particle size distribution for each fuel.

Table 3.3 Particle size distribution (% mass retained) for each fuel including geometric mean diameter (GMD)

		ASF	WPF	RSF	WWF	SLF	NPF
Sieve Size	Sieve opening[1] (mm)						
10	2.000	0.6	0.0	0.1	0.1	4.7	12.6
14	1.410	3.3	0.1	0.1	0.1	20.5	19.0
20	0.851	6.5	3.0	0.8	1.1	22.4	21.5
40	0.420	27.5	65.0	37.4	41.7	30.6	26.6
100	0.149	32.2	22.5	43.4	35.8	13.6	11.6
PAN	<0.149	29.7	9.2	17.8	20.8	8.1	7.9
GMD (mm)		0.30	0.23	0.22	0.23	0.43	0.50

[1] Based on U.S. Standard Sieve Sizes

3.1.4 Bulk, true and apparent density

Bulk, true and apparent densities are displayed in Table 3.4. Apparent and true densities were measured at Stanford University (Mitchell and Campbell, 2001). Bulk density was calculated using ASTM E873.

Table 3.4 Bulk, true and apparent densities (g cm^{-3})

	Bulk Density	Apparent Density	True Density
ASF	0.55	1.07	1.50
WPF	0.31	1.01	1.49
RSF	0.21	0.94	1.44
WWF	0.19	1.04	1.43
SLF	0.78	1.49	1.52
NPF	0.09	1.30	1.49

True density is fairly constant between the six fuels (varies by about 6%) because pore volume and inter-particle voids, which have a much lower density (of air), are excluded from the measurement. Apparent density includes the pore volume resulting in a lower density than true density. Bulk density is similar to apparent density but also includes the voids between particles and thus has the lowest density of the three measurements.

3.1.5 Mass Balance Summary

Material compositions

The elemental composition of all inputs and outputs from gasification tests are described in this section.

Fuel

Ultimate, ash elemental and ash fusion analyses of each fuel are displayed in Table 3.5. RSF had the highest level of chlorine at 0.58 % followed by SLF at 0.10 %. Both ASF and NPF had chlorine levels of 0.03 % while both WPF and WWF had less than 0.01%. Chlorine facilitates the volatilization of alkali from the biomass. Potassium chloride is among the most stable high-temperature, gas phase, alkali-containing species. Chlorine concentration often dictates the amount of alkali vaporized during combustion as strongly as does the alkali concentration. In most cases, the chlorine appears to play a shuttle role, facilitating the transport of alkali from the fuel to surfaces, where the alkali often forms sulfates in substituting sulfur for chlorine. In the absence of chlorine, alkali hydroxides are the major stable gas-phase species in moist, oxidizing environments, such as combustion gases (Baxter et al., 1996). Ash concentrations in the analysis of Table 3.5 differ from those of Table 3.1 because the analyses were performed by two difference laboratories.

WWF with the highest carbon content of 51.15 % also had the highest heating value of 20.4 MJ kg^{-1} (See Table 3.1 for a review of HHVs). On an ash free basis, however, the high carbon concentration in the organic fraction of sludge manifests in a higher ash free heating value. Carbon content for the six fuels ranged from 36.20 to 51.15 % and HHV's ranged from 14.8 MJ kg^{-1} for RSF to 20.4 MJ kg^{-1} for WWF.

Figure 3.1 shows HHV plotted against fuel carbon content. A regression yields:

$$HHV = 0.34*C(\%) + 2.56 \qquad r^2 = 0.950 \qquad [3.3]$$

The high degree of correlation is largely driven by the clustering into two groups – one around 37 MJ kg^{-1} and the other around 50 MJ kg^{-1}. Fuel blending to achieve values between these extremes was not performed. Again, primary differences among the organic fractions of the fuels are shown when reporting on an ash free basis.

The regression is similar to other published regressions between HHV and carbon content such as the one in equation [3.4] (Jenkins, 1989).

$$HHV = 0.39*C(\%) + 0.63 \qquad [3.4]$$

Results from the regression fit [3.3] and equation [3.4] are displayed in Table 3.6.

Table 3.5 Compositions and ash fusion temperatures of test fuels

	ASF	WPF	RSF	WWF	SLF	NPF
Ultimate Analysis (% db)						
Carbon	36.27	48.20	38.50	51.15	36.20	49.11
Hydrogen	3.94	4.41	3.56	3.40	4.46	5.08
Nitrogen	0.79	0.59	0.55	0.35	5.64	0.14
Sulfur	0.05	0.03	0.06	0.05	1.07	0.06
Ash	26.57	2.43	21.03	2.68	37.9	1.05
Oxygen (by diff.)	32.43	44.51	36.29	42.40	14.86	44.55
Chlorine	0.03	<0.01	0.58	<0.01	0.10	0.03
Elemental Ash (% db):						
SiO_2	65.05	5.80	76.36	33.77	47.1	25.30
Al_2O_3	12.70	2.25	0.99	7.69	17.9	23.11
TiO2	0.45	0.09	0.05	0.34	1.22	2.07
Fe_2O_3	4.32	1.23	0.31	1.25	5.64	1.37
CaO	4.20	43.90	2.17	29.00	8.65	19.50
MgO	2.10	8.08	1.71	3.54	2.98	4.56
Na_2O	1.87	0.31	0.30	1.21	1.33	6.31
K_2O	8.54	10.60	11.90	9.01	1.32	4.44
P_2O_5	0.72	2.32	1.55	1.83	14.7	5.75
SO_3	0.22	0.56	0.67	0.43	1.38	2.73
Cl	0.08	0.15	2.39	0.19	<0.01	0.25
CO_2	0.48	23.68	0.22	3.36	0.21	1.52
Total	100.73	98.97	98.62	91.62	102.39	96.91
Ash Fusion Temperatures (°C)						
Oxidizing Atmosphere						
Initial	1172	1482+	1240	1210	1111	1202
Softening	1231		1378	1216	1127	1218
Hemispherical	1290		1429	1222	1144	1223
Fluid	1352		1470	1232	1189	1232
Reducing Atmosphere						
Initial	1192	1482+	1175	1216	1111	1095
Softening	1219		1367	1221	1121	1161
Hemispherical	1227		1406	1222	1134	1177
Fluid	1254		1420	1224	1189	1193
Ultimate Analysis (Moisture and ash free basis)						
Carbon	49.39	49.40	48.75	52.56	58.29	49.63
Hydrogen	5.37	4.52	4.51	3.49	7.18	5.13
Nitrogen	1.08	0.60	0.70	0.36	9.08	0.14
Sulfur	0.07	0.03	0.08	0.05	1.72	0.06

Oxygen (by diff.)	44.16	45.62	45.95	43.57	23.93	45.02

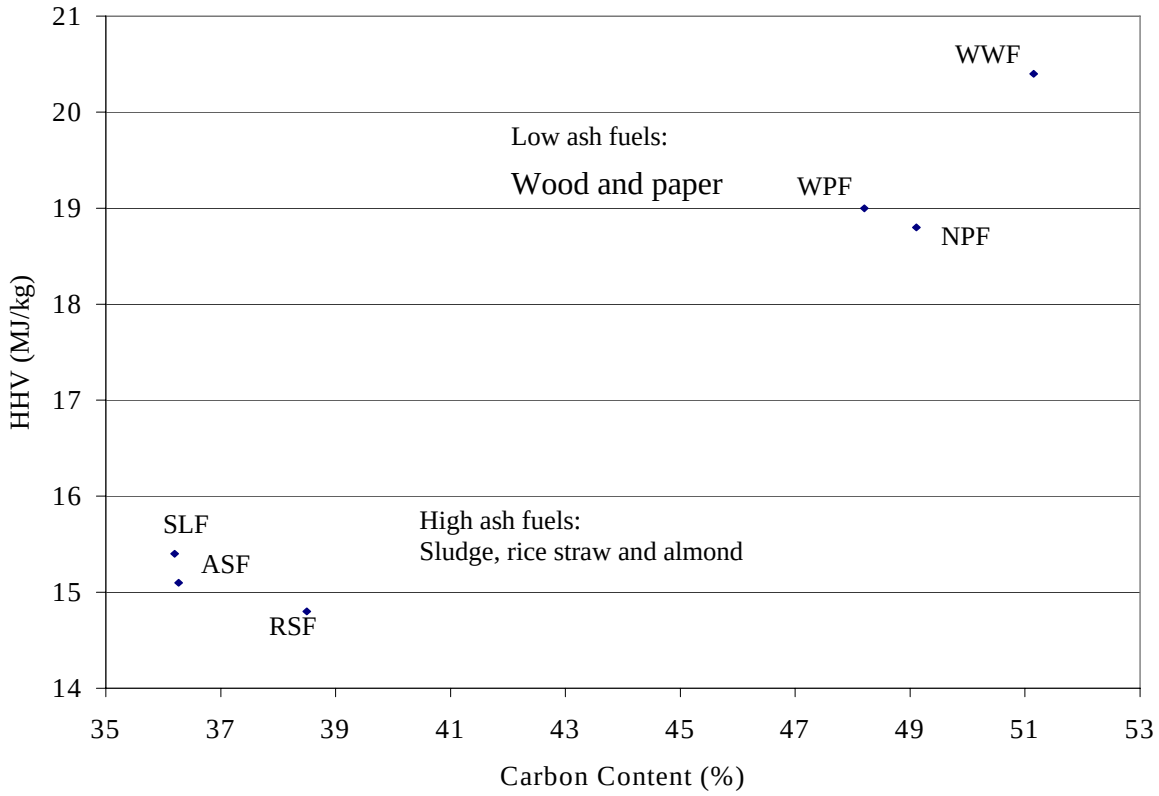

Figure 3.1 HHV versus carbon content for tested fuels

Table 3.6 Comparison of HHV from published and experimental regressions

Fuel	Carbon content (%)	Experimental Values of HHV [MJ kg^{-1}]	HHV from equation [3.4] (MJ kg^{-1} db)	HHV from equation [3.3] (MJ kg^{-1} db)	Ratio: [3.3]/ [3.4] regressions	Ratio: Experimental/ [3.4] regressions
SLF	36.20	15.4	14.75	14.86	1.01	1.04
ASF	36.27	15.1	14.78	14.88	1.01	1.02
RSF	38.50	14.8	15.65	15.64	1.00	0.95
WPF	48.20	19.0	19.43	18.93	0.97	0.98
NPF	49.11	18.8	19.78	19.24	0.97	0.95
WWF	51.15	20.4	20.58	19.94	0.97	0.99

HHV was also compared to carbon content on moisture and ash free (organic matter) basis. This plot is displayed in Figure 3.2. In general, there is good correlation between the ash free HHV and the carbon content based on an ash free basis. The degraded nature of the sludge fuel leading to a higher carbon concentration in organic matter is apparent. For reasons unknown, whole tree wood (WWF) lies rather outside the trend for other biomass in terms of maf carbon concentration.

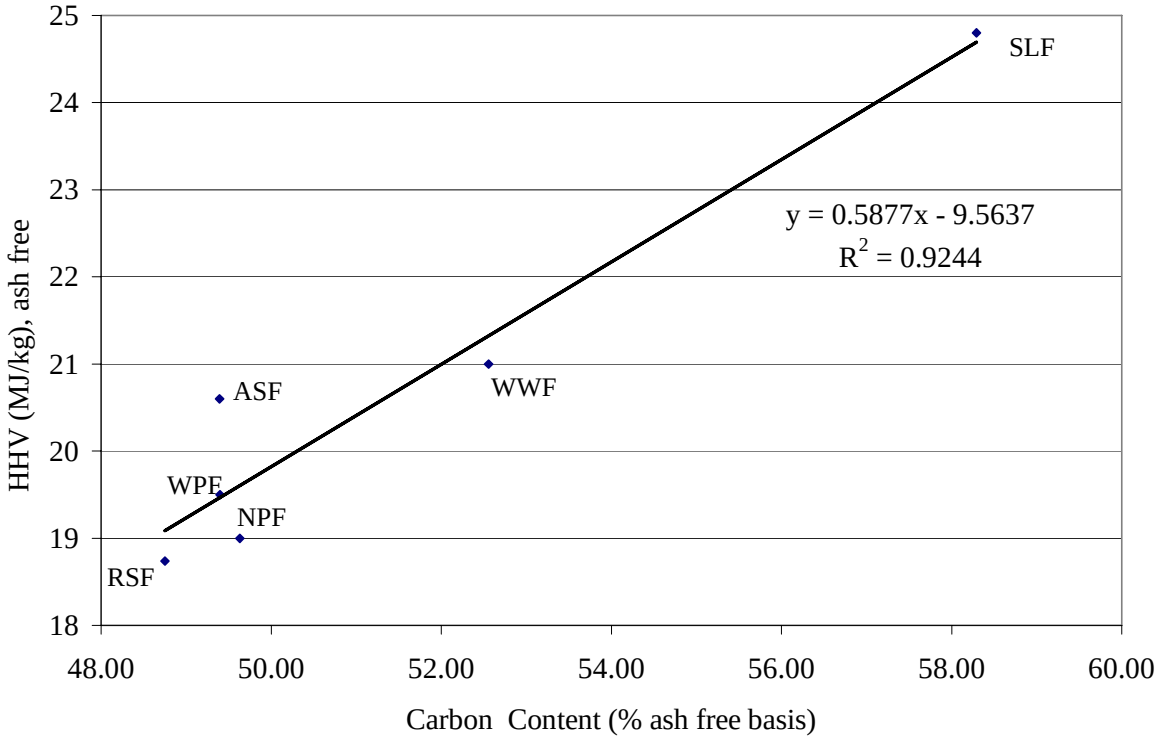

Figure 3.2 Moisture and ash-free HHV versus moisture and ash free carbon content for tested fuels.

3.1.6 Metals

Metals analysis was conducted only for sludge (Table 3.7). Since the sample was ashed at 600 °C, mercury and other low boiling-point metals show as ND.

Table 3.7 Metals in SLF

Element	(mg kg^{-1} ash)	Federal Limits* (mg kg^{-1} ash)
Antimony	ND	NL
Arsenic	10.5	75
Barium	ND	NL
Beryllium	ND	NL
Cadmium	11	85
Chromium VI	ND	NL
Chromium	310	NL
Cobalt	20	NL
Copper	1170	4300
Fluorine	ND	NL
Lead	230	840
Mercury	ND	57
Molybdenum	ND	75
Nickel	170	420
Selenium	<0.5	100
Silver	63	NL
Thallium	ND	NL
Vanadium	ND	NL
Zinc	1970	7500

ND = Not detected
Sample was ashed at 600 ° C

*USEPA. 1993 Standards for the Use of Disposal of Sewage Sludge, 40 CFR Part 503.

NL = no limit

Supplied Air

Laboratory compressed air was used for the gasification tests. A standard dry air composition plus humidity was assumed for the mass balances as listed in Table 3.8.

Table 3.8 Standard dry air composition used for mass balances

Air Constituent	Volume (%)	Weight (%)
Nitrogen	78.09	75.52
Oxygen	20.95	23.14
Argon	0.93	1.29
Carbon Dioxide	0.03	0.05
Total	100.00	100.00

An absolute humidity of 4 g kg^{-1} dry air was assumed in all cases. The preheat temperature of supply air for each test is listed in Table 3.9. The preheat air temperature was set in the laboratory. The temperature set point was varied by test run and prior to steady state in an attempt to achieve favorable gasification conditions. For ASF test1, the air preheater was not working, so only ambient temperature air was available.

Table 3.9 Supply air preheat temperatures for test fuels

	ASF		WPF		RSF		WWF		SLF		NPF	
Test No.	1	2	1	2	1	2	1	2	1	2	1	2
Temperature of supply air [°C]	20	302	303	302	302	303	342	352	302	326	352	351

Char and ash in ash dropouts

Char consists of both ash and fixed carbon and was collected along with elutriated bed material in 2 locations: the horizontal dropout and the cyclone (Figure 2.2). Spent bed material was drained from the reactor at the end of each test.

Table 3.10 displays the ultimate analysis of the collected material in the bed, horizontal pass, and cyclone for all fuels and also alkali filter cake for ASF and RSF. Only two filter cake samples provided enough material to be analyzed. Table 3.11 displays the elemental analysis of the ash component from the bed, horizontal pass location, cyclone, and alkali filter cake.

Tar

Table 3.12 displays the ultimate analysis of the collected tar deposits in condenser 1 and condenser 2 where available. Additionally, the ultimate analysis of the dry residue collected from the methanol impingers for WPF, and all tar components mixed together and dried for ASF, are provided in this same table. Table 3.13 displays the elemental ash analysis of the recovered tar.

Table 3.10 Ultimate analysis of spent bed (Bed), horizontal pass (HP), cyclone (Cycl) and filter cake (Cake) from alkali filter

	ASF				WPF			RSF				WWF			SLF			NPF		
	Bed	HP	Cycl	Cake	Bed	HP	Cycl	Bed	HP	Cycl	Cake	Bed	HP	Cycl	Bed	HP	Cycl	Bed	HP	Cycl
Ultimate Analysis (%,db):																				
Carbon	2.23	34.64	25.63	28.69	20.9	65.33	42.09	1.37	23.56	18.98	21.46	3.49	66.03	45.44	20.88	18.70	18.58	5.94	69.92	64.84
Hydrogen	0.10	0.11	0.22	0.21	0.08	0.60	0.35	0.24	0.02	0.08	0.07	0.02	0.32	0.22	0.06	0.15	0.29	0.02	0.32	0.40
Nitrogen	0.01	0.48	0.67	0.80	0.18	0.86	0.93	0.03	0.33	0.31	0.28	<0.01	0.62	1.20	1.01	1.51	2.79	0.01	0.46	0.61
Sulfur	<0.01	0.04	0.07	0.07	<0.01	<0.01	0.02	0.03	0.04	0.15	0.09	<0.01	<0.01	2.52	0.67	0.71	1.21	<0.01	0.18	0.39
Ash	98.18	62.89	72.18	66.70	82.85	25.88	48.53	94.54	74.19	76.48	74.43	95.33	26.80	48.95	80.01	80.99	77.38	94.35	27.29	30.39
Oxygen (by diff.)	0.00	1.84	1.33	3.64	0.00	7.33	8.18	4.14	1.91	4.19	3.54	1.14	6.42	2.34	0.01	0.00	0.00	0.00	1.90	3.54
Total	100.54	100.00	100.00	100.00	104.01	100.01	100.00	100.00	100.00	100.19	100.00	100.00	100.00	100.00	102.64	102.07	100.26	100.34	100.00	100.00
Chlorine	0.03	0.10	0.11	0.13	0.02	0.08	0.10	0.89	1.55	1.38	1.57	0.02	0.22	0.46	0.08	0.18	0.58	0.01	0.09	0.29

Table 3.11 Ash elemental analysis from spent bed (Bed), horizontal pass (HP), cyclone (Cycl) and alkali filter cake (Cake) from alkali filter

	ASF				WPF			RSF				WWF			SLF			NPF		
	Bed	HP	Cycl	Cake	Bed	HP	Cycl	Bed	HP	Cycl	Cake	Bed	HP	Cycl	Bed	HP	Cycl	Bed	HP	Cycl
Ash (%, d.b.)	98.18	62.89	72.18	66.70	82.85	25.88	48.53	94.54	74.19	76.48	74.43	95.33	26.8	48.95	80.01	80.99	77.38	94.35	27.29	30.39
Elemental Ash:																				
SiO_2	54.58	56.25	49.08	57.74	46.72	33.53	48.3	27.77	57.34	76.65	76.73	53.78	30.6	39.46	45.58	46.8	46.7	52.62	39.47	35.6
Al_2O_3	39.98	26.15	28.13	15.12	36.76	20.71	11.3	8.61	2.36	1.61	<0.01	36.42	7.51	10.77	18.5	17.5	15.3	38.53	29.65	23.51
TiO_2	1.89	0.92	0.53	0.65	1.78	0.71	0.52	0.40	0.13	0.07	0.04	1.97	0.43	0.78	1.38	1.31	1.16	1.68	6.09	6.64
Fe_2O_3	1.83	3.16	5.96	7.46	1.8	2.04	4.80	1.08	0.48	0.36	0.57	3.42	4.59	5.48	5.55	5.29	5.94	1.88	3.89	4.06
CaO	0.47	3.16	4.67	5.01	3.65	26.10	18.50	1.99	2.02	2.44	3.69	0.43	28.2	18.4	7.33	7.81	8.32	0.62	10.8	15.4
MgO	0.12	1.38	2.58	3.10	0.72	5.76	4.31	50.6	22.8	8.90	6.51	0.09	3.23	3.28	2.64	2.96	3.3	0.20	2.73	3.82
Na_2O	0.32	1.23	1.77	1.37	0.06	0.30	1.39	0.08	0.18	0.20	0.04	0.07	0.81	1.16	1.16	1.22	1.27	0.26	3.20	3.77
K_2O	0.68	7.01	8.70	10.6	1.21	7.20	8.79	3.44	8.63	8.36	9.55	0.76	7.67	4.87	1.25	1.34	1.74	2.35	1.73	2.65
P_2O_5	0.14	0.97	1.26	1.45	0.27	2.45	1.89	0.28	1.67	1.12	1.15	0.16	2.88	6.89	13.18	13.4	13.5	0.20	1.31	2.96
SO_3	0.04	0.20	0.39	0.40	2.26	0.31	0.18	2.96	0.37	0.50	0.21	0.04	2.2	2.45	1.31	1.6	2.14	0.04	1.35	3.07
Cl	<0.01	0.08	0.09	0.08	<0.01	0.23	0.09	1.18	2.01	1.83	1.83	<0.01	0.69	0.73	<0.01	<0.01	0.04	<0.01	0.06	0.16
CO_2	0.03	0.21	0.16	0.46	0.72	1.42	0.89	0.33	0.10	0.09	0.09	0.05	8.10	2.17	0.05	0.04	0.05	0.02	1.58	0.49
Total:	100.08	100.72	103.32	103.44	95.95	100.76	100.96	98.72	98.09	102.13	100.41	97.19	96.91	94.40	97.93	99.2	99.40	98.4	101.90	102.13

(Ash calcined @ 600 °C prior to analysis)

Table 3.12 Composition of tar (% dry basis) and mass of each component

Fuel Sample	ASF	WPF			RSF		WWF	SLF		NPF
Location	All Components	Condenser 1	Condenser 2	Impingers	Condenser 1	Condenser 2	Condenser 1	Condenser 1	Condenser 2	Condenser 1
Ultimate Analysis (%, db):										
Carbon	68.43	62.25	70.87	77.03	27.00	31.50	66.38	41.98	50.71	80.63
Hydrogen	5.54	6.34	5.42	6.55	0.43	0.50	1.81	1.12	3.80	1.75
Nitrogen	11.73	10.86	6.66	3.73	1.41	2.32	1.77	9.24	22.77	1.25
Sulfur	0.71	0.68	0.50	0.23	0.44	0.85	0.27	4.14	7.11	0.83
Ash	2.66	5.30	4.26	0.06	63.35	59.91	26.67	48.21	13.16	15.41
Oxygen (by diff.)	11.01	14.39	12.29	12.40	7.66	5.68	3.81	0.00	2.03	0.23
Totals	100.00	100.00	100.00	100.00	100.00	100.00	100.00	104.69	100.00	100.00
Chlorine	0.04	0.32	0.08	0.05	0.88	0.95	0.18	0.54	0.65	0.07

Tar air-dried in atmospheric fume hood.
WWF and NPF: No condenser 2 solids due to small, unrecoverable amount.
Impingers from only one fuel analyzed as check.

Table 3.13 Analysis of ash from tar samples

	ASF	WPF	WPF	WPF	RSF	RSF	WWF	SLF	SLF	NPF
Location	All Components	Condenser 1	Condenser 2	Impingers	Condenser 1	Condenser 2	Condenser 1	Condenser 1	Condenser 2	Condenser 1
Elemental Ash										
SiO_2	19.77	14.05	17.17	*	69.03	64.19	27.01	37.88	36.04	25.88
Al_2O_3	5.72	5.33	6.67	*	1.16	1.22	10.19	16.98	22.77	17.66
TiO_2	0.37	0.35	0.27	*	0.04	0.22	0.40	1.25	1.24	6.78
Fe_2O_3	3.65	3.29	4.19	*	1.68	0.66	6.93	7.02	5.55	11.01
CaO	4.65	40.60	35.60	*	4.76	5.97	27.60	9.55	7.07	13.70
MgO	1.82	5.99	6.70	*	6.52	6.25	3.13	2.51	1.66	2.89
Na_2O	2.19	1.09	1.18	*	0.29	0.45	0.78	0.98	1.08	2.90
K_2O	3.93	7.02	7.32	*	6.63	9.18	5.18	1.32	1.01	1.60
P_2O_5	1.70	4.34	5.45	*	1.06	1.21	3.87	15.74	14.69	3.64
SO_3	11.30	6.78	3.84	*	1.50	2.57	3.29	3.21	4.24	2.71
Cl	+	+	+	*	1.15	1.65	0.66	<0.01	<0.01	<0.01
CO_2	+	+	+	*	0.38	0.66	4.92	0.21	0.12	0.05
Total:	55.10†	88.84	88.39	*	94.20	94.23	93.96	96.65	95.47	88.82

*WPF impinger tar sample had extremely low ash yield and insufficient material for analysis of ash
†Poor recovery due to small amount of ash in the tar sample
+Insufficient material to conduct analysis

Recovery of ash in the tar samples ranged from 88.39 % to 96.65 % with the exception of ASF. Recovery was generally poor because of difficulties in collecting tar samples. Recovery for ASF was low in part because the amount of total original ash represented only 2.66% of all ASF tar samples. The analysis of ash for WPF impingers was not possible because of insufficient ash in the tar sample.

Filter Cake

The process stream was sampled isokinentically (temperature range of 225 °C to 275 °C) for the alkali extraction train at the cyclone exit just prior to flaring. A filter cake was collected on the 5 μm filter and gas phase elements were absorbed in the distilled water impingers and methanol scrubbers. Although five filter cake samples were collected, only two were large enough for chemical analysis: one for ASF and one for RSF. The ultimate analysis of the filter cake is shown in Table 3.10. The filter cake ash elemental analysis is shown in Table 3.11.

Bed Material

The analysis of the fresh bed material is shown in Table 3.14.

Table 3.14 Composition of fresh bed material (%)*

SiO_2	53.5
Al_2O_3	43.5
TiO_2	2.1
Fe_2O_3	0.55
CaO	0.05
MgO	0.05
Na_2O	0.13

K_2O	0.13
P_2O_5	NR
SO_3	NR
Cl	NR
CO_2	NR
Undetermined	NR
Total	100

*Reported by manufacturer (North American Refractories Company, Pittsburgh, Pennsylvania).

NR = Not reported

Mass Balance

For each run, detailed material balances were conducted. Material inputs include:

1) Biomass fuel (including moisture)

2) Primary air (including humidity)

3) Feeder purge air (including humidity)

4) Bed Material

Material outputs include:

1) Recovered material from the horizontal pass and cyclone

2) Spent bed material

3) Stack gas and particles

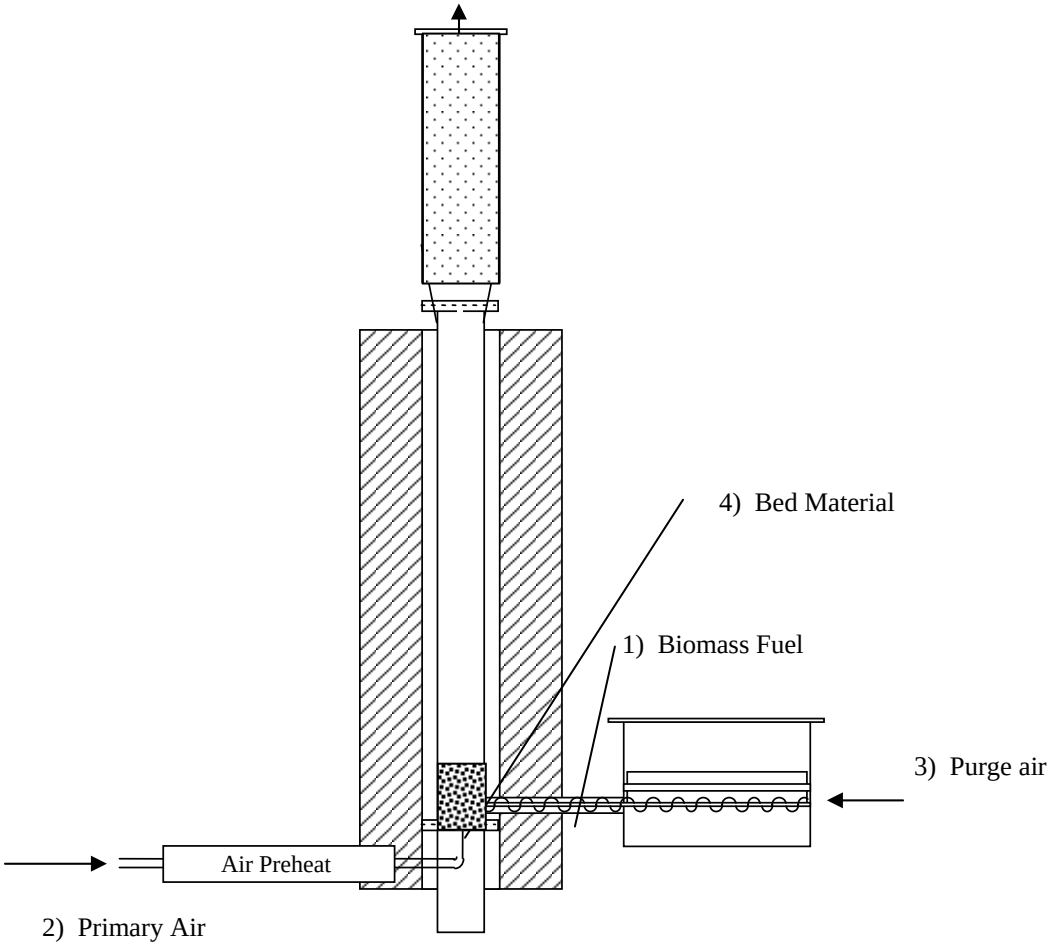

Figure 3.3 Material inputs to fluidized bed reactor system

The overall mass balance for the reactor is given in equation [3.5]:

$$m_{air} + m_{fuel\ dry} + m_{fuel\ wet} + m_{bed\ fresh} = m_{bed\ out} + m_{ash} + m_{stack} \quad [3.5]$$

m_{air} = mass of supplied moist air [g]

$m_{fuel\ dry}$ = total dry weight of burned fuel [g]

$m_{fuel\ wet}$ = total moisture present in fuel [g]

$m_{bed\ fresh}$ = total weight of fresh bed material loaded into reactor [g]

$m_{bed\ out}$ = total weight of spent bed removed after test [g]

m_{ash} = total weight of material in ash dropouts [g]

m_{stack} = mass of particles and gas leaving the system at the stack (including sample flows) [g]

All parameters above except m_{stack} are measured (in a few cases the stack particles were also measured) and the mass output into the stack can be calculated with equation [3.5]. The cyclone stack mass consists of a particle (or solid phase) and a vapor phase.

$$m_{stack} = m_{particle\ phase} + m_{gas\ phase} \quad [3.6]$$

$m_{particle\ phase}$ = mass of particles in the stack flow [g]

$m_{gas\ phase}$ = mass of gas (or vapor) in the stack flow [g]

Partitioning to particles

The mass ratio of solid particles to gas phase in stack is

$(m_{particle\ phase}/(m_{stack} - m_{particle\ phase})$ [3.7]

3.1.7 Concentration of Solids and Condensibles

Solids and condensibles were collected in the condensers (condenser 1 and condenser 2) that were located in the gas sampling train. The material was then air dried after each test. The solids remaining after evaporation of moisture were usually a small fraction of the initial amount. Values for condensibles can be seen in the material balance summaries for each of the twelve tests discussed later in this chapter.

3.1.8 Power Balance

Power inputs to the system consisted of the power supplied by the 3.48 kW electric heater, the fuel, and in the preheated air. Since the heater was on only intermittently during gasification runs, only a fractional amount of the maximum heater power was applied.

The fluidized bed gases absorbed heat from the reactor system and also transferred heat to the associated reactor equipment. The power balance for the system is shown in equation 3.8:

$$\dot{q}_{fuel} + \dot{q}_{heater} + \dot{q}_{air} = \dot{q}_{ash} + \dot{q}_{stack} + \dot{q}_{system} \quad [3.8]$$

where

$\dot{q}_{fuel}$ = power represented by the fuel input [W]

$\dot{q}_{heater}$ = supplied power from external electric furnace heater through reactor wall [W]

$\dot{q}_{air}$ = power of preheated supplied air [W]

$\dot{q}_{ash}$ = power of the ash (chemical) [W]

$\dot{q}_{stack}$ = power of stack gas (sensible + chemical) [W]

$\dot{q}_{system}$ =power lost as heat to the environment [W]

The sensible power from the ash is included in $\dot{q}_{system}$.

Fuel Power

Power input in fuel was calculated by equation [3.9]

$$\dot{q}_{fuel} = \dot{m}_{fuelwet} * HHV \quad [kW] \qquad [3.9]$$

$\dot{m}_{fuelwet}$ = wet fuel feed rate [kg s^{-1}]

HHV = higher heating value at constant volume [MJ kg^{-1}], wet basis

Supplied Air

The power of the supplied air is calculated by equation [3.10]:

$$\dot{q} = \dot{m}_{airdry} * (h_a + w * h_w) \quad [kW] \qquad [3.10]$$

$\dot{m}_{airdry}$ = dry air mass flow rate [kg s^{-1}]

h_a = enthalpy of dry air [MJ/kg]

w = mass fraction of vapor in dry air

h_w = enthalpy of vapor in air

As long as no condensation occurs, this equation can be re-written as:

$$\dot{q} = \dot{m}_{air} * \sum_{1}^{j} MassFraction_j C_{p\,j} * (T_2 - T_1) \qquad [3.11]$$

where

$\dot{m}_{air}$ = mass of supplied air including humidity

Mass $Fraction_j$ = mass fraction components of humid air mass

C_{pj} = specific heat of a component of humid air mass in kJ $kmol^{-1}$ K^{-1} at average temperature $(T_1 + T_2)/2$

T_2 = preheat gas temperature

T_1 = ambient temperature

with values of C_p taken from the expressions in Table 3.15.

Table 3.15 Polynomial expression for specific heat capacities of gases (average temperature was used) as a function of gas temperature (K) (Van Wylen and Sonntag (1982) as adapted by Turn, 1994)

Gas	C_p [kJ kmol^{-1} K^{-1}]
O_2	$_{Cp} = 37.342 + 0.020102x10^{-3}T^{1.5} – 178.57x10^{3}T^{-1.5} + 236.88x10^{4}T^{-2}$
N_2	$_{Cp} = 39.060 – 512.79x10^{3}T^{-1.5} +1072.7x10^{4}T^{-2} – 840.40x10^{6}T^{-3}$
H_2O_{vapor}	$_{Cp} = 143.05 – 58.04T^{-.25} +8.2751T^{-0.5} – 3.6989x10^{-2}T$
H_2	$_{Cp} = 56.505 – 22.223x10^{3}T^{-.75} +1165x10^{2}T^{-1} – 560.70x10^{3}T^{-1.5}$
CO_2	$_{Cp} = -3.7357 + 3.0529T^{0.5} – 4.1034x10^{3}T + 2.4198x10^{-6}T^{2}$
CH_4	$_{Cp} = -672.87 + 139.058T^{0.25} - 0.78662T^{0.75} + 3238.8T^{-0.5}$
CO	$_{Cp} = 69.145 – 22.282x10^{-3}T^{0.75} – 2007.7T^{-0.5} + 5589.6T^{-0.75}$

Reactor Heater Power

The electric heater for the reactor is rated 3.48 kW at 208 V. The heat supplied to the reactor can be calculated with the outside surface furnace wall temperature, average temperature inside the reactor and the heat transfer coefficient of the reactor. The heat transfer coefficient for the reactor was determined in a test that was conducted separately by Pfaff (1999) using the following procedure. Primary air was preheated to 350 °C and heater temperature was set to 800 °C. The temperature increase of the supplied air after flowing through the reactor was determined and the amount of heat absorbed by the air was calculated from this and the mass flow rate of air through the reactor. The overall thermal conductance of the reactor heater was calculated as 2.5 W K^{-1}.

Supplied power from the electric heater was calculated with equation [3.12].

$\dot{q}_{heater}$ = U * ($T_{furnace} - T_{reactor}$) [3.12]

for $T_{furnace} > T_{reactor}$

and $\dot{q}_{heater}$ = 0 otherwise (implying heat loss represented in $\dot{q}_{system}$)

U = heat transfer coefficient furnace to reactor [$W K^{-1}$] = 2.5 $W K^{-1}$

$T_{furnace}$ = average surface temperature of furnace [°C]

$T_{reactor}$ = average gas temperature inside reactor [°C]

To be included as furnace power input, the temperature of the gas inside the reactor had to be lower than the heater wall temperature, otherwise reactor heat loss was lumped with $\dot{q}_{system}$.

Power in ash and char

The power associated with ash and char is determined from the heating value, exit temperature and mass flow rate. These values are shown in Table 3.16. Only tests for which complete compositional analysis could be performed are included, so that only one test is shown for WPF, RSF, WWF, and SLF. Heating values were not measured directly but were instead computed from the carbon concentrations and equation [3.4].

Table 3.16 Power (kW) of ash, char and recovered material for tested fuels

Location	ASF		WPF	RSF	WWF	SLF	NPF	
Test No.	1	2	1	2	2	2	1	2
Remaining ash in bed	0.3	0.6	1.0	0.1	0.2	3.5	0.22	0.2
Horizontal dropout	7.1	4.8	3.1	1.1	0.6	1.5	0.18	0.3

Cyclone dropout	1.6	0.8	0.4	0.3	0.1	0.1	0.12	0.06
Total Power	9.0	6.2	4.5	1.5	0.9	5.1	0.5	0.6

Producer Gas Power

The power associated with the producer gas is made up of two components: the chemical power (heating value) and sensible power. The chemical power comes only from CO, CH_4 and H_2 in the stack gas (and other combustibles not measured in these tests). Their individual heating values and mass fractions are used to calculate the HHV of the stack gas. The HHV of the stack gas is then used in equation [3.13] and the sensible energy is calculated by use of equation [3.14].

$$\dot{q}_{chemical} = \dot{m}_{stack} * HHV_{stack\ gas} \quad [W] \quad [3.13]$$

$$\dot{q}_{sensible} = \dot{m}_{stack} * C_p * (T_{2c} - T_1) \quad [W] \quad [3.14]$$

T_{2c} = average gas temperature at the exit of the cyclone

T_1 = ambient temperature

Cp = specific heat at average temperature $(T_1 + T_{2c})/2$

The heating values for H_2, CO and CH_4 are listed in Table 3.16a. These values are shown in MJ kg^{-1} and MJ m^{-3} units in order to determine energy input levels on a mass or volume basis.

Table 3.16a Higher heating values for H_2, CO, and CH_4

Constituent	HHV (MJ kg^{-1})	HHV (MJ m^{-3})
H_2	141.9	11.5
CO	10.1	11.5
CH_4	55.6	36.1

The producer gas mass flow is $\dot{m}_{stack}$ and average heat capacity of the gas is Cp. Average gas temperatures at the exit of the cyclone, noted as T_{2c}, varied but were in the range of 225 °C to 275 °C and the reference temperature for all sensible energy calculations is taken as ambient temperature. The gas mass flow rate was computed by dividing the total mass obtained from the overall mass balance [3.5] by the steady run time. The mass flow rates, power and composition of the combustible gases (CO, CH_4 and H_2), are listed in Table 3.17.

Table 3.17 Mass flow rate (g s^{-1}), power of dry gas (kW)* and dry composition (% v/v) of energy carrier gases in producer gas in stack from GC analysis.

	ASF		WPF		RSF		WWF		SLF**		NPF	
	Test 1	Test 2	Test 1	Test 2	Test 1	Test 2	Test 1	Test 2	Test 1	Test 2	Test 1	Test 2
Mass Flow	0.39	0.35	0.43	0.49	0.15	0.24	0.20	0.24	-	0.42	0.21	0.22
Power	8.8	8.2	8.6	10.8	3.3	3.9	3.9	3.9	-	8.3	3.5	3.4
H_2	13	18	10	12	4	9	13	8	21	15	8	7
CO	20	20	22	21	10	17	15	18	15	11	21	20
CH_4	7	8	7	8	4	4	5	5	8	6	6	5

**Insufficient data for SLF test 1 due to tar plugging
*Power of dry gases does not include power of water vapor, tar or other particles and sensible power

Listed in Table 3.18 are the input, output and unaccounted powers. The unaccounted power is the system power and includes all sources unaccounted for including the heat losses from equipment to the environment. This power can be affected by conditions such as mass flow, ambient temperature and operating temperature.

Table 3.18 Power input and output summary (kW)

Power Component	ASF		WPF		RSF		WWF		SLF		NPF	
Test No.	1	2	1	2	1	2	1	2	1	2	1	2
Inputs												
Fuel	29.0	21.6	24.1	26.0	12.5	11.1	-	10.3	-	32.0	6.0	7.1
Air	0.0	0.1	0.1	0.1	0.1	0.1	-	0.1	-	0.2	0.1	0.1
Heater	0.3	0.3	0.4	0.3	0.2	0.2	-	0.2	-	0.2	0.2	0.1
Total Input	29.3	22.0	24.6	26.4	12.8	11.4	-	10.6	-	32.4	6.3	7.3
Outputs												

Ash	9.0	6.2	4.5	4.9	0.2	1.5	-	0.9	-	5.1	0.5	0.6
Stack gas	8.8	8.2	8.6	10.8	3.3	3.9	-	3.9	-	8.3	3.5	3.4
Tar, Particles and Vapor	2.6	2.1	2.1	1.1	0.3	0.9	-	1.0	-	14.2	0.3	0.4
Total Output	20.4	16.5	15.2	16.8	3.8	6.3	-	5.8	-	27.6	4.3	4.4
Unaccounted*	8.9	5.5	9.4	9.6	9.0	5.1	-	4.8	-	4.8	2.0	2.9
(%)	30.0	25.0	38.0	36.4	70.0	44.7	-	45.3	-	14.8	32.0	39.7

*Unaccounted for power is system power and also includes power of any remaining fuel, or ash not accounted for in other parts of the power balance. Incomplete power data for WWF test 1 and SLF test 1.

3.1.9 Gas phase ammonia, hydrogen cyanide, chlorine and potassium

Impinger concentrations for Cl, K and NH_3 are shown in Tables 3.19, 3.20 and 3.21 respectively.

Table 3.19 Impinger concentrations (mg L^{-1}) for Cl^-

Impinger Number	ASF		WPF		RSF		WWF		SLF		NPF	
	1	2	1	2	1	2	1	2	1	2	1	2
1	1310	480	92	5	433	338	70	14	44847	13185*	9	8
2	33	3	2	5	28	13	98	19	3718	1315*	1	2
3	-	-	-	5	-	-	2	10	445	-	2	14

*Suspect due to interference problems with Cl detection for SLF tests 1 and 2

Table 3.20 Impinger concentrations (mg L^{-1}) for K^+

Impinger Number	ASF		WPF		RSF		WWF		SLF		NPF	
	1	2	1	2	1	2	1	2	1	2	1	2
1	21.2	13.6	16.96	3.85	27.76	32.99	8.43	4.78	6.12	33.27	2.51	1.75
2	9.8	16.91	0.8	3.85	6.15	5.09	0.32	0.48	14.80	6.44	0.30	0.41
3	-	-	-	3.85	-	-	0.53	0.50	2.02	-	0.52	0.32

Table 3.21 Impinger concentrations (mg-N L^{-1}) of NH_3

	ASF		WPF		RSF		WWF		SLF		NPF	
Test No.	1	2	1	2	1	2	1	2	1	2	1	2
Impinger Number												
1	3646	2381	18051	1961	2845	2836	524	1403	9472	8416	94	72
2	145	57	274	113	31	20	6	44	4238	2205	16	9
3	20	10	34	17	1	1	1	10	173	38	<1	3

Table 3.22 summarizes the average gas phase concentration in the dry stack gas of ammonia, hydrogen cyanide, chloride, potassium, carbon monoxide, hydrogen and methane for each fuel test

Table 3.22 Average gas phase concentration in the dry stack gas of ammonia, hydrogen cyanide, chloride, potassium, carbon monoxide, hydrogen and methane for each fuel test. Fuel N shown for comparison.

Test No.	ASF Test 1	ASF Test 2	ASF Test 3	WPF Test 1	WPF Test 2	RSF Test 1	RSF Test 2	RSF Test 3	WWF Test 1	WWF Test 2	SLF Test 1	SLF Test 2	NPF Test 1	NPF Test 2
Fuel Nitrogen (% dry matter)	0.79	0.79	0.79	0.59	0.59	0.55	0.55	0.55	0.35	0.35	5.64	5.64	0.14	0.14
NH_3 (% v/v)	0.50	0.48	-	0.20	0.27	0.31	0.29	-	0.085	0.118	3.99	1.00	0.009	0.007
HCN (ppmv)	-	-	2.3	-	-	-	-	24.0	-	-	-	-	-	-
Cl (ppmv)	810	440	-	98	22	260	280	-	250	71	79700*	24700*	9	17
K (ppmv)	17	22	-	17	16	17	26	-	13	8	30	61	2	2
H_2 (% v/v)	13	18	-	10	12	4	9	-	13	8	21	15	8	7
CO (% v/v)	20	20	-	22	21	10	17	-	15	18	15	11	21	20
CH_4 (% v/v)	7	8	-	7	8	4	4	-	5	5	8	6	6	5

*Suspect due to problems with Cl detection for SLF tests 1 and 2

3.1.10 Hot and cold gas efficiency

Hot and cold gas efficiencies were calculated with the following equations:

$$\eta_{\text{hot gas}} = \frac{\text{sensible energy + chemical energy in producer gas}}{\text{(fuel input power + furnace heater power + air input power)}} \quad [3.15]$$

$$\eta_{\text{cold gas}} = \frac{\text{chemical energy in producer gas}}{\text{(fuel input power + furnace heater power + air input power)}} \quad [3.16]$$

Efficiencies are listed in Table 3.23. As noted later, efficiencies may have been higher than shown due to possible errors associated with measurements of air and fuel flow rates and stack gas composition.

Table 3.23 Hot and cold gas efficiencies in (%)

	ASF		WPF		RSF		WWF		SLF		NPF	
Test No.	1	2	1	2	1	2	1	2	1	2	1	2
$\eta_{\text{hot gas}}$	31.3	38.6	37.0	43.1	25.7	36.0	-	38.1	-	26.1	55.1	48.1
$\eta_{\text{cold gas}}$	29.9	37.3	35.2	41.2	24.1	34.5	-	36.7	-	25.3	53.7	46.4

Complete data for WWF and SLF unavailable due to earlier than expected termination of test and tar plugging of gas sampling train respectively.

3.1.11 Element Closures

Elemental closure is a method of tracking and accounting for material (at the elemental level) that enters the system in known amounts. Elemental closures compared the elemental outputs against the original elemental inputs for all species determined in the ultimate and ash analyses.

Elemental inputs included the following:

Dry air, air moisture, dry fuel, fuel moisture and fresh bed material

Elemental outputs included the following:

Recovered material from the spent bed, horizontal pass and cyclone; dry stack gas, tars and particulates in stack gas, stack moisture, stack NH_3, and stack HCN. Table 3.24 shows the elemental closures for the six tests with complete compositional data.

Table 3.24 Total element outputs as (%) of original inputs

	ASF	WPF	RSF	WWF	SLF	NPF
Element	Test 1	Test 1	Test 2	Test 2	Test 2	Test 2
C	82	74	78	69	52	79
H	74	71	97	107	98	98
O	99	89	119	93	158	101
N	178	159	123	130	198	111
S	107	296	322	110	47	45
K	75	133	73	122	65	620
Cl	485	402	138	555	2880	42
Si	75	116	49	104	49	98
Al	114	103	13	88	41	88
Ti	99	99	13	99	50	94
Fe	87	328	114	606	64	345
Ca	74	104	139	107	59	118
Mg	68	120	2423*	105	61	124
Na	66	152	47	69	57	96
P	129	181	88	290	61	95

*MgO not accounted for in rice straw bed material

Elemental closures are poor in many cases due to low total input of specific elements. However, poor closure on carbon and nitrogen suggest experimental error in one or more of the three major flows in the system: air, fuel, and stack gas. Closing the carbon and nitrogen balances suggests that the measured value of air flow rate was in general biased low. For SLF, the carbon balance also suggests that the measured concentration of CO was low. Closing the carbon balance also indicates that hot and cold gas efficiencies were more typically in the range of 50 – 70%, as expected.

Table 3.25 shows how air flow might have been biased low for all runs. The average air flow rate to close the carbon balance was 59.2 L min^{-1} (excluding sludge) versus an

average experimental air flow of only 24.4 L min^{-1}. This represents an average difference of about 140%, again excluding sludge. SLF2 fuel had the extreme value for air flow needed to close the carbon balance. Fuel feed rate was high for all runs.

Measured values of air and fuel feed rates were assessed by calculating flow rates that individually would close the carbon balance. Results are listed in Table 3.25 along with the measured experimental values. For example, if the carbon balance for ASF1 is closed by adjusting the air flow rate alone, a rate of 52.2 L min^{-1} is needed, a factor 2.4 times higher than the measured value of 21.5 L min^{-1}. Similarly, if the carbon balance is closed by adjusting only the fuel feed rate, making no adjustments to the measured air flow rate or stack gas composition, a fuel rate of 96 g min^{-1} is needed, a factor 0.83 times the measured value of 115.7 g min^{-1}. The very poor closure obtained with SLF2 is likely associated mostly with errors in the stack gas composition. Excluding SLF2, on average the air flow rate would need to be increased by a factor 2.4 times if it alone is used to close the carbon balance. Also excluding SLF2, fuel feed rate would need to be reduced on average by a factor 1.5 times if fuel feed rate only is used to close the carbon balance. These results do not suggest that the measurements are in fact in error by these magnitudes. Experimental checks, as noted later, suggest that individually the errors are much lower and that a combination of errors in air flow rate, fuel feed rate, and stack gas composition is contributing to the poor closure in many of the analyses.

Table 3.25 Calculated air and fuel flow rates needed to individually close the carbon balance

Fuel	Experimental Air Flow Rate [L/min]	Air Flow Rate To Close Carbon Balance [L/min]	Experimental Fuel Feed Rate [g/min]	Fuel Feed Rate To Close Carbon Balance [g/min]
ASF1	21.5	52.2	115.7	96.0
ASF2	24.0	41.8	86.0	74.0
WPF1	27.1	67.9	76.2	56.4
WPF2	25.9	108.2	55.0	36.0
RSF1	26.8	106.7	50.4	32.4
RSF2	24.8	44.0	44.9	35.4
WWF2	24.8	50.7	30.4	20.5
SLF2	24.8	171.6	124.8	64.3
NPF1	21.8	27.6	19.3	17.0
NPF2	22.1	33.6	22.6	18.0
Average	24.4	70.4	62.5	45.0
Difference [%]	189.3		-28.0	

Results for Individual Experiments

Thermocouples (TC1 through TC5), disengagement zone thermocouples (D1 through D3), deposition probe thermocouple (deposition probe) and cyclone exit thermocouple (cyclone exit) locations are shown in Figure 2.2 in Chapter 2. Refer to that figure for the location of these thermocouples.

Most variations of parameters (air, fuel, temperature) were made prior to the steady state period. Minor variations made after a steady state period was started are noted where applicable and were made to investigate other how the reactor performed at other AF ratios. Generally, before a steady state period began, attempts were made to maximize the levels of CO and H_2 and achieve a robust flame.

3.2 Almond Shell (ASF)

3.2.1 Test 1 and 2

Figures 3.4 through 3.8 and Tables 3.26 through 3.29 summarize the data from this test.

The first test of ASF was run at an average air-factor of 0.07 (the range for all tests was approximately ± 5% of stated average air-factor but as noted above air factors were likely higher due to possible errors in the air flow rate measurement). The test utilized a deep bed (in this case, the bed depth was approximately twice bed diameter) of 866 grams of the NARCO alumina-silicate bed media. Average furnace wall temperature was 872 °C, average primary fluidizing air flow rate was 28.8 g min^{-1} and average fuel feed rate (dry basis) was 116 g min^{-1} during the 57 minute test run period.

Primary fluidizing air was not preheated for the first ASF run due to heater failure. Bed temperatures along the main reactor column varied by only approximately 20 °C throughout the course of the experiment. Average column (the vertical 1 m length of the 73 mm diameter section of fluidized bed) temperature was approximately 736 °C.

Figure 3.4, shows that the lower bed temperature (TC1) increases as fuel is initially added to the reactor while (TC2) falls by more than 200 °C the instant fuel is introduced. TC3 at first sees an increase of approximately 100 °C from the hot combustion gases emitted from the few grams of burning fuel, but soon declines steadily as more cold fuel mass is injected at higher flow rates moving from high heat release of combustion to lower heat release and endothermic reactions of gasification. After the abrupt change due to fuel addition, TC1 and TC2 begin to track one another and steadily rise as heat of reaction and

heat transfer from the walls heat up the bed media. TC1 and TC2 temperatures increase with TC3 and the three continue to rise together until leveling off at the same steady temperature. The lower bed temperature increases as the feed rate of fuel is increased until a steady state temperature is reached.

Upper bed temperatures (TC4 and TC5) are already above the furnace wall temperature before fuel introduction. These temperatures do not seem to be influenced much by the fuel introduction (only small increases initially) until approximately 5 minutes after fuel flow begins. At this point, the temperatures decrease until reaching the same uniform temperature as the lower bed temperatures. The lower bed temperatures are initially at 870°C and decrease rapidly as both the colder primary air and fuel are introduced into the reactor. After approximately 30 minutes, bed temperatures are steady and the upper temperatures are comparable to the temperatures in the lower bed.

After the fuel feed is stopped, the upper bed temperatures initially rise to the set furnace temperature of 872 °C but then retreat when power to the furnace is shut off.

Bed differential pressure is created by the mass of the bed being lifted on the incoming airflow. Over time, much of the initial bed material is lost through attrition. Typically, this bed material flows beyond the disengagement section and into the ash dropouts or out the stack. As the bed material diminishes, the corresponding drop in bed differential pressure can be seen in Figure 3.7. At 1.2 hours after the start of the stable period, the bed differential pressure declined to approximately 75% of the original value.

3.2.1.1 Operating parameters

Table 3.26 Operating Parameters for ASF during steady state periods

Parameter		Test 1	Test 2
Steady Period	(min)	57	46
Average Fuel Feed Rate (db)	(g min^{-1})	116	86
Fuel Moisture	(% wb)	9.0	9.0
Total Wet Fuel Burned	(g)	7250	4350
Total Dry Fuel Burned	(g)	6598	3959

Average Air Flow	(g min^{-1})	28.8	32.2
Air : Fuel Ratio (AF)	(-)	0.25	0.37
Stoichiometric AF	(-)	3.73	3.73
Air Factor	(-)	0.07	0.10
Inlet air Superficial Velocity at ambient temp	(m s^{-1})	0.10	0.11
Inlet air Superficial Velocity at operating temp	(m s^{-1})	0.33	0.35
Average Furnace Wall Temperature	(°C)	872	801
Primary Air Preheat Temperature	(°C)	20	302
Cyclone Exhaust Temperature	(°C)	221	182
Postflare Probe Temperature Average	(°C)	376	253
Average Post Flare Temperature	(°C)	178	123
Average Pressure Drop across Bed	(Pa)	1883	2027
Equivalent Bed Mass Computed from Mean Pressure Drop	(g)	807	869

Note that the reported superficial velocities include only the air and do not include the gas evolution from the fuel.

3.2.1.2 Mass balance summary

Table 3.27 Mass Balance Summary for ASF

	Test 1		Test 2	
Parameter	Mass (g)	Percent of flow	Mass (g)	Percent of flow
Inputs				
m_{air}	1644	16.8	1480	22.1
$m_{dry\ fuel}$	6598	67.6	3959	59.1
$m_{fuel\ moist}$	653	6.7	392	5.9
$m_{fresh\ bed}$	866	8.9	866	12.9
Total	9761	100.0	6697	100.0
Outputs				
$m_{bed\ out}$	752	7.7	1014	15.1
$m_{horz\ pass}$	1731	17.7	943	14.1
$m_{cyclone}$	507	5.2	203	3.0
$m_{stack\ dry}$	5502	56.4	3358	50.2
$m_{stack\ sol/cond}$*	1252	12.8	1168	17.4
m_{NH3}**	17	0.2	10.7	0.2
Total	9761	100.0	6697	100.0

*$m_{stack\ sol/cond}$ includes the total air dried tar in the stack flow of 132 g and 109 g respectively for Tests 1 and 2. These total tar values are derived from 43 g of tar in condenser 1 and no collectable of tar in condenser 2 (for Test 1) and 36 g in condenser 1 and no collectable in condenser 2 (for Test 2).

**m_{NH3} represents the total ammonia in stack flow derived from a sample collected in the ammonia train. There may be some additional ammonia in solution collected in the $m_{stack\ sol/cond}$.

3.2.1.3 Stack gas grab sample average analysis, gas phase NH_3, HCN, Cl, K and concentration of solids and condensibles for ASF

Table 3.28 Stack gas grab sample average analysis (GC) and concentration of solids and condensibles for ASF

	Test 1	Test 2	Test 3
Constituent	Mean Concentration (% v/v)	Mean Concentration (% v/v)	
CO	20	20	
H_2	13	18	
CH_4	7	8	
CO_2	20	22	
N_2	39	32	
O_2	1	0	
	Mean Concentration (ppm)	Mean Concentration (ppm)	
NH_3	5030	4846	
Cl	810	440	
K	17	22	
HCN	-	-	2.3
Total (%)	100.59	100.53	
Higher Heating Value ($MJ\ m^{-3}$)	6.1	7.3	
Solids and Condensibles	Concentration ($mg\ L^{-1}$ dry gas)	Concentration ($mg\ L^{-1}$ dry gas)	
With condensed water	260	378	
Air dried, room temperature	27.4	38	

3.2.1.4 Power balance and hot and cold gas efficiency

Table 3.29 Power Balance and hot and cold gas efficiencies for ASF

Power Component	Test 1	Test 2
Total Input (W)	29338	21984
Total Output (W)	20437	16492
Unaccounted (W)	8901	5492
Total Output/ Total Input (%)	70	75
$\eta_{\text{hot gas}}$ (%)	31.3	38.6
$\eta_{\text{cold gas}}$ (%)	29.9	37.3

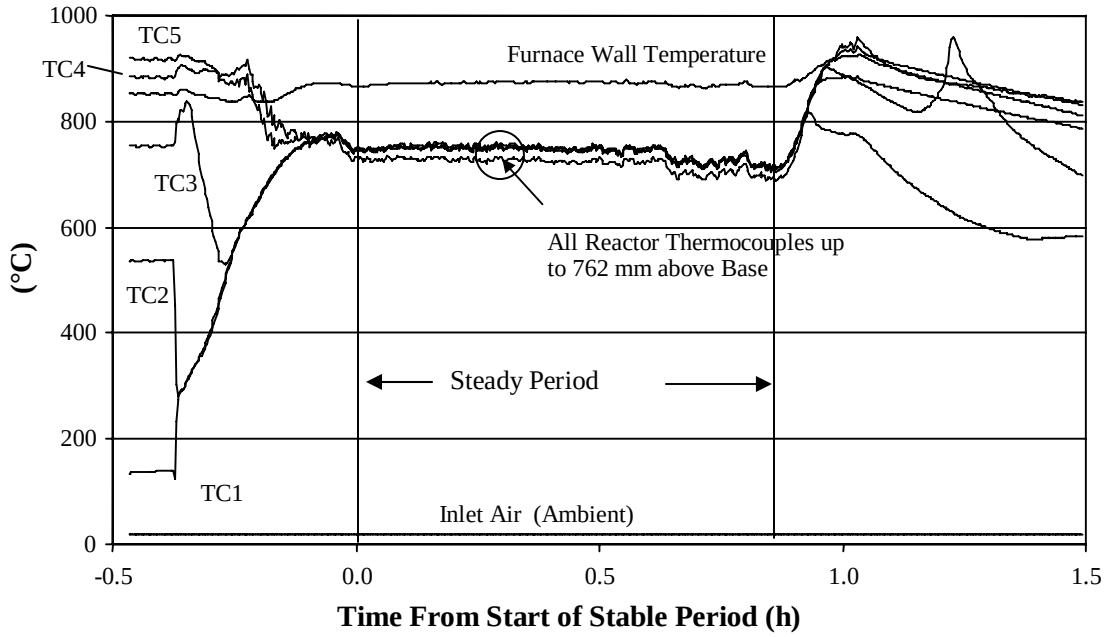

Figure 3.4 Reactor temperatures versus time for ASF test 1

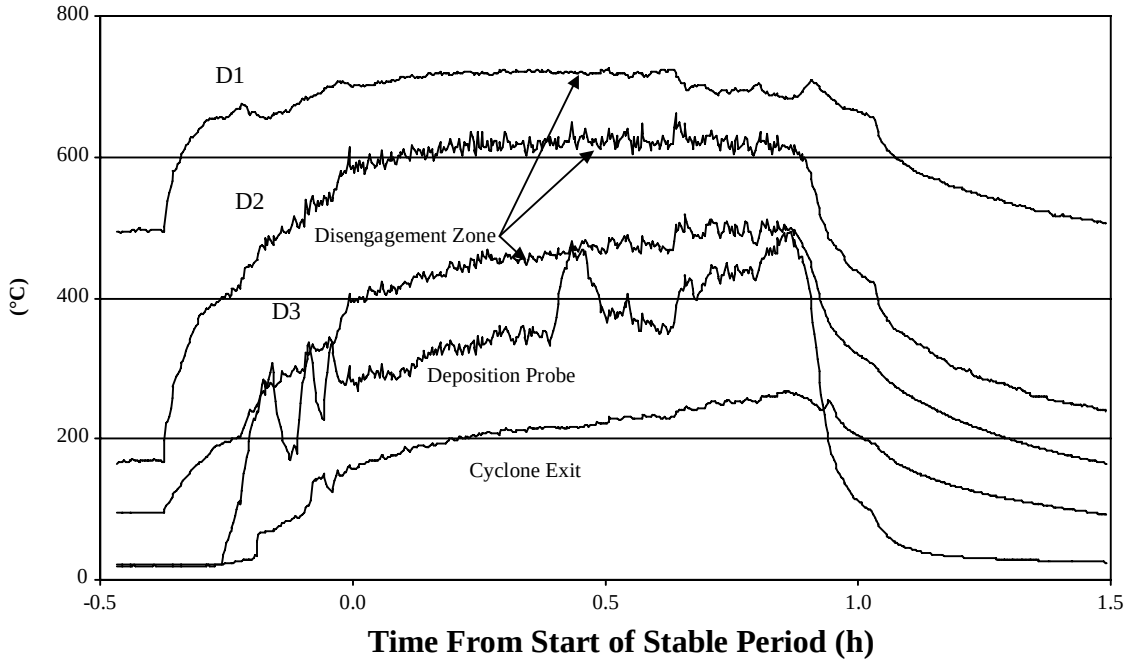

Figure 3.5 Temperatures downstream of reaction zone for ASF test 1

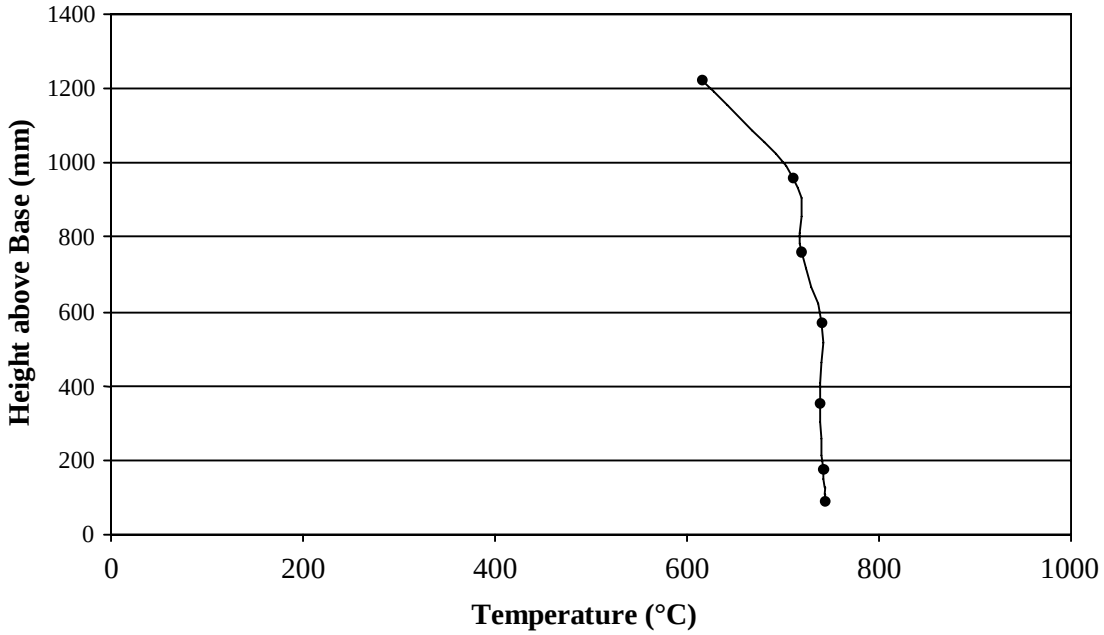

Figure 3.6 Reactor temperature profile for ASF, test 1 at steady state

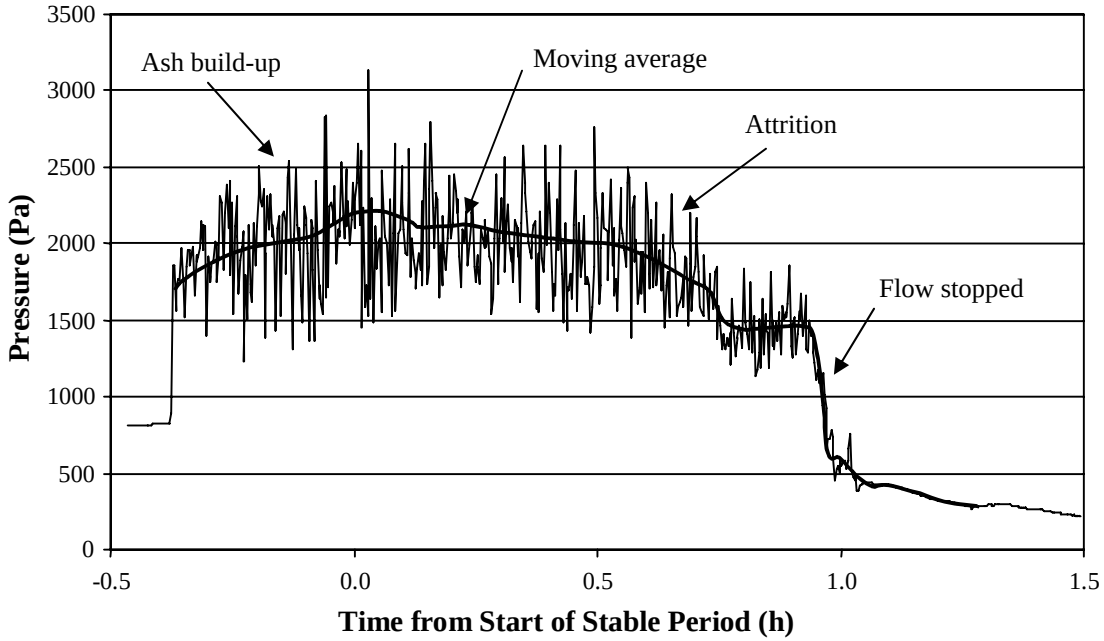

Figure 3.7 Bed differential pressure for ASF test 1

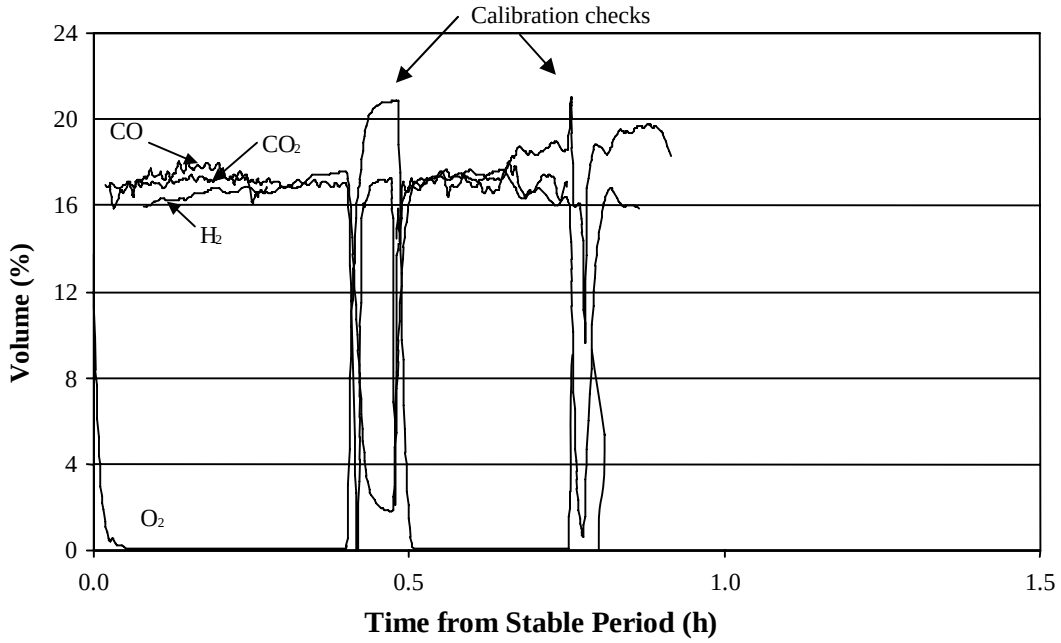

Figure 3.8 Producer gas concentrations for ASF test 1, continuous analysis

ASF

Test 2

Figures 3.9 through 3.13 and Tables 3.26 through 3.29 summarize data from this test.

The second test was run at an average air-factor of 0.10 utilizing a deep bed of 866 grams of the alumina-silicate bed media. Reactor preheat temperature was 801°C, average primary fluidizing air flow rate was 32.2 g min^{-1} and average fuel feed rate (dry basis) was 86 g min^{-1} during the 46 minute steady period. The average reactor wall temperature and fuel feed were lowered from 872 °C and 116 g min^{-1} respectively in test 1 to try and improve the air factor.

Primary fluidizing air was preheated to 302°C. Bed temperatures along the main reactor column varied by only approximately 15°C throughout the course of the experiment. Average column temperature was approximately 689°C, which was considerably lower than in test 1 partly as a result of lowering the wall temperature by an average of 70°C from test 1.

From Figure 3.9, it can be seen that the lower bed temperatures (TC1 and TC2) increase as fuel is initially added to the reactor. These bed temperatures increase as the feed rate of fuel is increased until the steady state temperature is reached. The start-up temperature gradient for this run is less dramatic than with test 1 and is a result of the decreased feed rate. The bed differential pressure is higher for this run in part because of the increased airflow through the reactor.

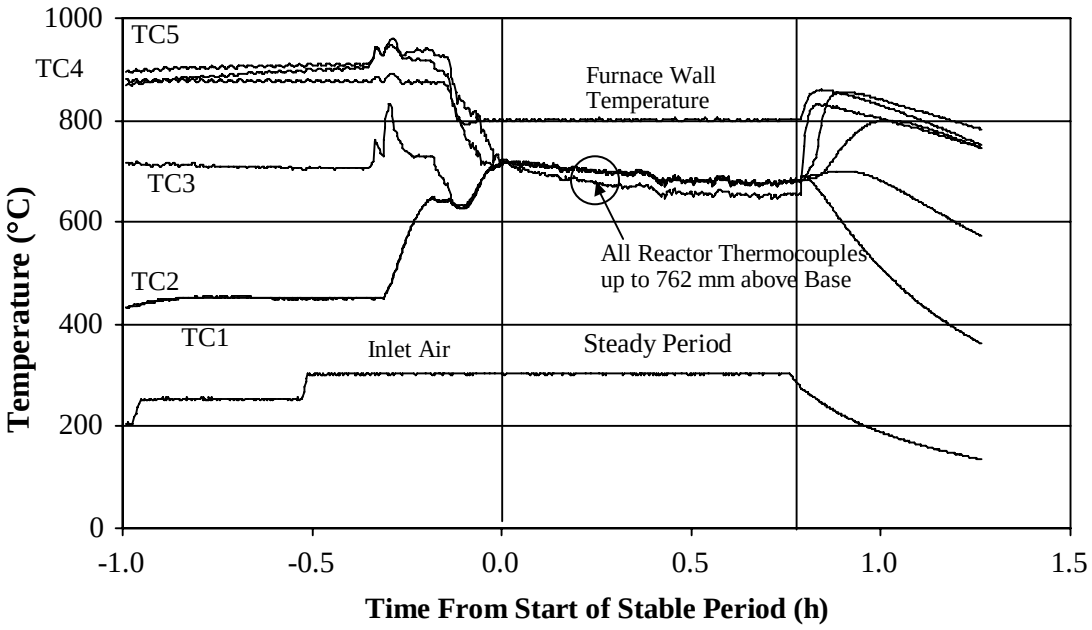

Figure 3.9 Reactor temperatures versus time for ASF test 2

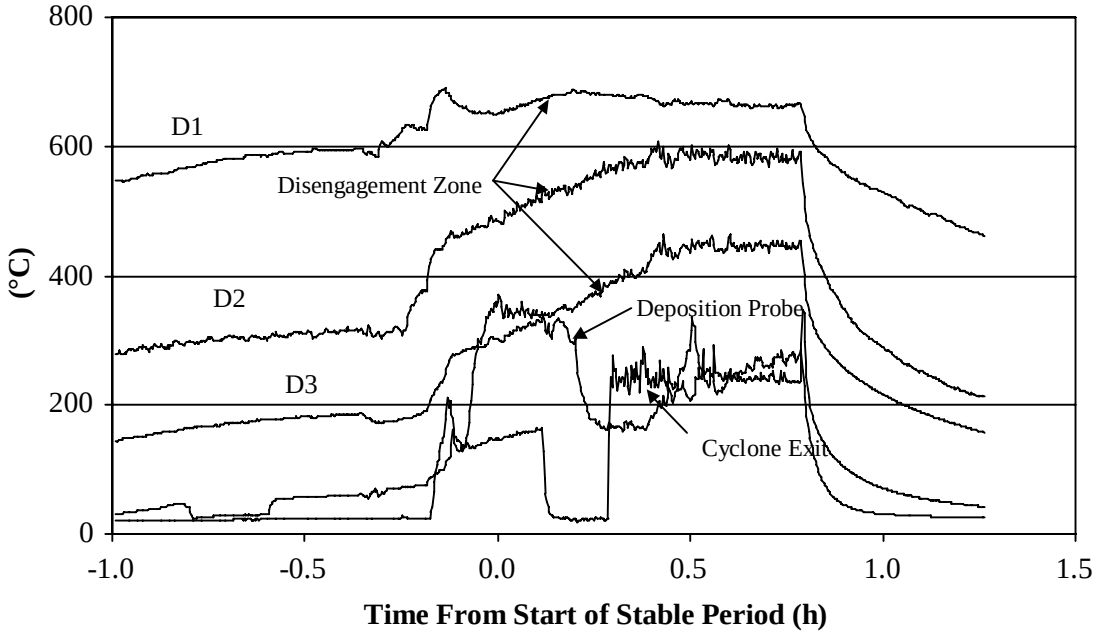

Figure 3.10 Temperatures downstream of reaction zone for ASF test 2

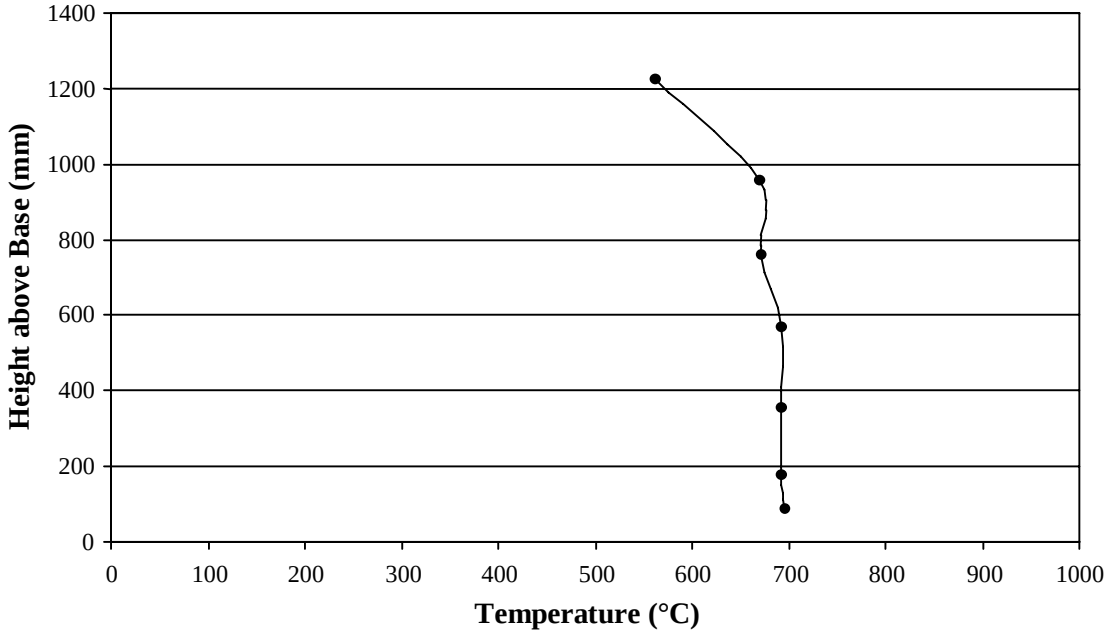

Figure 3.11 Reactor temperature profile for ASF, test 2 at steady state

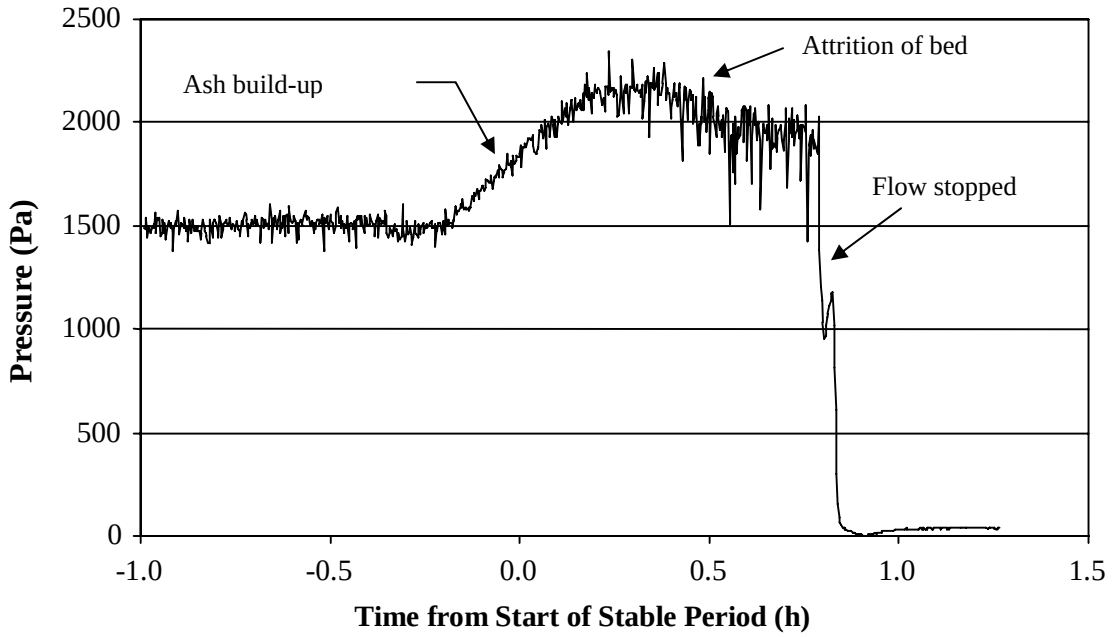

Figure 3.12 Bed differential pressure for ASF test 2

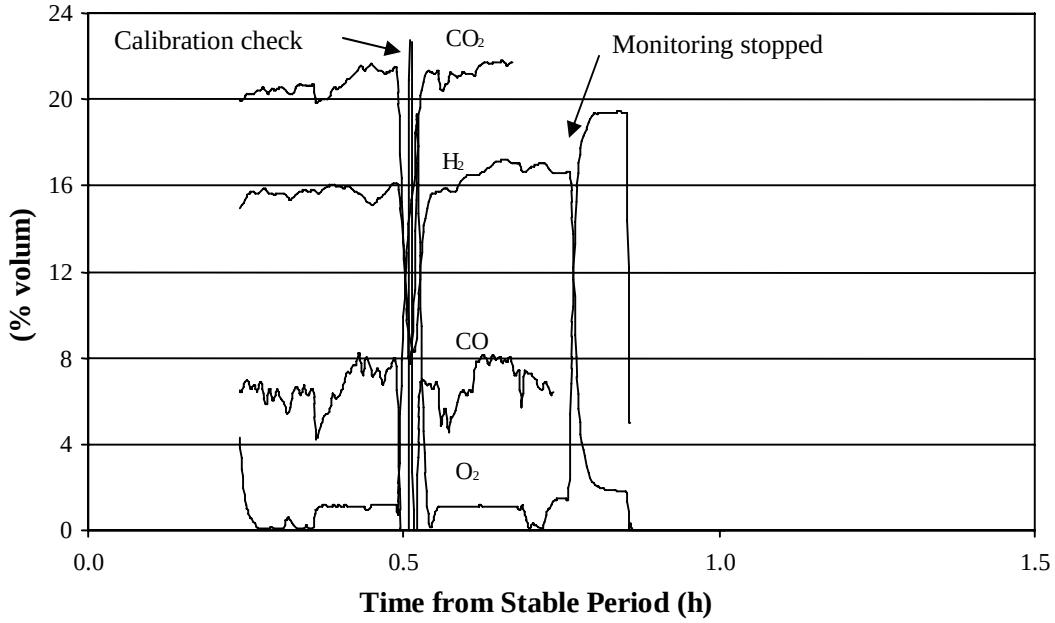

Figure 3.13 Producer gas concentrations for ASF test 2, continuous analysis

Walnut Prunings (WPF)

3.3.1 Test 1 and 2

Figures 3.14 through 3.18 and Tables 3.30 through 3.33 summarize some of the data associated with this test run.

The first test was run at an average air-factor of 0.11 utilizing a shallow bed of 433 grams of the alumina-silicate bed media. Average reactor furnace temperature was 855°C, average primary fluidizing air flow rate was 36.3 g min^{-1} and average fuel feed rate (dry basis) was 76 g min^{-1} during the 76 minute test run period.

Primary fluidizing air preheat was 303°C. Bed temperatures along the main reactor column varied by only approximately 14°C throughout the course of the experiment. Average column temperature was approximately 744 °C.

Figure 3.14 shows that all temperatures (TC1 through TC5) initially increase as fuel is added to the reactor. Temperatures TC1 through TC3, however, decrease as more fuel is added to the reactor and the shift from combustion to gasification takes place. These bed temperatures eventually increase as the feed rate of fuel is increased until a steady state temperature is reached.

Differential pressure for WPF test 1 was significantly less than the ASF test runs due to the lower bed mass used. The temperature within the bed also deviates more

dramatically than with the ASF tests towards the top portion of the fluidized bed. WPF contained a higher level of volatiles than ASF and a lower level of ash.

3.3.1.1 Operating parameters

Table 3.30 Operating Parameters for WPF during steady state periods

Parameter		Test 1	Test 2
Total Steady Period	(min)	76	70
Average Fuel Feed Rate (db)	(g min^{-1})	76.2	82.0
Fuel Moisture	(% wb)	14.3	14.3
Total Wet Fuel Burned	(g)	6759	6695
Total Dry Fuel Burned	(g)	5792	5737
Average Air Flow	(g min^{-1})	36.3	34.7
Air : Fuel Ratio (AF)	(-)	0.48	0.42
Stoichiometric AF	(-)	4.38	4.38
Air Factor	(-)	0.11	0.10
Inlet Air Superficial Velocity at ambient temp	(m s^{-1})	0.12	0.12
Inlet Air Superficial Velocity at operating temp	(m s^{-1})	0.42	0.40
Average Furnace Wall Temperature	(°C)	855	843
Primary Air Preheat Temperature	(°C)	303	302
Cyclone Exhaust Temperature	(°C)	231	214
Postflare Probe Temperature Average	(°C)	478	477
Average Post Flare Temperature	(°C)	166	176
Average Pressure Drop across Bed	(Pa)	767	832
Equivalent Bed Mass Computed from Mean Pressure Drop	(g)	329	356

3.3.1.2 Mass balance summary

Table 3.31 Mass Balance Summary for WPF

	Test 1		Test 2	
Parameter	Mass (g)	Percent of flow	Mass (g)	Percent of flow
Inputs				
m_{air}	2758	27.7	2431	25.4
$m_{dry\ fuel}$	5792	58.2	5737	60.0
$m_{fuel\ moist}$	966	9.7	957	10.0
$m_{fresh\ bed}$	433	4.4	433	4.5
Total	9949	100.0	9558	100.0
Outputs				
$m_{bed\ out}$	531	5.3	376	3.9
$m_{horz\ pass}$	538	5.4	682	7.1
$m_{cyclone}$	107	1.1	105	1.1
$m_{stack\ dry}$	7594	76.3	6600	69.1
$m_{stack\ sol/cond}$*	1170	11.8	1784	18.7
m_{NH3}**	9	0.1	11	0.1
Total	9949	100.0	9558	100.0

*$m_{stack\ sol/cond}$ includes the total air dried tar in the stack flow of 136 g and 193 g respectively for Tests 1 and 2. These total tar values are derived from 19 g of tar in condenser 1 and 8 g of tar in condenser 2 (for Test 1) and 19 g in condenser 1 and 5 g in condenser 2 (for Test 2).

** m_{NH3} represents the total ammonia in stack flow derived from a sample collected in the ammonia train. There may be some additional ammonia in solution collected in the

$m_{stack\ sol/cond.}$

3.3.1.3 Stack gas grab sample average analysis, gas phase NH_3, HCN, Cl, K and concentration of solids and condensibles for WPF

Table 3.32 Stack gas grab sample average analysis (GC) and concentration of solids and condensibles for WPF

	Test 1	Test 2
Constituent	Mean Concentration (% v/v)	Mean Concentration (% v/v)
CO	22	21
H_2	10	12
CH_4	7	8
CO_2	16	17
N_2	42	41
O_2	3	1
	Mean Concentration (ppm)	Mean Concentration (ppm)
NH_3	1992	2669
Cl	98	22
K	17	16
HCN	-	-
Total	100.21	100.27
Higher Heating Value (MJ m^{-3})	5.9	6.7
Solids and Condensibles	Concentration (mg L^{-1} dry gas)	Concentration (mg L^{-1} dry gas)
With condensed water	177.1	301.9
Air dried, room temperature	7.0	34.4

3.3.1.4 Power balance and hot and cold gas efficiency

Table 3.33 Power Balance and hot and cold gas efficiencies for WPF

Power Component	Test 1	Test 2
Total Input (W)	24599	26431
Total Output (W)	15218	16846
Unaccounted (W)	9380	9585
Total Output/ Total Input (%)	62	64
$\eta_{\text{hot gas}}$ (%)	37.0	43.1
$\eta_{\text{cold gas}}$ (%)	35.2	41.2

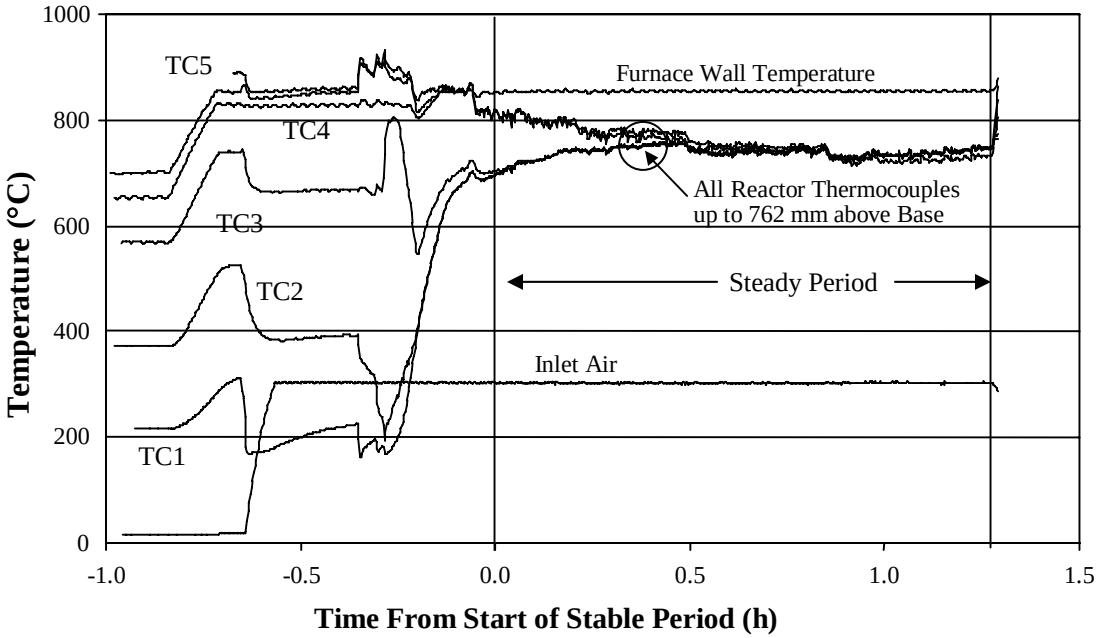

Figure 3.14 Reactor temperatures versus time for WPF test 1

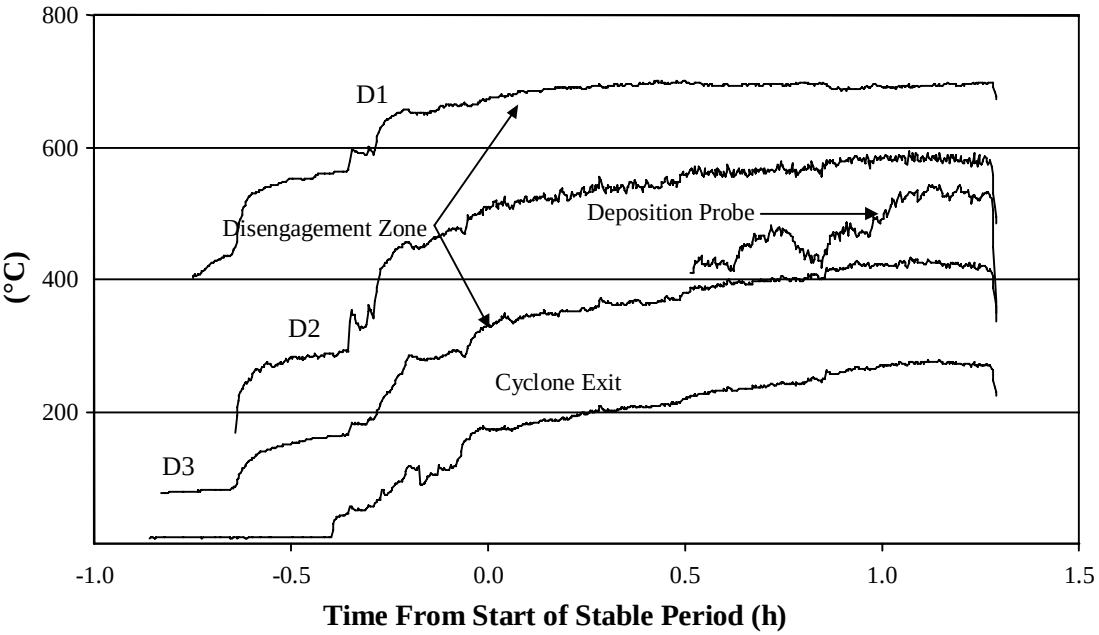

Figure 3.15 Temperatures downstream of reaction zone for WPF test 1

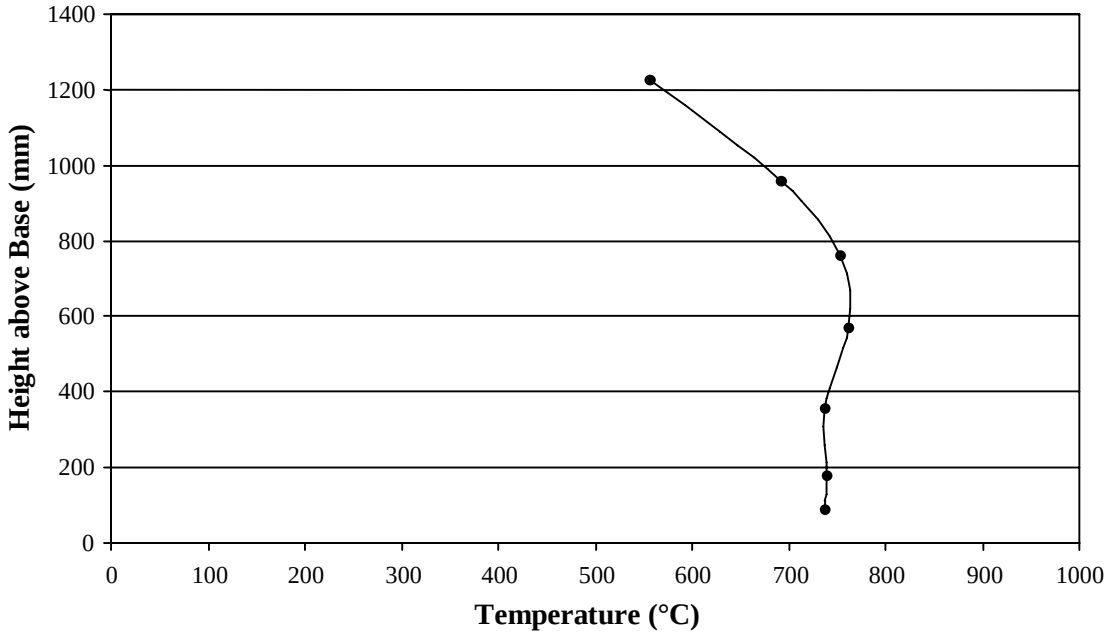

Figure 3.16 Reactor temperature profile for WPF, test 1 at steady state

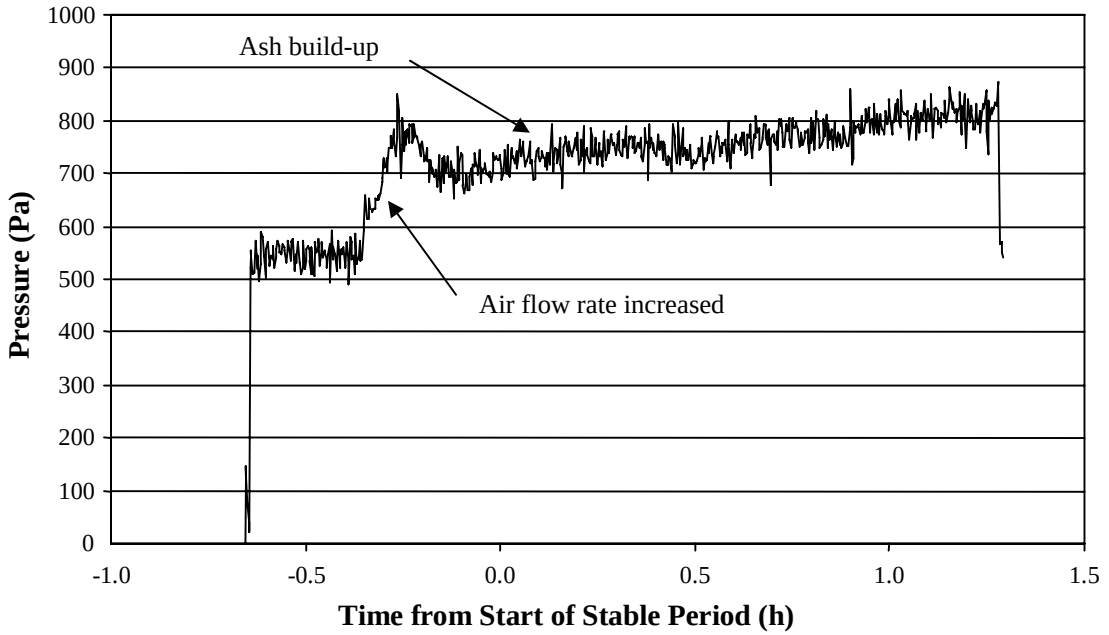

Figure 3.17 Bed differential pressure for WPF test 1

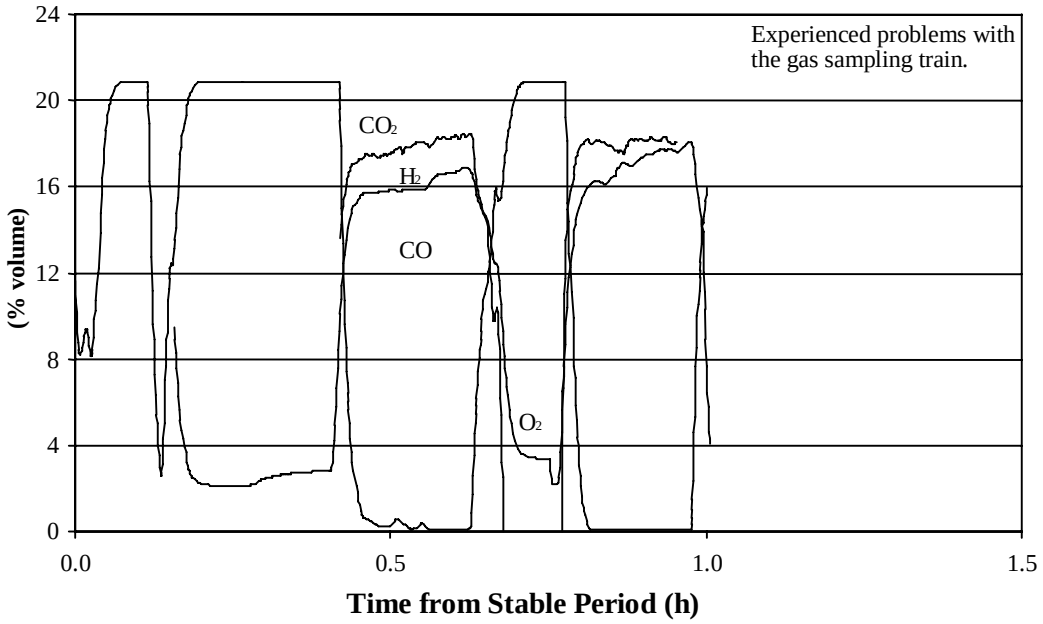

Figure 3.18 Gas analysis for WPF test 1, continuous analysis

Plugging in tar train was responsible for lack of data in the interval between 1.0 and 1.3 hr.

WPF

Test 2

Figures 3.19 through 3.23 and Tables 3.30 through 3.33 encompass some of the data associated with this test run.

The second test was run at an average air-factor of 0.10 utilizing a shallow bed of 433 grams of the alumina-silicate bed media. Average reactor wall temperature was 843°C, average primary fluidizing air flow rate was 34.7 g min^{-1} and average fuel feed rate (dry basis) was 82 g min^{-1} during the 70 minute test run period.

Primary fluidizing air preheat was 302°C. Bed temperatures along the main reactor column varied by only approximately 17°C throughout the course of the experiment. Average column temperature was approximately 719°C.

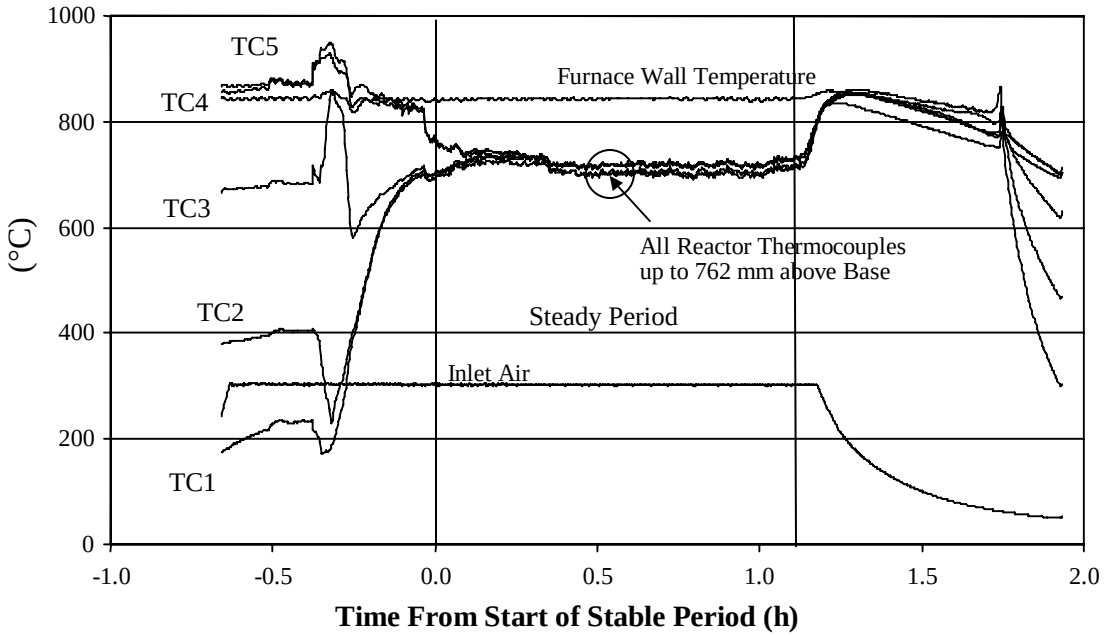

Figure 3.19 Reactor temperatures versus time for WPF test 2

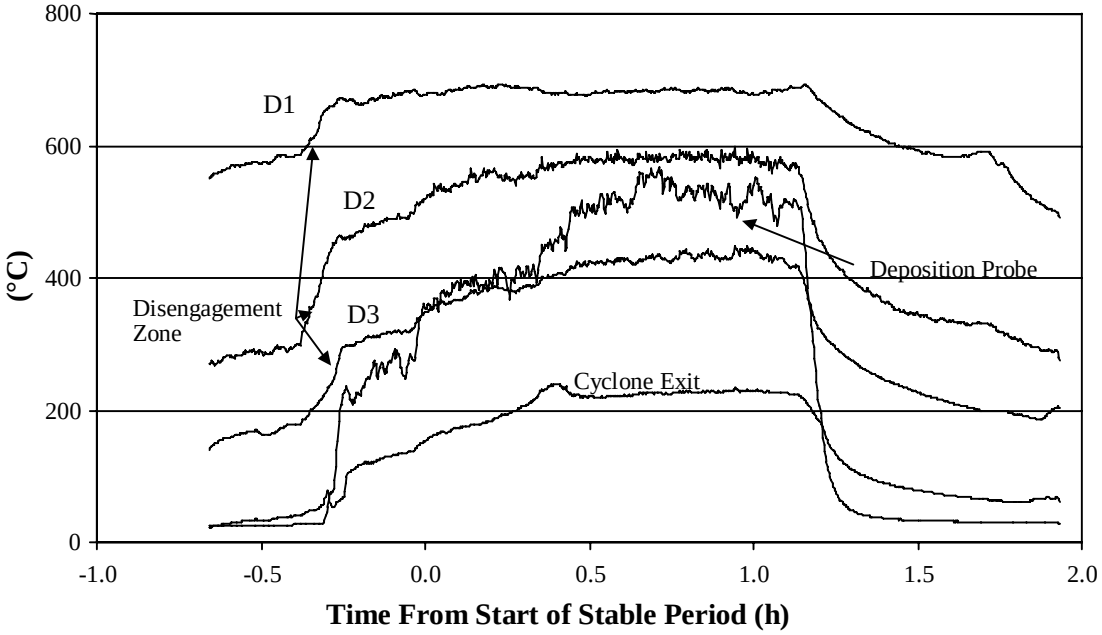

Figure 3.20 Temperatures downstream of reaction zone for WPF test 2

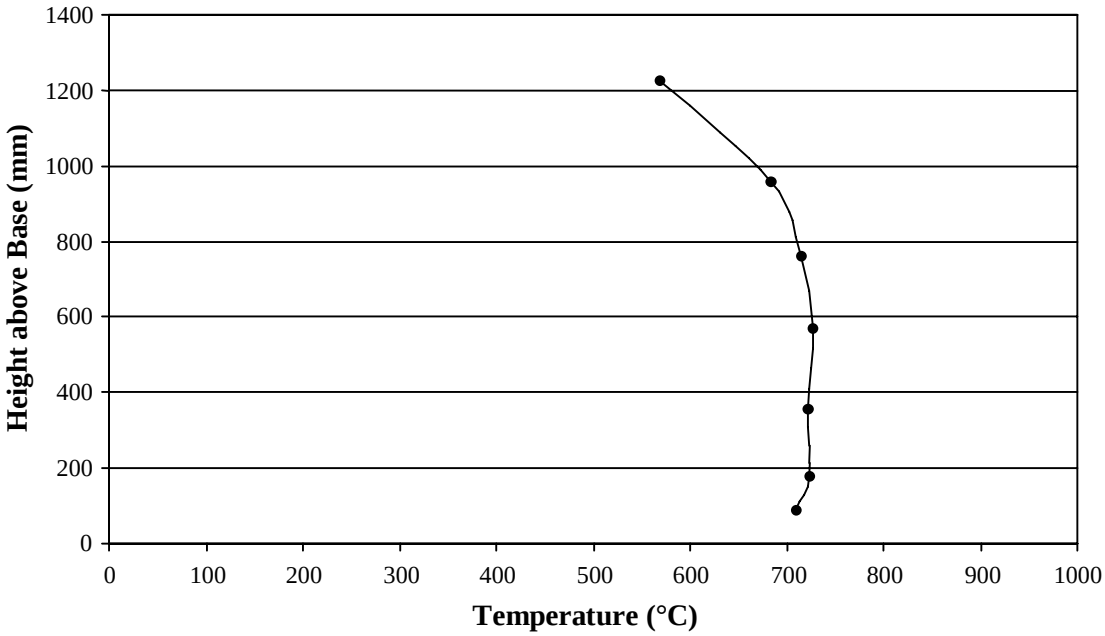

Figure 3.21 Reactor temperature profile for WPF, test 2 at steady state

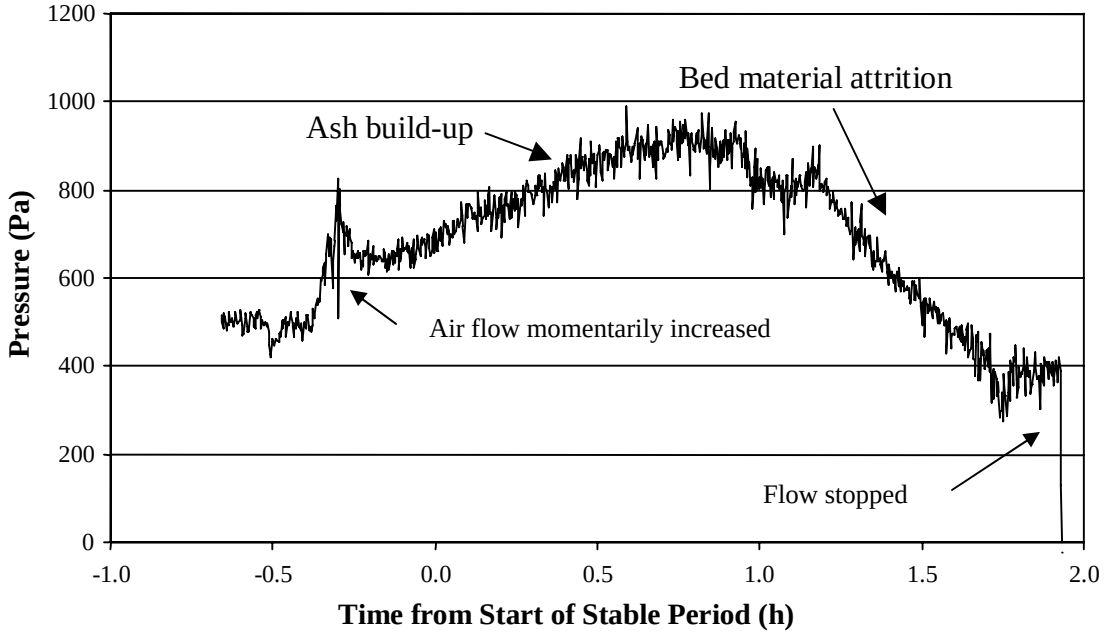

Figure 3.22 Bed differential pressure for WPF test 2

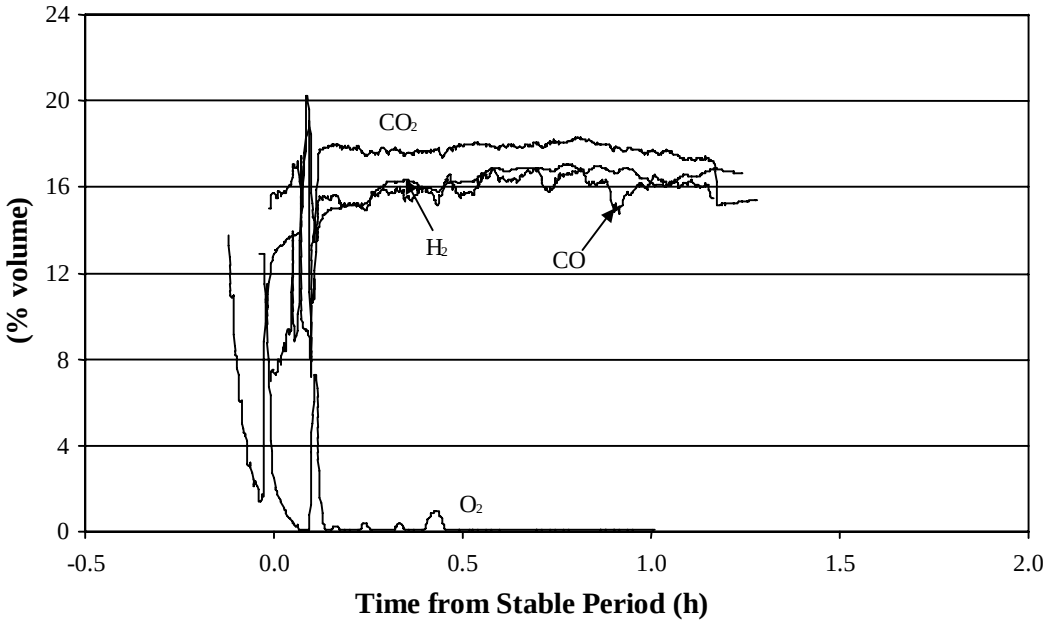

Figure 3.23 Producer gas concentrations for WPF test 2, continuous analysis.

3.4 Rice Straw (RSF)

3.4.1 Test 1 and 2

Figures 3.24 through 3.28 and Tables 3.34 through 3.37 summarize the data associated with this test.

The first gasification test with rice straw was conducted using a mixture of both magnesium oxide and alumina-silicate (NARCO Investocast 60) grain to prevent agglomeration of the bed. The average air factor was 0.19. Earlier experiments had shown agglomeration with the alumina silicate bed alone. The MgO was sieved from bulk. The fraction passing 40 mesh and retained by a 100 mesh sieve was used in the experiments. MgO fraction was 67% w/w in the first experiment.

Deep bed loading consisted of 441 g MgO combined with 222 g Investocast (663 g total) in the first test. The bulk densities of NARCO I60 sand and MgO are 1.46 kg L^{-1} and 0.93 kg L^{-1} respectively. After the steady state period, near the end of the first test (at approximately 0.8 hours), fuel and air flows were each increased by about 75%, maintaining the same AF. This resulted in a rapid decrease in pressure drop across the bed. Post-test investigation of the bed revealed that some agglomeration had occurred. However, much of the bed media was no longer present having blown out when the input flows were increased.

Air-fuel ratios (AF) were varied between 0.58 and 1.08 (air factors between 0.15 and 0.27). The air to fuel ratio was decreased at 0.5 hours. Overall average air-fuel ratio on the first test was 0.71. Primary air preheat temperatures and furnace wall temperatures for both tests were constant at 302°C and 847°C respectively. Air flow rates ranged from 26 L min^{-1} to 43 L min^{-1}. Average air flow was 35.9 g min^{-1}. Fuel moisture content for both tests was 6.0%.

3.4.1.1 Operating parameters

Table 3.34 Operating Parameters for RSF during steady state periods

Parameter		Test 1	Test 2
Total Steady Period	(min)	66	85
Average Fuel Feed Rate (db)	(g min^{-1})	50.4	44.9
Fuel Moisture	(% wb)	6.0	6.0
Total Wet Fuel Burned	(g)	3538	4059
Total Dry Fuel Burned	(g)	3326	3816
Average Air Flow	(g min^{-1})	35.9	33.2
Air : Fuel Ratio (AF)	(-)	0.71	0.74
Stoichiometric AF	(-)	3.82	3.82
Air Factor	(-)	0.19	0.19
Inlet Air Superficial Velocity at ambient temp	(m s^{-1})	0.12	0.12
Inlet Air Superficial Velocity at operating temp	(m s^{-1})	0.42	0.40
Average Furnace Wall Temperature	(°C)	847	851
Primary Air Preheat Temperature	(°C)	302	303
Cyclone Exhaust Temperature	(°C)	172	150
Postflare Probe Temperature Average	(°C)	168	190
Average Post Flare Temperature	(°C)	80	71
Average Pressure Drop across Bed	(Pa)	889	784
Equivalent Bed Mass Computed from Mean Pressure Drop	(g)	381	336

3.4.1.2 Mass balance summary

Table 3.35 Mass Balance Summary for RSF

	Test 1		Test 2	
Parameter	Mass (g)	Percent of flow	Mass (g)	Percent of flow
Inputs				
m_{air}	2369	36.1	2822	36.3
$m_{dry\ fuel}$	3326	50.6	3816	49.1
$m_{fuel\ moist}$	212	3.2	244	3.1
$m_{fresh\ bed}$	663	10.1	889	11.4
Total	6571	100.0	7771	100.0
Outputs				
$m_{bed\ out}$	241	3.7	474	6.1
$m_{horz\ pass}$	993	15.1	583	7.5
$m_{cyclone}$	199	3.0	203	2.6
$m_{stack\ dry}$	4712	71.7	5594	72.0
$m_{stack\ sol/cond}$*	426	6.4	917	11.5
m_{NH3}**	9	0.1	10	0.1
Total	6571	100.0	7771	100.0

*$m_{stack\ sol/cond}$ includes the total air dried tar in the stack flow of 84 g and 104 g respectively for Tests 1 and 2. These total tar values are derived from 10 g of tar in condenser 1 and 1 g of tar in condenser 2 (for Test 1) and 10 g in condenser 1 and 4 g in condenser 2 (for Test 2).

** m_{NH3} represents the total ammonia in stack flow derived from a sample collected in the ammonia train. There may be some additional ammonia in solution collected in the $m_{stack\ sol/cond}$.

3.4.1.3 Stack gas grab sample average analysis, gas phase NH_3, HCN, Cl, K and concentration of solids and condensibles for RSF

Table 3.36 Stack gas grab sample average analysis (GC) and concentration of solids and condensibles for RSF

	Test 1	Test 2
Constituent	Mean Concentration (% v/v)	Mean Concentration (% v/v)
CO	10	17
H_2	4	9
CH_4	4	4
CO_2	13	19
N_2	64	48
O_2	3	5
	Mean Concentration (ppm)	Mean Concentration (ppm)
NH_3	3100	2900
Cl	260	280
K	17	26
HCN	<1	NA
Total	98.33	102.32
Higher Heating Value (MJ m^{-3})	3.1	4.3
Solids and Condensibles	Concentration (mg L^{-1} dry gas)	Concentration (mg L^{-1} dry gas)
With condensed water	109.7	196.2
Air dried, room temperature	23.3	22.3

3.4.1.4 Power balance and hot and cold gas efficiency

Table 3.37 Power Balance and hot and cold gas efficiencies for RSF

Power Component	Power Test 1	Power Test 2
Total Input (W)	12778	11394
Total Output (W)	3765	6315
Unaccounted (W)	9028	5080
Total Output/ Total Input (%)	29	55
$\eta_{\text{hot gas}}$ (%)	25.7	36.0
$\eta_{\text{cold gas}}$ (%)	24.1	34.5

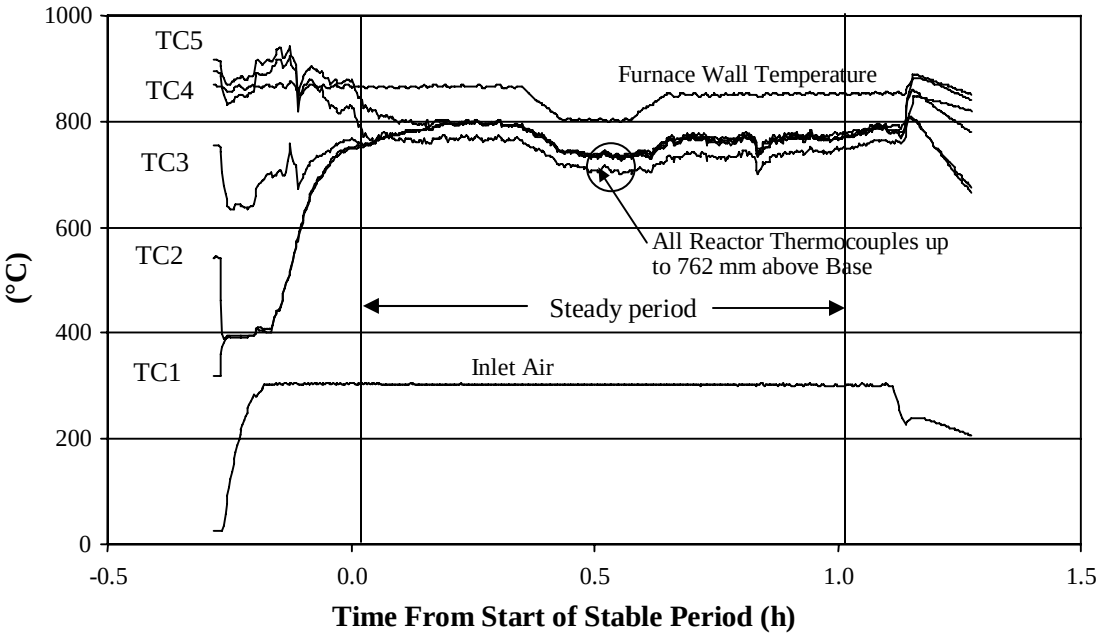

Figure 3.24 Reactor temperatures versus time for RSF test 1

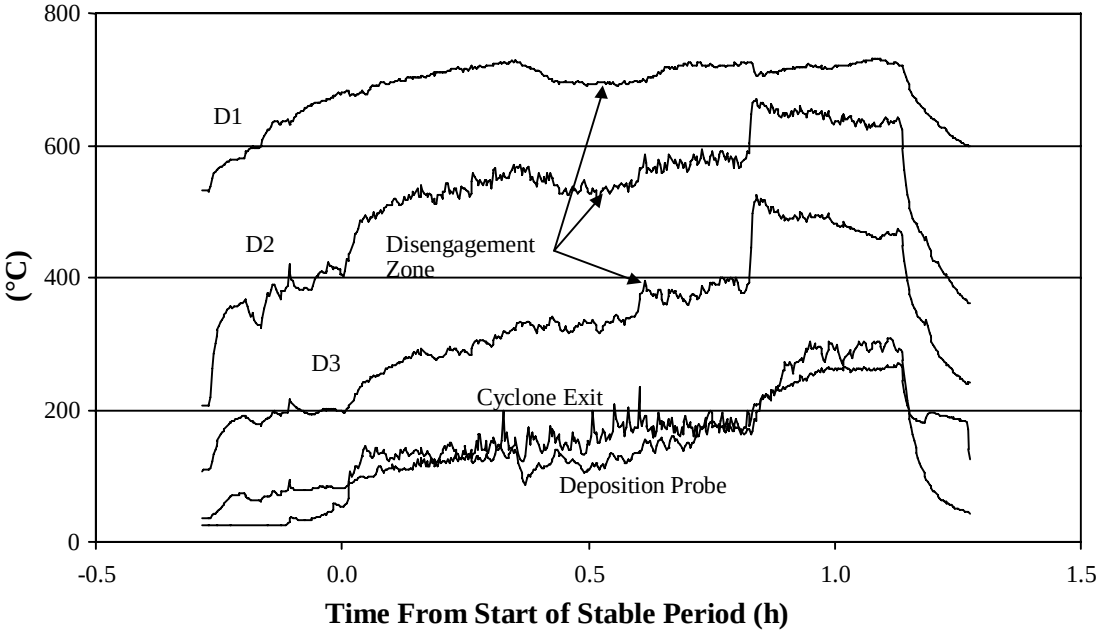

Figure 3.25 Temperatures downstream of reaction zone for RSF test 1

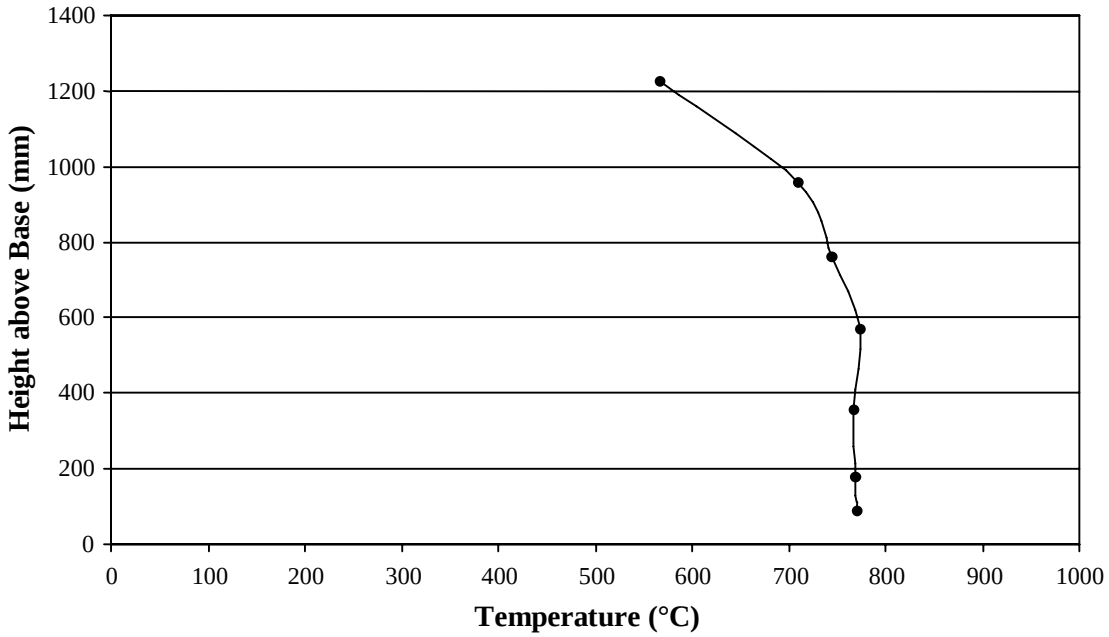

Figure 3.26 Reactor temperature profile for RSF, test 1 at steady state

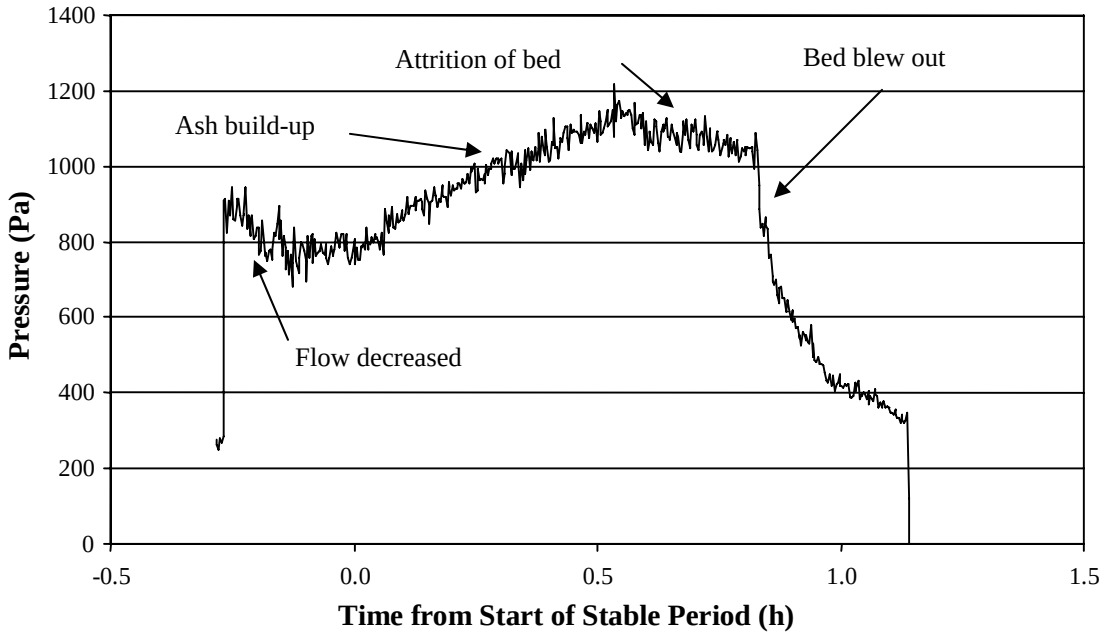

Figure 3.27 Bed differential pressure for RSF test 1

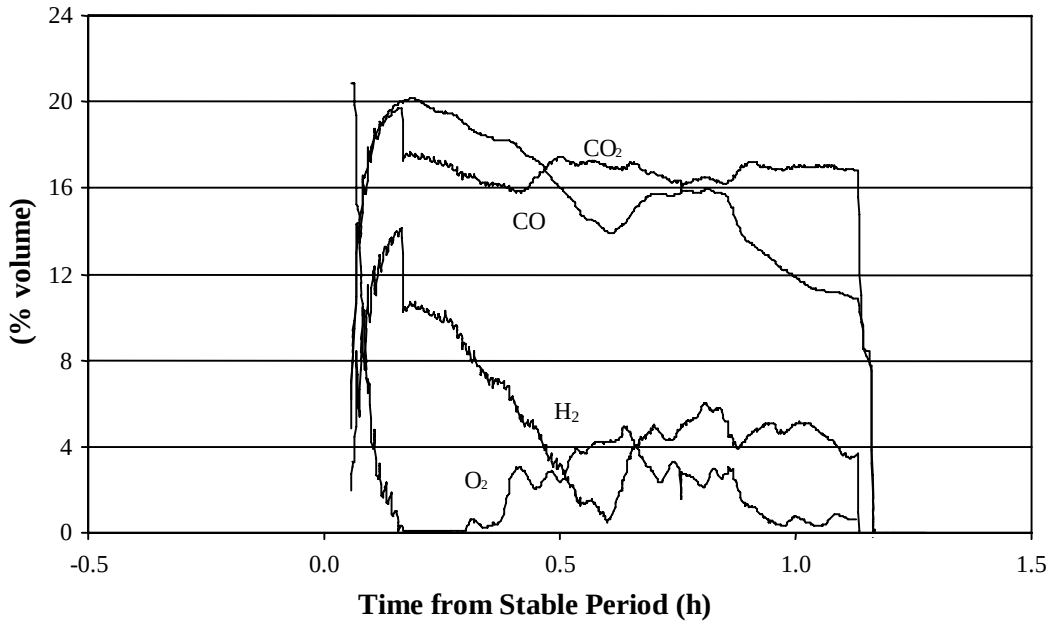

Figure 3.28 Producer gas concentrations for RSF test 1, continuous analysis

Rice Straw

Test 2

Figures 3.29 through 3.33 and Tables 3.34 through 3.37 encompass some of the data associated with this test run.

The second gasification test with rice straw was conducted using a mixture of both magnesium oxide and alumina-silicate (NARCO Investocast 60) grain to prevent agglomeration of the bed. The MgO was sieved from bulk; the fraction passing 40 mesh and retained by a 100 mesh sieve was used in the experiments. Overall MgO fraction was 87.5% w/w in the second test.

Deep bed loading consisted of 530 g MgO combined with 109 g alumina-silicate initially for this second test. An additional 250 g of MgO was added after 85 minutes to replace that lost due to attrition. No bed agglomeration was detected during the second rice straw test and bed pressure drop remained relatively stable over the course of the run (slight drop between 0.8 and 1.2 hours).

Air-fuel ratios (AF) were varied between 0.58 and 1.08 (air factors between 0.15 and 0.27). At approximately 0.55 hours, the AF ratio was increased from 0.58 to 1.08 by varying air and fuel in an attempt to achieve a more robust gas at the flare. Overall average air-fuel ratio was 0.74 on the second test and average air factor was 0.19. Primary air preheat temperatures and furnace wall temperatures for both tests were constant at 303°C and 851°C respectively. Average air flow rate was 33.2 g min^{-1}. Fuel moisture content for test no. 2 was 6%.

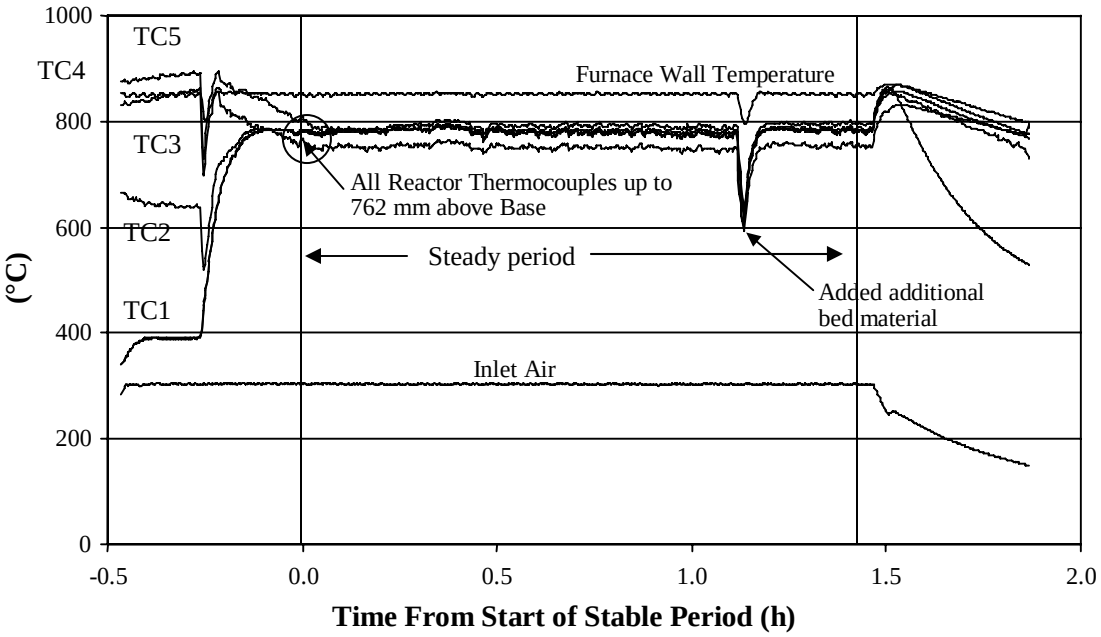

Figure 3.29 Reactor temperatures versus time for RSF test 2

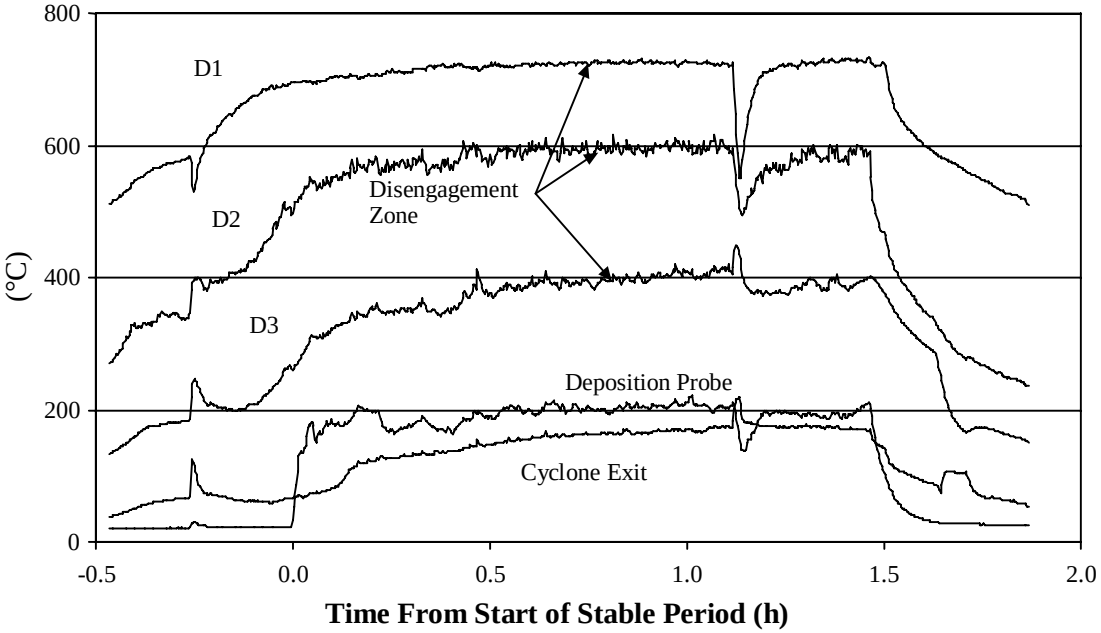

Figure 3.30 Temperatures downstream of reaction zone for RSF test 2

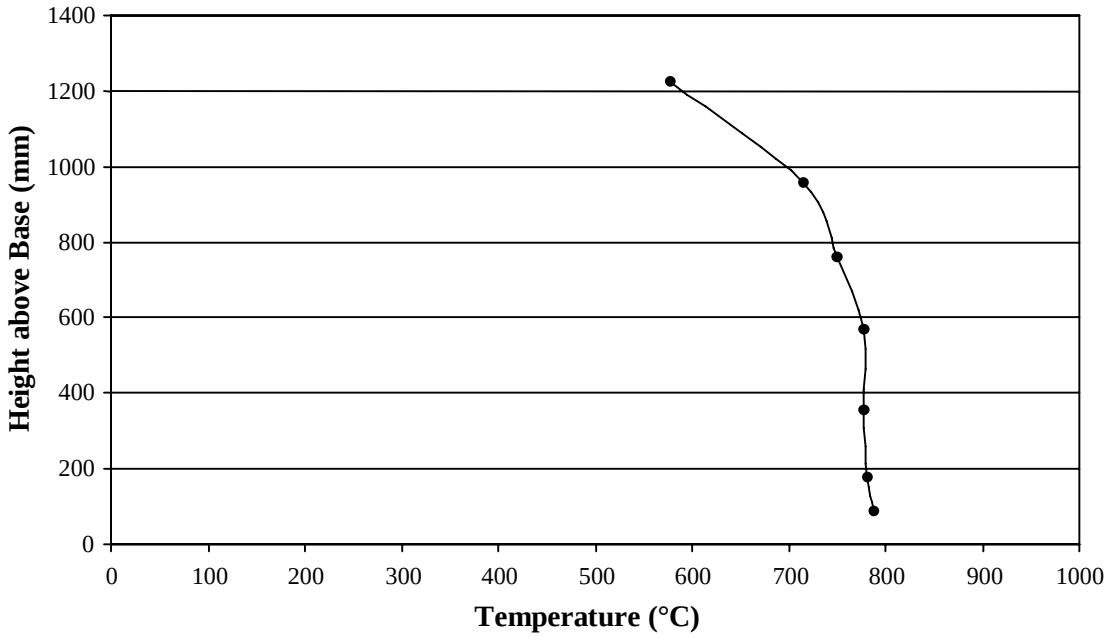

Figure 3.31 Reactor temperature profile for RSF, test 2 at steady state

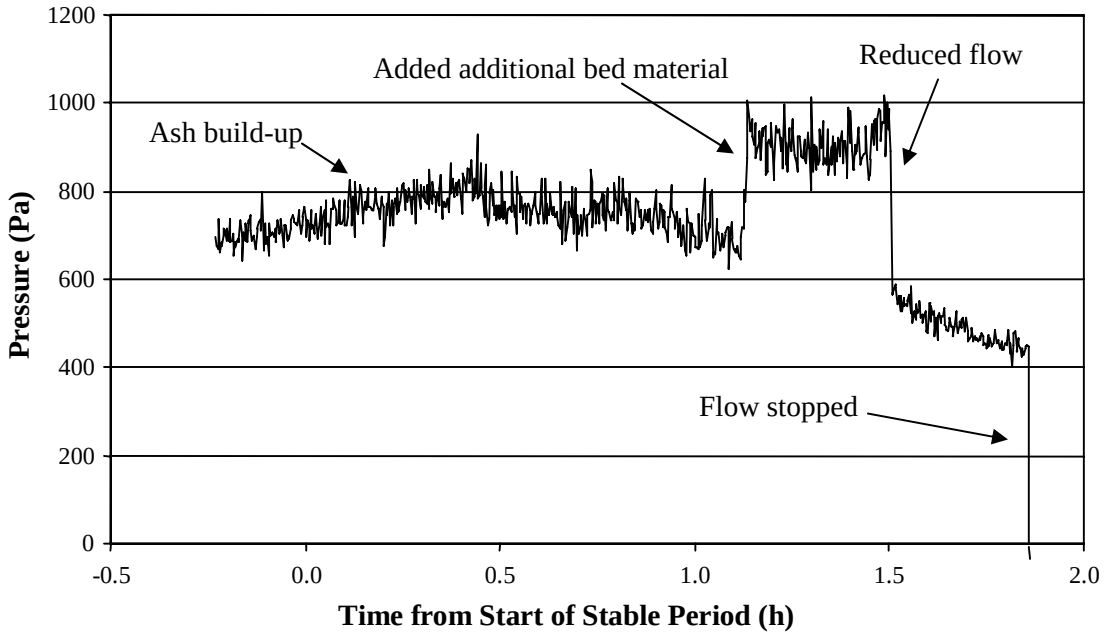

Figure 3.32 Bed differential pressure for RSF test 2

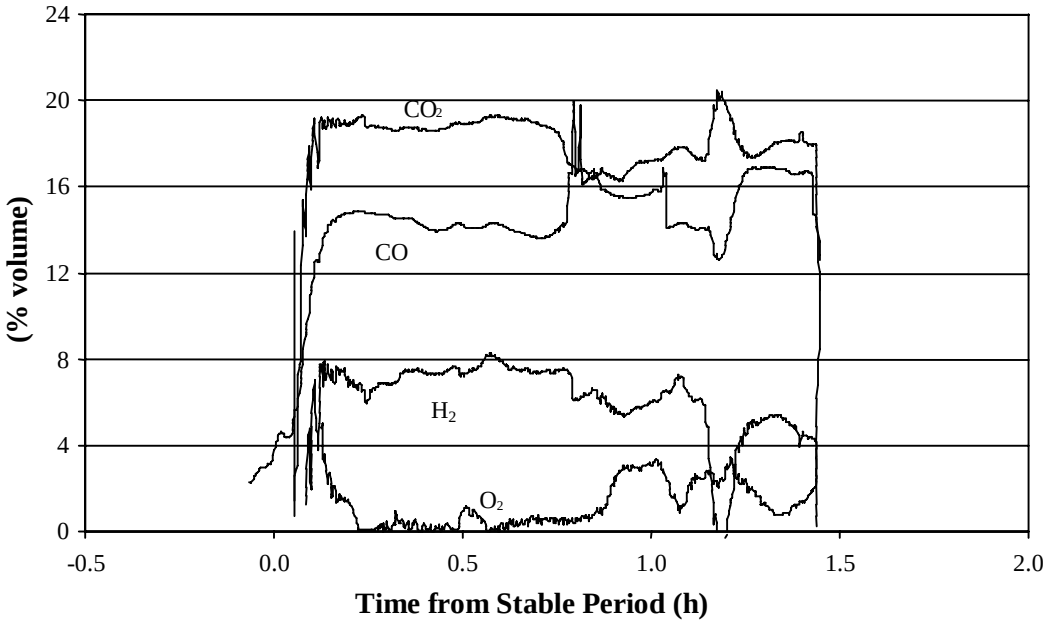

Figure 3.33 Producer gas concentrations for RSF test 2, continuous analysis

3.5 Whole Tree Wood Chips (WWF)

3.5.1 Test 1 and 2

Figures 3.34 through 3.38 and Tables 3.38 through 3.41 summarize data from this test.

The first test was run at an average air-factor of 0.30 utilizing a deep bed of 866 grams of the alumina-silicate bed media. Reactor preheat temperature was 853°C, average primary fluidizing air flow rate was 33.2 g min^{-1} and average fuel feed rate (dry basis) was 23 g min^{-1} during the 71 minute steady period.

Primary fluidizing air preheat was 342°C. Bed temperatures along the main reactor column varied by approximately 180°C throughout the course of the experiment. Average column temperature was approximately 800°C.

Figure 3.34, shows that the lower bed temperatures (TC1 and TC2) increase as fuel is initially added to the reactor. These bed temperatures increase as the feed rate of fuel is increased until the steady state temperature is reached. But as shown in Figure 3.36, this fuel produces a higher temperature in the freeboard, a characteristic of wood fuels in bubbling beds.

Bed differential pressure was very consistent throughout the 71 minute steady test run period. Average pressure was approximately 1500 Pa for the entire run and did not drop off appreciably until the flow was stopped. WWF had among the lowest ash contents (2.68 %db) of the tested fuels and this relatively steady pressure is due, in part, to the lack of ash build-up. No operational problems were experienced with this fuel. The bed media was alumina silicate with no additives. No signs of agglomeration were observed. For test 1, the great majority of data was unavailable due to an accident with the equipment and early termination of test.

3.5.1.1 Operating parameters

Table 3.38 Operating Parameters for WWF during steady state periods

Parameter		Test 1	Test 2
Total Steady Period	(min)	71	80
Average Fuel Feed Rate (db)	(g min^{-1})	23.0	30.4
Fuel Moisture	(% wb)	6.0	7.5
Total Wet Fuel Burned	(g)	1740	2627

Total Dry Fuel Burned	(g)	1635	2430
Average Air Flow	(g min^{-1})	33.2	33.2
Air : Fuel Ratio (AF)	(-)	1.44	1.09
Stoichiometric AF	(-)	4.88	5.07
Air Factor	(-)	0.30	0.22
Inlet Air Superficial Velocity at ambient temp	(m s^{-1})	0.11	0.11
Inlet Air Superficial Velocity at operating temp	(m s^{-1})	0.41	0.41
Average Furnace Wall Temperature	(°C)	853	852
Primary Air Preheat Temperature	(°C)	342	352
Cyclone Exhaust Temperature	(°C)	99	143
Postflare Probe Temperature Average	(°C)	134	156
Average Post Flare Temperature	(°C)	43	70
Average Pressure Drop across Bed	(Pa)	1494	555
Equivalent Bed Mass Computed from Mean Pressure Drop	(g)	640	237

3.5.1.2 Mass balance summary

Table 3.39 Mass Balance Summary for WWF

	Test 1		Test 2	
Parameter	Mass (g)	Percent of flow	Mass (g)	Percent of flow
Inputs				
m_{air}	2357	47.5	2655	46.5
$m_{dry\ fuel}$	1635	32.9	2430	42.5
$m_{fuel\ moist}$	104	2.1	197	3.4
$m_{fresh\ bed}$	866	17.5	433	7.6
Total	4962	100.0	5715	100.0
Outputs				
$m_{bed\ out}$	869	-	472	8.3

$m_{horz\ pass}$	ND	ND	114	2.0
$m_{cyclone}$	ND	ND	22	0.4
$m_{stack\ dry}$	ND	ND	4537	79.4
$m_{stack\ sol/cond*}$	ND	ND	567	9.9
m_{NH3**}	0	0	3	<0.1
Total	-	-	5715	100.0

ND - Not determined due to early termination of test

*$m_{stack\ sol/cond}$ includes the total air dried tar in the stack flow of 193 g for Test 2. This total tar value is derived from 13 g of tar in condenser 1 and 1 g of tar in condenser 2 (for Test 2).

** m_{NH3} represents the total ammonia in stack flow derived from a sample collected in the ammonia train. There may be some additional ammonia in solution collected in the $m_{stack\ sol/cond.}$

3.5.1.3 Stack gas grab sample average analysis, gas phase NH_3, HCN, Cl, K and concentration of solids and condensibles for WWF

Table 3.40 Stack gas grab sample average analysis (GC) and concentration of solids and condensibles for WWF

	Test 1	Test 2
Constituent	Mean Concentration (% v/v)	Mean Concentration (% v/v)
CO	15	18
H_2	13	8
CH_4	5	5
CO_2	13	11
N_2	46	56
O_2	1	2
	Mean Concentration (ppm)	Mean Concentration (ppm)
NH_3	850	1181
Cl	250	71
K	13	8

HCN	NA	NA
Total	93.1	100.13
Higher Heating Value (MJ m^{-3})	5.1	4.6
Solids and Condensibles*	Concentration (mg L^{-1} dry gas)	Concentration (mg L^{-1} dry gas)
With condensed water	ND	142.3
Air dried, room temperature	ND	27

*Solids and condensibles for test 1 were ND because test was terminated early.

3.5.1.4 Power balance and hot and cold gas efficiency

Table 3.41 Power Balance and hot and cold gas efficiencies for WWF

Power Component	Power Test 1	Power Test 2
Total Input (W)	-	10563
Total Output (W)	-	5770
Unaccounted (W)	-	4829
Total Output/ Total Input (%)	-	55
$\eta_{\text{hot gas}}$ (%)	-	38.1
$\eta_{\text{cold gas}}$ (%)	-	36.7

Insufficient data for analysis of Test 1 because test was terminated early.

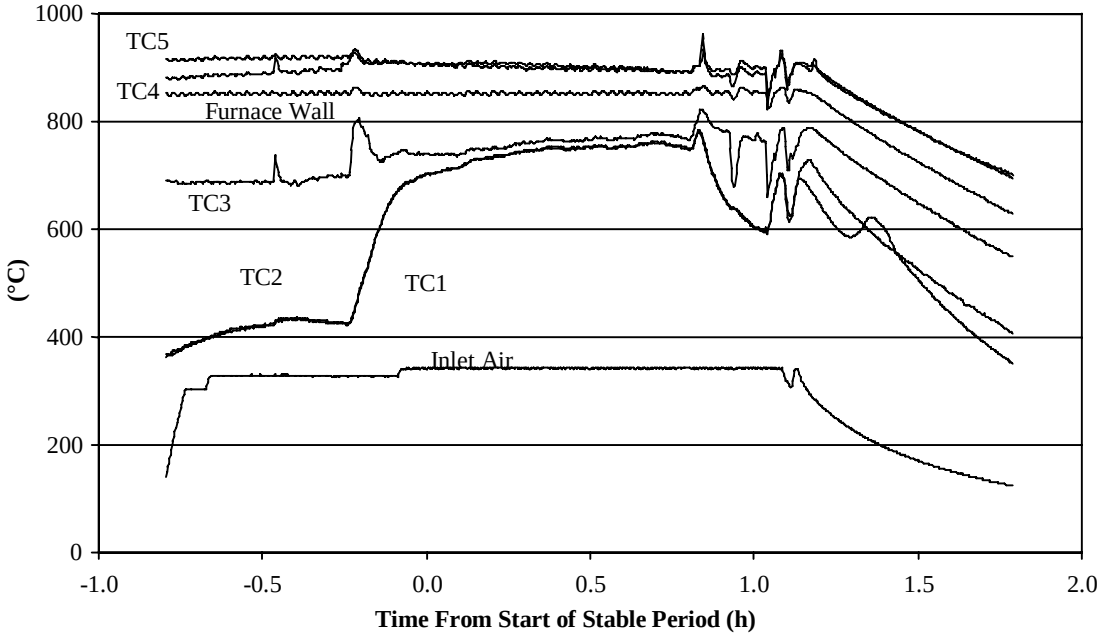

Figure 3.34 Reactor temperatures versus time for WWF

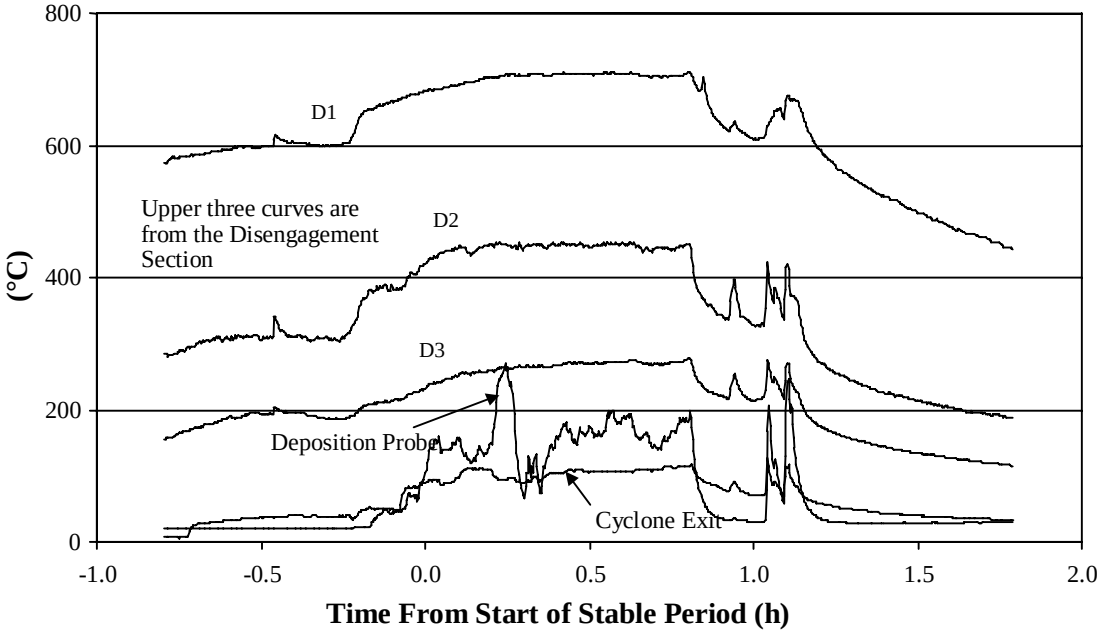

Figure 3.35 Temperatures downstream of reaction zone for WWF test 1

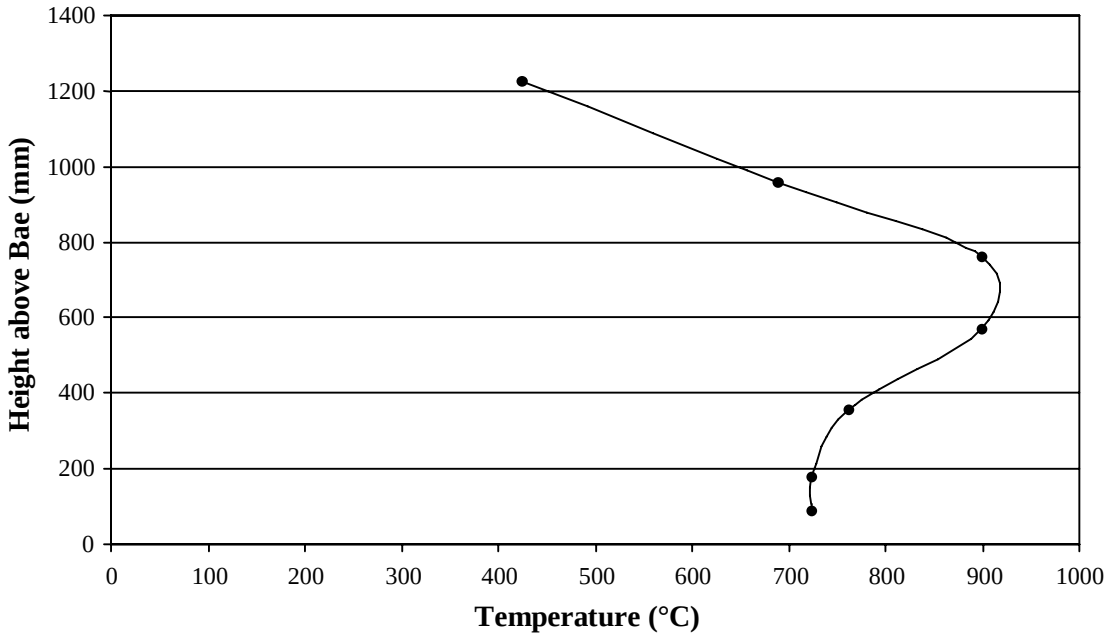

Figure 3.36 Reactor temperature profile for WWF, test 1 at steady state

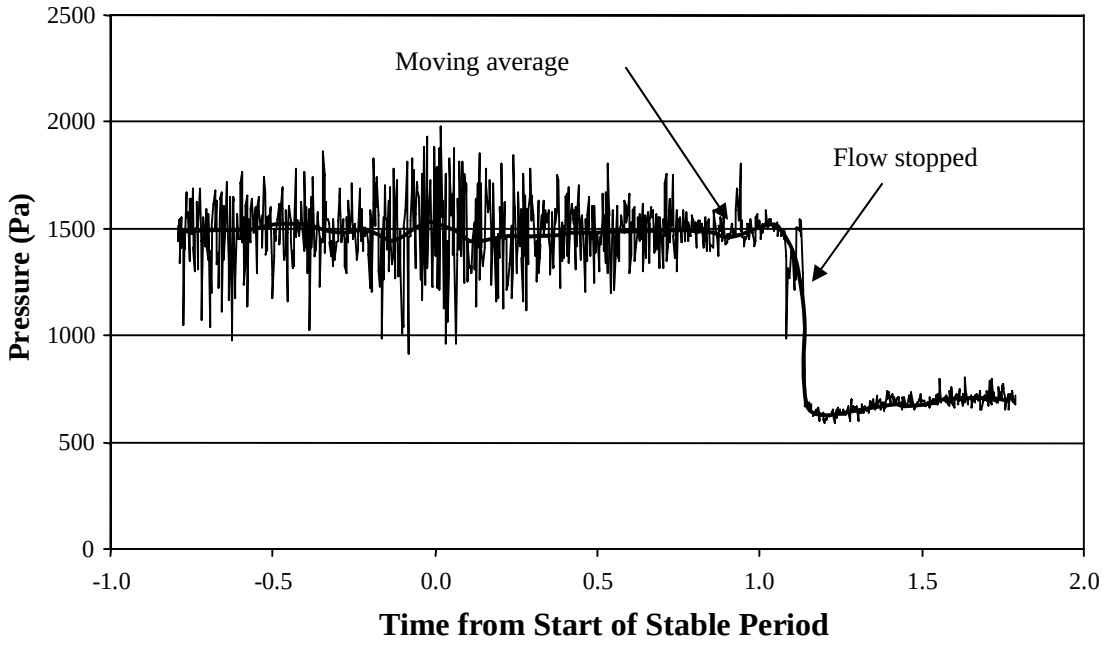

Figure 3.37 Bed differential pressure for WWF test 1

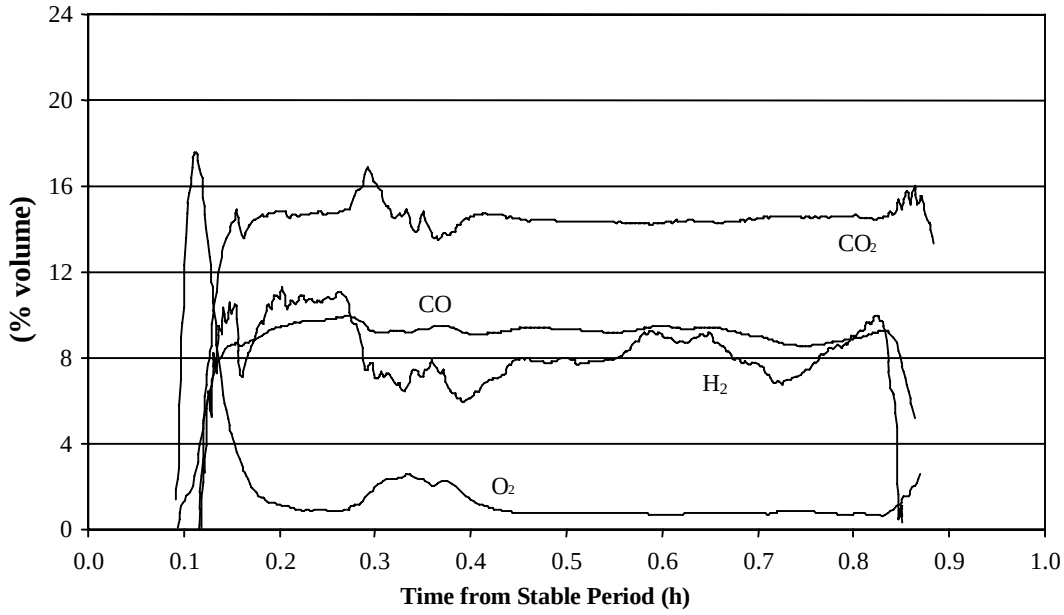

Figure 3.38 Producer gas concentrations for WWF test 1, continuous analysis

WWF

Test 2

Figures 3.39 through 3.43 and Tables 3.38 through 3.41 encompass some of the data associated with this test run.

The second test was run at an average air-factor of 0.22 utilizing a shallow bed of 433 grams of the alumina-silicate bed media. Reactor preheat temperature was 850°C, average primary fluidizing air flow rate was 33.2 g min^{-1} and average fuel feed rate (dry basis) was 30 g min^{-1} during the 80 minute steady period.

Primary fluidizing air preheat was 352°C. Bed temperatures along the main reactor column varied by approximately 150°C throughout the course of the experiment. Average column temperature was approximately 800°C.

From Figure 3.39, it can be seen that the lower bed temperatures (TC1 and TC2) increase as fuel is initially added to the reactor. These bed temperatures increase as the feed rate of fuel is increased until the steady state temperature is reached. The higher temperature due to volatile burning in the freeboard is apparent in Figure 3.41.

Fuel feed was approximately 32% higher than test 1 and a larger proportional increase in bed pressure drop occurs.

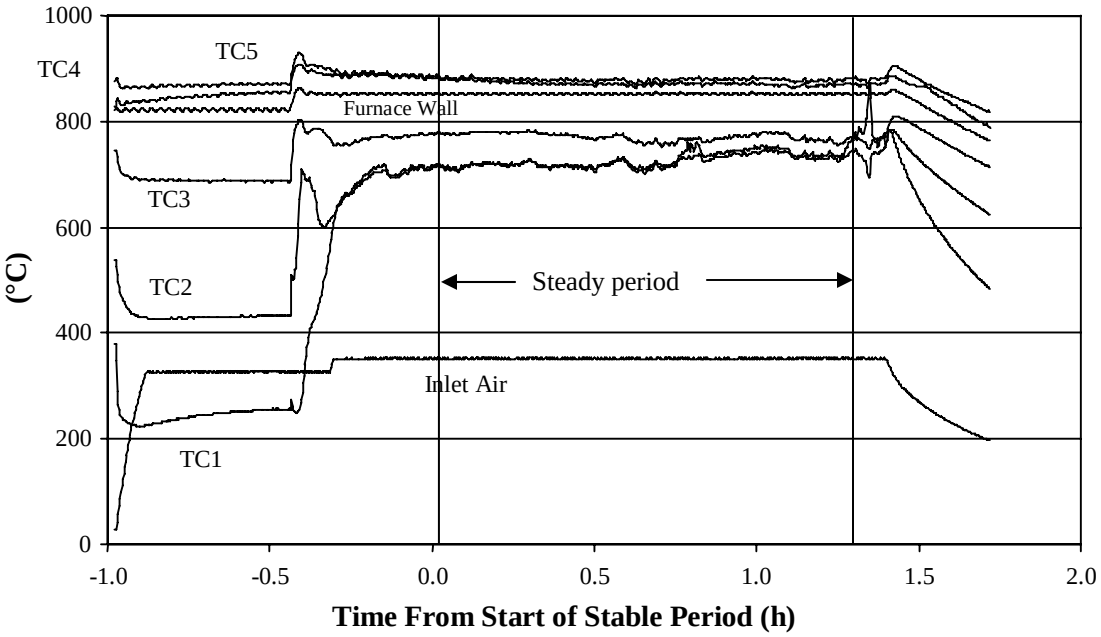

Figure 3.39 Reactor temperatures versus time for WWF test 2

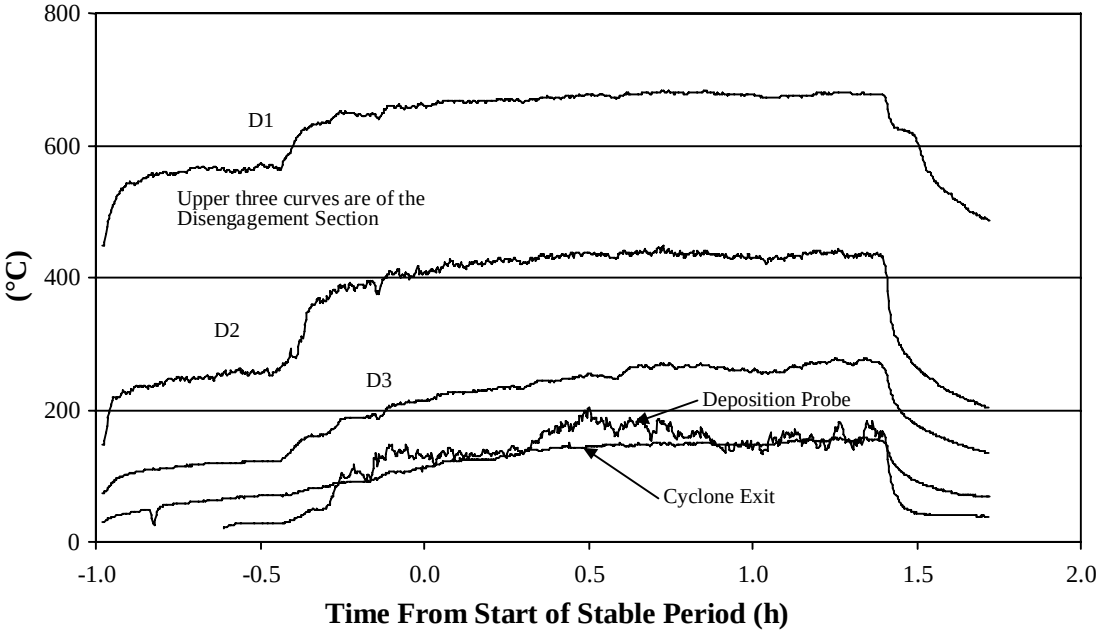

Figure 3.40 Temperatures downstream of reaction zone for WWF test 2

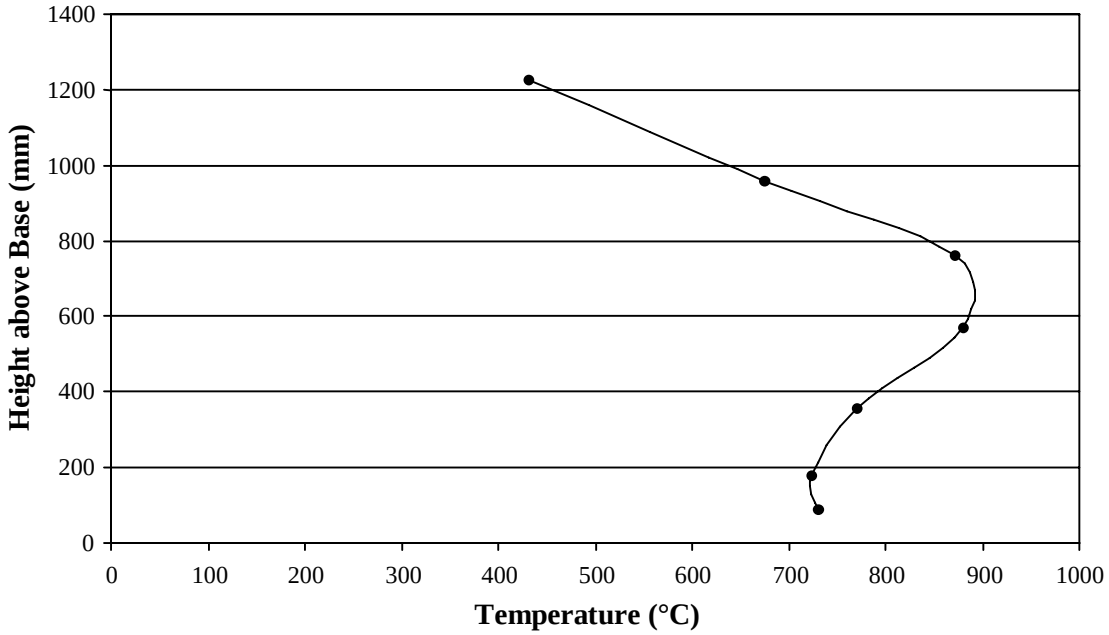

Figure 3.41 Reactor temperature profile for WWF, test 2 at steady state

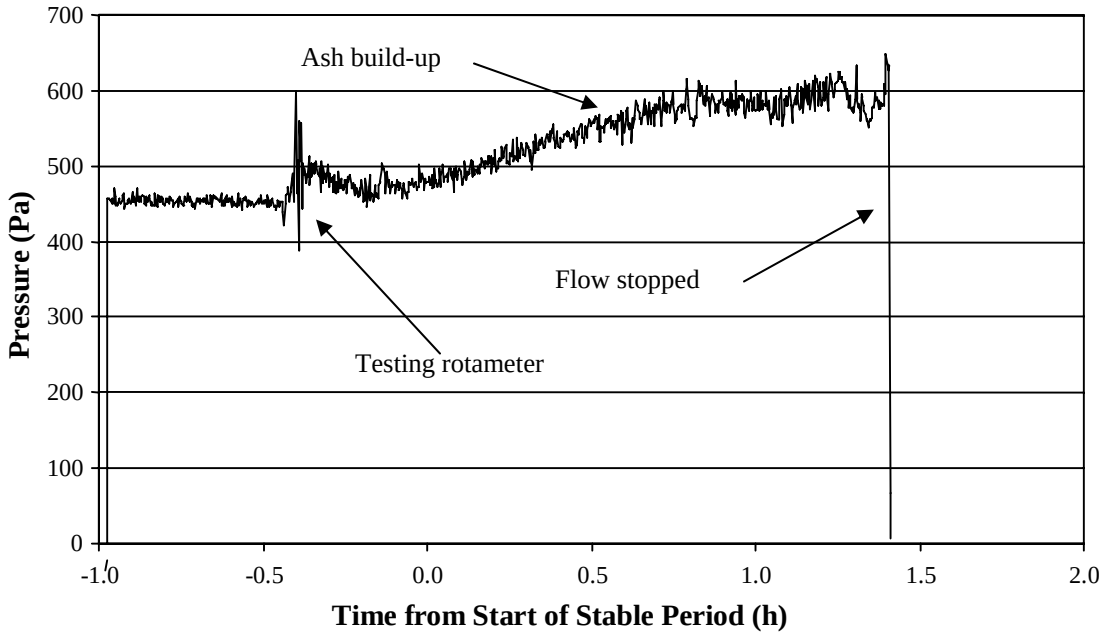

Figure 3.42 Bed differential pressure for WWF test 2

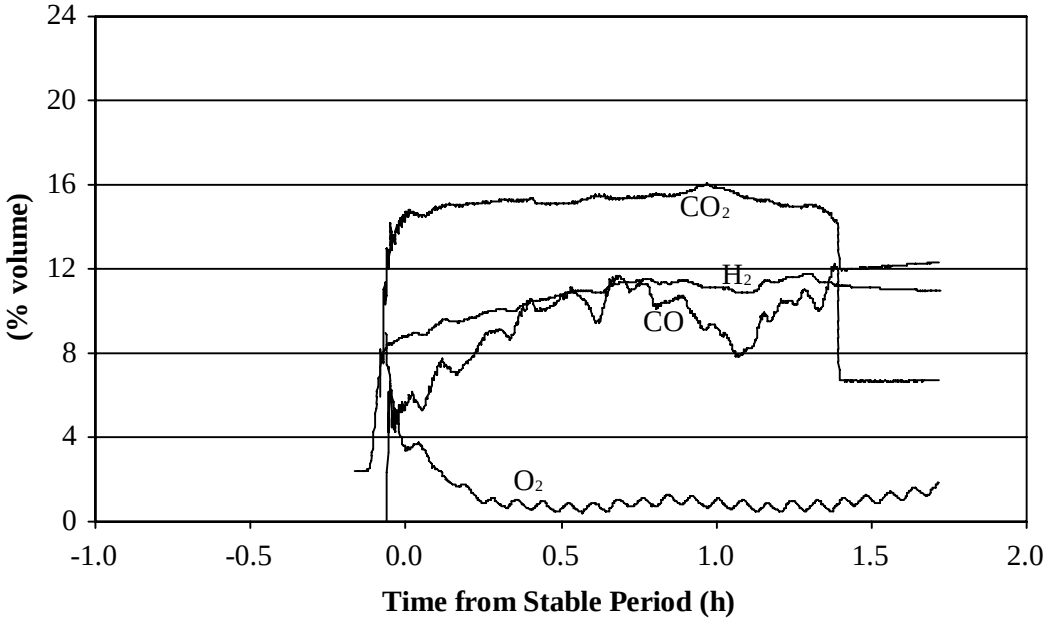

Figure 3.43 Producer gas concentration for WWF test 2, continuous analysis.

Fluctuations in O_2 readings at low concentration due to power line noise, later corrected.

3.6 SLF (Sewage Sludge)

3.6.1 Test 1 and 2

Figures 3.44 through 3.48 and Tables 3.42 through 3.45 summarize some of the data associated with this test run.

The first test was run at an average air-factor of 0.07 utilizing a bed of 866 grams of the alumina-silicate bed media. Reactor preheat temperature was 827 °C, average primary fluidizing air flow rate was 26.5 g min^{-1} and average fuel feed rate (dry basis) was 82 g min^{-1} during the 30 minute test run period.

Primary fluidizing air preheat was 302°C. Bed temperatures along the main reactor column varied by only approximately 27 °C throughout the course of the experiment. Average column temperature was approximately 650 °C.

From Figure 3.44, it can be seen that the lower bed temperatures (TC1 and TC2) increase as fuel is initially added to the reactor. These bed temperatures increase as the feed rate of fuel is increased until an approximately steady state temperature is reached. No true steady state was attained for this test.

Insufficient data was available for calculating the power balance for Test 1 with SLF due to excessive tar plugging in the gas sampling train.

3.6.1.1 Operating parameters

Table 3.42 Operating Parameters for SLF during steady state periods

Parameter		Test 1	Test 2
Total Steady Period	(min)	30	102
Average Fuel Feed Rate (db)	(g min^{-1})	81.8	124.8
Fuel Moisture	(% wb)	8.0	8.0
Total Wet Fuel Burned	(g)	2668	13839
Total Dry Fuel Burned	(g)	2455	12732
Average Air Flow	(g min^{-1})	26.5	33.2
Air : Fuel Ratio (AF)	(-)	0.32	0.27
Stoichiometric AF	(-)	4.66	4.66
Air Factor	(-)	0.07	0.06

Inlet Air Superficial Velocity at ambient temp	($m\ s^{-1}$)	0.09	0.11
Inlet Air Superficial Velocity at operating temp	($m\ s^{-1}$)	0.30	0.39
Average Furnace Wall Temperature	(°C)	827	851
Primary Air Preheat Temperature	(°C)	302	326
Cyclone Exhaust Temperature	(°C)	195	147
Postflare Probe Temperature Average	(°C)	365	257
Average Post Flare Temperature	(°C)	174	105
Average Pressure Drop across Bed	(Pa)	3373	2679
Equivalent Bed Mass Computed from Mean Pressure Drop	(g)	1445	1148

3.6.1.2 Mass balance summary

Table 3.43 Mass Balance Summary for SLF

	Test 1		Test 2	
Parameter	Mass (g)	Percent of flow	Mass (g)	Percent of flow
Inputs				
m_{air}	794	18.3	3386	18.3
$m_{dry\ fuel}$	2455	56.8	12732	68.7
$m_{fuel\ moist}$	214	4.9	1107	6.0
$m_{fresh\ bed}$	866	20.0	1299	7.0
Total	4328	100.0	18524	100.0
Outputs				
$m_{bed\ out}$	2456	56.8	2344	12.7
$m_{horz\ pass}$	1262	29.1	1193	6.4
$m_{cyclone}$	115	2.7	113	0.6
$m_{stack\ dry}$	260	6.0	10315	55.7
$m_{stack\ sol/cond}$	232	5.4	4501	24.0
m_{NH3}	-	-	58	0.3
Total	4325	100.0	18524	100.0

Partial data collected due to plugging of tar train on Test 1.

*$m_{stack\ sol/cond}$ includes the total air dried tar in the stack flow of 685 g Test 2. The total tar value is derived from 41 g of tar in condenser 1 and 16 g of tar in condenser 2 (for Test 2).
** m_{NH3} represents the total ammonia in stack flow derived from a sample collected in the ammonia train. There may be some additional ammonia in solution collected in the $m_{stack\ sol/cond.}$

3.6.1.3 Stack gas grab sample average analysis, gas phase NH_3, HCN, Cl, K and concentration of solids and condensibles for SLF

Table 3.44 Stack gas grab sample average analysis (GC) and concentration of solids and condensibles for SLF

	Test 1	Test 2
Constituent	Mean Concentration (% v/v)	Mean Concentration (% v/v)
CO	15	11
H_2	21	15
CH_4	8	6
CO_2	11	10
N_2	44	55
O_2	1	2
	Mean Concentration (ppm)	Mean Concentration (ppm)
NH_3	39900	9950
Cl	79700	24700
K	30	61
HCN	NA	NA
Total	111.96	102.47
Higher Heating Value (MJ m^{-3})	7.1	5.1
Solids and Condensibles	Concentration (mg L^{-1} dry gas)	Concentration (mg L^{-1} dry gas)
With condensed water	900.9	470.4
Air dried, room temperature	240	76

3.6.1.4 Power balance and hot and cold gas efficiency

Table 3.45 Power Balance and hot and cold gas efficiencies for SLF

Power Component	Power Test 1	Power Test 2
Total Input (W)	-	32381
Total Output (W)	-	27550
Unaccounted (W)	-	4831
Total Output/ Total Input (%)	-	92
$\eta_{\text{hot gas}}$ (%)	-	26.1
$\eta_{\text{cold gas}}$ (%)	-	25.3

Insufficient data for analysis of Test 1 due to plugging of tar train.

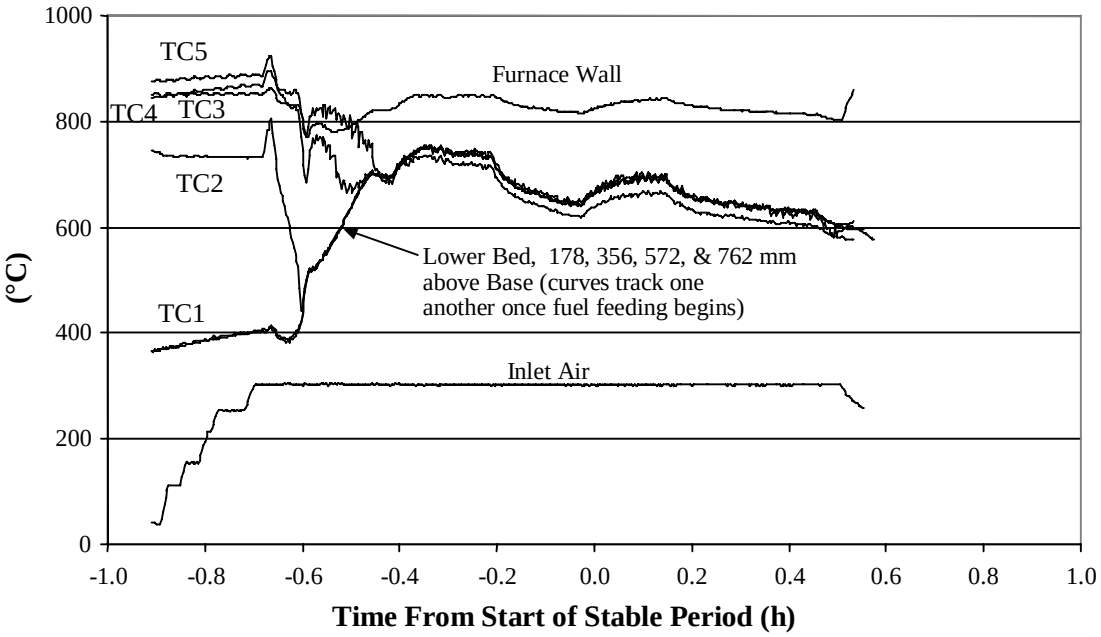

Figure 3.44 Reactor temperatures versus time for SLF test 1

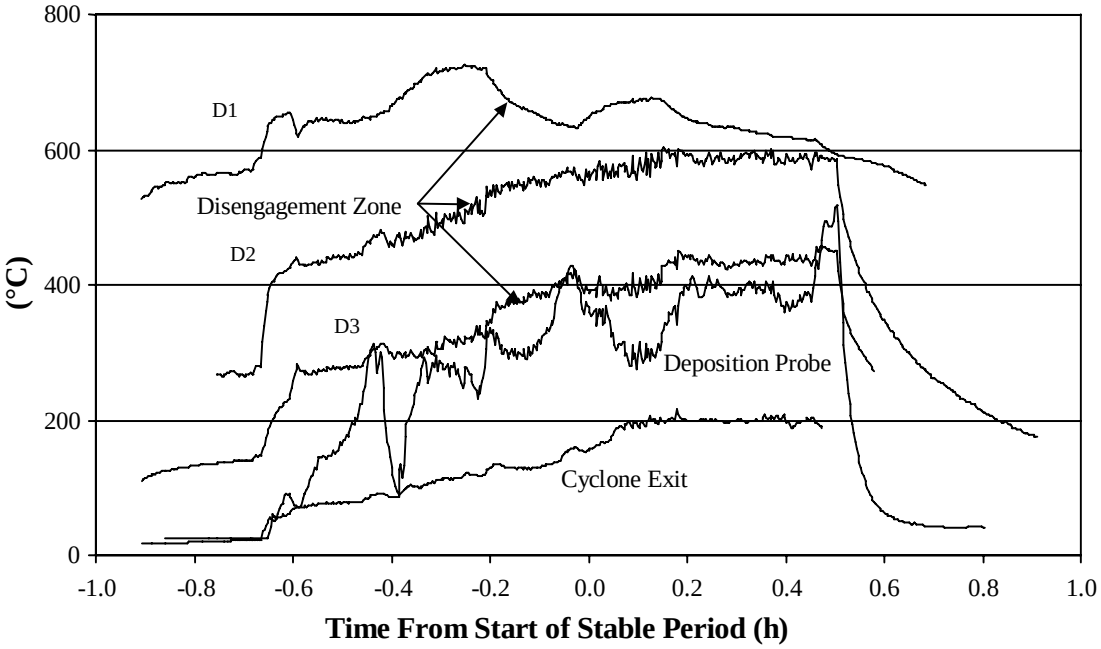

Figure 3.45 Temperatures downstream of reaction zone for SLF test 1

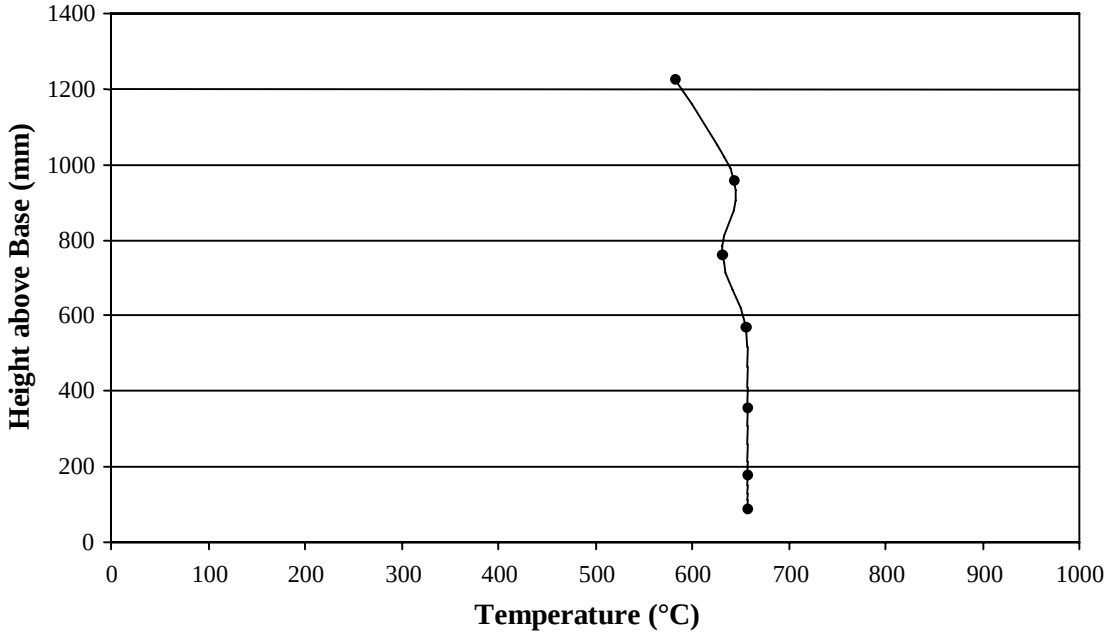

Figure 3.46 Reactor temperature profile for SLF, test 1 at steady state

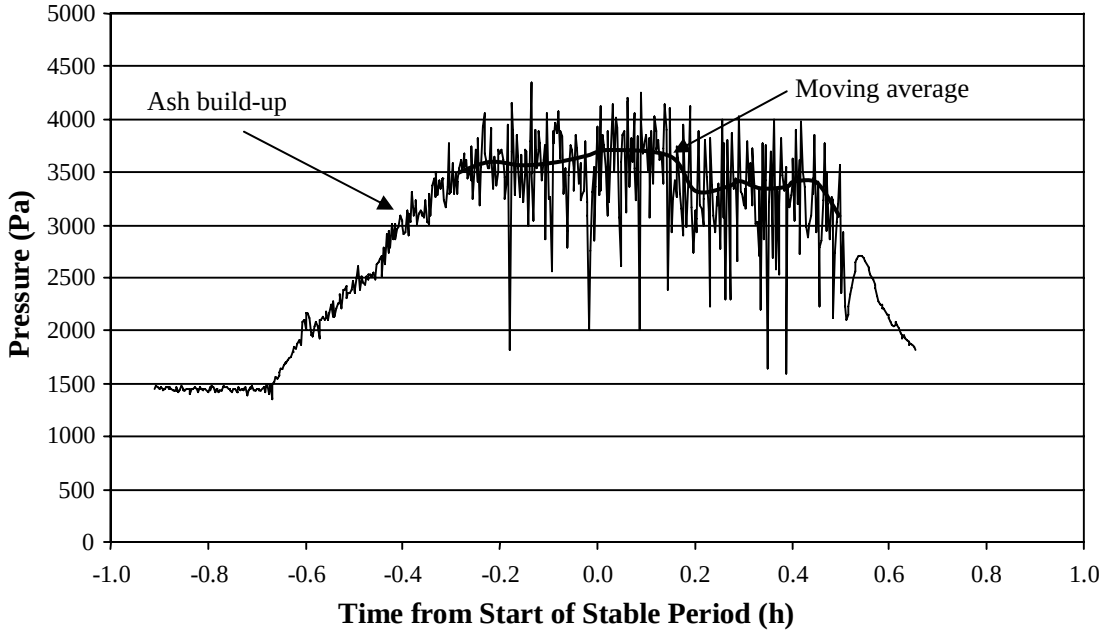

Figure 3.47 Bed differential pressure for SLF test 1

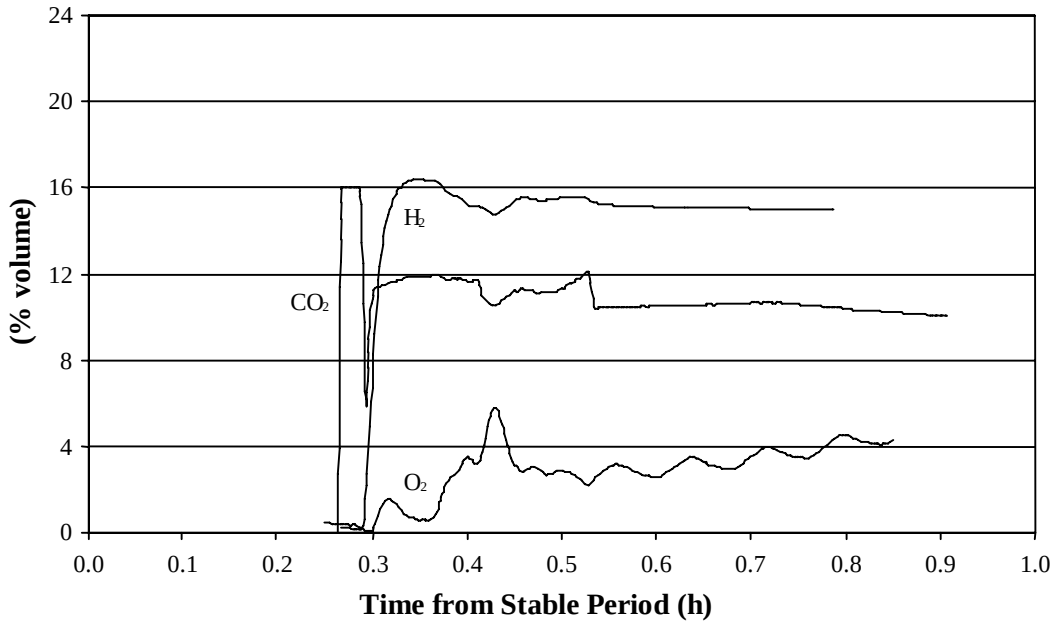

Figure 3.48 Producer gas concentration for SLF test 1, continuous analysis. CO not shown due to failure of instrument.

Sludge

Test 2

Figures 3.49 through 3.53 and Tables 3.42 through 3.45 summarize some of the data associated with this test run.

The second test was run at an average air-factor of 0.06 utilizing a bed of 866 g initially with 433 g added later. The alumina-silicate bed media was used. Reactor preheat temperature was 851 °C, average primary fluidizing air flow rate was 33.2 g min^{-1} and average fuel feed rate (dry basis) was 125 g min^{-1} during the 102 minute test run period.

Primary fluidizing air preheat was 326°C. Bed temperatures along the main reactor column varied by approximately 16 °C throughout the course of the experiment. Average column temperature was approximately 760 °C.

From Figure 3.49, it can be seen that the lower bed temperatures (TC1 and TC2) increase as fuel is initially added to the reactor. These bed temperatures increase as the feed rate of fuel is increased until a steady state temperature is reached.

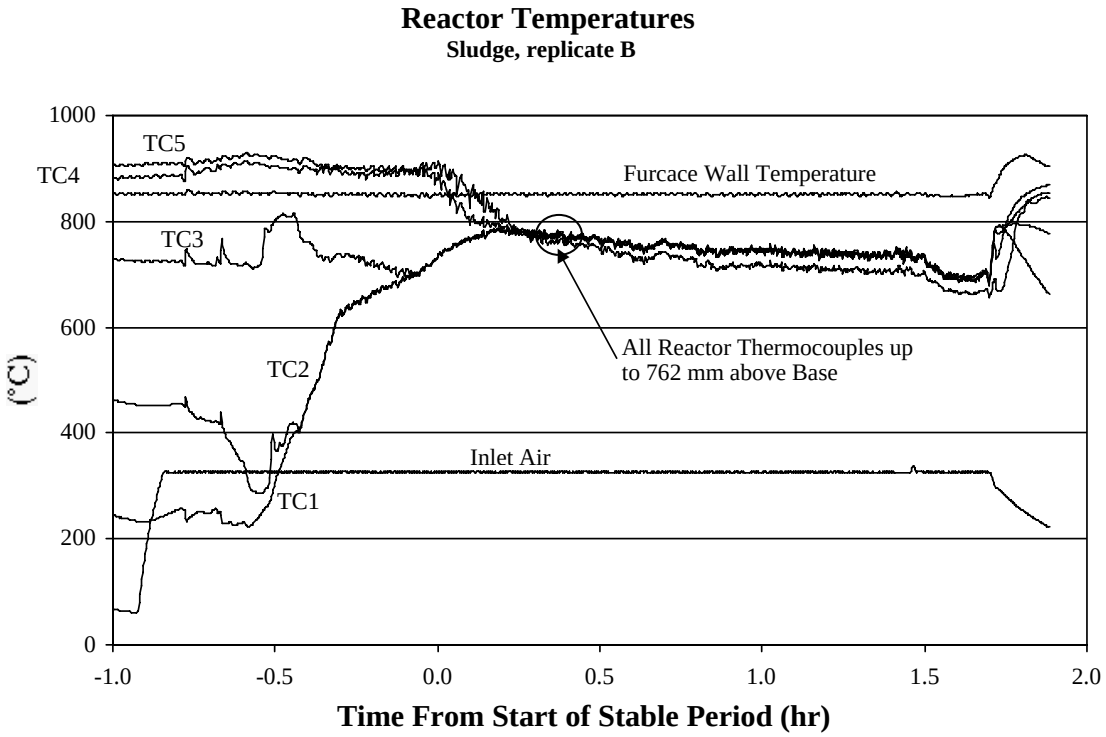

Figure 3.49 Reactor temperatures versus time for SLF test 2

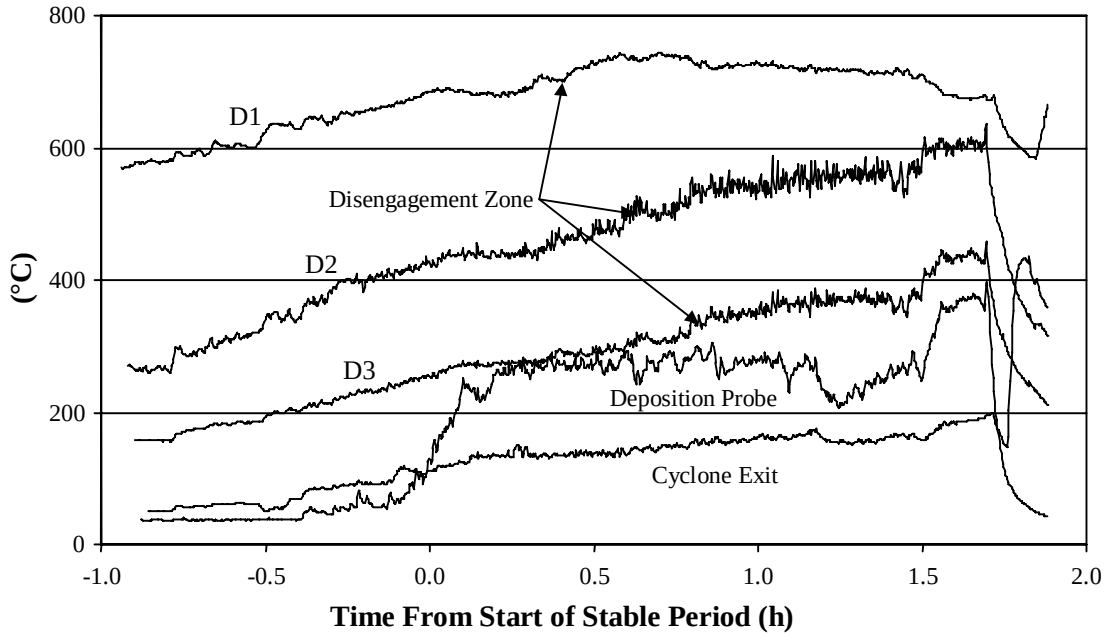

Figure 3.50 Temperatures downstream of reaction zone for SLF test 2

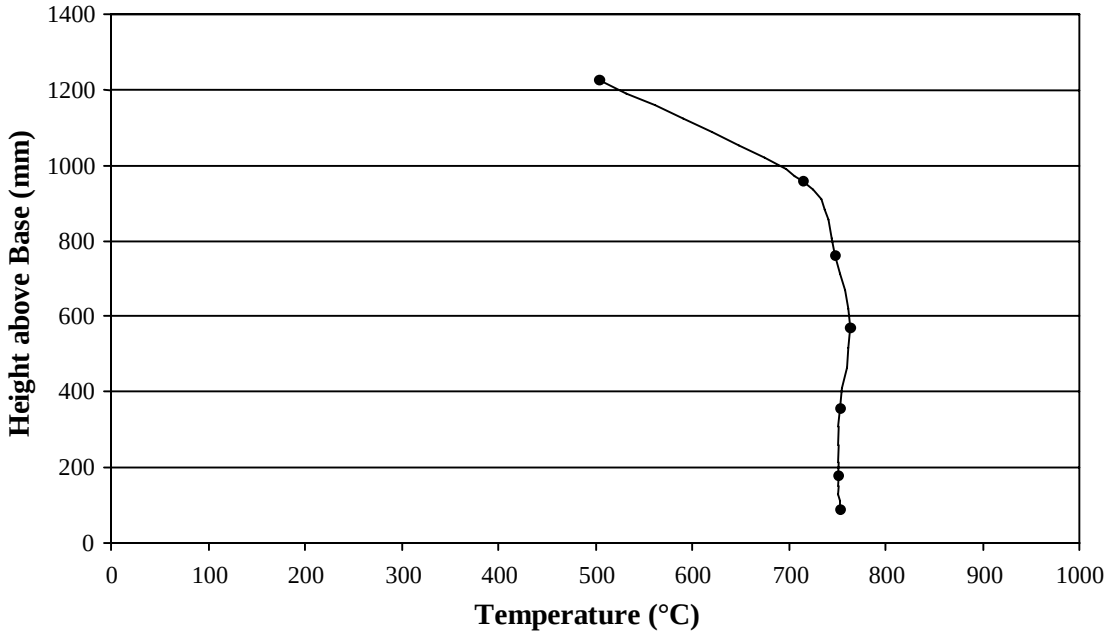

Figure 3.51 Reactor temperature profile for SLF, test 2 at steady state

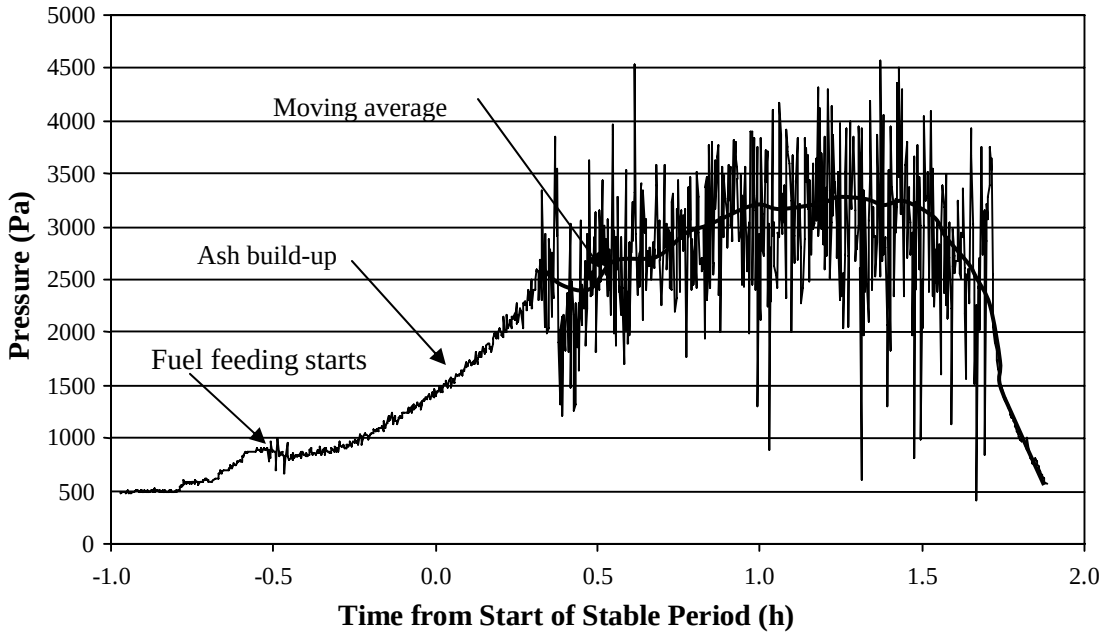

Figure 3.52 Bed differential pressure for SLF test 2

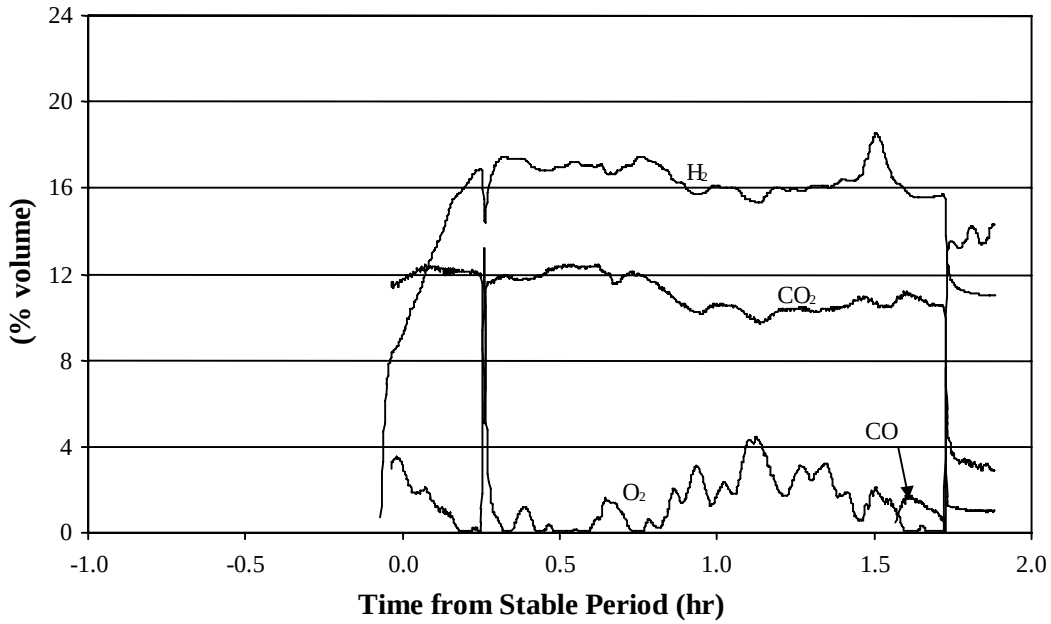

Figure 3.53 Producer gas concentrations for SLF test 2, continuous analysis. CO analyzer failed during most of the run.

3.7 Non-Recyclable Waste Paper (NPF)

3.7.1 Test 1 and 2

Figures 3.54 through 3.58 and Tables 3.46 through 3.49 summarize data associated with this test run.

The first test was run at an average air-factor of 0.30 utilizing a bed of 433 grams of the alumina-silicate bed media. Reactor preheat temperature was 850°C, average primary fluidizing air flow rate was 29.2 g min^{-1} and average fuel feed rate (dry basis) was 19 g min^{-1} during the 101 minute test run period.

Primary fluidizing air preheat was 352°C. Bed temperatures along the main reactor column varied by approximately 200 °C throughout the course of the experiment. Average column temperature was approximately 775 °C but the profile in Figure 3.56 shows the characteristic high freeboard temperature associated with volatile burning above the main bed.

From Figure 3.54, it can be seen that the lower bed temperatures (TC1 and TC2) increase as fuel is initially added to the reactor. These bed temperatures increase as the feed rate of fuel is increased until a steady state temperature is reached.

3.7.1.1 Operating parameters

Table 3.46 Operating Parameters for NPF during steady state periods

Parameter		Test 1	Test 2
Total Steady Period	(min)	101	110
Average Fuel Feed Rate (db)	(g min^{-1})	19.3	22.6
Fuel Moisture	(% wb)	6.3	6.3
Total Wet Fuel Burned	(g)	2076	2657
Total Dry Fuel Burned	(g)	1946	2489
Average Air Flow	(g min^{-1})	29.2	29.6
Air : Fuel Ratio (AF)	(-)	1.51	1.31
Stoichiometric AF	(-)	5.09	5.09
Air Factor	(-)	0.30	0.26
Inlet Air Superficial Velocity at ambient temp	(m s^{-1})	0.10	0.10

Inlet Air Superficial Velocity at operating temp	(m s^{-1})	0.34	0.33
Average Furnace Wall Temperature	(°C)	850	853
Primary Air Preheat Temperature	(°C)	352	351
Cyclone Exhaust Temperature	(°C)	130	149
Postflare Probe Temperature Average	(°C)	189	229
Average Post Flare Temperature	(°C)	70	70
Average Pressure Drop across Bed	(Pa)	522	506
Mean Bed Mass	(g)	223	217

3.7.1.2 Mass balance summary

Table 3.47 Mass Balance Summary for NPF

	Test 1		Test 2	
Parameter	Mass (g)	Percent of flow	Mass (g)	Percent of flow
Inputs				
m_{air}	2946	54.0	3257	51.4
$m_{dry\ fuel}$	1946	35.7	2489	39.2
$m_{fuel\ moist}$	131	2.4	167	2.6
$m_{fresh\ bed}$	433	7.9	433	6.8
Total	5456	100.0	6346	100.0
Outputs				
$m_{bed\ out}$	444	8.2	449	7.1
$m_{horz\ pass}$	40	0.7	81	1.3
$m_{cyclone}$	28	0.5	15	0.2
$m_{stack\ dry}$	4256	78. 0	5099	80.4
$m_{stack\ sol/cond}$*	687	12.6	702	11.0
m_{NH3}**	<1	0.0	<1	0.0
Total	5455	100.0	6346	100.0

*$m_{stack\ sol/cond}$ includes the total air dried tar in the stack flow of 26 g and 26 g respectively for Tests 1 and 2. These total tar values are derived from 3 g of tar in condenser 1 and 1 g of tar in condenser 2 (for Test 1) and 4 g in condenser 1 and 1 g in condenser 2 (for Test 2).

** m_{NH3} represents the total ammonia in stack flow derived from a sample collected in the ammonia train. There may be some additional ammonia in solution collected in the $m_{stack\ sol/cond.}$ Values computed as 0.20 g and 0.19 g for tests 1 and 2 respectively.

3.7.1.3 Stack gas grab sample average analysis, gas phase NH_3, HCN, Cl, K and concentration of solids and condensibles for NPF

Table 3.48 Stack gas grab sample average analysis (GC) and concentration of solids and condensibles for NPF

	Test 1	Test 2
Constituent	Mean Concentration (% v/v)	Mean Concentration (% v/v)
CO	21	20
H_2	8	7
CH_4	6	5
CO_2	13	13
N_2	50	53
O_2	1	1
	Mean Concentration (ppm)	Mean Concentration (ppm)
NH_3	3	70
Cl	9	17
K	2	2
HCN	NA	NA
Total	99.00	99.01
Higher Heating Value (MJ m^{-3})	5.5	5.0
Solids and Condensibles	Concentration (mg L^{-1} dry gas)	Concentration (mg L^{-1} dry gas)
With condensed water	183	158
Air dried, room temperature	6.8	5.8

3.7.1.4 Power balance and hot and cold gas efficiency

Table 3.49 Power balance and hot and cold gas efficiencies for NPF

Power Component	Power Test 1	Power Test 2
Total Input (W)	6349	7314
Total Output (W)	4331	4427
Unaccounted (W)	2018	2887
Total Output/ Total Input (%)	68	60
$\eta_{\text{hot gas}}$ (%)	55.1	48.1
$\eta_{\text{cold gas}}$ (%)	53.7	46.4

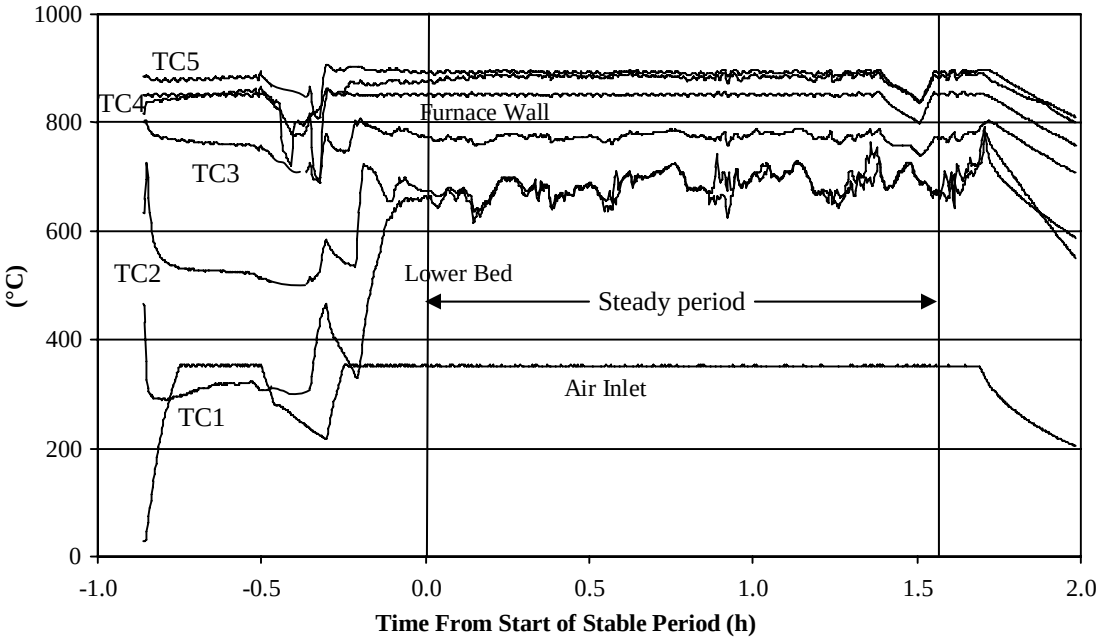

Figure 3.54 Reactor temperatures versus time for NPF test 1. Temperature fluctuations due to irregular feed with this fuel.

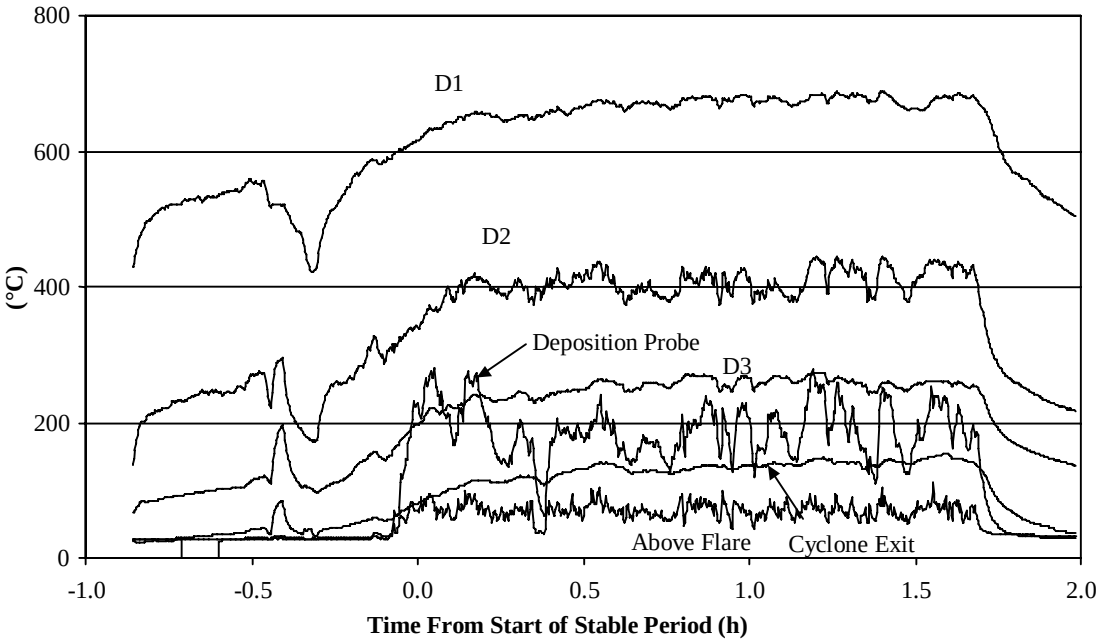

Figure 3.55 Temperatures downstream of reaction zone for NPF test 1

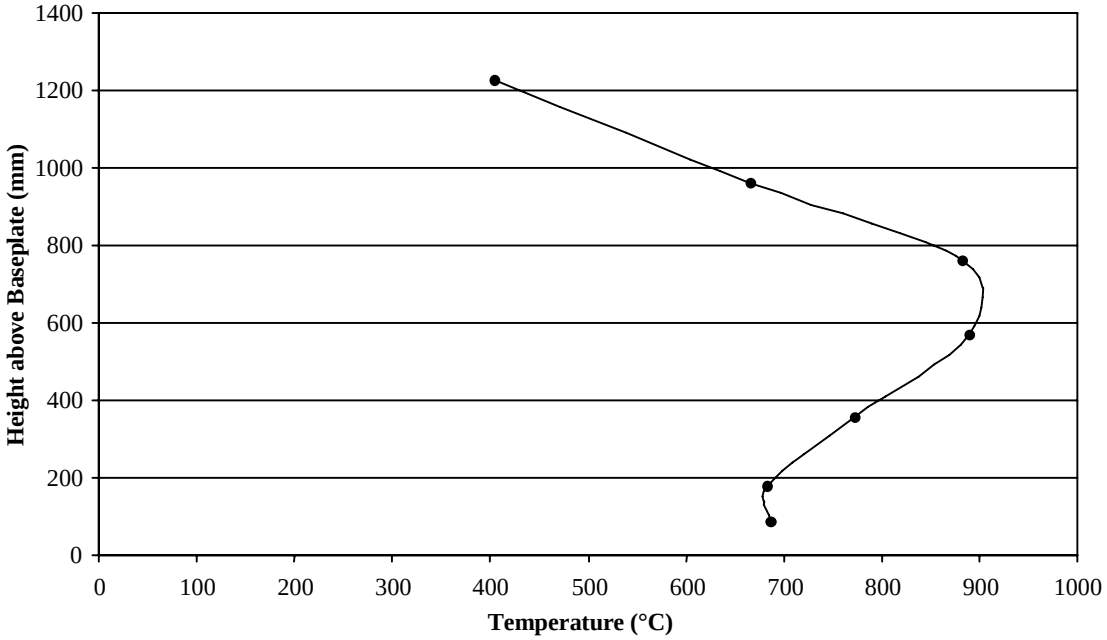

Figure 3.56 Reactor temperature profile, test 1 at steady state

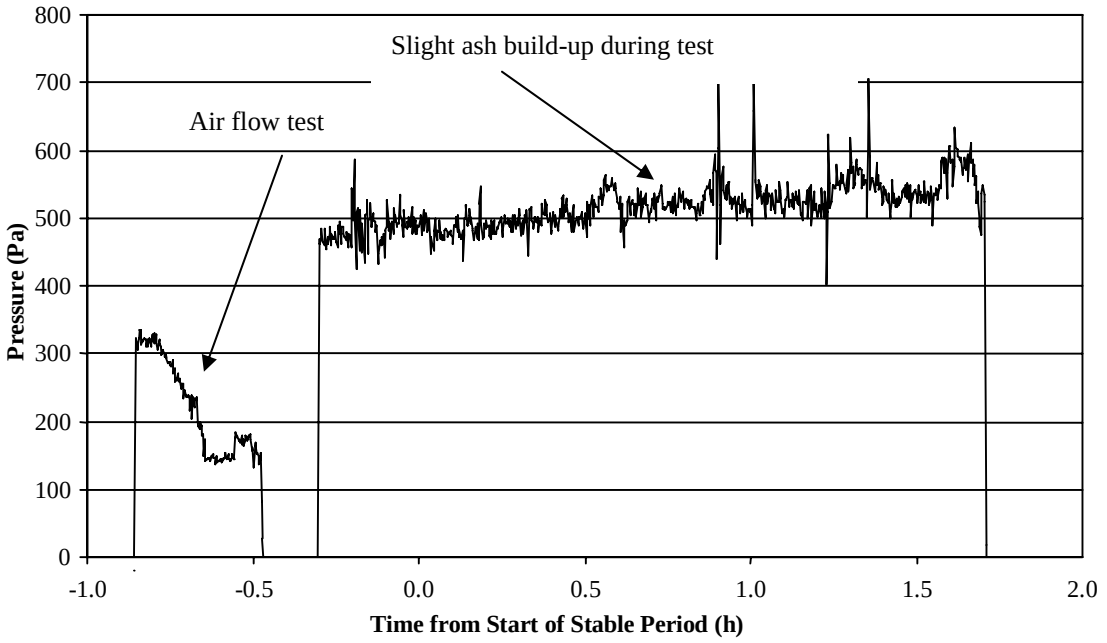

Figure 3.57 Bed differential pressure for NPF test 1

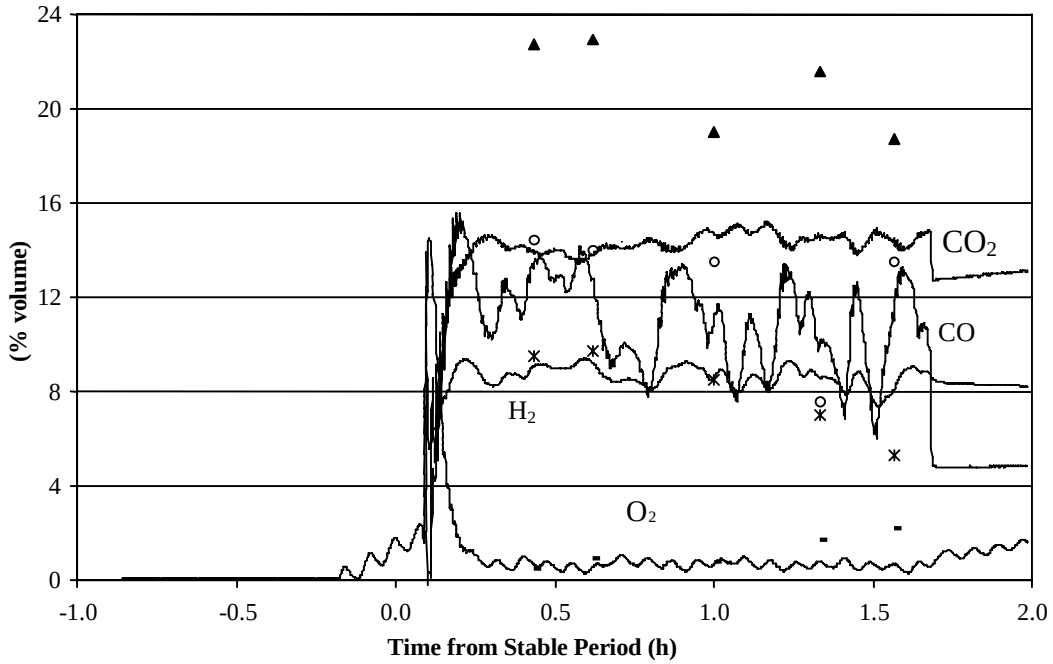

Figure 3.58 Producer gas concentrations for NPF test 1, continuous analysis. Also shown for comparison are point measurements obtained via GC: CO (filled triangles), CO_2 (open circles), H_2 (X), O_2 (-).

Test 2

Figures 3.59 through 3.63 and Tables 3.46 through 3.49 summarize data associated with this test run.

The second test was run at an average air-factor of 0.26 utilizing a shallow bed of 433 grams of the alumina-silicate bed media. Reactor preheat temperature was 850 °C, average primary fluidizing air flow rate was 29.6 g min^{-1} and average fuel feed rate (dry basis) was 23 g min^{-1} during the 110 minute test run period.

Primary fluidizing air preheat was 351°C. Bed temperatures along the main reactor column varied by approximately 185 °C throughout the course of the experiment. Average column temperature was approximately 790 °C, but again showed a distinct increase in the freeboard. Irregularities in the fuel feed cause the fluctuations in temperature observed throughout the test.

From Figure 3.11, it can be seen that the lower bed temperatures (TC1 and TC2) increase as fuel is initially added to the reactor. These bed temperatures increase as the feed rate of fuel is increased until a steady state temperature is reached.

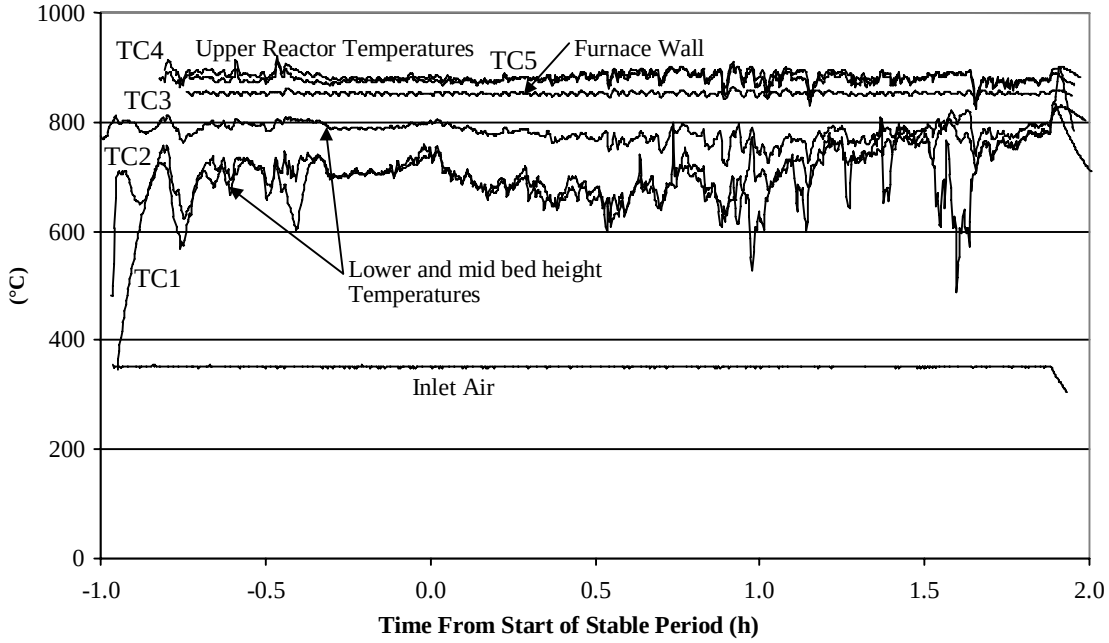

Figure 3.59 Reactor temperatures versus time for NPF test 2

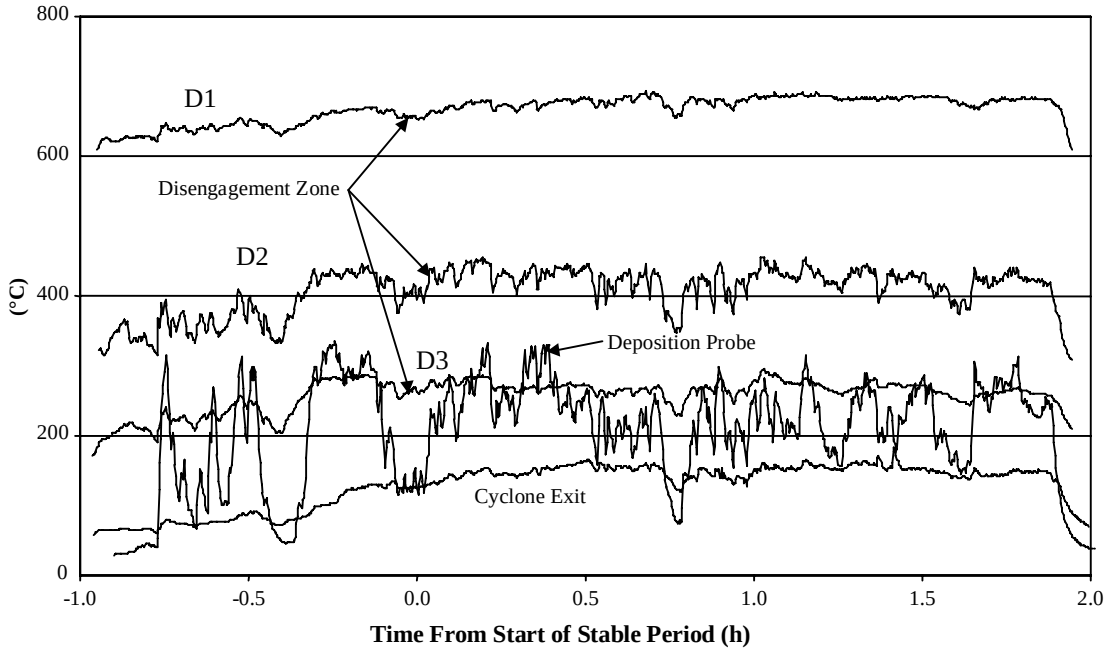

Figure 3.60 Temperatures downstream of reaction zone for NPF test 2

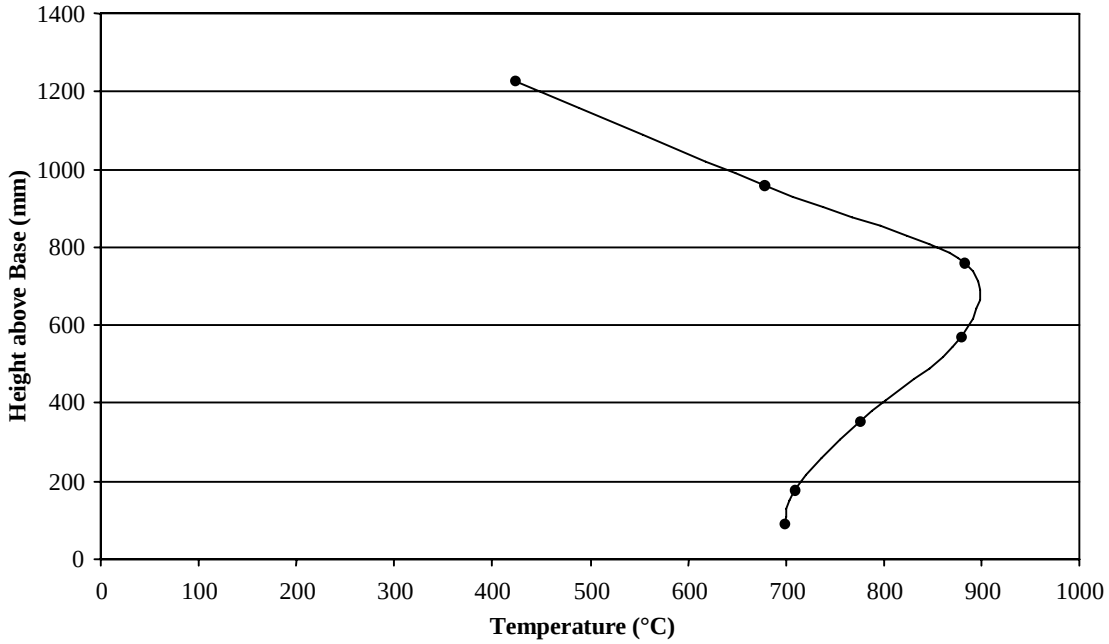

Figure 3.61 Reactor temperature profile for NPF, test 2 at steady state

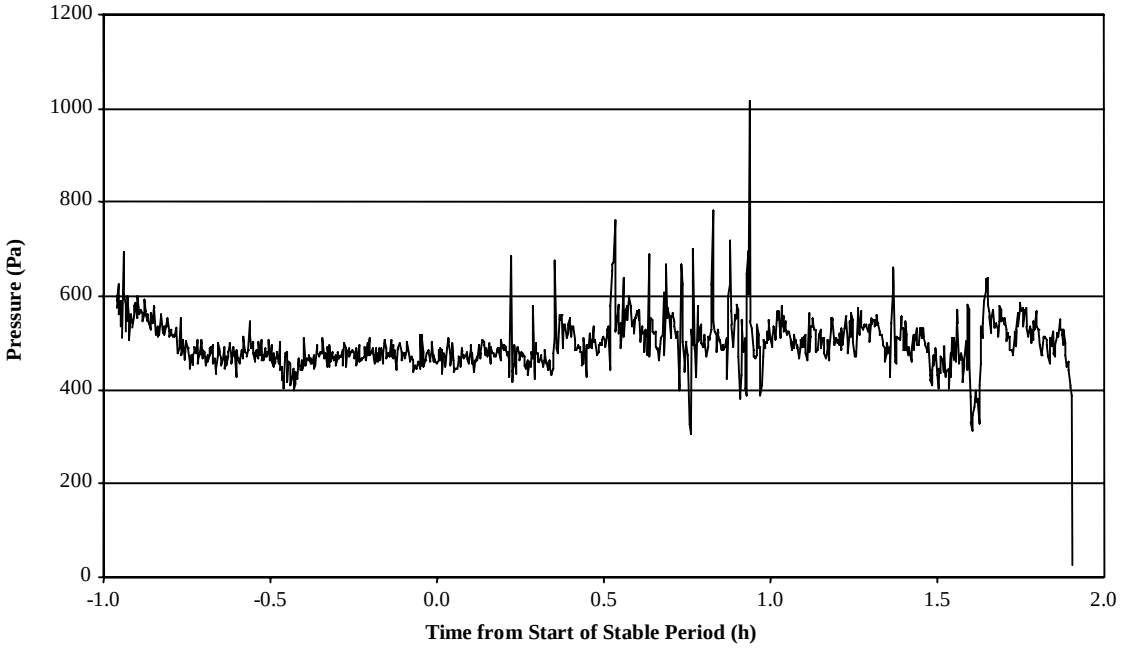

Figure 3.61 Bed differential pressure for NPF test 2

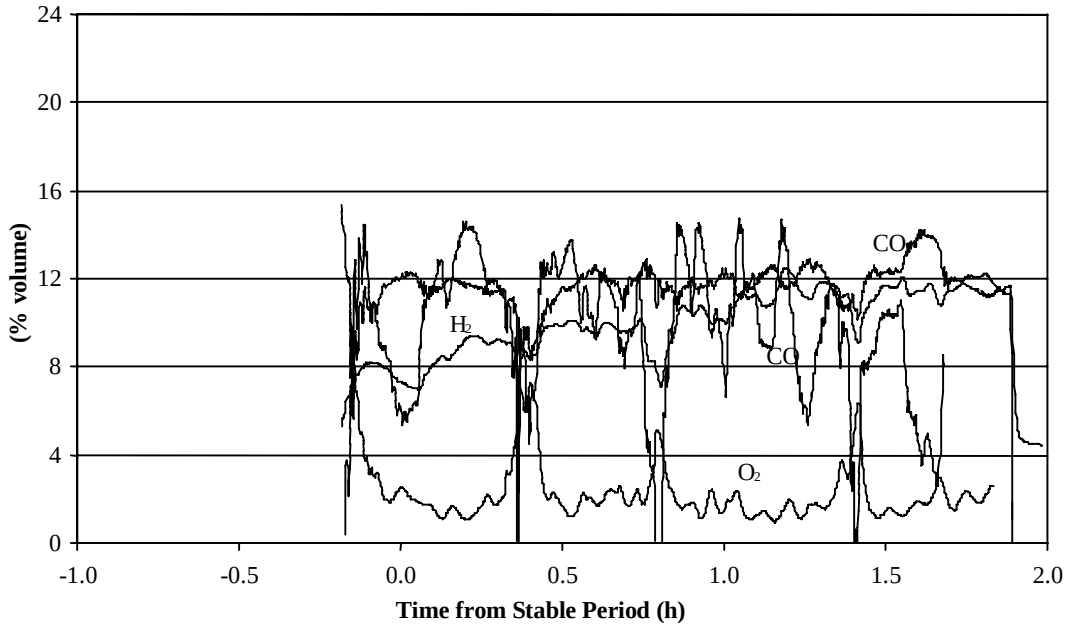

Figure 3.62 Producer gas concentrations for NPF test 2, continuous analysis

CHAPTER 4 PREDICTIONS FROM MODELING OF FLUIDIZED BED

4.1 Introduction

Using fluidized beds for combustion and gasification has many advantages. The main advantages in comparison with other combustion and gasification processes are the superior mixing properties and the enhanced heat transfer rates between the gas and the particles as well as between the particles and the heat exchanger surfaces.

A fluidized bed is therefore well suited for gasification of biomass because of the non-homogeneous nature of biomass and because there is a great deal of surface area contact between the solid and the gas. The efficient mixing rates in a fluidized bed create an almost isothermal condition in the gasifier, which can also lead, in some instances, to reduced emissions because of the lower operating temperatures. The interactions occurring in a fluidized bed gasifier depend in large part on the hydrodynamics of the fluidized bed and involve complex phenomena including, chemical reactions, heat and mass transfer, particle size reductions (through devolatilization and char burn) and even attrition of particles and bed material.

4.2 Comprehensive Simulator for Fluidized Bed Equipment (CSFB) Model

Experimental results were compared to results obtained by running a commercially available computer model performing a comprehensive simulation of fluidized-bed equipment (CSFB Version 3.5) written by de Souza-Santos (2001). The model is one-dimensional and first-order in reaction rate. The version of the model that was procured did not provide access to the devolatilization routine or the kinetics module.

The model considers numerous chemical reactions and also includes other processes such as devolatilization and drying of carbonaceous solid fuel. The model includes up to 18 gas and 14 solid chemical components. Gas components include CO_2, CO, O_2, N_2, H_2O, H_2, CH_4, SO_2, NO, C_2H_6, H_2S, NH_3, C_2H_4, C_3H_6, H_3C_8, C_6H_6, tar, and hydrogenated oil. The solid components include carbonaceous solid (fuel), inert (sand or other) and/or limestone solid particles. The central mass and energy balances lead to a non-linear and strongly coupled system of differential equations.

4.2.1 Basic Model Hypotheses:

1. The model simulates the steady-state operation of fluidized bed reactors.
2. The species taking part in the emulsion are the interstitial gas and one or more of the three possible solid species. The (bed) inert material and/or limestone may be

assumed to be batch or continuously fed to the reactor. The carbonaceous fuel feeding is assumed to be continuous or added at regular intervals.

3. The bubbles are free of particles.
4. Any variations that occur are assumed to occur only in the vertical or axial "z" direction.
5. At the base of the bed (z = 0), two-phase flow is assumed. The emulsion phase is at minimum fluidization condition and the excess of gas inflow is diverted to the bubble phase. For levels above the base (z > 0) this simplification is abandoned and the mass flow through each phase is governed by the mass and energy balances.
6. Plug-flow regime is assumed for the gas flow through the emulsion, bubble phase and freeboard.
7. No restrictions are imposed for the temperature variations of each gas and solid phase throughout the bed and freeboard.
8. The program assumes a homogeneous composition for each solid phase throughout the bed.
9. The gas-solid reactions are described by one of two possible basic models: unreacted-core and exposed core. The former assumes that the reacting particle maintains a layer of spent material (ash, for instance) around the unreacted nucleus. In this case, the layer that surrounds the core has enough mechanical strength to survive the attrition due to shocks and impacts against other particles and surfaces. The exposed-core model assumes that the residual layer is segregated from the particle as soon as it is formed. The unreacted-core model is the most common during the combustion and gasification of carbonaceous particles in a fluidized bed. For the devolatilization of carbonaceous solid, drying of all solids and calcination and other reactions involving limestone, the model assumes the unreacted-core model. The unreacted-core model is more representative of actual conditions. (The unreacted-core model was used in all runs).
10. Convection, conduction and radiation heat transfer occur between all phases as well as between these phases and internal surfaces (walls). However, the gas phases are considered transparent concerning the radiation heat transfer. The approximation does not introduce any major deviation because the gas layers between the particles are relatively thin. In addition, the empirical or semi-empirical relationships for the heat transfer due to convection include radiation heat transfer.

4.2.2 Model Inputs

Inputs to the model are:

1. Mass flow rate and characterization of a fluidizing agent, such as air, steam and other possible gases and their mixtures.
2. Mass flow rate and characterization of a particulate solid such as biomass
3. Batch loading and characterization of particulate solid such as sand
4. Batch loading and characterization of optional particulate solid such as limestone

5. External heating of reactor
6. Intermediate injection points
7. Steam injection
8. Bed operating pressure
9. Primary air preheat temperature

4.2.3 Model Outputs

Outputs from the model are:

1. Concentration and mass flow profiles of the 18 gas components throughout the bed in the emulsion and bubble phases.
2. Concentration and mass flow profiles of these species through the freeboard.
3. Composition, circulation rates, and particle size distributions of all solid species in the bed.
4. Concentration, mass-flow, and particle size distribution profiles of all solid species throughout the freeboard.
5. Temperature profiles of gas in the emulsion, gas in the bubble, carbonaceous, limestone (if added) and inert solids throughout the bed.
6. Temperature profiles of the gas phases and the three possible solid phases throughout freeboard.
7. Parameters related to the fluidization dynamics at each point of the bed, such as bubble sizes and velocities, mass flows through each phase, particle turnover rates, void fractions, etc.
8. Pressure losses in the distributor and in the bed.
9. Typical engineering parameters such as efficiencies, heat losses to surroundings, external wall temperature profiles, heating value and adiabatic flame temperature of the produced gas, compositions of the exit streams, entrainment parameters, and other details.

4.2.4 Model Sensitivity

The model is particularly sensitive to the following parameters:

-Ultimate and proximate analysis of the carbonaceous feeding solid.
-Heating value of the fuel.
-Particle size distributions of the solid fuel or the inert material.
-Mass flows, pressure and composition of the streams injected into the bed.
-Geometry of the equipment (height and equivalent inside hydraulic diameter). Variables can change, however, only in the vertical direction as the model assumes constant values in the radial direction.

4.2.5 Chemical Reactions Considered by the Model

Reactions used by CSFB are reported by deSouza-Santos (2001) and are reproduced here using the same nomenclature. The numbering scheme was developed by others in order

to allow short notations for the mathematical and computational treatment. For the components of the solid phase (carbonaceous and inert), the numbering appearing in Karapetyants (1978), added to 500, is used. For the gas phase components, the numbering given by Reid (1977) is used.

$$CH_{a531}O_{a551}N_{a546}S_{a563} + (\frac{a_{531}}{4} - \frac{a_{551}}{2} + \frac{a_{546}}{2} + a_{563})O_2 \rightarrow CO2 + \frac{a_{531}}{2} H_2O +$$

$$a_{546}NO + a_{563}SO_2 \qquad (R1)$$

$$CH_{a531}O_{a551}N_{a546}S_{a563} + (1\text{-}a_{551})\ H_2O \leftrightarrow (1+\frac{a_{531}}{2} - a_{551} - a_{563})H_2 + CO$$

$$+ \frac{a_{546}}{2} N_2 + a_{563}H_2S \qquad (R3)$$

$$CH_{a531}O_{a551}N_{a546}S_{a563} + CO_2 \leftrightarrow 2CO + a_{551}H_2O + (\frac{a_{531}}{2} - a_{551} - \frac{3a_{546}}{2} - a_{563})H_2$$

$$+ a_{546}NH_3 + a_{563}H_2S \qquad (R4)$$

$$CH_{a531}O_{a551}N_{a546}S_{a563} + (2 - \frac{a_{531}}{2} + a_{551} + \frac{3}{2} a_{546} + a_{563})H_2 \leftrightarrow CH_4 + a_{551}H_2O +$$

$$(a_{546}NH_3 - a_{563})H_2S \qquad (R5)$$

$$CH_{a531}O_{a551}N_{a546}S_{a563} + (2 - a_{551})NO \leftrightarrow (\frac{a_{531}}{2} - a_{563})H_2 + CO_2 +$$

$$(1+\frac{a_{546}}{2} - \frac{a_{551}}{2})N_2 + a_{563}H_2S \qquad (R6)$$

$$\text{Volatiles} \rightarrow \text{Tar} \qquad (R7)$$

$$\text{Volatiles} \rightarrow a_{v,19}H_2 + a_{V,20}H_2O + a_{V,21}H_2S + a_{V,22}NH_3 \qquad (R8)$$

$$\text{Volatiles} + (b_{514}\beta + \frac{b_{531}}{4} - \frac{b_{551}}{2} + \frac{b_{546}}{2} + b_{563)}\ O_2 \rightarrow (2b_{514}\beta\text{-}1)CO_2$$

$$+(2\text{-}2b_{514}\beta)CO + \frac{b_{531}}{2} H_2O + b_{546}NO + b_{563}SO_2 \qquad (R9)$$

$$\text{Wet} - \text{Carbonaceous} - \text{Solid} \Leftrightarrow \text{Dry} - \text{Carbonaceous} - \text{Solid} + H_2O \qquad (R10)$$

$CaCO_3 \Leftrightarrow CaO + CO_2$ (R21)

$2CaO + 2SO_2 + O_2 \Leftrightarrow 2CaSO_4$ (R22)

$Wet - Limestone \Leftrightarrow Dry - Limestone + H_2O$ (R23)

$Wet - Inert - Solid \Leftrightarrow Dry - Inert - Solid + H_2O$ (R31)

$CO + H_2O \Leftrightarrow CO_2 + H_2$ (R41)

$2CO + O_2 \Leftrightarrow 2CO_2$ (R42)

$2H_2 + O_2 \Leftrightarrow 2HO_2$ (R43)

$CH_4 + 2O_2 \Leftrightarrow CO_2 + 2H_2O$ (R44)

$C_2H_6 + 7O_2 \Leftrightarrow 4CO_2 + 6H_2O$ (R45)

$4NH_3 + 5O_2 \Leftrightarrow 4NO + 6H_2O$ (R46)

$2H_2S + 3O_2 \Leftrightarrow 2SO_2 + 2H_2O$ (R47)

$N_2 + O_2 \Leftrightarrow 2NO$ (R48)

$$Tar(or\ oil) + (b_{514}\beta + \frac{b_{531}}{4} + \frac{b_{551}}{2} + \frac{b_{546}}{2} + b_{563})\,O_2 \rightarrow (2b_{514}\beta\text{-}1)CO_2$$

$$+(2\text{-}2b_{514}\beta)CO + \frac{b_{531}}{2}H_2O + b_{546}NO + b_{563}SO_2 \quad \text{(R49)}$$

$Tar(or\ oil) \rightarrow b_{v,19}H_2 + b_{v,20}H_2O + b_{v,21}H_2S + b_{v,22}NH_3 + \ldots$ (R50)

$Tar\ (or\ oil) \rightarrow Coke$ (R51)

$C_2H_4 + 3O_2 \Leftrightarrow 2CO_2 + 2H_2O$ (R52)

$2C_3H_6 + 9O_2 \Leftrightarrow 6CO_2 + 6H_2O$ (R53)

$C_3H_8 + 5O_2 \Leftrightarrow 3CO_2 + 4H_2O$ (R54)

$2C_6H_6 + 15O_2 \Leftrightarrow 12CO_2 + 6H_2O$ (R55)

where a_n, b_n, c_n and β are stoichiometric coefficients.

4.2.6 Solution procedure used by the model

The first nine reactions involve the carbonaceous solid material in biomass. The basic composition is assumed to be represented by C, H, O, N, S and ash. Of particular importance to gasification are reactions 1, 3 and 41. These reactions occur at higher rates than other reactions used by the model. Reaction 1 is an exothermic reaction, which also proceeds concurrently with reaction 3, which is an endothermic reaction.

The simulation program considers the combined effects of most of the physical phenomena, which take part during the operation of gasifiers and general fluidized-bed reactors. After the data are read, calculations necessary for the solutions of differential mass and energy balances throughout the bed and the freeboard are conducted.

1. The user inputs the estimated values for conversions of components in the solid phases (other than the entered value for fixed-carbon). The program applies default values for data not provided by the user.

2. The program applies global devolatilization routines to evaluate the composition of the solid fraction.

3. The program assumes a fixed-carbon conversion where the minimum and maximum values of fractional fixed carbon converted in the bed are entered by the user. Other solid conversions are automatically set by the program.
4. The program then uses the conversion of solids and the basic model for the heterogeneous reaction model to compute the average particle size distribution in the bed for each solid species. For this an iterative process involving computations of average fluidization conditions, first values for rates of attrition, and entrainment of solids is performed.

5. Next, the boundary conditions at the base of the fluidized bed are set for the system of differential equations that describe the mass and energy balances. This step includes a procedure to compute the temperature of the solids at that point.

6. The solution of the system of non-linear differential equations is performed for the minimum and maximum fixed-carbon conversions entered as data by the user from the bottom to the top of the fluidized bed .

7. The program then verifies if the fixed-carbon conversions, obtained by integration as described in the last step, are above the minimum and below the maximum assumed fixed-carbon conversion. If not, the program stops and asks the user to start again with new minimum and maximum values of fixed-carbon conversions.

Otherwise, the computation assumes an intermediate value for the fixed-carbon conversion and returns to step (4).

8. Each time the program returns to step (4), it assumes the last computed conversions of other solid species as the new guessed values.
9. Once the convergence for fixed-carbon is achieved, the convergence for conversions of other solid species is also achieved. If not, the program would inform the user and provide instructions to set more stringent criteria for the maximum deviation of fixed-carbon conversion.

10. The program then uses the conditions of flows, compositions, and temperatures at the top of the bed as the boundary conditions for the system of differential mass and energy balances in the freeboard.

11. The program then solves the system of differential mass and energy balance in the freeboard.

12. The program then performs post-processing computations for presentation of the results.

4.3 CSFB model predictions

Data from each experimental run were input to the CSFB model. The software was used without modifications to the devolatilization or kinetics routines.

Data for reactor geometry, insulation, heat transfer between heating jacket and reactor, stream characterization including higher heating value and rate of carbonaceous feed, ultimate analysis of fuel, particle size distribution of fuel and inerts, density of fuel, sphericity of fuel and inert particles, operating pressure of reactor and fluidizing air composition were input into the model. For each of the 12 experimental runs that were modeled, roughly 50 separate simulations were performed for a total of approximately 600 individual runs. Typically, of these 50 runs, 2 would converge. It was difficult to find the best set of parameters that would allow the model to converge. The large number of runs performed for each experimental run reflect that difficulty. Only one run should be required.

Initial Model Predictions

In comparing the model to the experimental runs, without any modifications of the devolatilization or kinetics routine, the most noticeable difference was seen in the low levels of predicted energy carrier gases carbon monoxide, hydrogen and methane. Carbon monoxide, in particular, had extremely low predicted concentrations.

In some cases, when the inert material mean diameter was entered as the experimental size of 210 microns, the model had a limiting temperature above which it would not converge. For these cases, the model was run at a temperature lower than the experimental temperature but as high as possible while still converging. In other cases, the model would not converge below a temperature that was higher than the experimental temperature. In both of these cases, the temperature (produced by varying the jacket heat input) that most closely approximated the experimental conditions was used. The heat inputs shown in Tables 4.2, 4.4, 4.6, 4.8, 4.10 and 4.12 following are those yielding the best approximations to actual temperatures.
Additionally, when the experimental fuel particle size distribution was used, the model in some cases would not converge, so a modified (larger) particle size was used while keeping the same experimental distribution. This larger assigned particle size was selected based on successful runs using test cases presented by the author of the CSFB model. Later in section 4.4, a larger inert particle size was used and again based upon successful runs using test cases presented by the author of the CSFB model.

The particle size was changed (to the larger size) after careful consideration of all parameters and experimentation with modifying other model parameters. To have representative fuel energy inputs, the fuel's ultimate and proximate values were not changed. Attempts were made to adjust air flow (or air input temperature) in numerous runs but it was found that these adjustments alone did not lead to convergence. Through a process of elimination, parameters that would allow the model to converge were selected. The data presented represent the best of the various attempts after this exhaustive process of elimination took place. Fuel particle size in conjunction with temperature (by adjusting the heater input) ended up being the only way to make the model converge. In these modified runs, the experimental mass fractions (unique to each fuel) were still used but with a modified (larger) particle size associated with each fraction. This modified fuel particle size is shown in Table 4.1. The relative difference is determined solely by the difference in size between the experimental runs and the author's successful test cases with other fuels that were enclosed as examples with the model. The size – experimental or modified – used for each test is noted on the last line of the input parameters for the respective test, shown in Tables 4.2, 4.4, 4.6, 4.8, 4.10 and 4.12.

Tables 4.3, 4.5, 4.7, 4.9, 4.11 and 4.13 compare the modeled and experimental results for each of the six fuels that were tested. Relative differences are computed using the experimental values as the base case.

Table 4.1 Experimental and modified mean fuel particle sizes

Sieve size	Experimental (mm)	Modified (mm)	Relative difference (%)
10	2.00	2.54	27
14	1.40	1.81	29
20	0.85	1.27	49
40	0.425	0.635	49
100	0.150	0.254	69
PAN	0.045	0.100	122

Table 4.2 CSFB Input Parameters for ASF test 1 and 2

Parameter		
	Test 1	Test 2
Heat transfer between jacket and reactor (kW)	0.45	0.40
HHV of fuel (MJ kg^{-1})	15.1	15.1
Inerts (g)	866	866
Type of inerts	alumino silicate	alumino silicate
Carbonaceous mass flow (g s^{-1})	1.93	1.43
Inert average size (microns)	210	210
Carbonaceous temperature (K)	298	298
Apparent density (kg m^{-3})	1070	1070
True density (kg m^{-3})	1500	1500
Inlet gas flow (g s^{-1})	0.48	0.54
Inlet gas temperature (K)	293	575
Fuel particle distribution	Modified	Experimental

Table 4.3 ASF test no. 1 and 2

	Test 1			Test 2		
	CSFB	Exp.	Relative. Diff.	CSFB	Exp.	Relative Diff.
Temperature (K)	960	1023	-6	1086	923	18
Gas Constituent	Mean Conc. (% v/v)	Mean Conc. (% v/v)	(%)	Mean Conc. (% v/v)	Mean Conc. (% v/v)	(%)
H_2	3.1	13	-82	3.2	18	-82
CO	1.3	20	-92	1.7	20	-92
CH_4	2.1	7	-70	2.3	8	-71
CO_2	22.9	16	43	21.8	22	-1
N_2	69.5	43	62	70.0	32	118
O_2	0	1	-100	0	0	0
Total	98.9	100	-1	99.0	100	-1

All CSFB values have been normalized to near 100% based on exclusion of tar. Light hydrocarbons and argon make up the balance for all CSFB runs.

Table 4.4 CSFB Input Parameters for WPF test 1 and 2

Parameter		
	Test 1	Test 2
Heat transfer between jacket and reactor (kW)	0.1	0.1
HHV of fuel (MJ kg^{-1})	19.0	19.0
Inerts (g)	433	433
Type of inerts	alumino silicate	alumino silicate
Carbonaceous mass flow (g s^{-1})	1.27	1.37
Inert average size (microns)	210	210
Carbonaceous temperature (K)	298	298
Apparent density (kg m^{-3})	1010	1010
True density (kg m^{-3})	1490	1490
Inlet gas flow (g s^{-1})	0.60	0.58
Inlet gas temperature (K)	676	676
Fuel particle distribution	Experimental	Experimental

Table 4.5 WPF test no. 1 and 2

	Test 1			Test 2		
	CSFB	Exp.	Relative. Diff.	CSFB	Exp.	Relative Diff.
Temperature (K)	870	1013	-14	840	1178	-29
Gas Constituent	Mean Conc. (% v/v)	Mean Conc. (% v/v)	(%)	Mean Conc. (% v/v)	Mean Conc. (% v/v)	(%)
H_2	0.9	10	-91	1.4	12	-88
CO	0.1	22	-100	0.2	21	-99
CH_4	1.3	7	-81	1.7	8	-79
CO_2	23.3	16	46	24.5	17	44
N_2	73.2	42	74	70.7	41	72
O_2	0	3	-100	0	1	-100
Total	98.8	100	-1	98.5	100	-1

Table 4.6 CSFB Input Parameters for RSF test 1 and 2

Parameter		
	Test 1	Test 2
Heat transfer between jacket and reactor (kW)	0.05	0.07
HHV of fuel (MJ kg^{-1})	14.8	14.8
Inerts (g)	663	639
Type of inerts	alumino silicate MgO (67 % w/w)	Alumino silicate MgO (87.5 % w/w)
Inert average size (microns)	210	210
Carbonaceous mass flow (g s^{-1})	0.84	0.75
Carbonaceous temperature (K)	298	298
Apparent density (kg m^{-3})	940	940
True density (kg m^{-3})	1440	1440
Inlet gas flow (g s^{-1})	0.60	0.55

Inlet gas temperature (K)	575	673
Fuel particle distribution	Experimental	Modified

Table 4.7 RSF test no. 1 and 2

	Test 1			Test 2		
	CSFB	Exp.	Relative. Diff.	CSFB	Exp.	Relative Diff.
Temperature (K)	1047	1058	-1	1114	1068	4
Gas Constituent	Mean Conc. (% v/v)	Mean Conc. (% v/v)	(%)	Mean Conc. (% v/v)	Mean Conc. (% v/v)	(%)
H_2	0.0	4	-100	2.3	9	-74
CO	0.2	10	-98	3.5	17	-79
CH_4	0.6	4	-85	2.1	4	-48
CO_2	22.8	13	75	22.3	19	17
N_2	74.9	64	17	68.1	48	42
O_2	0	3	-100	0	5	-100
Total	98.5	98	0	99.1	102	-3

Table 4.8 CSFB Input Parameters for WWF test 1 and 2

Parameter		
	Test 1	Test 2
Heat transfer between jacket and reactor (kW)	0	0
HHV of fuel (MJ kg^{-1})	20.4	20.4
Inerts (g)	866	433
Type of inerts	alumino silicate	Alumino silicate
Inert average size (microns)	210	210
Carbonaceous mass flow (g s^{-1})	0.38	0.51
Carbonaceous temperature (K)	298	298
Apparent density (kg m^{-3})	1040	1040
True density (kg m^{-3})	1430	1430
Inlet gas flow (g s^{-1})	0.55	0.55
Inlet gas temperature (K)	350	350

Fuel particle distribution	Modified	Experimental

Table 4.9 WWF test no. 1 and 2

	Test 1			Test 2		
	CSFB	Exp.	Relative. Diff.	CSFB	Exp.	Relative Diff.
Temperature (K)	1271	1098	16	1167	1073	9
Gas Constituent	Mean Conc. (% v/v)	Mean Conc. (% v/v)	(%)	Mean Conc. (% v/v)	Mean Conc. (% v/v)	(%)
H_2	1.3	13	-90	1.0	8	-88
CO	3.6	15	-76	1.9	18	-89
CH_4	3.0	5	-40	2.1	5	-59
CO_2	24.0	13	85	23.7	11	115
N_2	67.3	46	25	70.0	56	25
O_2	0	1	-100	0	2	-100
Total	99.2	93	6	98.7	100	-1

Table 4.10 CSFB Input Parameters for SLF test 1 and 2

Parameter		
	Test 1	Test 2
Heat transfer between jacket and reactor (kW)	0.7	0.7
HHV of fuel (MJ kg^{-1})	15.4	15.4
Inerts (g)	866	1299
Type of inerts	alumino silicate	alumino silicate
Inert average size (microns)	210	210
Carbonaceous mass flow (g s^{-1})	1.36	2.08
Carbonaceous temperature (K)	298	298
Apparent density (kg m^{-3})	1490	1490
True density (kg m^{-3})	1520	1520
Inlet gas flow (g s^{-1})	0.44	0.55
Inlet gas temperature (K)	575	599
Fuel particle distribution	Experimental	Experimental

Table 4.11 SLF test no. 1 and 2

	Test 1			Test 2		
	CSFB	Exp.	Relative. Diff.	CSFB	Exp.	Relative Diff.
Temperature (K)	938	948	-10	766	1008	-24
Gas Constituent	Mean Conc. (% v/v)	Mean Conc. (% v/v)	(%)	Mean Conc. (% v/v)	Mean Conc. (% v/v)	(%)
H_2	0.1	21	-99	0.0	15	-100
CO	0.0	15	-100	0.2	11	-98
CH_4	0.1	8	-99	0.1	6	-98
CO_2	17.4	11	58	18.6	10	14
N_2	80.8	44	84	78.4	55	42
O_2	0	1	-100	0	2	-100
Total	98.4	100	-2	97.3	99	-2

Table 4.12 CSFB Input Parameters for NPF test 1 and 2

Parameter		
	Test 1	Test 2
Heat transfer between jacket and reactor (kW)	0	0
HHV of fuel (MJ kg^{-1})	18.8	18.8
Inerts (g)	433	433
Type of inerts	alumino silicate	alumino silicate
Inert average size (microns)	210	210
Carbonaceous mass flow (g s^{-1})	0.32	0.38
Carbonaceous temperature (K)	298	298
Apparent density (kg m^{-3})	1300	1300
True density (kg m^{-3})	1490	1490
Inlet gas flow (g s^{-1})	0.49	0.49
Inlet gas temperature (K)	500	500
Fuel particle distribution	Modified	Modified

Table 4.13 NPF test no. 1 and 2

	Test 1			Test 2		
	CSFB	Exp.	Relative. Diff.	CSFB	Exp.	Relative Diff.
Temperature (K)	1042	1073	-3	1071	1073	2
Gas Constituent	Mean Conc. (% v/v)	Mean Conc. (% v/v)	(%)	Mean Conc. (% v/v)	Mean Conc. (% v/v)	(%)
H_2	1.0	8	-88	1.2	7	-83
CO	1.8	21	-91	1.9	20	-91
CH_4	1.1	6	-82	1.0	5	-80
CO_2	20.5	13	58	22.2	13	71
N_2	74.5	50	49	72.6	53	45
O_2	0	1	-100	0	1	-100
Total	98.9	99	0	98.9	99	0

CSFB predictions for energy carrier gases

The range of predictions for hydrogen was approximately 0 % to 2.3 % v/v. The range of predictions for carbon monoxide were approximately 0 % to 3.6 % v/v, and the range of predictions for methane were approximately 0 % to 3.0 % v/v. In all cases the model fails to adequately predict gas composition.

In Figures 4.1 through 4.3 are plotted the CSFB-predicted producer gas levels for all 12 runs versus the experimental gas levels. A 1:1 line is shown for comparison. All graphs show the low predicted levels.

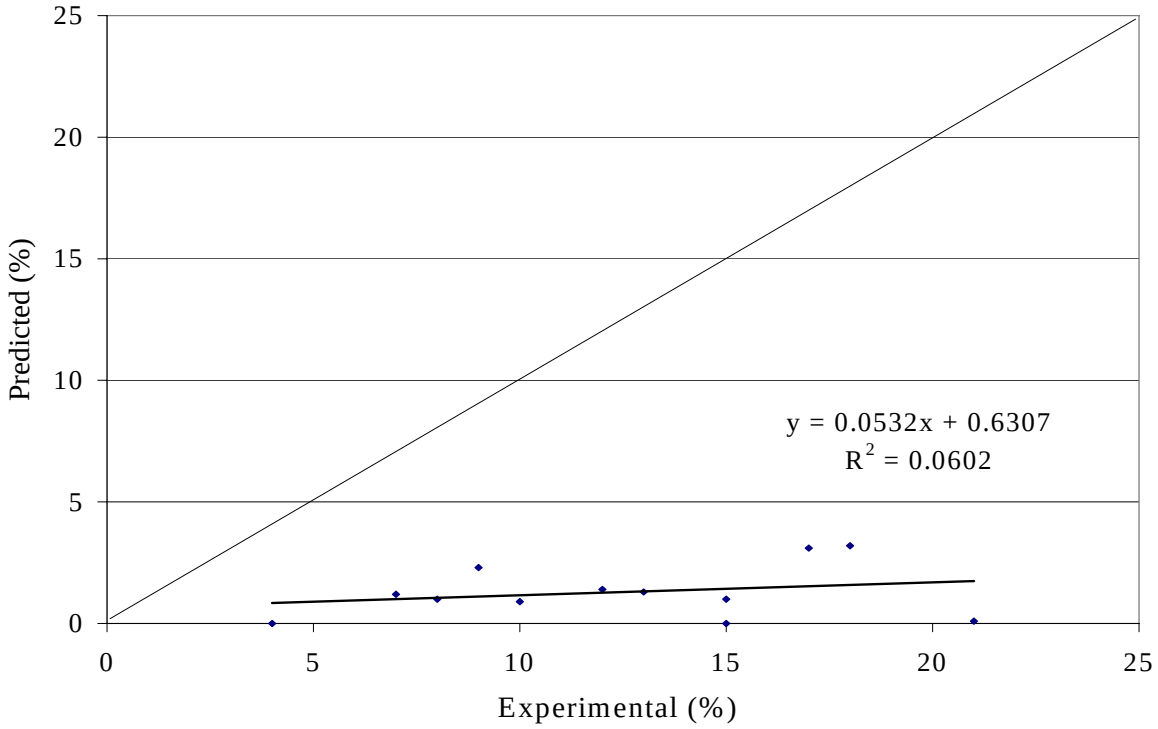

Figure 4.1 CSFB predicted versus experimental for H_2

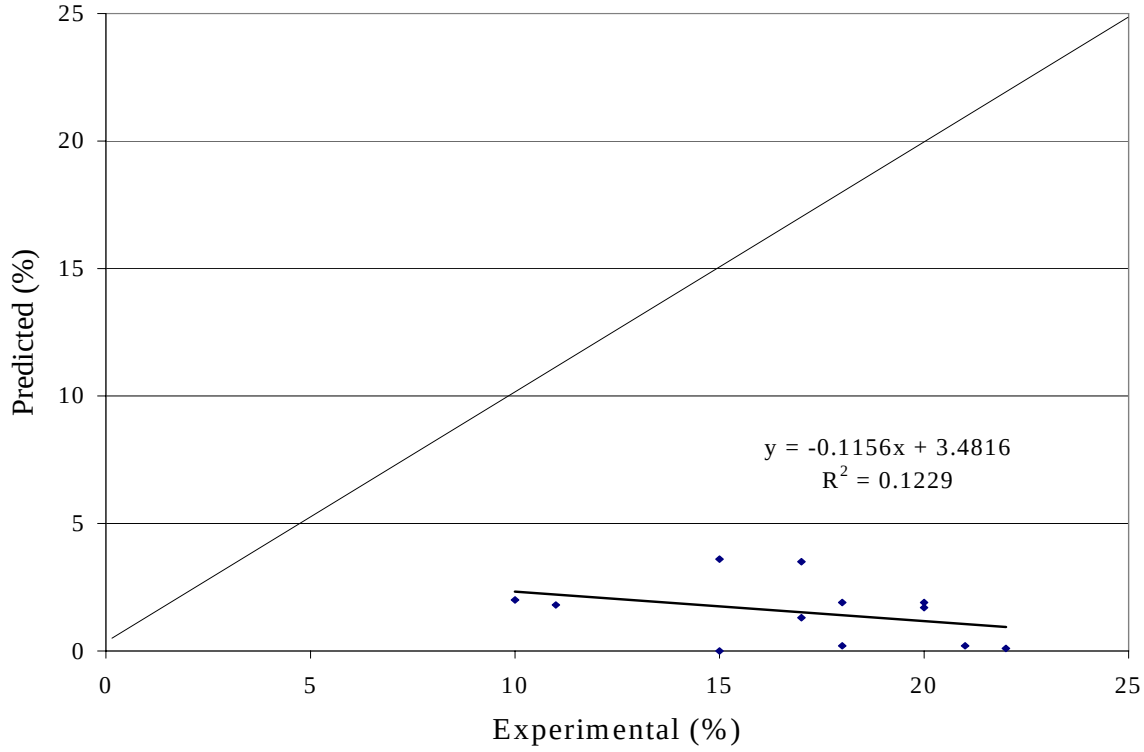

Figure 4.2 CSFB predicted versus experimental for CO

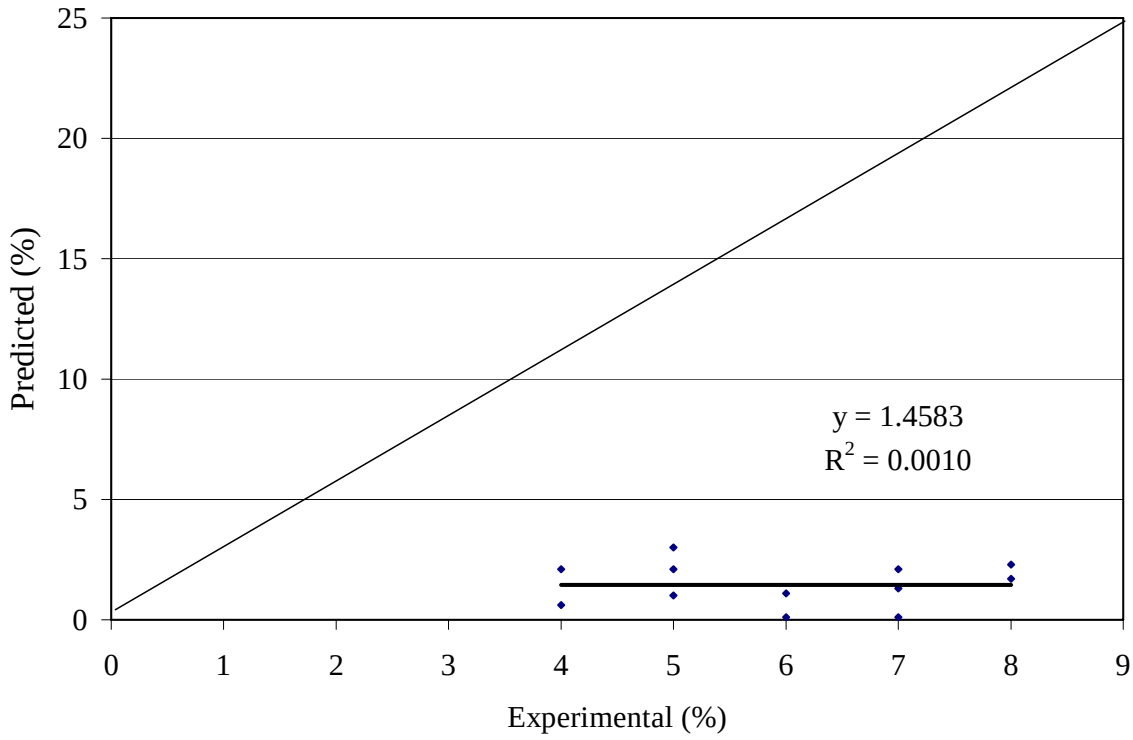

Figure 4.3 CSFB predicted versus experimental for CH_4

4.4 CSFB Sensitivity Analysis

Because CSFB initially predicted the gas concentrations at much lower levels than the experimental runs, sensitivity analysis was conducted to determine if increasing temperature and increasing inert size would make an appreciable difference.

Increasing fuel size

As described in section 4.3, the larger fuel particle size was used again so the model would converge.

Increasing temperature

With all fuels, when the temperature of a given run using the CSFB model was artificially increased through applying a higher amount of external heating on the bed, the levels of all energy carrier gases increased. In some instances, if the temperature were increased high enough (typically about 200 to 350 °C above experimental conditions) the experimental concentrations were more closely predicted or even matched. In other instances, when the temperature was increased in the range of 200 to 350 °C, the model would not converge.

Increasing inert size

For some fuel runs, the model would not converge above a given temperature that was in some cases lower than the experimental temperature. For all follow-on sensitivity runs, the inert material was artificially increased to allow running at higher than experimental temperatures to see how the CSFB model responded to elevated temperatures. The fuel particle sizes, identified earlier in this chapter as "modified" (See Table 4.1) were also used with all sensitivity runs to allow establishing data points at higher temperatures and also to allow the model to converge. The revised larger inert distribution is shown in Table 4.14. Tables 4.15 through 4.20 represent the CSFB producer gas values predicted at higher temperatures and with an overall larger inert distribution. The experimental runs are included in the tables for comparison.

Table 4.14 Revised inert particle size distribution

Actual Mean Inert Particle Size [mm]	Revised Mean Inert Particle Size [mm]	Revised Inert Particle Size [mm]	Percent of Total [%]
0.210	0.295	0.420	0.3
		0.350	54.4
		0.297	37.1
		0.250	7.8
		0.210	0.3

	0.177	0.1

This particular size distribution was selected because it was one well tested by the model's author and allowed convergence at higher temperatures with all fuels. The revised inert distribution from Table 4.14 has an approximately 40% larger inert geometric mean compared to the experimental geometric mean value of 0.210 mm.

Table 4.15 ASF test no. 1 and 2 with increased temperature, increased fuel particle size and increased inert size

	Test 1			Test 2		
	CSFB with increased temperature and inert size	Exp.	Relative. Diff.	CSFB with increased temperature and inert size	Exp.	Relative Diff.
Temperature (K)	1157	1023	3	1267	973	30
Gas Constituent	Mean Conc. (% v/v)	Mean Conc. (% v/v)	(%)	Mean Conc. (% v/v)	Mean Conc. (% v/v)	(%)
H_2	10.2	13	-40	13.0	18	-28
CO	6.9	20	-59	16.7	20	-17
CH_4	6.0	7	-14	10.7	8	34
CO_2	20.8	16	30	20.1	22	-9
N_2	53.0	43	23	38.8	32	21
O_2	0	1	-100	0	0	0
Total	96.9	100	-3	99.3	100	-1

All CSFB values have been normalized to near 100% based on exclusion of tar. Light hydrocarbons and argon make up the balance for all CSFB runs. The above temperatures provided the closest gas predictions to the experimental values while still allowing the model to converge. Increased fuel particle size means using the modified size are indicated in Table 4.1.

Table 4.16 WPF test no. 1 and 2 with increased temperature, increased fuel particle size and increased inert size

	Test 1			Test 2		
	CSFB with increased temperature and inert size	Exp.	Relative. Diff.	CSFB with increased temperature and inert size	Exp.	Relative Diff.
Temperature (K)	1171	1013	16	983	1178	-17
Gas Constituent	Mean Conc. (% v/v)	Mean Conc. (% v/v)	(%)	Mean Conc. (% v/v)	Mean Conc. (% v/v)	(%)
H_2	12.9	10	29	12.1	12	1
CO	11.1	22	-50	9.6	21	-54
CH_4	6.4	7	-9	6.4	8	-25
CO_2	22.2	16	39	19.3	17	12
N_2	42.6	42	1	51.2	41	25
O_2	0	3	-100	0	1	-100
Total	95.3	100	-4	98.6	100	-1

Table 4.17 RSF test no. 1 and 2 with increased temperature, increased fuel particle size and increased inert size

	Test 1			Test 2		
	CSFB with increased temperature and inert size	Exp.	Relative. Diff.	CSFB with increased temperature and inert size	Exp.	Relative Diff.
Temperature (K)	1213	1058	15	1148	1068	7
Gas Constituent	Mean Conc. (% v/v)	Mean Conc. (% v/v)	(%)	Mean Conc. (% v/v)	Mean Conc. (% v/v)	(%)
H_2	11.4	4	185	4.9	9	-46
CO	15.8	10	58	6.8	17	-60
CH_4	8.9	4	123	3.1	4	-23
CO_2	19.6	13	51	18.7	19	-2
N_2	42.1	64	-34	63.8	48	33
O_2	0	3	-100	0	5	-100
Total	97.8	98	0	97.2	102	-5

Table 4.18 WWF test no. 1 and 2 with increased temperature, increased fuel particle size and increased inert size

	Test 1			Test 2		
	CSFB with increased temperature and inert size	Exp.	Relative. Diff.	CSFB with increased temperature and inert size	Exp.	Relative Diff.
Temperature (K)	1258	1098	15	1111	1073	4
Gas Constituent	Mean Conc. (% v/v)	Mean Conc. (% v/v)	(%)	Mean Conc. (% v/v)	Mean Conc. (% v/v)	(%)
H_2	7.8	13	-40	2.5	8	-70
CO	11.1	15	-26	2.3	18	-87
CH_4	2.4	5	-52	0	5	-100
CO_2	17.0	13	31	21.6	11	97
N_2	59.5	46	29	72.4	56	29
O_2	0	1	-100	0	2	-100
Total	97.8	93	5	95.8	100	-4

Table 4.19 SLF test no. 1 and 2 with increased temperature, increased fuel particle size and increased inert size

	Test 1			Test 2		
	CSFB with increased temperature and inert size	Exp.	Relative. Diff.	CSFB with increased temperature and inert size	Exp.	Relative Diff.
Temperature (K)	1240	948	31	1172	1008	16
Gas Constituent	Mean Conc. (% v/v)	Mean Conc. (% v/v)	(%)	Mean Conc. (% v/v)	Mean Conc. (% v/v)	(%)
H_2	16.5	21	-21	8.8	15	-41
CO	13.1	15	-13	6.5	11	-41
CH_4	4.7	8	-33	1.8	6	-70
CO_2	14.2	11	29	16.2	10	62
N_2	51.1	44	16	64.7	55	18
O_2	0	1	-100	0	2	-100
Total	99.6	100	0	98.0	99	-1

Table 4.20 NPF test no. 1 and 2 with increased temperature, increased fuel particle size and increased inert size

	Test 1			Test 2		
	CSFB with increased temperature and inert size	Exp.	Relative. Diff.	CSFB with increased temperature and inert size	Exp.	Relative Diff.
Temperature (K)	1189	1073	11	1095	1073	2
Gas Constituent	Mean Conc. (% v/v)	Mean Conc. (% v/v)	(%)	Mean Conc. (% v/v)	Mean Conc. (% v/v)	(%)
H_2	2.9	8	-63	3.8	7	-45
CO	8.0	21	-62	0.5	20	-97
CH_4	2.7	6	-55	1.2	5	-77
CO_2	18.0	13	39	21.2	13	63
N_2	67.1	50	34	72.1	53	36
O_2	0	1	-100	0	1	-100
Total	98.7	99	0	98.8	99	0

Values predicted by CSFB in Tables 4.15 through 4.20 were taken and plotted for each individual fuel in Figures 4.14 through 4.19. The rather dramatic increase in predicted gas concentrations for CO, H_2, and CH_4 can be seen in each Figure.

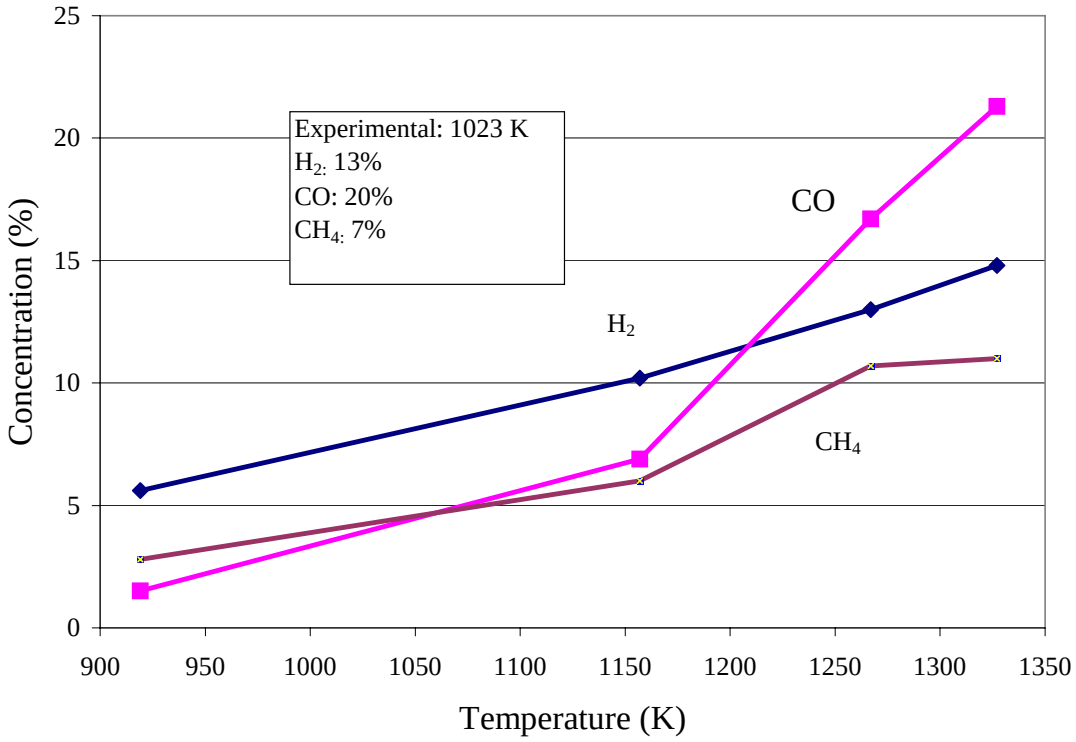

Figure 4.4 CSFB predictions for ASF for increased inert particle size, increased fuel particle size and increased temperature.

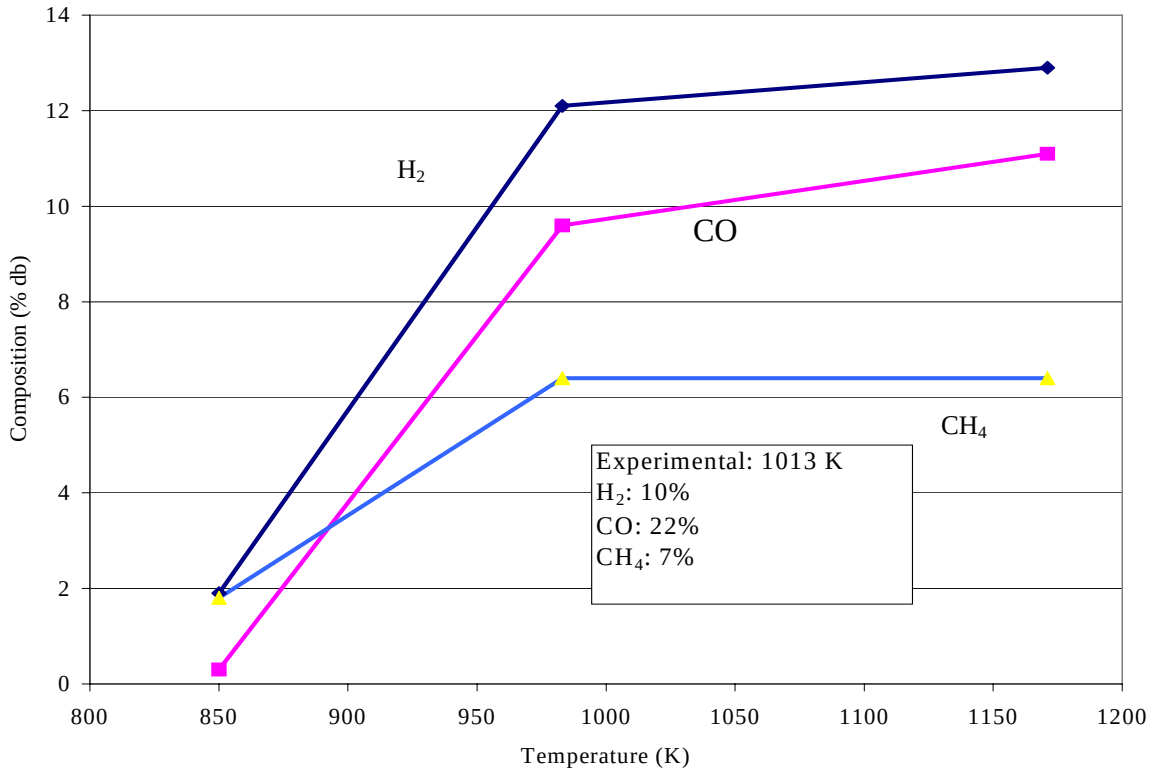

Figure 4.5 CSFB predictions for WPF for increased inert particle size, increased fuel particle size and increased temperature

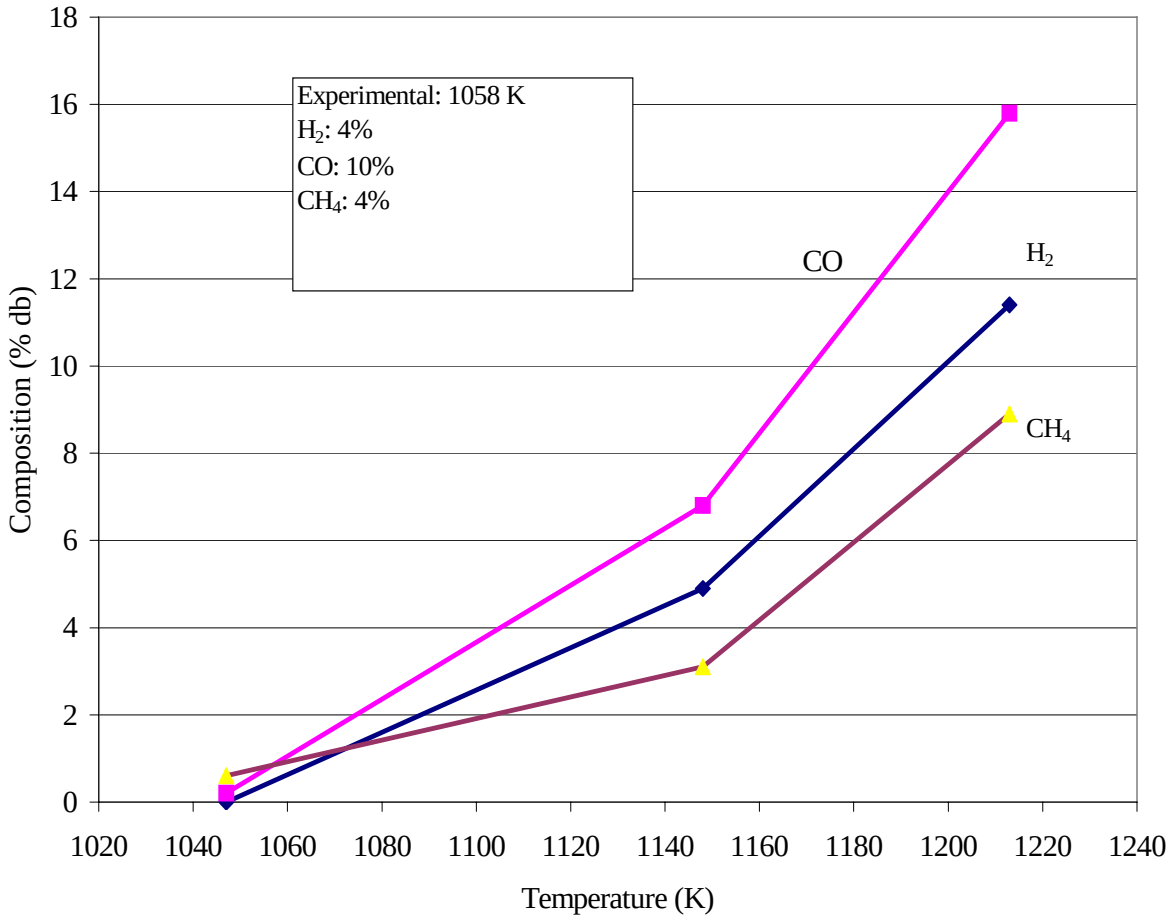

Figure 4.6 CSFB predictions for RSF for increased inert particle size, increased fuel particle size and increased temperature

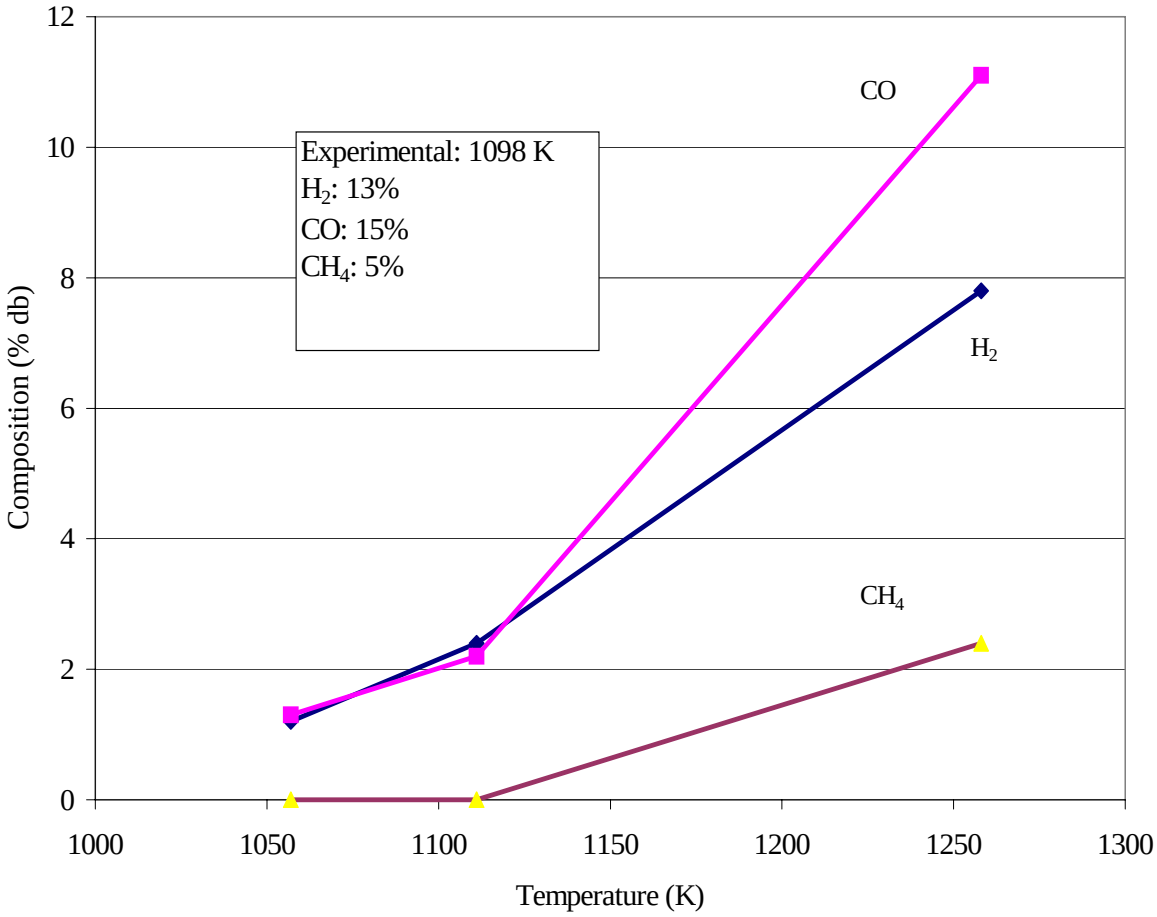

Figure 4.7 CSFB predictions for WWF for increased inert particle size, increased fuel particle size and increased temperature

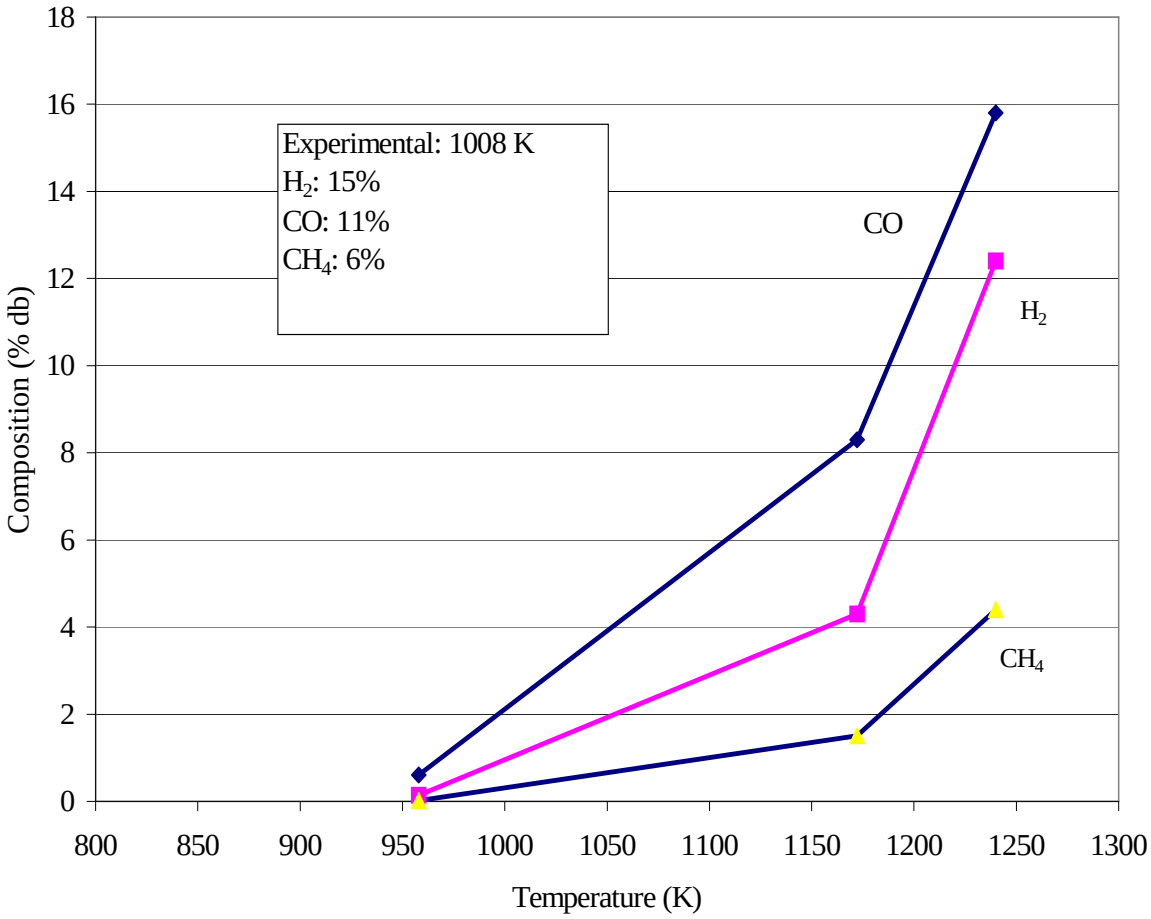

Figure 4.8 CSFB predictions for SLF for increased inert particle size, increased fuel particle size and increased temperature

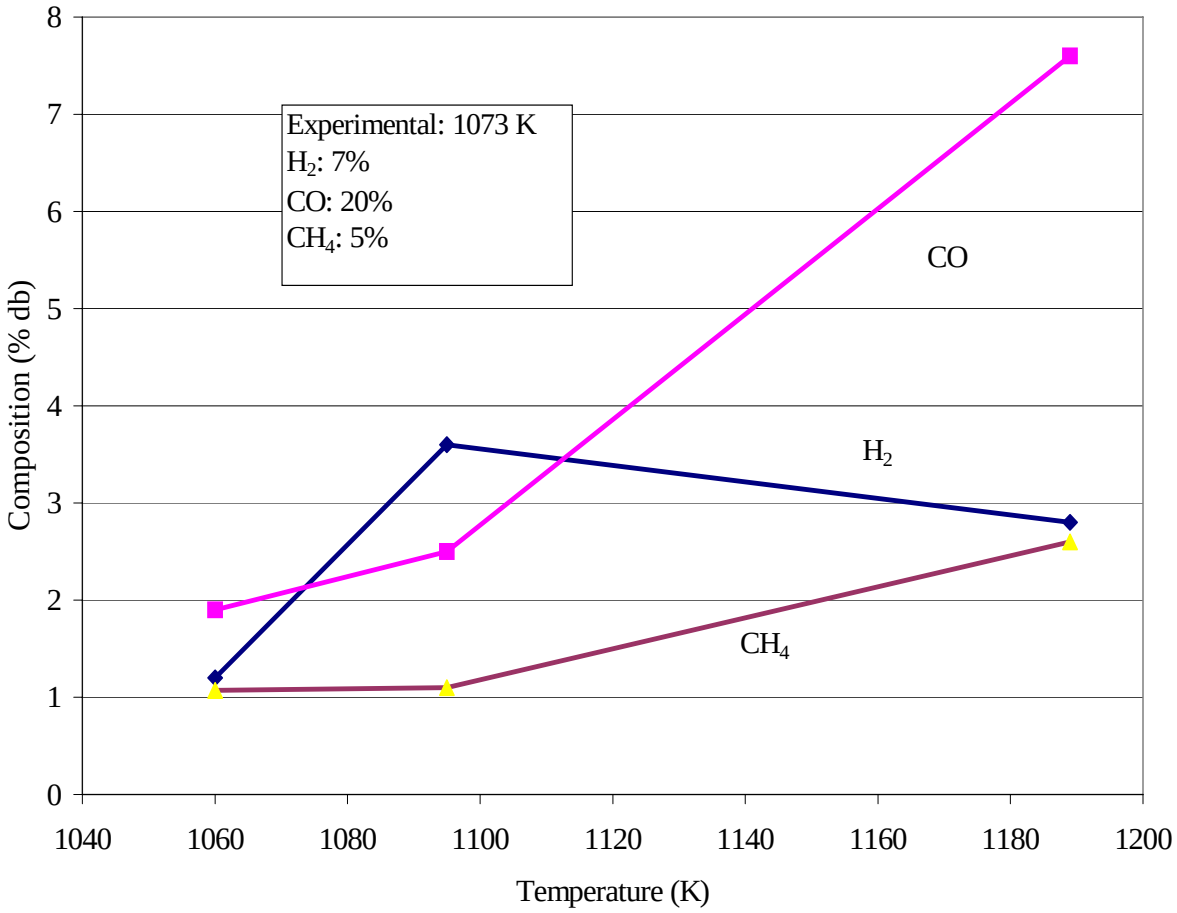

Figure 4.9 CSFB predictions for NPF for increased inert particle size, increased fuel particle size and increased temperature

4.5 Modified CSFB Routine

Towards the end of this project, a modification (patch) was received from the author of CSFB version 3.5. Although none of the changes were disclosed, the patch appeared to eliminate the tar fraction and redirect the former tar output into other gases. Using the actual experimental data from the first set of runs in section 4.3, the modified model was used to predict the various gas species of interest. Of the 12 runs, 6 converged and had results that were better but still off.

Runs that would not converge are as follows:
WPF tests 1 and 2, RSF test 2, WWF test 1 and 2 and, NPF test 1

General error messages reported by CSFB for runs not converging (with both the original version and the modified one) were varied but primarily included the following (CSFB, Technologix Corporation, Chicago, Il. (de Souza-Santos, 2001)):
-"The integration of differential equations failed because the problem may be very stiff" (i.e. difficult to solve numerically).
-"The bubble diameter is the same as the equipment diameter."
-"Increase the average particle size of inerts or other solids present in the process."
-"Verification of the high heat value set for the feeding carbonaceous has shown a probability of mistake during data input."
-"The search is not progressing well. Try new initial guesses for fixed carbon conversion."
-"Transport disengagement height is greater than the freeboard height."
-"Problems with elemental mass verification encountered."
Tables 4.21 through 4.23 show the results for the runs that converged on a solution.

Table 4.21 ASF test no. 1 and 2 with patch

	Test 1			Test 2		
	CSFB patch	Exp.	Relative. Diff.	CSFB patch	Exp.	Relative Diff.
Temperature (K)	1187	1023	16	1101	923	19
Gas Constituent	Mean Conc. (% v/v)	Mean Conc. (% v/v)	(%)	Mean Conc. (% v/v)	Mean Conc. (% v/v)	(%)
H_2	6.1	13	-54	13.2	18	-27
CO	11.4	20	-43	12.5	20	-38
CH_4	9.0	7	29	13	8	63
CO_2	20.9	16	31	23.9	22	9
N_2	51.0	43	19	34.8	32	9

O_2	0	1	-100	0	0	0
Total	98.4	100	-1	97.4	100	-3

Light hydrocarbon and argon makeup the balance of CSFB output. Unlike the original version of the model, the output of the patch did not contain a tar fraction.

Table 4.22 RSF test no. 1 with patch

	Test 1		
	CSFB patch	Exp.	Relative. Diff.
Temperature (K)	1074	1058	2
Gas Constituent	Mean Conc. (% v/v)	Mean Conc. (% v/v)	(%)
H_2	8.1	4	103
CO	8.7	10	-13
CH_4	8.5	4	113
CO_2	22.8	13	75
N_2	50.8	64	21
O_2	0	3	-100
Total	98.9	98	1

Table 4.23 SLF test no. 1 and 2 with patch

	Test 1			Test 2		
	CSFB patch	Exp.	Relative. Diff.	CSFB patch	Exp.	Relative Diff.
Temperature (K)	1027	948	8	961	1008	-5
Gas Constituent	Mean Conc. (% v/v)	Mean Conc. (% v/v)	(%)	Mean Conc. (% v/v)	Mean Conc. (% v/v)	(%)
H_2	6.8	21	-68	3.3	15	-78
CO	2.2	15	-85	0.7	11	-94
CH_4	5.8	8	-25	5.8	6	-13
CO_2	20.8	11	91	22.1	10	121

N_2	62.5	44	42	66.7	55	21
O_2	0	1	-100	0	2	-100
Total	98.1	100	-1	98.6	99	0

Table 4.24 NPF test no. 2 with patch

	Test 2		
	CSFB patch	Exp.	Relative Diff.
Temperature (K)	1148	1073	7
Gas Constituent	Mean Conc. (% v/v)	Mean Conc. (% v/v)	(%)
H_2	5.8	7	-17
CO	9.5	20	-53
CH_4	8.4	5	68
CO_2	21.5	13	65
N_2	53.5	53	1
O_2	0	1	-100
Total	98.7	99	0

4.6 STANJAN Equilibrium Predictions

Experimental data were also compared against predictions from the STANJAN equilibrium solver (Reynolds, 1986) to see how experimental results compared to equilibrium concentrations.

STANJAN uses the element-potential method for chemical equilibrium analysis. STANJAN accomplishes this by relating the phase mole fraction of each individual species to its minimum value of Gibbs free energy, to the atomic make-up of its molecule, and to a set of undetermined multipliers (the Lagrange multipliers) to be determined from the atomic constraints. The multiplier λ_i is called the element potential for i atoms and hence λ_i represents the minimum Gibbs free energy per mole of i atoms as described in equation 4-1 (Reynolds, 1986).

$$\frac{\bar{g}_j}{RT} = \sum_{i=1}^{a} \lambda_i n_{ij} \qquad [4\text{-}1]$$

where

$\bar{g}_j$ = the Gibbs free energy of species j [J]
R = universal gas constant [kJ $kmol^{-1}$ K^{-1}]
T = absolute temperature [K]
j = species
i = atom in the system
n_{ij} = number of i atoms in molecule j

The STANJAN routine provides a means for solving complicated problems involving one or more phases. There is one element for each independent atom in the system, and element potentials, plus the total number of moles in each phase, are the only variables that must be adjusted for the solution. In large problems, this is a much smaller number than the number of species, and hence far fewer variables need be adjusted. The program assumes ideal gas behavior and ideal solutions in the condensed phases.

Basic Solution Procedure Used by STANJAN

1. STANJAN allows the user to select the species data file. All runs in this study used the COMB.SUD species data file which includes the following species: C, C(s), CH_4, CO, CO_2, C_3H_8, H, HO, H_2, H_2O, H_2O(l), N, NO, NO_2, N_2, N_2O, O, O_2, and O_3.

2. The STANJAN program then allows the user to select the desired species (generally a subset of what is included in the COMB.SUD data file) to be included in each phase of the reactant system.

3. STANJAN then allows the user to specify the moles of each species in each phase of the reactants.

4. STANJAN then obtains the state parameters from the user. The state is defined by two parameters in one of a number of ways, including:
i) temperature and pressure,
ii) pressure and entropy,
iii) enthalpy and pressure,
iv) volume and entropy.
In all runs conducted for this study, temperature and pressure were used to define the thermodynamic state.

5. The STANJAN program takes data from the JANAF tables and then solves for the equilibrium state using Lagrange multipliers and the method of element potentials (Powell and Sarner, 1959; Reynolds, 1986). The above references provide detailed information on element potentials and the method of Lagrange multipliers.

6. The program requires the user to specify species in the products. For all runs, the program option to include all gas species for the products was specified.

7. STANJAN solves for the equilibrium product composition based on the populations and the state.

Before running the STANJAN routine, the atom populations were determined for each individual experimental test run. The test run atom populations had both ash and sulfur content removed. Ash and sulfur compounds were not included in the species thermochemical data file employed in this case, so they were removed so that only atoms recognized by the model were available for reactions. Table 4.25 lists the atom populations for each of the runs that were entered into the STANJAN code. All atom populations have been normalized on carbon.

Table 4.25 Experimental atom populations used with STANJAN (atoms (C, H, N and O)/atoms C)

	Biomass Fuels											
Atom(s) Involved In Reactions	ASF		WPF		RSF		WWF		SLF		NPF	
	Test 1	Test 2	Test 1	Test 2	Test 1	Test 2	Test 1	Test 2	Test 1	Test 2	Test 1	Test 2
C	1.00	1.00	1.00	1.00	1.00	1.00	1.00	1.00	1.00	1.00	1.00	1.00
H	1.66	1.66	1.55	1.55	1.32	1.32	0.96	1.00	1.79	1.79	1.42	1.42
N	0.51	0.76	0.77	0.68	1.31	1.36	1.98	1.52	0.78	0.66	2.17	1.88
O	0.98	1.05	1.12	1.10	1.16	1.18	1.23	1.13	0.64	0.64	1.35	1.27

Table 4.26 Example calculation of atom population for ASF

	ASF	
	Test 1	
Dry Fuel Analysis (% dry basis)		
C	36.27	
H	3.94	
N	0.79	
O	32.38	
S	0.05	
Ash	26.57	
Cl	-	
Fuel Consumption rate (g/min, wet basis)	115.7	
Fuel Moisture (% wet basis)	9.0	
Fuel Consumption rate (g/min, dry basis)	105.3	
Moisture rate (g/min) (db)	10.4	
Air Rate (g/min)	28.8	
Mol. Wts.		
C	12.011	
H	1.0079	
N	14.0067	
O	15.9994	
Air Fractions (vol %)		
O_2	21.00	
N_2	79.00	
Mol. Wt. of Air	28.85033	
Air Fractions (mass %)		
O_2	0.232918 x 100	
N_2	0.767082 x 100	
Atom Populations (moles of each atom)		Normalized on C
C	3.18	1
H	5.27	1.66
N	1.65	0.51
O	3.13	0.98

Equations for C, H, N and O are as follows:

$$C = \frac{36.27}{100} * \frac{\dot{m}_{f(db)}}{12.011}$$

$$H = \frac{3.94}{100} * \frac{\dot{m}_{f(db)}}{1.0079} + \frac{Moisture(\%)}{(2(1.0079) + 15.9994) * 2}$$

$$N = \frac{0.79}{100} * \frac{\dot{m}_{f(db)}}{14.0067} + \frac{0.79 * \dot{m}_{a(db)}}{14.0067}$$

$$O = \frac{32.38}{100} * \frac{\dot{m}_{f(db)}}{15.9994} + \frac{Moisture(\%)}{(2(1.0079) + 15.9994)} + \frac{0.21 * \dot{m}_{a(db)}}{15.9994}$$

where

$\dot{m}_{f(db)}$ = Mass flow rate of fuel (dry basis) [g s-1]

$\dot{m}_{a(db)}$ = Mass flow rate of air (dry basis) [g s-1]

Moisture (%) = Percent moisture in the fuel and the constants are molecular weights or convert from percent to ratio. Note that all calculations assume dry air, and that steady state fuel mass flow rate, air flow rate and moisture content were different for each fuel tested.

Tables 4.27 through 4.31 list the equilibrium gas concentrations predicted by the STANJAN code. All equilibrium gas concentrations were run at 1 atm pressure and utilize the experimental peak temperature.

Table 4.27 STANJAN ASF tests no. 1 and 2

	Test 1			Test 2		
	STANJAN	Exp.	Relative. Diff.	STANJAN	Exp.	Relative Diff.
Temperature (K)	1023	1023	0	973	973	0
Gas Constituent	Mean Conc. (% v/v)	Mean Conc. (% v/v)	(%)	Mean Conc. (% v/v)	Mean Conc. (% v/v)	(%)
H_2	34.6	13	166	33.8	18	88
CO	46.4	20	132	42.9	20	114
CH_4	3.7	7	-47	2.0	8	-75
CO_2	1.9	16	-88	2.7	22	-88
N_2	13.4	43	-69	18.3	32	-43
O_2	0	1	0	0	0	0
Total	100.0	100	0	99.8	100	0

Table 4.28 STANJAN WPF tests no. 1 and 2

	Test 1			Test 2		
	STANJAN	Exp.	Relative. Diff.	STANJAN	Exp.	Relative Diff.
Temperature (K)	1013	1013	0	1078	1078	0
Gas Constituent	Mean Conc. (% v/v)	Mean Conc. (% v/v)	(%)	Mean Conc. (% v/v)	Mean Conc. (% v/v)	(%)
H_2	32.45	10	223	34.9	12	191
CO	42.7	22	94	45.5	21	117
CH_4	1.4	7	-79	0.0	8	-100
CO_2	4.7	16	-71	3.1	17	-82
N_2	18.8	42	-55	16.8	41	-59
O_2	0	3	-100	0	1	-100
Total	99.9	100	0	100.0	99	1

Table 4.29 STANJAN RSF tests no. 1 and 2

	Test 1			Test 2		
	STANJAN	Exp.	Relative. Diff.	STANJAN	Exp.	Relative Diff.
Temperature (K)	1058	1058	0	1068	1068	0
Gas Constituent	Mean Conc. (% v/v)	Mean Conc. (% v/v)	(%)	Mean Conc. (% v/v)	Mean Conc. (% v/v)	(%)
H_2	26.3	4	557	25.8	9	187
CO	39.6	10	296	39.0	17	129
CH_4	<0.1	4	-100	<0.1	4	-100
CO_2	4.6	13	-64	4.9	19	-74
N_2	29.1	64	-54	29.8	48	-38
O_2	0	3	-100	0	5	-100
Total	99.6	98	2	99.6	102	2

Table 4.30 STANJAN WWF tests no. 1 and 2

	Test 1			Test 2		
	STANJAN	Exp.	Relative. Diff.	STANJAN	Exp.	Relative Diff.
Temperature (K)	1098	1098	0	1073	1073	0
Gas Constituent	Mean Conc. (% v/v)	Mean Conc. (% v/v)	(%)	Mean Conc. (% v/v)	Mean Conc. (% v/v)	(%)
H_2	16.9	13	30	20.5	8	156
CO	35.2	15	135	40.9	18	127
CH_4	<0.1	5	-100	<0.1	5	-100
CO_2	6.5	13	-50	4.1	11	-63
N_2	41.3	46	-10	34.3	56	-39
O_2	0	1	-100	0	2	-100
Total	99.9	93	7	99.8	100	0

Table 4.31 STANJAN SLF tests no. 1 and 2

	Test 1			Test 2		
	STANJAN	Exp.	Relative. Diff.	STANJAN	Exp.	Relative Diff.
Temperature (K)	948	948	0	1008	1008	0
Gas Constituent	Mean Conc. (% v/v)	Mean Conc. (% v/v)	(%)	Mean Conc. (% v/v)	Mean Conc. (% v/v)	(%)
H_2	10.3	21	-51	7.2	15	-52
CO	40.6	15	171	42.1	11	283
CH_4	23.7	8	196	27.6	6	360
CO_2	0.2	11	-98	<0.1	10	-100
N_2	25.1	44	-43	23.0	55	-58
O_2	0	1	100	0	2	-100
Total	99.8	100	0	99.9	99	1

Table 4.32 STANJAN NPF tests no. 1 and 2

	Test 1			Test 2		
	STANJAN	Exp.	Relative. Diff.	STANJAN	Exp.	Relative Diff.
Temperature (K)	1073	1073	0	1073	1073	0
Gas Constituent	Mean Conc. (% v/v)	Mean Conc. (% v/v)	(%)	Mean Conc. (% v/v)	Mean Conc. (% v/v)	(%)
H_2	21.3	8	166	23.6	7	237
CO	29.6	21	41	32.9	20	64
CH_4	0.0	6	-100	0.0	5	-100
CO_2	8.0	13	-39	6.4	13	-50
N_2	40.8	50	-18	36.9	53	-30
O_2	0	1	-100	0	1	-100
Total	99.8	99	1	99.8	99	1

With one exception (CH_4 for SLF) the equilibrium concentrations for CH_4 are lower and CO and H_2 higher than experimental concentrations at the same temperature. The predicted concentrations are sensitive both to temperature and the atom populations. The latter are affected by the fraction of unreacted or partially reacted fuel remaining in the solid phase.

4.7 STANJAN Sensitivity Analysis

Adjustments for carbon, hydrogen, nitrogen and oxygen

Adjustments to the input atom populations were made for fuel carbon, hydrogen, nitrogen and oxygen collected in the spent bed, horizontal pass and cyclone. The total unreacted amount of carbon, hydrogen, nitrogen and oxygen were subtracted from original STANJAN atom populations. STANJAN runs were then performed at the same temperature as the experimental runs with these new atom populations. Shown below in Tables 4.33 through 4.38 are the revised STANJAN predictions with adjusted atom populations.

Table 4.33 Adjusted STANJAN predictions for ASF

	STANJAN Adjusted	STANJAN Original	Experimental
Temperature (K)	1023	1023	1023
Gas Constituent	Mean Concentration (% v/v) Test 1	Mean Concentration (% v/v) Test 1	Mean Concentration (% v/v) Test 1
H_2	39.7	34.6	13
CO	39.1	46.4	20
CH_4	1.0	3.7	7
CO_2	5.7	1.9	16
N_2	14.5	13.4	43
O_2	0	0	1
Total	100.0	100.0	100

Table 4.34 Adjusted STANJAN predictions for WPF

	STANJAN Adjusted	STANJAN Original	Experimental
Temperature (K)	1013	1013	1013
Gas Constituent	Mean Concentration (% v/v) Test 1	Mean Concentration (% v/v) Test 1	Mean Concentration (% v/v) Test 1
H_2	34.4	32.5	10
CO	33.9	42.7	22
CH_4	0.4	1.4	7
CO_2	10.0	4.7	16
N_2	21.4	18.8	42
O_2	0	0	3
Total	100.0	99.9	100

Table 4.35 Adjusted STANJAN predictions for RSF

	STANJAN Adjusted	STANJAN Original	Experimental
Temperature (K)	1058	1058	1058
Gas Constituent	Mean Concentration (% v/v) Test 1	Mean Concentration (% v/v) Test 1	Mean Concentration (% v/v) Test 1
H_2	26.1	26.3	4
CO	30.8	39.6	10
CH_4	<0.1	<0.1	4
CO_2	9.9	4.6	13
N_2	33.3	29.1	64
O_2	0	0	3
Total	100.0	99.6	98

Table 4.36 Adjusted STANJAN predictions for WWF

	STANJAN	STANJAN	Experimental
	Adjusted	Original	
Temperature (K)	1098	1098	1098
Gas Constituent	Mean Concentration (% v/v) Test 1	Mean Concentration (% v/v) Test 1	Mean Concentration (% v/v) Test 1
H_2	15.8	16.9	13
CO	29.1	35.2	15
CH_4	0	0	5
CO_2	10.1	6.5	13
N_2	44.9	41.3	46
O_2	0	0	1
Total	100.0	99.9	93

Table 4.37 Adjusted STANJAN predictions for SLF

	STANJAN	STANJAN	Experimental
	Adjusted	Original	
Temperature (K)	948	948	948
Gas Constituent	Mean Concentration (% v/v) Test 1	Mean Concentration (% v/v) Test 1	Mean Concentration (% v/v) Test 1
H_2	28.9	10.3	15
CO	26.9	40.6	21
CH_4	0.8	23.7	8
CO_2	19.8	0.2	11
N_2	23.6	25.1	44
O_2	0	0	1
Total	100.0	99.8	100

Table 4.38 Adjusted STANJAN predictions for NPF

	STANJAN Adjusted	STANJAN Original	Experimental
Temperature (K)	1073	1073	1073
Gas Constituent	Mean Concentration (% v/v) Test 1	Mean Concentration (% v/v) Test 1	Mean Concentration (% v/v) Test 1
H_2	20.8	21.3	8
CO	26.8	29.6	21
CH_4	-	-	6
CO_2	9.6	8.0	13
N_2	42.7	40.8	50
O_2	0	0	1
Total	100.0	99.8	99

In comparing the original STANJAN runs to the ones with adjusted atom populations, the results are mixed (some gas concentrations higher and some lower than original). The results, however, can be partially explained in terms of relative atom populations between the original and adjusted runs. Table 4.39 shows the relative atoms populations for the experimental (original) and adjusted STANJAN runs. These figures have all been normalized on carbon and therefore the carbon value will be displayed as 1 for both sets of runs. The ratios of the other atoms (H, N, O) to carbon, for the adjusted runs, have changed significantly in some cases, from the original atom populations.

In all of the adjusted runs, the amount of carbon monoxide predicted is less than the original due to the reduction in gas phase carbon relative to other elements. In the adjusted runs, disproportionately more carbon remained in the bed, horizontal pass and the cyclone (See Table 3.10). For both the hydrogen and methane gas predictions, however, the results are nearly split in that approximately half of the runs predicted higher levels of hydrogen and methane and half of the runs predicted a lower level or the same level of hydrogen and carbon monoxide. In some cases, where the relative proportion of hydrogen atoms in the adjusted run exceeded those in the original tests, the impact of disproportionately fewer carbon atoms has an overall impact that results in less methane and more H_2 being produced (See sludge fuel).

The level of nitrogen between the two sets of tests (original and adjusted) changed by a maximum of 13.3 %. The large difference between experimental nitrogen concentrations (GC) and STANJAN predictions for nitrogen (for both original and adjusted runs), is due to the higher equilibrium concentrations of CO and H_2. The concentration of nitrogen is

decreased even though the same number of nitrogen atoms, as used in the experimental run, are still present. This was also confirmed by modeling a run at a lower temperature. In the lower temperature case, the nitrogen concentration increases and CO and H_2 decrease. An additional reason for higher experimental values of N_2 may be from air leaking into grab sample flasks, which would inflate the actual concentration of nitrogen. Lastly, the uncertainty associated with the gas chromatograph, as displayed in Appendix A, accounts for a portion of the difference, albeit small. Figures 4.10 through 4.15 display STANJAN equilibrium predictions for H_2, CO and CH_4 as a function of temperature, based on the adjusted atom populations.

Table 4.39 Experimental and adjusted atom populations used with STANJAN (atoms (C, H, N and O)/atoms C) for Test 1 of each fuel

	Biomass Fuels											
Atom(s) Involved In Reactions	ASF		WPF		RSF		WWF		SLF		NPF	
	Exp.	Adj.	Exp.	Adj.	Exp.	Adj.	Exp.	Adj.	Exp.	Adj.	Exp.	Adj.
C	1.00	1.00	1.00	1.00	1.00	1.00	1.00	1.00	1.00	1.00	1.00	1.00
H	1.66	2.02	1.55	1.90	1.32	1.64	0.96	1.10	1.79	7.60	1.42	1.52
N	0.51	0.63	0.77	0.96	1.31	1.63	1.98	2.28	0.78	3.22	2.17	2.34
O	0.98	1.20	1.12	1.39	1.16	1.42	1.23	1.39	0.64	2.77	1.35	1.45

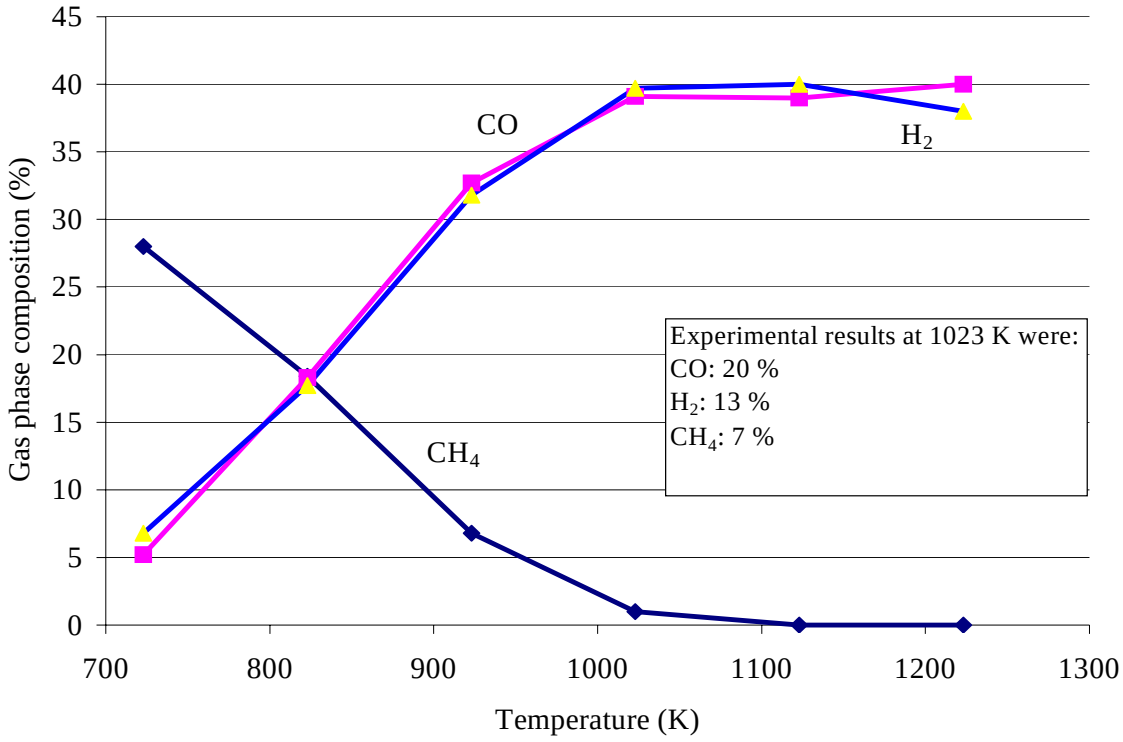

Figure 4.10 STANJAN composition predictions for ASF versus temperature for CH_4, CO and H_2

The experimental gas concentrations best fit the STANJAN equilibrium results for H_2, CO and CH_4 at 780 K, 840 K and 912 K respectively. These temperatures are all well below the experimental temperature of 1023 K.

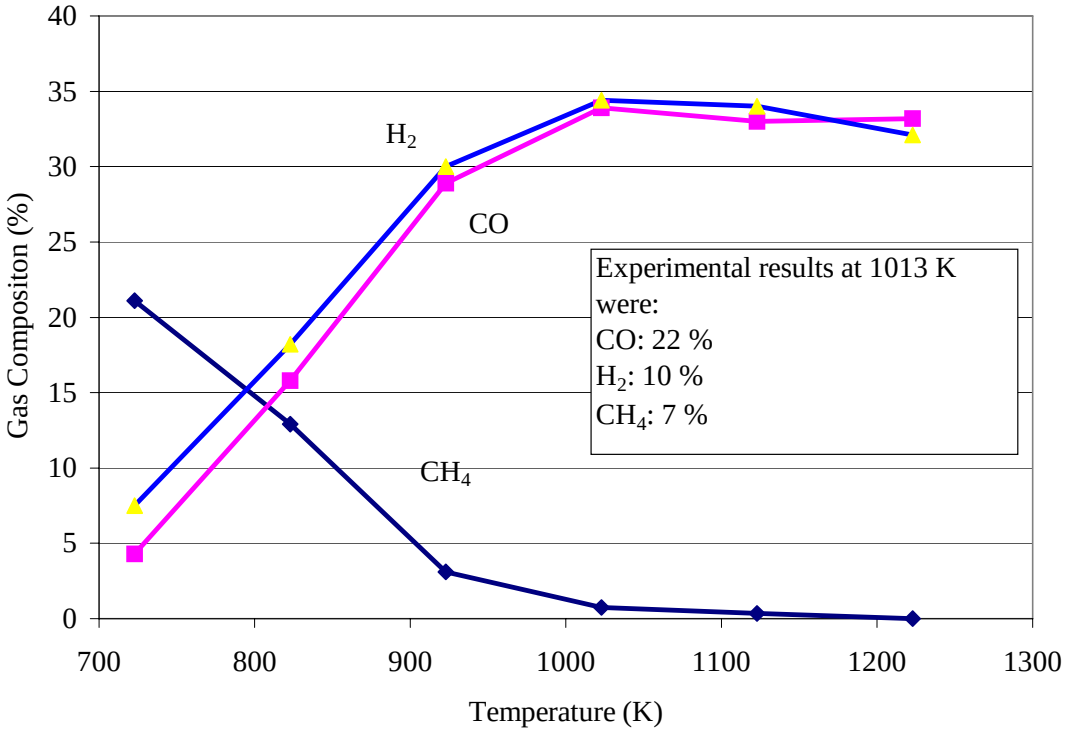

Figure 4.11 STANJAN composition predictions for WPF versus temperature for CH_4, CO and H_2

The experimental gas concentrations best fit the STANJAN equilibrium results for H_2, CO and CH_4 at 750 K, 875 K and 877 K respectively. These temperatures are all well below the experimental temperature of 1013 K.

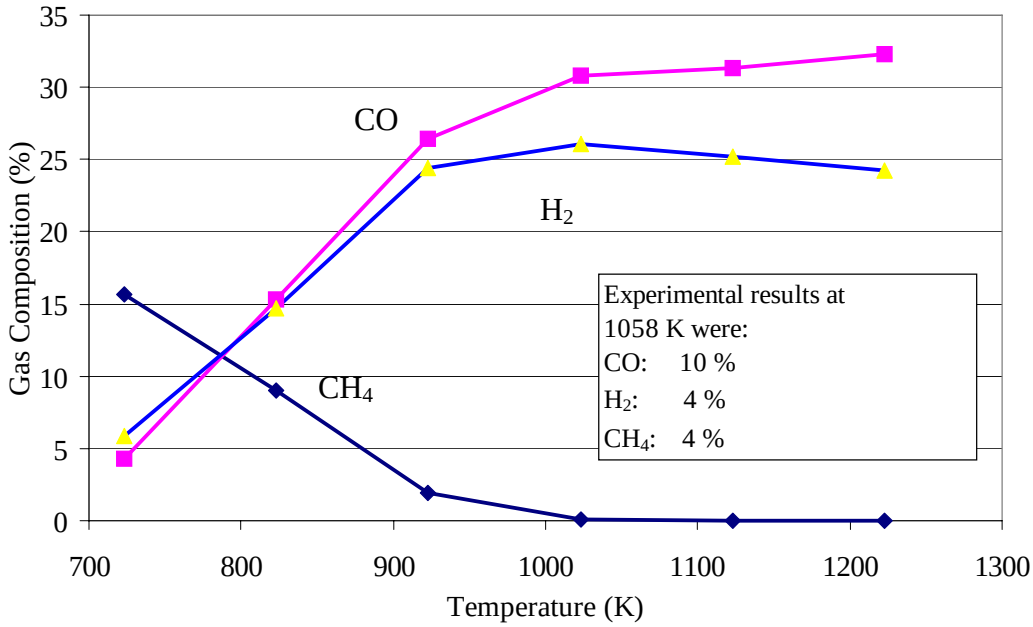

Figure 4.12 STANJAN composition predictions for RSF versus temperature for CH_4, CO and H_2

The experimental gas concentrations best fit the STANJAN equilibrium results for H_2, CO and CH_4 at 700 K, 773 K and 883 K respectively. These temperatures are all well below the experimental temperature of 1058 K.

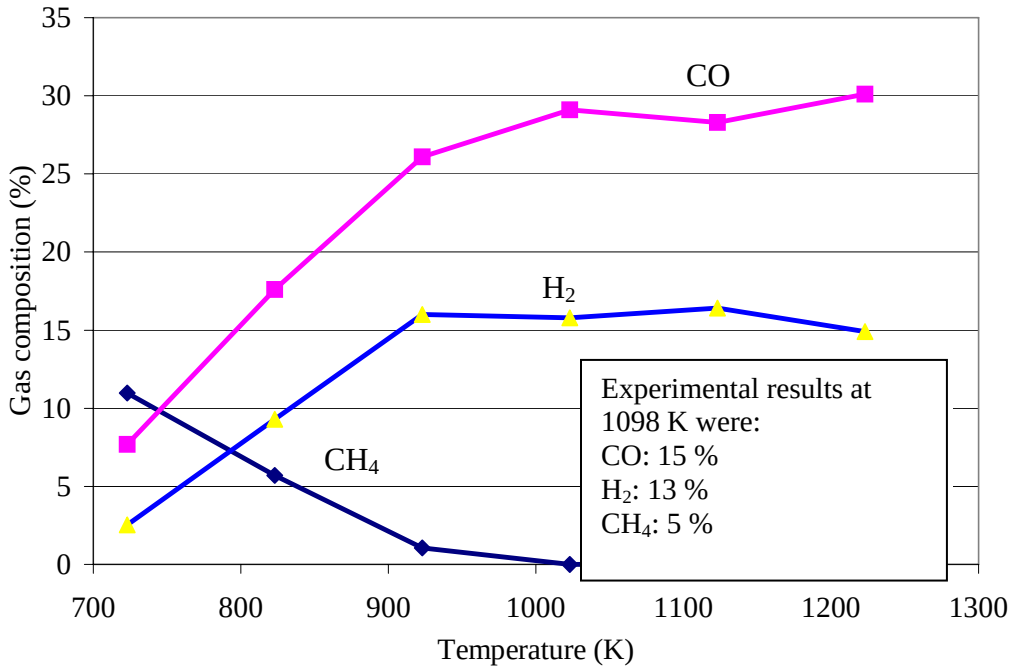

Figure 4.13 STANJAN composition predictions for WWF versus temperature for CH_4, CO and H_2

The experimental gas concentrations best fit the STANJAN equilibrium results for H_2, CO and CH_4 at 881 K, 795 K and 833 K respectively. These temperatures are all well below the experimental temperature of 1098 K.

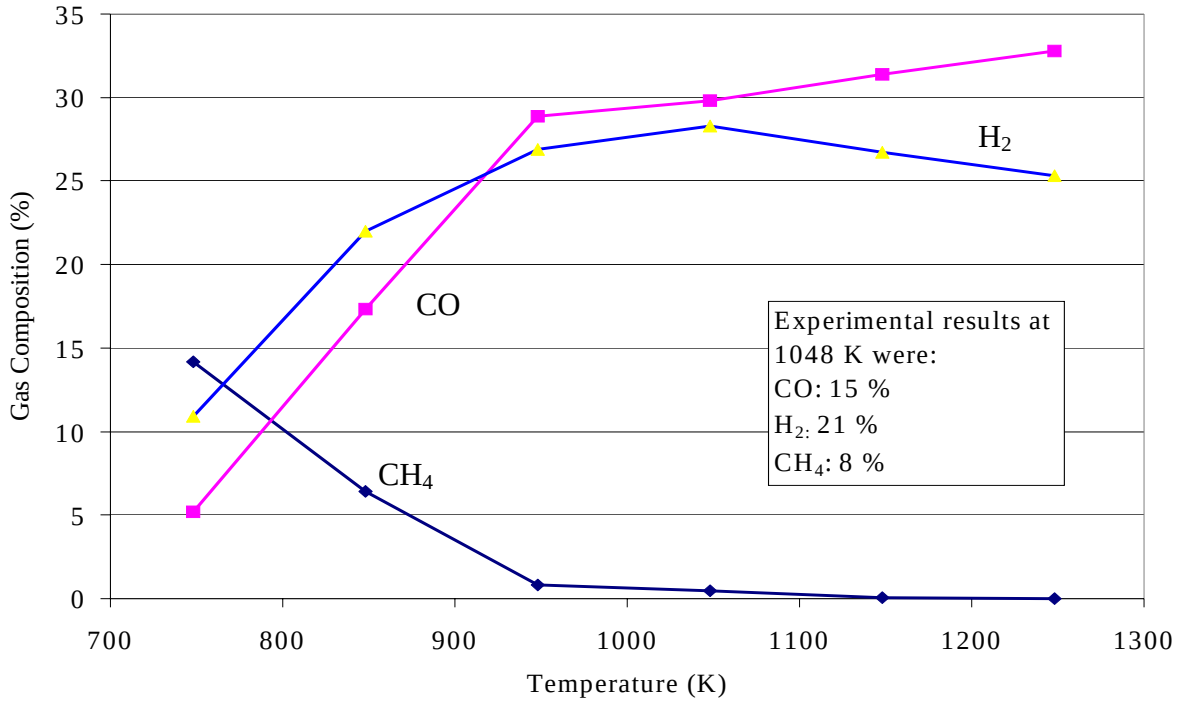

Figure 4.14 STANJAN composition predictions for SLF versus temperature for CH_4, CO and H_2

The experimental gas concentrations best fit the STANJAN equilibrium results for H_2, CO and CH_4 at 776 K, 875 K and 849 K respectively. These temperatures are all well below the experimental temperature of 1048 K.

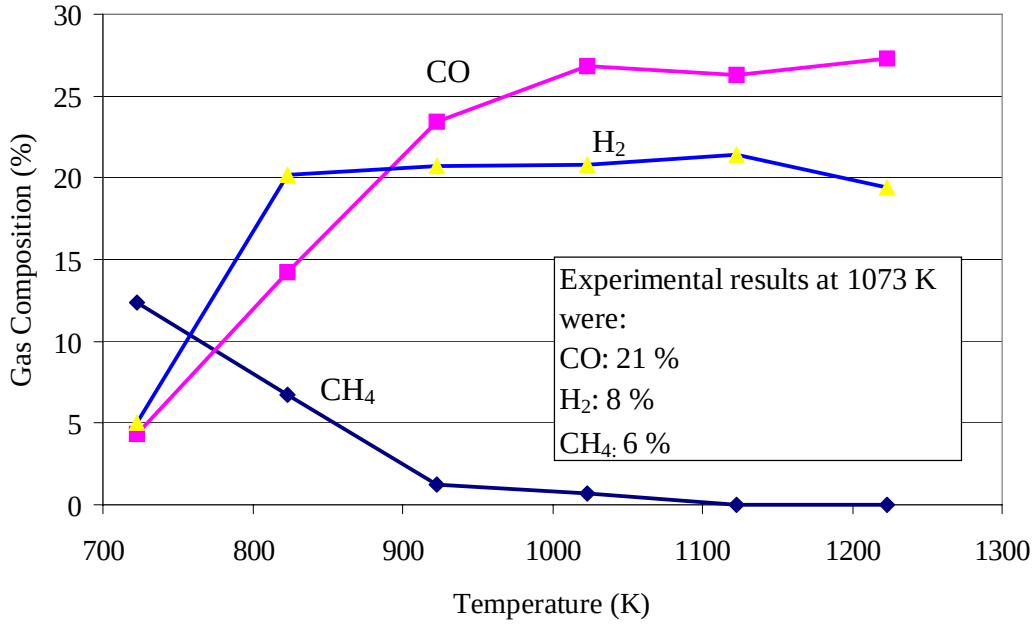

Figure 4.15 STANJAN composition predictions for NPF versus temperature for CH_4, CO and H_2

The experimental gas concentrations best fit the STANJAN equilibrium results for H_2, CO and CH_4 at 742 K, 893 K and 840 K respectively. These temperatures are all well below the experimental temperature of 1073 K.

4.8 Potential utility of model for general application

The CSFB model was used to simulate the twelve experimental test runs performed at the UC Davis biomass laboratory.

The model, in its original form and with previously described modifications provided by its author failed to predict the experimentally observed gas compositions. Most notable were the low levels of carbon monoxide, hydrogen and methane (energy carrier gases). The values predicted seem to be more representative of a relatively unreactive fuel. The fuels tested in this study are highly reactive and produce substantial quantities of energy carrier gases.

The model is sensitive to particle size distribution as evidenced by the convergence difficulty when inert and/or fuel particle sizes were set to the experimental values. It is believed that the inability to converge with smaller particle size distributions may be related to a variety of problems associated with transport disengagement height, reaction kinetics and devolatilization.

In some instances, the maximum heat transfer rate between the reactor jacket and the bed, allowed by the model in order to produce a solution that converged, created a bed temperature that was higher or lower than the actual operating temperature during experimental runs. When a different (larger) particle size distribution was run, the model would allow higher and lower temperatures because constraints on transport disengagement height were met. The superficial velocity of particles is higher temperatures. When higher temperatures were run in conjunction with increased inert particle size, the predictions from CSFB improved substantially. When lower temperatures were run, the predictions were worse.

It is difficult to ascertain from the model runs (since access to the source code was not available) whether CSFB is simply not allowing sufficient carbon conversion (not converting the fuel carbon to gas via the devolatilization scheme), or whether the kinetic scheme for the gas phase may be reverting some CO (the reversion from CO to CO_2 may be too high).

Although there is a noticeable temperature drop in the disengagement zone of the reactor, and CSFB seems to do a fairly good job in modeling this, experimentally, the gas concentrations should remain mostly frozen above the bed. CSFB appears to predict substantial CO reversion in this zone (substantial in that about half of the CO for a number of runs reverts to CO_2 in the disengagement zone). The absolute reversion may be appropriate, but the CO concentration predicted at the bed exit is too low. When temperatures used in the model were elevated by approximately 200 to 300 °C, most of the levels of energy carrier gases increased but the prediction was still poor. When the patch received from the author was tested with the same inputs used in the original version, it did not improve the predictions from the model by much.

Gas composition predictions using the STANJAN model were more closely aligned and were higher (for CO and H_2) and lower (CH_4) than experimental values even when the atom populations were adjusted for carbon, hydrogen, nitrogen and oxygen solid residual in the bed, horizontal pass and cyclone locations. Experience with the reactor used in our tests has shown that carbon conversion efficiency is low (approximately 60%) and from prior tests (Pfaff, 1999) we know approximately what will be remaining in the bed, horizontal pass and cyclone.

There may be a number of reasons for the disparity between the equilibrium plots and the experiment values including energy carrier gases, nitrogen and carbon monoxide. These reasons are as follows: The gas sampling was performed at temperatures substantially less than the average peak bed temperature used with the equilibrium model. The compositions are mostly frozen somewhere between the bed and the sampling location. The fluidized bed that was used for the experiments is short and the residence time may be less than the interval time needed to complete reactions. This fact is supported by the substantial amount of power remaining in the recovered ash, char and recovered material as displayed in Table 3.16. Adjusting for elements remaining in the solid phase shows that the equilibrium compositions are in better agreement at somewhat lower temperatures than peak bed temperature.

Due to these reasons, the experimental concentrations typically corresponded to equilibrium values predicted by STANJAN for temperature ranges of approximately 80 K, centered at about 190 K to 280 K less than the experimental temperature, and more consistent with the upper freeboard.

The CSFB-predicted gas compositions and STANJAN-predicted gas compositions differ substantially. In comparing figures 4.4 to 4.10, 4.5 to 4.11 and 4.9 to 4.15 for example, the most noticeable difference is the level of producer gases in all plots. In many cases, the combined CO, H_2 and CH_4 predicted by CSFB is an order of magnitude less than the STANJAN predictions. Since CSFB may not be converting fuel carbon via the current devolatilization scheme the gas predictions are indeed low. Additionally, if the kinetics are not calibrated correctly the basic shape of the curves, as in the case of methane, will also be inaccurate. Although the predictions are again low, the CSFB figure 4.5 plot best approximates the basic shape of the associated equilibrium curve (figure 4.11), however, without further revisions to the model, the version tested here does not currently provide adequate simulation for design purposes.

CHAPTER 5 DISCUSSION

5.1 The relationship of producer gas quality to fuel composition

The ASF, even with a high percentage of ash, had the highest average producer gas HHV of the six tested fuels at 6.9 MJ m^{-3}. RSF, with a producer gas HHV of 3.6 MJ m^{-3} had the lowest. There was poor correlation between producer gas quality (determined by GC) and the fuel composition parameters of carbon, hydrogen, oxygen or ash content. The r^2 values ranged from 0.03 to 0.16. The correlation between producer gas HHV and producer gas volatile content was also poor. As discussed previously in Chapter 3, there was good correlation between fuel HHV and fuel carbon content (r^2=0.95).

5.2 The relationship between fuel HHV and ash content.

Figure 5.1 displays the plot of fuel HHV versus fuel ultimate ash content. The correlation was good with r^2 = 0.77. Fuels with higher ash content generally have lower HHVs due to dilution of organic matter with incombustible material.

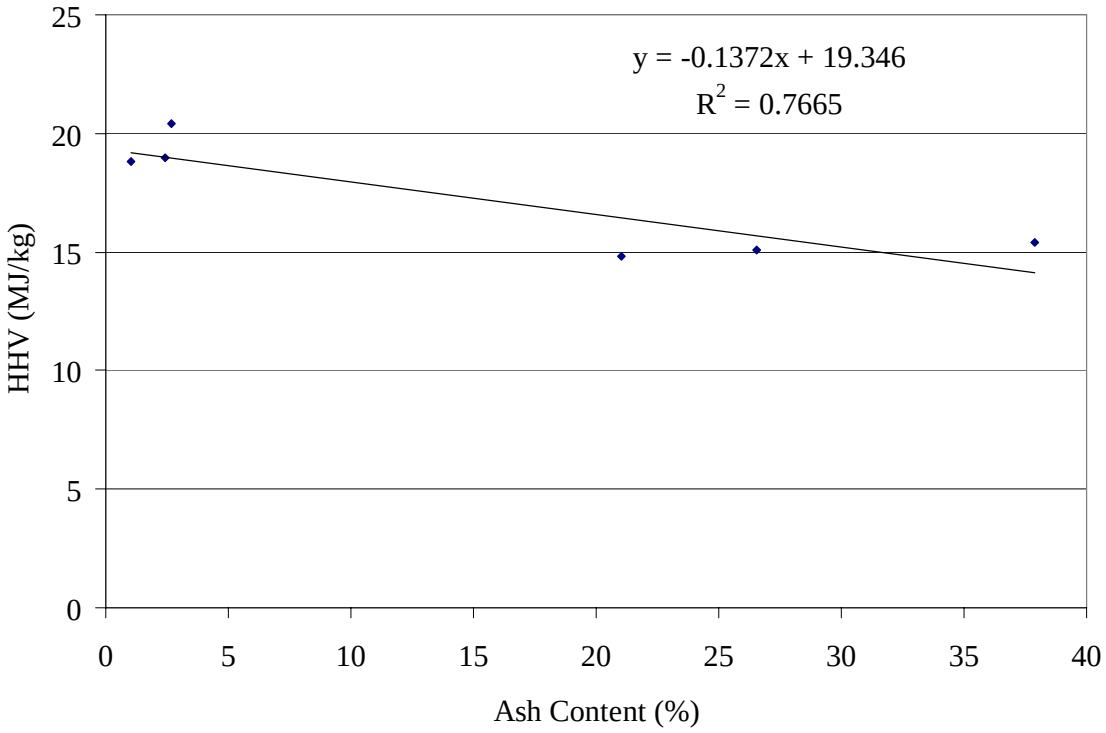

Figure 5.1 HHV versus ash content for tested fuels

5.3 Producer gas concentrations (GC) of tested fuels related to equilibrium concentration predictions

In general, H_2 concentrations ranged from 4 to 21%, CO concentrations ranged from 10 to 22% and CH_4 concentrations ranged from 4 to 8%. SLF produced the highest concentration of H_2 (21% v/v) while RSF produced the lowest level (4% v/v). Equilibrium concentrations based on using STANJAN modeling for these fuels show that corresponding levels of hydrogen gas occur at approximately 875 K and 700 K respectively which is significantly below the experimental bed temperatures (1048 and 1058 K) indicating that the gases are likely being frozen as the gas cools (concentration may be changing as gas cools) between the bed and the sampling location. WPF had the highest concentration of CO (22% v/v) while RSF had the lowest level for one run (10% v/v). Again these levels are well below the equilibrium concentrations based on actual experimental bed temperatures (1013 and 1058 K respectively) and instead correspond to an equilibrium concentration at a temperature of approximately 875 K and 773 K respectively. Both ASF and WPF had the highest levels of CH_4 in their test runs (both at 8% v/v) while RSF showed the lowest concentrations (4% v/v for both runs). These methane levels correspond to an equilibrium concentration at approximately 912 K for ASF, 827 K for WPF and 883 K for RSF. Experimental temperatures were 1023 K for ASF, 1013 K for WPF and 1058 K for RSF. Again, this indicates that the gas composition freezes between the bed and sampling point, as expected. Overall carbon conversion is low in the reactor tested as it appears to be short for gasification conditions (although not for combustion). Higher CO concentrations may be possible with added reactor length.

5.4 Air to Fuel Ratios

Overall, most of the measured AF ratios were very low, accounting for some of the low carbon conversion in the bed. Air-fuel ratio (AF) for the ASF tests was 0.25 and 0.37 respectively. The ASF (Test 1) had the lowest AF ratio, partly due to the high bulk density of the milled fuel. The AF ratio for the WWF tests were 1.44 and 1.07 and are high partly due to the lower bulk density of the milled fuel and the difficulty in feeding due to its tendency to bridge in the feeder. NPF was the most difficult fuel to feed and had a very low bulk density. The difficulty in feeding this fuel was due to the type of feed system that was used. AF ratios for this fuel ranged from 1.51 to 1.31. For the first SLF experiment, the AF was 0.32. During the second SLF run, the AF was about 0.27. The SLF fuel had a considerably higher bulk density and was more granular compared to WWF, for example, and could be run at much lower AF. RSF and WPF both fed easily. The AF ratios for these two fuels were 0.48 and 0.42 for WPF and 0.71 to 0.74 for RSF. In Figure 5.2 is a plot of AF versus bulk density. The curve is hyperbolic in shape, but too little information exists to determine the full behavior.

For a discussion of experimental air flow rates, see section 5.12, Uncertainty Analysis. By knowing the fuel feed belt speed during the steady state period, the experimental bulk density during a test run can be compared against the measured bulk density. Equation 5.1 relates AF to belt speed, fuel feed frontal area and fuel density. Figure 5.2 displays AF versus both the measured bulk density of the fuel and the product of measured bulk

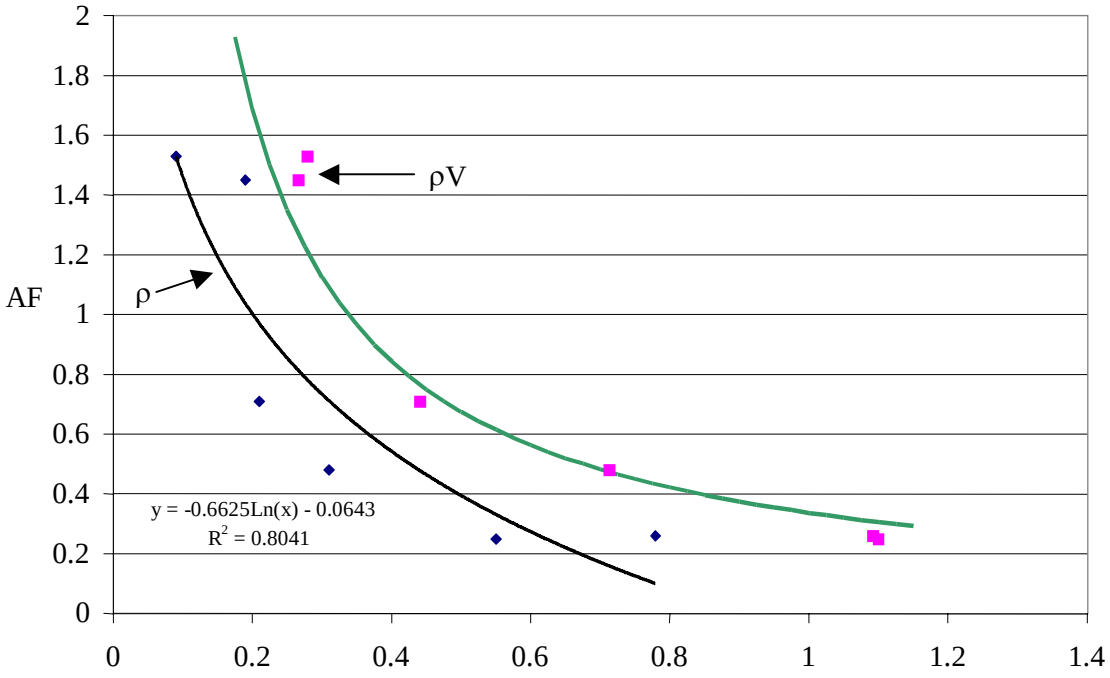

Bulk Density (g cm^{-3}, diamonds) or ρv (g cm^{-2} min^{-1}, squares)

density and feeder belt speed (ρV). The hyberbolic behavior in ρV is apparent. The hyperbola plotted in the figure for ρV uses the average air flow rate of 0.55 g s^{-1}.

Figure 5.2 AF versus bulk density

$$AF = \frac{\dot{m}_a}{\dot{m}_f} = \frac{c_1}{\rho A V} = \frac{c_1}{c_2 \rho V} \qquad [5.1]$$

where

$\dot{m}_a$ = mass flow rate of air (constant) in g s^{-1}

$\dot{m}_f$ = mass flow rate of fuel in g s^{-1}

c_1 = constant

c_2 = constant

ρ = density of fuel in g cm^{-3}

A = frontal area of fuel on belt in mm^2

V = velocity of feed belt in mm min^{-1}

Table 5.1 is a comparison of experimental and calculated bulk densities.

Table 5.1 Comparison of experimental and calculated bulk densities

Fuel	$\dot{m}_a$ (g s^{-1})	$\dot{m}_f$ (g s^{-1})	V (mm min^{-1})	ρ computed from belt speed (g cm^{-3})	Experimental ρ measured by ASTM E873 (g cm^{-3})
ASF	0.48	1.93	20	0.49	0.55
WPF	0.61	1.27	23	0.30	0.31
RSF	0.60	0.84	21	0.22	0.21
WWF	0.55	0.38	14	0.17	0.19
SLF	0.55	2.08	14	0.75	0.78
NPF	0.49	0.32	31	0.07	0.09

In general, most of the computed densities are slightly lower (one higher) than the experimental values measured according to ASTM E873. This was expected as fuel feeding from the hopper does not get compacted to the same degree that fuel compacts while undergoing the drop test as prescribed by ASTM E873. Overall, however, the agreement is quite good.

5.5 Gas phase ammonia, hydrogen cyanide, chloride and potassium

Gas-phase ammonia concentration

Gas phase ammonia concentration appears to be highly dependent on the nitrogen content of the fuel that was gasified. SLF with 5.64% db nitrogen produced an ammonia concentration of 3.99% in the gas. Conversely, NPF with 0.15% db nitrogen produced an ammonia concentration of only 0.007%.

In general, NH_3 seems to correlate well with fuel N but the data are clustered. SLF gives an extreme value of ammonia. No fuel blending was performed to test for intermediate values. All runs, except for SLF run 2, had excellent correlation. Ishimura (1994) concluded that NH_3 is strongly dependent on temperature, but only weakly dependent on equivalence ratio and residence time. NH_3 decreases with increasing temperature and residence time (Ishimura, 1994). The correlation coefficient for the data obtained here and shown in the figure is r^2=0.66. The plot of gas phase ammonia versus fuel nitrogen content is shown in Figure 5.3. When correlated for only the other five fuels (excluding SLF), the slope changes (becomes steeper) to 0.730 with an r^2=0.93.

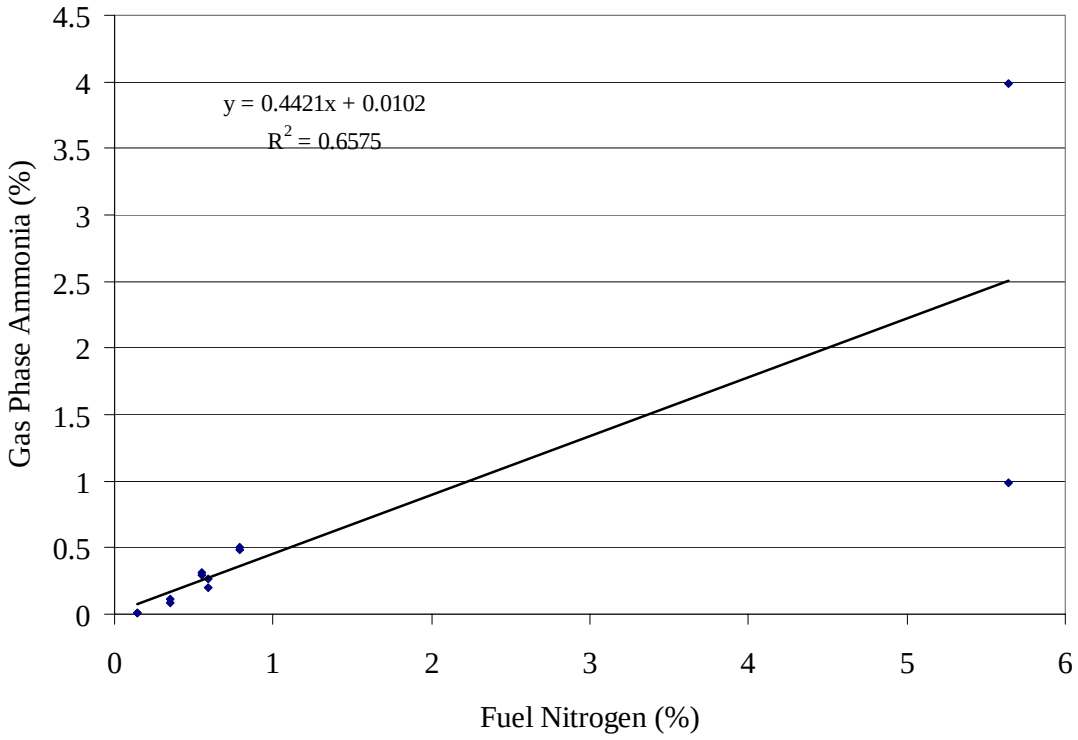

Figure 5.3 Gas phase ammonia versus fuel nitrogen content

Ammonia can generally react via one of the two following pathways:

$$NH_3 + NO \rightarrow N_2 + H_2O + H \quad [5.1]$$

$$NH_3 + O_2 \rightarrow NO + H_2O + H \quad [5.2]$$

At lower temperatures and in fuel rich regions, equation 5.1 is dominant leading to reduced NO and at higher temperatures and in fuel lean regions, equation 5.2 is dominant leading to the production of NO, which is undesirable.

The fuel-N content of each fuel varied. The fuel-N content and the percentage of fuel-N that was converted to gaseous NH_3-N is shown in Table 5.2.

Table 5.2 Fuel-N content and the percentage of fuel-N that was converted to gaseous NH_3-N for each fuel

Fuel	Fuel-N (% db)	NH_3-N/Fuel-N (%)
ASF	0.79	27.5
WPF	0.59	22.6
RSF	0.55	38.1
WWF	0.35	32.4
SLF	5.64	6.6
NPF	0.14	5.4

The correlation for these data are poor, mostly due to the wide range of conditions over which each fuel was tested and the lack of intermediate values between biomass and sludge. The trend is not inconsistent with what is generally known about fuel N conversion, however, in that conversion typically declines as fuel N increases.

Hydrogen cyanide

Hydrogen cyanide levels were determined only for ASF and RSF. Values ranged from 2.3 ppmv for ASF to 24.0 ppmv for RSF. Due to the limited number of tests conducted, a comprehensive evaluation of HCN was precluded. Ishimura (1994) concluded in his experiments that HCN is not a prominent species (representing only a small percentage of the fuel-nitrogen). The tests here confirm that HCN is relatively minor compared with NH_3. Ishimura also concluded in his experiments that HCN increases with increasing temperature and residence time.

Gas-phase chlorine concentration

Gas phase chlorine concentrations ranged from 9 ppmv for NPF (test 1) to 810 ppmv for ASF (test 1). These gas phase concentrations are up to 6 % and 225 % respectively of the stoichiometric yields (136 and 360 ppmw for NPF1 and ASF1 respectively) based on the fuel Cl concentration (0.03%) for both fuels. Tests revealed that there was poor correlation between gas-phase chlorine content and fuel chlorine content. Cl condenses with alkali particles at temperatures well above the sampling temperature so Cl may have been removed before entering the sampling train. Particles were captured in the spent bed, in the ash dropouts and on the 5 μm filter. The correlation of gas-phase chlorine to

fuel chlorine was quite poor (r^2 = 0.0007). Although Cl can condense or react with particles, it also forms HCl and gas phase Cl would have been expected to better conform to fuel Cl concentration. The low measured values of the latter preclude much in the way of conclusion in this regard due to possible analysis error with these concentrations. Total Cl collected for ASF1 and RSF1 at the stack (particles collected with filter cake and gas collected in impingers) was 816 and 330 ppmv respectively. This represents 227 and 8% of stoichiometric yield for ASF1 and RSF1 respectively. The amount of Cl in the bed, horizontal pass, cyclone, tar ash and leaving the stack is shown in Table 5.3 for all fuels. ASF1 and RSF1 were the only two fuels for which filter cakes of sufficient quantity for analysis were collected. This table shows the partitioning between gas and particle phases (collected in the impingers and in the filter cake respectively). Only RSF and SLF had any appreciable amount of Cl in the fuel (0.58 and 0.10 % db respectively), however the amount of gas phase Cl produced in SLF is substantially more than for RSF. RSF contains substantially more alkali (mostly as potassium) than SLF and since Cl condenses with alkali particles (as KCl) at temperatures well above the sampling temperatures used with these experiments, it is possible that more Cl was removed at the filter before entering the impinger train. Additionally, quantitative analysis by ion specific electrode was more difficult with impinger fluids from the SLF tests due to the greater concentration of tars, and this may have led to interference with the Cl^- determination.

Table 5.3 Cl in the spent bed, horizontal pass, cyclone, impingers, tar ash and filter cake as percent mass basis of input chlorine for all fuels.

Fuel	Bed (%)	HP (%)	Cyclone (%)	Impingers (%)	Tar (%)	Cake (%)	Total (%)
ASF1	11.4	131.4	44.8	294.3	2.7	0.1	484.7
WPF1	18.3	129.5	26.5	166.1	61.1		401.5
RSF2	19.1	80.1	25.5	8.7	4.2	0.2	137.8
WWF2	39.1	189.2	75.3	172.3	79.4		555.3
SLF2	14.7	16.9	5.4	2809.5	33.3		2879.8
NPF2	6.0	11.6	6.9	14.9	2.4		41.8

Note: Only ASF1 and RSF2 had filter cake data.

Gas and solid phase potassium

Potassium is the dominant source of alkali in most biomass fuels. Gas phase potassium was produced in small quantities ranging from 2 ppmv to 61 ppmv. SLF test 2 had the highest concentration of potassium at 61 ppmv (air factor 0.06) at the cyclone exit (147 °C). There was essentially no correlation (r^2=0.0007) between gaseous K collected from the stack and K levels in the fuel, certainly due to the low sampling temperatures for which most alkali is expected to have condensed on particles. The amount of K in the bed, horizontal pass, cyclone, tar ash and filter cake (ASF and RSF) is shown in Table 5.4 for all fuels. ASF1 and RSF2 were the only two fuels that a filter cake was collected.

Table 5.4 K in the spent bed, horizontal pass, cyclone, impingers, tar ash and filter cake as percent mass basis of input potassium for all fuels.

Fuel	Bed (%)	HP (%)	Cyclone (%)	Impingers (%)	Tar (%)	Cake (%)	Total (%)
ASF1	3.3	50.5	21.1	<0.1	0.1	0.1	75.2
WPF1	34.8	64.6	29.0	1.6	3.1		133.0
RSF2	16.0	38.6	13.4	<0.1	4.9	0.2	73.2
WWF2	54.1	36.7	7.7	0.0	23.2		121.6
SLF2	35.6	20.1	2.4	1.9	5.4		65.4
NPF2	585.2	22.6	7.2	0.8	3.7		619.6

Note: Only ASF1 and RSF2 had filter cake data.

Most of the potassium is in the HP and cyclone catch, which is not unexpected. This could constitute both condensed potassium as well as potassium that never volatilized which is a potential advantage of gasification compared with combustion due to the lower temperature. The K_2O concentrations in the filter cake (Table 3.11) are elevated compared with the other samples, suggesting enrichment, possibly via condensation. The low totals on SLF2 and ASF1 make interpretation difficult, as does the very high total on NPF2. Partitioning between solid and gas phase in the stack (using filter cake and impinger samples) shows solid to gas phase ratios of approximately 15:1 and 10:1 for ASF1 and RSF2 respectively.

Gas-phase sodium

Gas phase sodium was not measured and therefore a discussion on the partitioning between solid and gas phase sodium is precluded. The great majority of sodium condenses on bed and fuel particles and eventually ends up in the residue of the bed, horizontal pass, cyclone or is carried out with particles in the stack gas. The amount of sodium in the spent bed, horizontal pass, cyclone, tar ash and filter cake (ASF 1 and RSF 2) is shown in Table 5.5. ASF 1 and RSF 2 were the only two fuels that a filter cake was colleted.

Table 5.5 Na in the spent bed, horizontal pass, cyclone, tar ash and filter cake as percent mass basis of input sodium for ASF1 and RSF1.

Fuel	Bed (%)	HP (%)	Cyclone (%)	Tar (%)	Cake (%)	Total (%)
ASF1	7.2	39.4	19.1	0.4	<0.1	66.2
WPF1	27.6	41.4	69.0	13.8		151.7
RSF2	10.2	22.1	8.8	6.2	<0.1	47.3
WWF2	19.8	19.8	9.9	19.8		69.3
SLF2	33.6	18.2	1.7	4.0		57.4
NPF2	50.3	32.5	8.0	5.3		96.0

Note: Only ASF1 and RSF1 had filter cake data.

Most of the sodium is also in the HP and cyclone catch. This also could constitute both condensed sodium as well as sodium that never volatilized. Unlike with potassium, however, the Na_2O concentrations in the cake (Table 3.11) are not elevated compared with the other samples. The low totals on ASF 1, RSF 2, WWF 2 and SLF 2 make interpretation difficult, as does the high total on WPF1.

5.6 Reburning

Ammonia effect on reburning

The presence of NH_3 in the reburning fuel could affect the efficiency of NO_x reduction. At high temperatures NH_3 is mostly oxidized to NO_x and reduces efficiency of NO_x reduction by the reburning fuel. At low temperatures, however, as was demonstrated in an advanced reburning process (Zamansky et al., 1997 and Zamansky et al., 1999c), NH_3 can reduce NO_x. The efficiency of NO_x reduction increased with a decrease in temperature. The optimum temperature for NO_x reduction by NH_3 is about 982 ^oC (Lyon, 1975; Arand et al., 1980). The optimum in NO_x reduction occurs at even lower

temperatures in the presence of CO and H_2 (Chen, 1988, Zamansky et al., 1997 and Alzueta, 1997). Since concentrations of CO and H_2 in the gasification products of all tested biomass fuels were relatively high, the efficiency of NO_x reduction with ASF reburning, for example, is projected to reach a maximum at about 943 ^oC to 982 ^oC (Lissianski et al., 2000). All test fuels produced a measurable amount of NH_3. All gasified test fuels are potentially valuable at reducing NO_x emissions provided the reburn temperature is conducive (as described and referenced in the previous paragraph) to the reduction of NO_x.

Hydrogen Cyanide effect on reburning

From a reburning perspective, available HCN can generally proceed as shown in equations 5.3 and 5.4. In fuel rich regions, HCN is generally reduced to N_2 as shown below in equation 5.3.

$$HCN + NO \rightarrow N_2 + \ldots \quad [5.3]$$

In fuel lean regions HCN is generally oxidized to form NO as shown below in equation 5.4.

$$HCN + O_2 \rightarrow NO + \ldots \quad [5.4]$$

The two fuels that were tested for HCN (ASF and RSF) are potentially valuable at reducing NO_x emissions through reactions with HCN provided the reburn temperature is again conducive to the reduction of NO_x and the conditions are predominantly fuel rich. However, HCN concentrations are low and thus this will not be a primary mechanism for NO_x reduction. NH_3 will instead dominate.

5.7 Deposition

Chlorine effect on deposition

Baxter et al. (1998) notes that chlorine can be an important facilitator in fouling, leading to the condensation of alkali chlorides on heat transfer surfaces in the boiler and promoting the development of alkali sulfates. Chlorides are among the most stable alkali-bearing species in the gas phase. Essentially all of the fuel chlorine is released early in the gasification process and much of it combines with available alkali to form alkali chloride vapors. In many cases, the amount of alkali vaporized during biomass combustion is determined more by the amount of chlorine available to form stable vapors than by the amount of alkali in the fuel. In a qualitative sense, based upon a visual inspection, fuels with a high Cl and alkali content, most notably RSF, ASF, SLF and NPF, appeared to have larger post flare deposits, but no quantitative information was obtained.

Alkali metal effect on deposition

The apparent mechanisms of fouling on boiler surfaces include condensation of inorganic vapors, inertial impaction and sticking of particles, thermophoresis and possibly electrophoresis, and chemical reaction (Baxter, 1993, Raask, 1985). The order in which these occur, and the relative rates, are important to the morphology and mechanical properties of the deposits. There are undesirable effects associated with deposits: deposits retard heat transfer and lead to an eventual decline in boiler efficiency and capacity if they cannot be removed. Deposits can grow and whether small or extreme can retard heat transfer. Deposits are associated with corrosion. Deposits which are less tenacious and easily removed (e.g., by soot blowing) represent less of a problem to facility operators than those that are hard to remove and require shutting down the boiler for cleaning (Baxter et al., 1998).

For these biomass fuels, potassium is the major alkali element of concern from a deposition perspective. By contrast, sodium is the most troublesome alkali component for most coal-fired systems (Baxter et al., 1998), but sodium is not a major species in most biomass. The production of saline biomass as a phytoremediation technique may in the future lead to Na becoming a problem, but in most cases K will be the dominant alkali element.
Fuels, such as clean wood, containing little ash alkali or silica generally lead to the development of fewer and more manageable deposits in that soot blowers and boiler maintenance techniques are able to sustain operation of a facility for longer periods without unscheduled shutdowns.

Silica effect on deposition

Silica in combination with alkali and alkaline earth metals, especially with the readily volatilized forms of potassium present in biomass, can lead to the formation of low melting point compounds which readily slag and foul at normal biomass boiler furnace temperatures (800-900°C) (Baxter et al., 1998). Fuels containing high alkali and silica concentrations form alkali silicates that melt or sinter at low temperatures. The rates of deposit growth and sintering/melting increase with increasing temperature and chlorine concentration but are high at all boiler-relevant temperatures and chlorine concentrations. RSF, with high levels of Cl, alkali and silica had the highest deposition based upon a visual inspection. A low silica fuel such as WWF had little deposition but again no quantifiable information was obtained and specific controlled experiments to asses this were not conducted.

5.8 NO_x reduction

Potassium effect on NO_x reduction

Other research has shown that when K was co-injected with the main fuel in the absence of reburning, the resulting decrease in NO_x was approximately 21% absolute (Lissianski

et al., 2001). This same research found the decrease in NO_x when sodium was injected to be approximately 20% (absolute).

Gas phase potassium content in the six fuels tested here ranged from 2 to 61 ppmv. Based on prior research (Lissianski et al., 2001), it is reasonable to expect that these concentrations may lead to reductions of up to approximately 15% in NO_x if co-injected with the main fuel in the absence of reburning and if the form of K behaves in the same manner as that used in Lissianski's determination. However, there is no direct evidence from these experiments to support this. Since NO_x formation via thermal and fuel-N mechanisms strongly depends on the local combustion environment, NO_x formation in the main combustion zone can be inhibited because H, OH and O concentrations in the combustion zone are decreased in the presence of alkali metals (Lissianski et al., 2000). Since H, OH and O concentrations in the combustion zone are decreased, there are fewer radicals (radicals need H, OH and O to form) available to form NO_x. Further, experiments would be required to determine specifically whether the K carrying over in the stack gas could lead to NO_x reduction as seen with other research.

5.9 Advanced Reburn

Both potassium and sodium are known to produce reductions in NO_x. In other research, injection of 100 ppmv K as KOH (liquid) with the main fuel in the presence of reburning, provided an additional 7% (absolute) reduction (Lissianski et al., 2001). In this same set of experiments, injection of 100 ppm sodium as Na_2CO_3 in the presence of reburning also provided an additional 7% (absolute) reduction in NO_x. Based on prior research (Lissianski et al., 2001), data here suggests that the potassium concentrations found in the test fuels may lead to increased NO_x reductions up to approximately 4% (linear response in scaling region) in the presence of reburning. Again, however, no direct evidence was obtained supporting this hypothesis.

5.10 Agglomeration

All tests were conducted well below the initial deformation temperatures (IDT) for each fuel under both oxidizing and reducing type environments as measured by the ASTM pyrometric cone test. However, the ASTM pyrometric cone test tends to overestimate the IDT.

For all of the tests, no agglomeration of the bed was detected and operation was largely stable, although rice straw was more difficult to run due to attrition and elutrification of the MgO added to mitigate agglomerating effects of the fuel ash. Prior tests with fresh rice straw showed evidence of agglomeration and to mitigate this problem with RSF a bed of alumina silica and magnesium oxide (MgO) was used. The first RSF test used a bed of 67% w/w MgO and the second test used 87.5% w/w MgO. Both were conducive to mitigating bed agglomeration.

5.11 Element closures

Carbon recovery varied from 52 % for SLF to 82 % for ASF. Roughly 30 wt. % of carbon from the ASF was retained in ash, the remainder mostly converted into gas phase compounds including CO and hydrocarbons. The relatively poor closures may be partly due to error in the primary air and fuel flow measurements or in the gas composition due to the exclusion of higher molecular weight hydrocarbon and other gases from the analysis. The nitrogen balances, however, also show poor closures using direct air flow measurements as do some of the O and H balances. Sulfur showed mixed recovery from a low of 45 % to excess at 322 %. In all cases, except for NPF, which was 42%, Cl was in excess ranging from 138% for RSF to 2880% for SLF. The low concentrations in most fuels lead to high sensitivity in the balances for these elements. A substantial fraction of Cl, for SLF, is contained in the gas phase.

Spent bed material contains carbon and ash along with silica and alumina from the original bed media. The alumina recovery varied from 13 % to 114 % with 49% to 116% for silica. The titanium, iron and phosphorous recoveries are mixed, ranging from 13 % to 99 % for titanium, 64 % to 606 % for iron and 88 % to 290 % for phosphorous. Recovery of potassium and calcium are mixed and range from 65 % to 620 % and 59 % to 139 % respectively. Magnesium and sodium are also mixed with closures ranging from 61 % to 2423 % for magnesium and 47 % to 152 % for sodium. In general, element closures for these gasification tests were poor.

There was poor correlation r^2 = 0.28 between carbon closure and bed average temperature. Higher efficiencies with higher fuel volatile contents, however, suggests that errors in analysis of solids recovered from the horizontal pass and cyclone are contributing to poor element closures. The larger mass of solids in the horizontal pass and cyclone catch (associated with low volatile and low efficiency fuels) would have a greater impact on closures when errors in the solids analysis are present. Lower efficiency with lower volatile content is expected if lower volatiles are associated with higher fixed carbon that is not gasified, rather than just higher ash, however, this is not always the case (e.g., sludge has low fixed carbon). Overall elemental balances are impacted by the concentration of each element and recoveries for elements present only in small quantities in the fuel typically deviate substantially from 100% due to large experimental uncertainties relative to original concentration.

5.12 Uncertainty Analysis

Detailed results for an independent assessment of uncertainty analyses, including tables with individual component errors, are located in Appendix A. Uncertainty analyses were conducted for ASF 1 and SLF 2. For each fuel, presumed instrument and sampling errors were combined to yield individual expected measurement errors as well as an overall experimental uncertainty. Specifically listed are errors associated with GC gas concentrations for energy carrier gases (CO, H_2, and CH_4), NH_3 concentration, and balances for carbon, aluminum, and power.

The expected errors were determined by computing an experimental uncertainty associated with each measurement of each experiment (for ASF 1 and SLF 2). The aggregate of these individual uncertainties represents the total absolute uncertainty for a given parameter of interest (i.e. carbon closure, power balance, etc.). Once the errors were determined, experimental closures for carbon and aluminum were compared to see if they were within the expected error.

GC gas concentrations

For both ASF1 and SLF2, each individual gas concentration (CO, H_2 and CH_4) determined by GC has an expected experimental error between 2 – 3% absolute. This overall absolute error is comprised of sampling error, GC/column error and error associated with the GC detector signal acquisition and conversion. While a concerted effort was made to account for all errors affecting the GC concentrations, there may be additional errors that would lead to yet higher uncertainty. These errors may include the following: the GC results may deviate by a larger amount than estimated due to calibration errors, inadequate purging of sample extraction syringe and gas leakage from sample flasks, and averaging of discrete gas compositions to represent the average gas composition over the entire length of the test run.

A comparison of the GC concentrations and the continuous analyzer concentrations (from Chapter 2, Figures 2.10 and 2.12) shows differences as high as 5 and 8% absolute for CO and H_2 respectively. The CO concentrations as determined by continuous analysis, however, do not improve carbon balance closure (all continuous CO measurements were lower than the GC values) but the continuous concentrations for H_2 do, although the improvement is less the 1% absolute.

Ammonia

Gas phase ammonia concentration is expected to be determined to within an overall error of 4 - 5%. Error associated with ammonia concentration is a function of impinger volumes, sampling electrode error, gas volume and temperature. Ammonia, however, has little impact on closure for carbon, aluminum, or power.

Carbon and aluminum balances

The experimental closures for carbon and aluminum fell outside the uncertainty range for both ASF1 and SLF2. Uncertainties computed for the carbon balance were approximately 15 and 10% absolute and for the aluminum balance the uncertainties were 22 and 8% absolute respectively for ASF1 and SLF2 (for both fuels).

The primary reasons for failing to close material balances within the expected uncertainty are likely associated with measurements of air flow, fuel feed rate, and gas concentrations. Closing the carbon and nitrogen balances with air flow only, for example, suggests that actual air flow measurements are low (relative average difference using air to close carbon and nitrogen balances of approximately 140 and 90% respectively). The calibrated rotameters, procured from the manufacturer, were initially checked against a hot film mass flow meter. An additional calibration check of the rotameters against a dry test meter suggests the rotameters read low by an average of less than 8% over the full range of flow. At the normal primary air flow rate of 20 L min^{-1} used in the experiments however, the rotameter indicated 2 L min^{-1} higher than the dry test meter, while the feeder purge air rotameter indicated 2 L min^{-1} lower, compensating for the error in the primary air flow. Although the nitrogen balances as well as the carbon balances suggest errors associated with the air flow measurements, there is no direct evidence that these errors are of the magnitude required to close these balances.

Closing the carbon balance with fuel only suggests that fuel rate measurements might, on average, have been high by about 28%. Sludge, however, represents the extreme value and removing sludge from the average decreases the error closer to approximately 20%. Fuel feed for each type of fuel was calibrated prior to the experiments and there is little reason to expect that errors in fuel feed rate alone are responsible for the failure to close the element balances.

Gas concentrations in general represent an average of about 35 % of the total expected uncertainty in the carbon balance, but in at least one case (SLF 2) and for reasons not fully known the actual error is obviously larger than assumed. The major uncertainty with aluminum, for both fuels, is associated with the ultimate analysis of the fuel and uncertainties associated with recovered material in the bed, horizontal pass and cyclone. Specifically, when the fuel Al concentration is very low, small analysis errors can lead to large closure errors.

Power balance

The uncertainty for the power balance is approximately 13 and 17% absolute for ASF1 and SLF2 respectively, however, the balance calculation takes no account of heat losses from the system, hence closure within the uncertainties would not be expected. The power balances are inherently low because a significant amount of power is unaccounted for as a system loss (heat loss) in each fuel test. Like the other balances, the power balance is impacted by air flow, fuel feed rate, gas concentrations and to a lesser extent fuel HHV although the error associated with the latter is generally very small.

The results do not indicate that any one of the three principal measurements of fuel feed rate, air flow rate, and gas composition is alone responsible for element closure errors being larger than the expected errors, or that there is any particular failure in instrument

or meter calibration. Carbon and nitrogen balances can be closed in most cases with relative errors of the order of 10 to 20% associated with each of the three measurements. This implies that the independent assessment of errors making up the overall experimental uncertainty underestimates certain errors, especially in sampling. Further efforts will be needed to identify and reduce such errors.

5.13 Metals

Due to budget limitations, a metals analysis was performed only on SLF, the fuel anticipated to have higher concentrations of regulated heavy metals. The metal analysis for SLF showed the highest concentrations for Cu and Zn. Mercury was reported as non-detectable, but the samples were first ashed at 600° C.
Measured concentrations for the heavy metals Ar, Cd, Cu, Pb, Ni, Se and Zn were all well below the federal limits for sludge. See Table 3.7 for the Federal limits of heavy metals.

5.14 Power Balance

The power balances in general had a substantial fraction in unaccounted losses. Power balance is defined in equation 5.2.

Power Balance = Output Power/Input Power [5.2]

Output power = power of bed, horizontal pass, cyclone, tar, particles and stack in kW
Input power = power of moist fuel and moist air in kW

The power balance varied from 55 % for WWF to 92 % for SLF. Reasons for the power balances being low include system losses to the surroundings that were not measured or otherwise quantified, uncertainties associated with determining the stack flow rate, loss of some material on recovery, such as small amounts of material still remaining in the reactor after sample recovery.

Hot and cold gas efficiencies were also consistently low, again possibly due to errors in the air and/or fuel feed rate measurements leading to low stack gas flow rate determinations and errors associated with gas composition measurements. The correlation between hot and cold gas efficiencies and volatile content of the fuel is shown in Figure 5.4. The correlation coefficients of r^2 = 0.64 and 0.62, for hot and cold gas efficiencies respectively are good and show that for this group of fuels, those fuels with a higher volatile content generally had higher hot and cold gas efficiencies. Because cyclone exit temperature was generally low, hot gas efficiency shows relatively good correlation with cold gas efficiency.

Closing the carbon balance by increasing air flows increased both hot and cold gas efficiencies by 46%. Hot gas efficiencies after the carbon balance was closed were in the range of 42 to 65% and cold gas efficiencies were in the range of 40 to 63%.

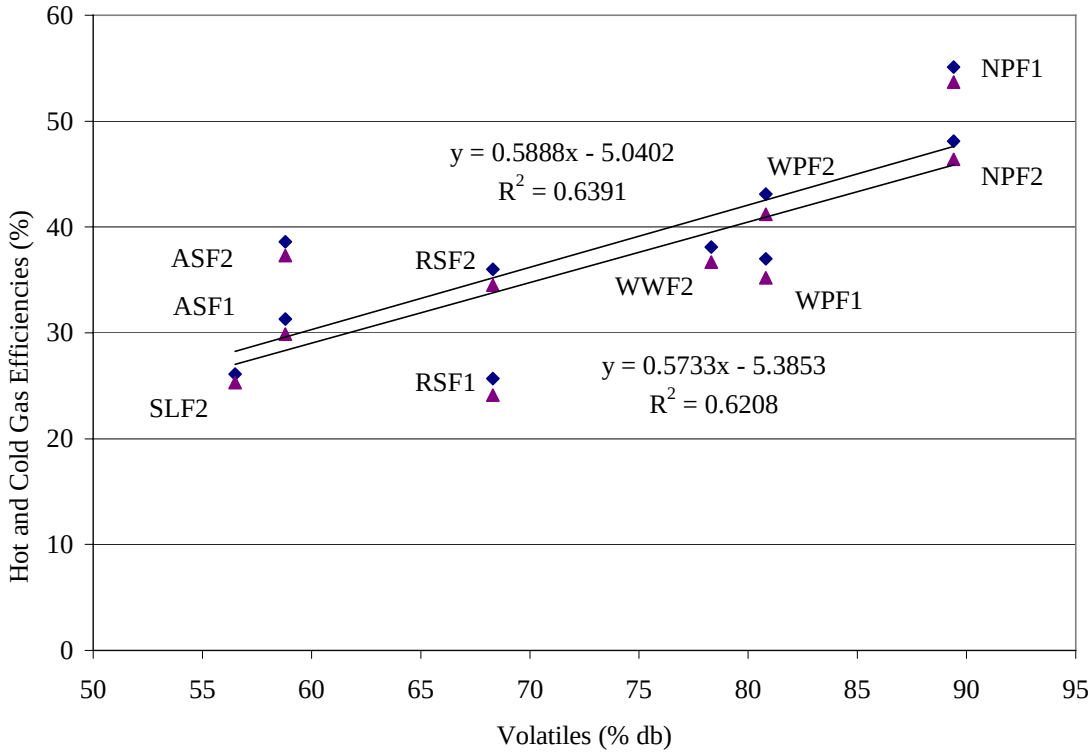

Figure 5.4 Hot (diamonds) and cold (triangles) gas efficiencies versus volatile content of fuel.

5.15 Model Results

Model results are discussed in detail in Chapter 4. The CSFB software consistently predicted low values for energy carrier gases CO, H_2 and CH_4. In order to use this model on further gasification studies with the reactor used for this experimental work, the model would need revision, probably of the kinetics module leading to a modified devolatilization routine (to allow higher total carbon conversion) and/or adjusted kinetic coefficients. The model's author did make a concerted effort to calibrate the model after seeing the poor results of the original modeling effort. That effort, provided in a follow-on patch, produced results that were better but still off and of little predictive or design value.

Gas composition predictions using the STANJAN model were also much different than the experimental values. In general STANJAN gas predictions were mostly higher with some exceptions than experimental values (some higher and some lower) even when the atom populations were adjusted for carbon, hydrogen, nitrogen and oxygen in solid residues collected in the spent bed, horizontal pass and cyclone locations.

As delineated in Chapter 4, there are a number of possible reasons for the disparity between the equilibrium plots and the experiment values. Perhaps the most important reason is that the fluidized bed that was used for the experiments is short and the residence time is less than the interval time needed to complete reactions. Deviations

from equilibrium might occur for two primary reasons: 1) continued evolution of gases from solids not modeled by the equilibrium assumption, and 2) use of a model temperature different from the true but unknown equilibrium temperature of the evolved gases. Equilibrium temperatures yielding similar compositions to the experiments are all lower than peak reactor temperatures, lending some credence to the latter.

The experimental concentrations typically correspond to equilibrium values that fall within a temperature range in a highly sensitive region that covers an average span approximately 80 - 100 K wide about 200 – 300 K less than the peak reactor temperatures. Although the average peak bed temperature was used for modeling STANJAN, this temperature may not be the most appropriate based on the equilibrium model outputs.

Table 5.6 Equilibrium temperature to match experimental temperature

Fuel	Equilibrium temperature to match experimental temperature K			Experimental temperature* K	ΔT_{CO} K	ΔT_{H2} K	ΔT_{CH4} K
	CO	H_2	CH_4				
ASF	840	780	912	1023	183	243	111
WPF	875	750	877	1013	138	263	136
RSF	773	700	883	1058	285	358	175
WWF	881	795	833	1098	217	303	265
SLF	776	875	830	1048	272	173	218
NPF	893	742	840	1073	180	331	233
Mean	840	780	863	1052	213	279	190

*determined at peak reactor temperature

REFERENCES

Agarwal, P.K. and La Nauze, R.D., 1989. Transfer processes local to the coal particle: a review of drying, devolatilization and mass transfer in fluidized bed combustion. Chemical Engineering Research Design 67: 457-480.

Allen, J.D. and Lee, T.M., 1974. Evaluation of the measurement of oxides of nitrogen in combustion products by the chemiluminescence method. Journal of the Institute of Fuel 25: 275 – 280.

Antal, M.J. Jr., 1983. Biomass pyrolysis: a review of the literature. Part I: carbohydrate pyrolysis. In: Boer, K.W. and J.A. Duffie (eds.), Advances in Solar Energy 1: 13-17 American Solar Energy Society, Boulder, CO.

Anwer, J. and Pyle, D.L., 1974. Proceedings of the International Symposium on Fluidization and its Applications, October 1-5, 1973, Toulouse, France.

Arand, J.K., Muzio, L.J., and Sotter, J.G., 1980. Urea reduction of NO_x in combustion effluents. U.S. Patent 4,208,386.

Babcock and Wilcox, 1992. Chapter 16. Atmospheric pressure fluidized-bed boilers. Steam, 40th edition, Babcock and Wilcox, Barberton, OH.

Bacon, D.W., Downie, J., Hsu, J.C. and Peters, J., 1985. Modeling of fluidized bed wood gasifiers. In: Fundamentals of Thermochemical Biomass Conversion. R.P. Overend., T.A. Miline and K.L. Mudge (eds). Elsevier Applied Science Publishers, London, England and New York, N.Y., 717-732.

Bain, R.L., Overend, R.P., Craig, K.P., 1996. Biomass-fired power generation. Proceedings of the Biomass Usage for Utility and Industrial Power. Engineering Foundation, New York, N.Y.

Bain, R.L., Overend, R.P., Craig, K.P., 1998. Biomass-fired power generation. Fuel Processing Technology 54: 1-16.

Bamford, C.H., Crank, J., Malan, D.H., 1945. The Combustion of Wood. Part 1. Proceedings of the Cambridge Philosophical Society, Vol. 42.

Bakker, R.R., Jenkins, B.M., Williams, R.B., Yomogida, D.E., Blunk, S.L., Pfaff, D., Goronea, M., 2000. Fuel Selection and Furnace Control in the Reduction of Operating Costs for Biomass Boilers, Vol. 3. Report prepared for California Energy Commission, University of California, Davis, CA.

Bakker-Dhaliwal, R., Jenkins, B.M., Lee, H. and Bernheim, 1998. Rice straw harvesting and handling for off-field utilization. Annual Report presented to U.S. Department of Agriculture, University of California, Davis, CA.
Baxter, L.L., 1993. Ash deposition during biomass and coal combustion: a mechanistic approach. Biomass and Bioenergy 4(2): 85-102

Bi, H.T. and Grace, J.R., 1995. Effects of measurement method on velocities used to demarcate the onset of turbulent fluidization. Chemical Engineering Journal 57: 261-271.

Blair, D.W., Wendt, J.O., and W. Bartok, 1976. Evolution of nitrogen and other species during controlled pyrolysis of coal. Sixteenth Symposium (International) on Combustion, 475-489.

Boelle, G. 1997. Validation of a two-fluid model applied to the simulation of dense fluidized beds, Ph.D. Dissertation Report HE-44/97/004/A, EDF, Chatou, France.

Borman, G.L. and Ragland, K.W., 1998. Combustion Engineering. McGraw Hill Companies, New York, N.Y.

Bowman, C.T., 1993. Compressibility effects in a reacting mixing layer. Twenty Fourth Symposium (International) on Combustion. The Combustion Institute, Pittsburgh, PA, 859-865.

Buekens, A.G. and Shoeters, J.G., 1982. Modeling of biomass gasification. In: Fundamentals of Thermochemical Biomass Conversion. R.P. Overend, T.A. Miline and K.L. Mudge (eds). Elsevier Applied Science Publishers, London, England and New York, N.Y., 619-689.

Burch T.E., Chen, W.Y., Lester, T.W., and Sterling A.M., 1993. Interaction of fuel nitrogen with nitric oxide during reburning with coal. Combustion and Flame 98: 391-401.

Carman H. and Amudson, N., 1979. Fluidized bed gasification reactor modeling. Model description and numerical results for a single bed. Industrial Engineering Chemical Processing Design Development 18: 80-102.

Chagger, H.K., Goddard, P.R., Murdoch, P. and Williams, A., 1991. Effect of SO_2 on the reduction of NO_x by reburning with methane. Fuel 70: 1137-1142.

Chen, T.P. and Saxena, S.C., 1977. Parametric studies on the combustion of char in fluidized beds operated under steady state conditions. Fuel 33: 145-153.

Chen, S.L., Cole, J.A., Heap, M.P., Kramlich, J.C., McCarthy, J.M., and Pershing, D.W., 1988. Proceedings of the Combustion Institute 22: 1135-1145.

Corella, J., Herguido, J. and Gonzalez-Saiz, J. 1989. Steam gasification of biomass in fluidized bed - Effect of the type of feed stock. In: Pyrolysis and Gasification. G.L. Ferrero, K. Maniatis, A. Buekens and A.V. Bridgewater (eds). Elsevier Applied Science, London, England, 618-623.

Coin, C.D., Kahraman, H. and Reifenstein, A.P., 1995. An improved ash fusion test. In Proceedings of the Engineering Foundation Ash Conference. Plenum Publishing, Waterville Valley, N.H., 541-556.

Chum, H.L., T.A. Milne, D.K. Johnson, and F.A. Agblevor, 1993. Feedstock characterization and recommended procedures. Proceedings First Biomass Conference of the Americas, Burlington, VT. NREL, Golden, CO, Vol. 3: 1685-1703.

Davidson, J.F. and Harrison, D., 1963. Fluidized particles. Cambridge University Press, London, England and New York, N.Y.

Dayton, D.C., French, R.J., Milne, T.A., 1995. Direct observation of alkali vapor release during biomass combustion and gasification. 1. Application of molecular beam/mass spectrometry to switchgear combustion. Energy and Fuels 9: 855-865.

de Souza-Santos., 2001. Comprehensive simulator for fluidized-bed equipment, Version 3.5: 1-7. Technologix Corporation, Chicago, Il.

Desrosiers R., 1981. Thermodynamics of gas-char reactions. In: Biomass Gasification Principles and Technology. T.B. Reed (ed). Noyes Data Corporation, Park Ridge, N.J., 119-153.

Domalski, E.S., Jobe, Jr., T.L., and T.A. Miline, 1987. Thermodynamic data for biomass materials and waste components. American Society of Mechanical Engineers, New York, N.Y.

Double, J. M. and Bridgewater, A.V., 1989. Sensitivity of theoretical gasifier performance to system parameters. In: Energy From Biomass. W. Palz, J. Coombs and D.O. Hall (eds.). Elsevier Applied Science Publishers, London, U.K., 915-919.

Driscoll, J.F., Chen, R.H., and Yoon, Y., 1992. Nitric oxide levels of turbulent jet diffusion flames: effects of varying residence time and Damkohler number. Combustion and Flame 88: 37-49.

Ebeling, J.M., and Jenkins, B.M., 1985. Physical and chemical properties of biomass fuels. Transactions of the ASAE 28(3): 898-902.

Enwald, H., 1997. A numerical study of the fluid dynamics of bubbling fluidized beds. Ph.D. Dissertation, Department of Thermo and Fluid Dynamics, Chalmers University of Technology, Goteborg, Sweden.

Ergudenler, A., Hamdullahpur, F., Ghaly, A.E., Al-Taweel, A.M., 1997. Mathematical modeling of a fluidized bed straw gasifier. I. Model Development, Energy Sources Journal 19(10): 1065-1084.

Ergun, S., 1952, Fluid flow through packed columns. Chemical Engineering 48: 89-94.

Fang, Y., Huang, J., Wang, Y., Zhang, B., 2000. Experiment and mathematical modeling of a bench-scale circulating fluidized bed gasifier. Fuel Processing Technology 69: 29-44.

Fenimore C.P., 1976. Prompt NO_x. Combustion and Flame 26: 249-267.

Fenimore C.P., 1979. Studies of fuel-nitrogen species in rich flame gases. Seventeenth Symposium (International) on Combustion, The Combustion Institute, Pittsburgh, PA, 1979, 661-671.

Fiveland, W.A., and Wessel, R.A., 1991. Model for Predicting Formation and Reduction of Nitric Oxide Pollutants in Three-Dimensional Furnaces Burning Pulverized Fuel, Journal of the Institute of Energy 64: 41-54.

Folsom, B.A., Sommer, T.M., Payne, R., 1991. Demonstration of combined NO_x and SO_2 emission control technologies involving gas reburning. AFRC-JFRC International Conference on Environmental Control of Combustion Processes, Honolulu, HI.
Foscolo, F.U. and Gilibaro, L.B., 1984, A fully predictive criterion for the transition between particulate and aggregate fluidization. Chemical Engineering Science 39: 1667-1675.

Furman, A.H, Kimura, S.G., Ayala, R.E. and Joyce, J.F., 1992. Biomass gasification pilot plant study – Final Report to EPA. EPA-600/R-93-170. GE Research and Development Corporation, Irvine, Ca.

Geldart, D., 1973. Types of gas fluidization. Powder Technology 7: 285-292.

Gil, J., Corella, J., Aznar, M.P., Caballero, M.A., 1999. Biomass gasification in atmospheric and bubbling fluidized bed: Effect of the type of gasifying agent on the product distribution. Biomass and Bioenergy 17: 389-403.

Glarborg, P. and Hadvig, S., 1991. Development and test of a kinetic model for natural gas combustion, report. Nordic Gas Technology Center, Copenhagen, Denmark. ISBN 87-89309-44-8.

Graboski, M. and Bain, R., 1981. Properties of biomass relevant to gasification. In: Biomass Gasification-Principles and Technology. T.B. Reed (ed). Noyes Data Corporation, Park Ridge, N.J.

Grace, J.R., 1984. Generalized models for isothermal fluidized bed reactors. In L.K. Doraiswamy (ed.), Recent Advances in the Engineering Analysis of Chemically Reacting Systems, Wiley Edition. Chapter 13, 237-255, New Delhi, India.

Grace, J.R., 1986. Chapter 2. Fluidized beds as chemical reactors. In: Gas Fluidization Technology. D. Geldart (ed). John Wiley & Sons Inc., New York, N.Y.

Guo, B., Li, D., Cheng, C., Lu, Z. and Shen, Y., 2000. Emulation of biomass gasification with hybrid neural network model. Bioresource Technology 76: 77-83.

Harding, N.S., Adams, B.R., 2000. Biomass as a reburning fuel: a specialized cofiring application. Biomass and Bioenergy 19: 429-445.

Hazen Research, 1995. Fuels Laboratory Quality Assurance/Quality Control Program. Hazen Research, Inc., Golden, CO.

Hill, S.C., Smoot, L.D. and Xu, H., 1998. NO_x control through reburning. Progress in Energy and Combustion Science 24: 385-408

Hill, S.C. and Smoot, D.L., 2000. Modeling of nitrogen oxides formation and destruction in combustion systems. Progress in Energy and Combustion Science 26: 417-458.

Ho, Chen, Seeker and Maly, 1993. Methods for controlling N_2O emissions and for the reduction of NO_x emissions in combustion systems while controlling N_2O emissions. US Patent 5,270,025.

Hori, M., 1988. Twenty-second Symposium (International) on Combustion, The Combustion Institute, Pittsburgh, PA, 1979, 647-654.

Howard, J.R., 1989. Fluidized Bed Technology – Principals and Applications. IOP Publishing Ltd., Bristol, England. ISBN 0-85274-055-7

Huilin, L., Guangbo, Z, Rushan, B., Yongjin, C. and Gidaspow, D., 1999. A coal combustion model for circulating fluidized bed boilers. Fuel 79: 165-172.

Hura, H.S. and Breent, B.P., 1993. Chemical kinetic simulation of nitric oxide reduction during natural gas reburning in pulverized coal fired boiler: combustion modeling, cofiring and NO_x control. ASME Fact 17: 51-69.

Ishii, M., 1975. Thermo-fluid dynamic theory of two-phase flow. Ph.D. Dissertation. Eyralles press, Paris, France.

Ishimura, D.M., 1994. Investigation of nitrogenous compound formation in biomass gasification. MSME thesis, University of Hawaii, HI.

Jacobs, J. P., 1999. The future of fluidized-bed combustion. Chemical Engineering Science 54: 5559-5563.

Jenkins, B.M., 1989. Physical Properties of Biomass. In: Hall, D.O., (ed.), Biomass Handbook. Gordon and Breach Science Publications, New York, N.Y., 860 - 891.

Jenkins, B.M., 1993. Properties of Biomass. In: Wiltsee, G.A. (ed.), Biomass Energy Fundamentals, Vol. 2: Appendices. EPRI TR-102107, Electric Power Research Institute, Palo Alto, California.

Jenkins, B.M., Baxter, L.L., Miles, T.R., Miles, T.R. Jr., Oden, L.L., Bryers, R.W., Winther, E., 1994. Composition of ash deposits in biomass fueled boilers: results of full-scale experiments and laboratory simulations. 1994 International Summer Meeting, Kansas City, Kansas, ASAE Paper No. 946007, ASAE, St. Joseph, MI.

Jenkins, B.M., Bakker, R.R., and Wei, J.B., 1996. On the properties of washed straw. Biomass and Bioenergy 10(4):177-200.

Jenkins, B.M., Williams, R.B. Bakker, R.R., Blunk, S., Yomogida, D.E., Carlson, W., Duffy, J., Bates, R., Stucki, K. and Tiangco, V., 1999. Combustion of leached rice straw fuel for power generation. In: Overend, R.P. and E. Chornet (eds.), Biomass: a growth opportunity in green energy and value-added products. Pergamon, Oxford, U.K.,1357-1363.

Jenkins, B.M., Baxter, L.L, Miles, T.R. Jr., Miles, T.R., 1998. Combustion properties of biomass. Fuel Processing Technology 54: 17 – 46.

Jennen, T., Hiller, R., Koneke, D. and Weinspach, P. M., 1999. Modeling of gasification of wood in a circulating fluidized bed. Chemical Engineering Technology 22: 10-22.

Joergensen, U. and Sander, B., 1997. Biomass requirements for power requirements for power production: how to optimize the quality by agricultural management. Biomass and Bioenergy 12(3):145-147.

Jones, J.M., Pourkashanian, M., Williams, A. and Hainsworth, D., 2000. A comprehensive biomass combustion model. Renewable Energy 19: 229-234.

Kaupp, A. and Goss, J.R., 1981. Technical and Economical Problems in the Gasification of Rice Hulls-Physical and Chemical Properties. Energy in Agriculture 1(3): 201-234

Kaupp, A. and Goss, J.R., 1984. Small scale gas producer-engine systems. Priedr Vieweg & Sohn, Wiesbaden, W. Germany.

Kee, R.J., Miller, J.A. and Jefferson, T.H., 1980. Sandia Tech. Rep. SAND80-8003 (Sandia Natational Laboratory) CHEMKIN: A General-Purpose, Problem Independent, Transportable, Fortran Chemical Kinetics Code Package, Reaction Design. San Diego, CA 92121.

Kicherer A., Spliethoff H., Maier H., Hein K.G., 1994. The effect of different reburning fuels on NO_x-reduction. Fuel: 73(9): 1443-1446

Kline, S.J., 1985. The purposes of uncertainty analysis, Journal of Fluids Engineering 107: 153-160.

Kosky P. and Floess, J., 1980. Global model of countercurrent coal gasifiers. Industrial Engineering Chemical Processing Design Development 19: 586-592.

Kramlich, J.C., Linak, W.P., 1994. Nitrous oxide behavior in the atmosphere, and in combustion and industrial systems. Progress in Energy and Combustion Science 20: 149-202.

Kunii, D. and Levenspiel, O., 1987. Fluidization Engineering (1st edition). Wiley. New York, N.Y.

Kulasekaran, S., Linjewile, T.M. and Agarwal, P.K., 1998. Mathematical modeling of fluidized bed combustion 3. Simultaneous combustion of char and combustible gases. Fuel 78: 403 –417.

Latham, R., Potter, O.E., 1970. Predicting gas back mixing. Chemical Engineering Journal 1:152-157.

Levin, E.M., McMurdie, H.F. and Hall, F.P., 1956. Phase diagrams for
ceramists, Vol. 1. The American Ceramic Society, Inc., Columbus, OH, 6.

Levy, J.M., Chen, L.K., Sarofim, A.F. and Baer, J.M., 1981. Eighteenth Symposium (International) on Combustion. The Combustion Institute, Pittsburgh, PA, 111.

Li, B.W., Wu, K.T., Moyeda, D.K. and Opayne, R., 1993. Use of computer models for reburning/cofiring boiler performance evaluations: Combustion modeling, cofiring and NO_x control. ASME Fact 17: 87-94.

Lim, K.S. Gururajan, V.S. and Agarwal, P.K., 1993. A comparative analysis of two solid mixing models suitable for coal fluidized bed combustors and gasifiers. Chemical Engineering Science 48: 2251.

Lissianski, V.V., Zamansky, V.M., and Maly, P.M., 1999. First Joint Meeting of the U.S. Sections of the Combustion Institute, Paper No. 194, Washington, D.C.

Lissianski, V.V., Zamansky, V.M., Maly, P.M. and Sheldon, M.S., 2000. Proceeding of the Combustion Institute 28: 2475-2482.

Lissianski, V.V., Zamansky, V.M., Maly, P.M. and Sheldon, M.S., 2001. Effect of metal-containing additives on NO_x reduction in combustion and reburning. Combustion and Flame 125: 1118-1127.
Lyon, R.K., 1975. Method for the reduction of the concentration of NO in combustion effluents using ammonia. U.S. Patent 3,900,554.

Maly, P.M., Zamansky, V.M., Ho, L. and Payne, R., 1998. Alternative fuel reburning. Fuel 78: 327-334.

Maniatis, K., Bridgewater, A.V. and Buekens, A., 1988. Fluidized bed gasification of wood. In: Research in Thermochemical Biomass Conversion. A.W. Bridgewater and Kluester (eds). Elsevier Applied Science, London, U.K., 1094-1105.

Matsen, J.M., 1996. Scale-up of fluidized bed processes: Principle and practice. Powder Technology 88: 237-244.

Miles, T.R., Jr., Miles, T.R., Baxter, L.L., Jenkins, B.M., Oden, L.L., 1993. Alkali slagging problems with biomass fuels. In: Proceedings of the First Biomass Conference of the Americas, August 30 – September 2 in Burlington, VT, National Renewable Energy Laboratory, Golden, CO.

Miles, T.R., Jr., Miles, T.R., Baxter, L.L., Bryers, R.W., Jenkins, B.M., Oden, L.L., 1995. Alkali deposits found in biomass power plants – a preliminary investigation of their extent and nature. Summary report for the National Renewable Energy Laboratory, NREL Subcontract TZ-2-11226-1, Golden, CO.

Mitchell, R. and Campbell, P., 2001. Laboratory determination of apparent and true density. Department of Mechanical Engineering, Stanford University, Palo Alto, California, 94305, Personal communication.

Mohsenin, N.N., 1970. Physical properties of plant and animal materials. Gordon and Breach Science Publishers, Inc, New York, NY., 71.

Myerson, A.L., Taylor, F.R., Faunce, B.G., 1957. Ignition limits and the products of multistage flames of propane-nitrogen dioxide mixtures. Proceedings of the 6th International Symposium on Combustion. The Combustion Institute, Pittsburgh, PA, 154.

Natarajan, E., Ohman, M., Gabra, M., Nordin, A., Liliedahl, T. and Rao, A.N., 1998. Experimental determination of bed agglomeration tendencies of some common agricultural residues in fluidized bed combustion and gasification. Biomass and Bioenergy 15(2): 163-169.

Navarez, I., Orio, A., Aznar, M.P., Corella, J., 1996. Biomass gasification with air in an atmospheric bubbling fluidized bed: Effect of six operational variables on the quality of the producer raw gas. Industrial Engineering Chemical Research. 35(7): 2110 - 2120.

Ohman, M., Nordin, A., 1997. A new method for quantification of fluidized bed agglomeration tendencies: a sensitivity analysis. Energy and Fuels 12: 90-94.

Ohman, M., Anders, N. 1999. Bed agglomeration characteristics during fluidized bed combustion of biomass fuels. Energy and Fuels 14: 169-178.

Olowson, P. and Almstedt, A.E., 1990, Influence of pressure and fluidization velocity on the bubble behavior and gas flow distribution in a fluidized bed. Chemical Engineering Science 45: 1733-1741.

Overend, R.L., Bain, R.L. and Craig, K.R., 1998. Biomass-fired power generation. Fuel Processing Technology 54: 1-16.

Palonen, J. and Nieminen, J., 1998. Thermie demonstrates biomass CFB gasifier at Lahti. Modern Power Systems, February, 37-41.

Pershing D.W. and Wendt J.L., 1979. Relative contributions of volatile nitrogen and char nitrogen to NOx emissions from pulverized coal flows. Industrial Engineering Chemical Process Design and Development 18: 60.

Pfaff, D., Jenkins, B.M. and Turn, S.Q., 2001. Elemental gas-particle partitioning in fluidized bed combustion and gasification of biomass. In: Bridgwater, A.V. (ed.), Progress in Thermochemical Biomass Conversion, Blackwell Science, Oxford, 713-729.

Powell, N.H. and Sarner, S.F., 1959. The use of element potentials in analysis of chemical equilibrium, Vol. 1, General Electric Co., Report R59/FPD. Irvine, CA.

Prins, W., 1987. Fluidized bed combustion of a single carbon particle, Ph.D. Dissertation, Twente University of Technology, The Netherlands, 1987.

Prudy, M., Felder, R.M. and Ferrell, J.K., 1981. Coal gasification in a pilot scale fluidized bed reactor I. Gasification of a devolatilized bituminous coal. Industrial Engineering Chemical Processing Design Development 20: 675-682.

Raask, E., 1985. Mineral Impurities in Coal Combustion. Hemisphere Publishing, Washington, D.C.

Reed, R.D., 1969. Process for the disposal of nitrogen oxide. John Zink Company, US Patent 1,274,637.

Reynolds, W.C., 1983. STANJAN Computer Code. Thermosciences Division, Department of Mechanical Engineering, Stanford University, Palo Alto, California 94305.

Rowe, P.N., Partridge, B.A., and Lyall, E., 1964. Cloud formation around bubbles in gas fluidized beds. Chemical Engineering Science 19: 973-985.

Salour, D., Jenkins, B.M., Vafaei, and M., Kayhanian, 1993. Control of in-bed agglomeration by fuel blending in a pilot scale straw and wood fueled AFBC. Biomass and Bioenergy 4: 117-133.

Schiefelbein, G. F., 1989. Biomass thermal gasification research: Recent results from the United States DOE's research program. Biomass 19: 145-159.

Seeker, Maly and Zamansky, 1998. Advanced reburning methods for high efficiency NO_x control. US Patent 5,756,059.

Shaw, J.T., 1973. Progress Review No. 64: A commentary on the formation, incidence, measurement, and control of nitrogen oxides in flue gas. Journal of the Institute of Fuel 170 – 178.

Smoot, L.D., Hill, S.C., Xu, H., 1997. NO_x control through reburning. Energy and Combustion Science 24: 385-408.

Sotudeh-Gharebaagh, R., Legros, R., Chaouki, J. and Paris, J., 1997. Simulation of circulating fluidized bed reactors using ASPEN PLUS. Fuel 77: 327-337.

Stull, D.R., Prophet, H. (Project Directors), 1971. JANAF Thermochemical Tables, Second Edition, National Standards Reference Data Series, National Bureau of Standards (Washington) 37: 1141.

Syamlal, M., 1994. MFIX Documentation, User's Manual, DOE/METC-95/1013 (DE95000031), US Department of Energy, Washington, D.C.

Tampella Power, 1992. Circulating Fluidized Bed Boilers (CFB), USA-Finland Executive Seminar on Power Generation and the Environment, Orlando, FL, Nov, 16, 1992. Tampella (DBA Kvaerner) Power, 8008 Corporate Center Drive, Charlotte, N.C.

Tillman, D.A., 2000. Biomass cofiring: The technology, the experience, the combustion consequences. Biomass and Bioenergy 19: 365-384.

Thorn, W.F., Hoskins, R.L. and Wilson, D., 1980. A study of the feasibility of cogeneration using wood waste as fuel. EPRI AP-1483. Electric Power Research Institute. Palo Alto, CA.

Toomey, R.D. and Johnstone, H.F., 1952, Gaseous fluidization of solid particles. Chemical Engineering 48: T60-T66.

Turn, S. Q., 1994. A transient model of a fixed-bed, open throat, co-current, rice hull gasifier. Ph.D. Dissertation, University of California, Davis, CA.

van den Aaren, F.G., Beenackers, A.A.C.M. and van Swaaij, W.P.M., 1986. Modeling of a fluidized bed wood gasifier. In: Fluidization. V.K. Ostergaard and A. Sorensen (eds). Engineering Foundation, New York, N.Y., 521-530.

Wall, T. F., Creelman, R.A., Gupta, R.P., Gupta, S., Coin, C. and Lowe, A., 1995. Coal ash fusion temperature-new characterization technique, and association with phase equilibria. In: Application of advanced technology to ash-related problems in boilers. L. Baxter and R. Desollar (eds)., Plenum publishing, Waterville Valley, N.H., 1995, 541-556.

Wang, Q., Luo, Z, Li, X, Fang, M, Ni, M and Cen, K., 1997. A mathematical model for a circulating fluidized bed (CFB) boiler. Energy 24: 633-653.

Wendt, J.L., Sternling, C.V., Matovich, M.A., 1973. Reduction of sulfur trioxide and nitrogen oxides by secondary fuel injection. Proceedings of the 14th International Symposium on Combustion. The Combustion Institute, Pittsburgh, PA., 897.

Werther, J., 1992. Scale-up modeling for fluidized bed reactors. Chemical Engineering Science 47: 2457-2462.

Werther, J. and Leckner, B., 2000. Scale-up of circulating fluidized bed combustion. Energy and Fuels 14: 1286-1292.

Weimer, A.E. and Clough, D.E., 1981. Modeling a low-pressure steam-oxygen fluidized bed coal gasifying reactor. Chemical Engineering Science 36: 549-567.

Williams, P.T. and Horne, P.A., 1994. The role of metal salts in the pyrolysis of biomass. Renewable Energy 4(1): 1-13.

Winter, F., Wartha C., Hofbauer, H., 1999. NO and N_2O formation during the combustion of wood, straw, malt waste and peat. Bioresource Technology 70: 39-49.

Zamansky, V.M., Folsom, B.A. and Seeker, W.R., 1996a. Advanced biomass reburning for high efficiency NO_x control. 7th National Conference Bioenergy 96, Nashville, TN, September 15-20. 898-904

Zamansky, V.M., Ho, L., Maly, P.M. and Seeker, W.R., 1997. Reburning promoted by nitrogen- and sodium-containing compounds, Twenty-Sixth Symposium (International) on Combustion. The Combustion Institute, Pittsburgh, PA, 2075-2082.

Zamansky, V.M., Tyson, T.J., Han D. and Mungal, M.G., 1999a. Prediction of NOx control by basic and advanced gas reburning using the two-stage lagrangian model. Combustion and Flame 119: 483-493.

Zamansky, V.M., B.M. Jenkins, T.R. Miles and V.M. Tiangco, 1999b. Hybrid combustion-gasification approach for environmentally safe utilization of biomass energy. In: Overend, R.P. and E. Chornet (eds.), Biomass: a growth opportunity in green energy and value-added products. Pergamon, Oxford, 1335-1340.

Zamansky, V.M., Sheldon, M.S., Maly, P.M., 1999c. Enhanced NO_x reduction by interaction of nitrogen and sodium compounds in the reburning zone, Twenty-Seventh Symposium (International) on Combustion. The Combustion Institute, Pittsburgh, PA, 3001-3008.

Zamansky, V.M., Lissianski, V.V., Maly, P.M., Ho, L., Rusli, D., and Gardiner, W.C., 1999d. Reactions of sodium species in the promoted SCNR process. Combustion and Flame 117: 821-831.

Zeldovich, Y.B., 1946. The oxidation of nitrogen in combustion and explosions. Acta Physicochim, U.S.S.R., 21: 577-593.

Appendix A

Uncertainty Analysis

Uncertainties associated with instruments and experimental techniques are very difficult to eliminate.

Uncertainties can be divided into one of two types of errors, bias errors and precision errors. Bias errors remain constant during a given series of measurements under fixed operating conditions. Precision errors will be observed as scatter in the measured data, and can be determined using statistics.

Since experimental runs were not run in replicates and no statistical data are available, uncertainty for these experiments was determined solely as bias error. Instrumentation

uncertainties varied and were generally 1 to 10% of reading. An example input and output sheet for the carbon balance for ASF 1 is included.

Some conditions of an experiment are dependent on parameters that cannot be directly measured with instruments. Therefore uncertainties associated with measured parameters can propagate in calculated parameters. Propagation error analysis is applied to errors in the measured parameters that propagate through to the final result when the final result is a functional relationship of one or more of the measured quantities.

Consider a set of measurements made to determine the result, $\dot{q}_{out}/\dot{q}_{in}$. The result can be expressed as a function of the independent variables, some of which are direct measurements.

For a calculated quantity, ψ, which depends on measured parameters, θ_i, the uncertainty, $\delta\psi$, can be found from equation A-1:

$$\partial\psi = \sqrt{\sum_{i=1}^{n}\left(\frac{\partial\psi}{\partial\theta_i}\partial\theta_i\right)^2} \qquad \text{[A-1]}$$

where $\partial\theta_i$ is the uncertainty of the measured parameter (Kline, 1985).

The partial derivatives are often described as sensitivity coefficients. They determine the contribution of uncertainty for their associated variable to the overall uncertainty. Uncertainty propagation is very useful in experimental design to isolate variables that are responsible for the majority of the error.

Results of uncertainty analysis, using the principles of Equation A-1 and based upon entering individual uncertainty values and totaling the overall uncertainty, are summarized in Table A-1. Additionally, individual calculation spreadsheets follow the summary table and are included for information in Tables A-2 through A-10. Two fuels, ASF 1 and SLF 2 were analyzed for gas concentrations, ammonia concentration, carbon and aluminum closures, and power balance uncertainties.

Table A-1 Results of Uncertainty Analysis for Calculated Parameters of ASF1 and SLF2

Parameter	Test Run	Symbol	Uncertainty (%) Absolute
Power Balance	ASF 1	$Power_{out/}$ $Power_{in}$	12.9
	SLF 2	$Power_{out}/Power_{in}$	16.6
Gas Concentrations (GC)	ASF 1	CO	2.4
(% volume in gas)		H_2	2.3
		CH_4	2.3
	SLF 2	CO	2.3
		H_2	2.4
		CH_4	2.3
Element Mass Balance	ASF 1	C	14.9
(kg_{out}/kg_{in})		Al	22.1
	SLF 2	C	10.0
		Al	8.1
NH_3	ASF 1		4.9
(concentration in gas % volume)	SLF 2		3.8

Table A-2
GC Uncertainty
ASF1 and SLF2

Test	Gas	Conc. [%]	Sampling Error [%] 5.0 Reading	GC/Column Error [%] 2.0 Absolute	Integrator Error [%] 1.0 Absolute	Absolute Total Error [%]
ASF 1	**CO**	19.7	1.0	2.0	1.0	**2.4**
	H_2	12.7	0.6	2.0	1.0	**2.3**
	CH_4	6.7	0.3	2.0	1.0	**2.3**
	CO_2	19.8	1.0	2.0	1.0	**2.4**
	N_2	39.7	2.0	2.0	1.0	**3.0**
	O_2	1.4	0.1	2.0	1.0	**2.2**
	Gas	Conc. [%]				
SLF 2	**CO**	11.6	0.6	2.0	1.0	**2.3**
	H_2	15.0	0.8	2.0	1.0	**2.4**
	CH_4	5.7	0.3	2.0	1.0	**2.3**
	CO_2	10.2	0.5	2.0	1.0	**2.3**
	N_2	53.0	2.7	2.0	1.0	**3.5**
	O_2	4.5	0.2	2.0	1.0	**2.2**

Table A-3
Ammonia Uncertainty
ASF 1

	Quantity	Error or Uncertainty (same units)
Impinger 1, ml	254.30	10
Impinger 2, ml	159.60	10
Impinger 3, ml	153.20	10
Electrode 1, mg/L	3646.00	25
Electrode 2, mg/L	145.00	10
Electrode 3, mg/L	20.00	10
Gas Volume, L	323.82	10
Temperature, K	293.00	2

Intermediate Calculations

Density of Ammonia Gas, g/L	0.71
Nitrogen in Impingers, mg N	953.3838
Nitrogen in Impingers, gmole N	0.068098843
Volume of NH3, L	1.637196323
Total Volume	13.54
Mole NH3/Mole Gas	0.00503029
Concentration, ppmv	5030.29

	New Quantity	**Concentration with error**	**Difference**	**Difference squared**
Impinger 1, ml	264.30	5221.66	-191.37	36621.53
Impinger 2, ml	169.60	5038.67	-8.38	70.20
Impinger 3, ml	163.20	5038.33	-8.04	64.68
Electrode 1, mg/L	3671.00	5063.66	-33.37	1113.82
Electrode 2, mg/L	155.00	5051.24	-20.95	438.73
Electrode 3, mg/L	30.00	5050.40	-20.11	404.25
Gas Volume, L	333.82	4880.34	149.95	22485.40
Temperature, K	295.00	5030.12	0.17	0.03
		Uncertainty, ppm		**247.38**
		Absolute Uncertainty, %		**4.92**

Table A-4
Ammonia Uncertainty
SLF 2

	Quantity	Error or Uncertainty (in same units)
Impinger 1, ml	235.60	10
Impinger 2, ml	158.30	10
Impinger 3, ml	152.10	10
Electrode 1, mg/L	8416.02	25
Electrode 2, mg/L	2204.58	10
Electrode 3, mg/L	37.78	10
Gas Volume, L	399.46	10
Temperature, K	293.00	2

Density of Ammonia Gas, g/L	0.71
Nitrogen in Impingers, mg N	2337.545664
Nitrogen in Impingers, gmole N	0.166967547
Volume of NH3, L	4.014145369
Total Volume	16.78
Mole NH3/Mole Gas	0.009948769
Concentration, ppmv	9948.77

	New Quantity	**Concentration with error**	**Difference**	**Difference squared**
Impinger 1, ml	245.60	10303.22	-364.50	132860.25
Impinger 2, ml	168.30	10041.61	-102.89	10586.35
Impinger 3, ml	162.10	9950.31	-11.59	134.33
Electrode 1, mg/L	8441.02	9973.54	-34.82	1212.43
Electrode 2, mg/L	2214.58	9955.39	-16.67	277.89
Electrode 3, mg/L	47.78	9955.13	-16.41	269.29
Gas Volume, L	409.46	9938.72	0.00	0.00
Temperature, K	295.00	9948.09	-9.37	87.80
		Uncertainty, ppm		**381.35**
		Absolute Uncertainty, %		**3.83**

Table A-5 ASF 1 Uncertainty
Carbon

	Experimental Value	Error in same units	Closure with Error	Difference	Difference Squared
Air					
Air flow rate, L/min	21.45	5	84.8	2.9	8.4
Air moisture content, (% wb)	0.40	0.05	81.9	0.0	0.0
Air temperature, C	21.00	1	81.9	0.0	0.0
Air Density, g/L	1.34	0.1	82.8	0.9	0.8
Fuel					
Fuel flow rate, g/min	115.75	23.1	68.3	-13.6	185.3
Fuel moisture content, (% wb)	9.00	1	81.9	0.0	0.0
Fuel ultimate analysis (%)	36.27	1	79.7	-2.2	4.6
Bed					
Bed In, g	866	1	82.0	0.1	0.0
Bed, HP and Cyclone Outputs					
Mass bed out, g	751.60	25	81.9	0.0	0.0
Mass HP out, g	1730.50	50	82.3	0.4	0.2
Mass cyclone out, g	507.30	25	82.0	0.1	0.0
Bed out ultimate analysis, (%)	2.23	1	82.3	0.4	0.1
HP ultimate analysis, (%)	34.64	1	82.7	0.8	0.6
Cyclone ultimate analysis (%)	25.63	1	82.2	0.3	0.1
HHV Bed Out, MJ/kg	1.50	0.2	81.9	0.0	0.0
HHV HP Out, MJ/kg	14.14	0.2	81.9	0.0	0.0
HHV Cyclone Out, MJ/kg	10.63	0.2	81.9	0.0	0.0
Stack					
Stack Gas (%)					
CO	19.70	2.4	84.4	2.5	6.3
CO_2	19.80	2.4	83.8	1.9	3.6
CH_4	6.70	2.3	84.7	2.8	7.8
H_2	12.70	2.3	82.9	1.0	1.0
N_2	39.70	3.0	80.5	-1.4	2.0
O_2	1.40	2.2	81.8	-0.1	0.0
Tar					
Tar concentration, mg/L	27.40	3.0	81.9	0.0	0.0
Tar, ultimate analysis (%)	68.43	1	82.0	0.1	0.0
HCN					
HCN, mg/L	2.30	0.1	81.9	0.0	0.0
Ammonia					
NH3, ppmv	5030.29	247.4	81.9	0.0	0.0
Miscellaneous					
Cp dry air, kJ/kg-K	1.03	0.02	81.9	0.0	0.0
Cp dry stack gas, kJ/kg-K	1.27	0.02	81.9	0.0	0.0
Cp moisture, kJ/kg-K	1.89	0.02	81.9	0.0	0.0
Run time, min	57	5	81.9	0.0	0.0
		Original Closure	81.9		

All error values have been <u>added</u> to calculate the closure with error value

Absolute Uncertainty (%) **14.9**
Carbon

Table A-6
ASF 1 Uncertainty
Aluminum

	Experimental Value	Error in same units	Closure with Error	Difference	Difference Squared
Air					
Air flow rate, L/min	21.45	5	113.9	0	0
Air moisture content, (% wb)	0.40	0.05	113.9	0	0
Air temperature, C	21.00	1	113.9	0	0
Air Density, g/L	1.34	0.1	113.9	0	0
Fuel					
Fuel flow rate, g/min	115.75	23.1	106.1	-7.8	60.84
Fuel moisture content, (% wb)	9.00	1	114.1	0.2	0.04
Fuel ultimate analysis (%)	1.79	1	94.3	-19.6	384.16
Bed					
Bed In, g	866	1	113.8	-0.1	0.01
Bed, HP and Cyclone Outputs					
Mass bed out, g	751.60	25	115.6	1.7	2.89
Mass HP out, g	1730.50	50	115.3	1.4	1.96
Mass cyclone out, g	507.30	25	114.8	0.9	0.81
Bed out ultimate analysis, (%)	20.77	1	116.3	2.4	5.76
HP ultimate analysis, (%)	8.70	1	119.4	5.5	30.25
Cyclone ultimate analysis (%)	10.75	1	115.5	1.6	2.56
HHV Bed Out, MJ/kg	1.50	0.2	113.9	0	0
HHV HP Out, MJ/kg	14.14	0.2	113.9	0	0
HHV Cyclone Out, MJ/kg	10.63	0.2	113.9	0	0
Stack					
Stack Gas (%)					
CO	19.70	2.4	113.9	0	0
CO_2	19.80	2.4	113.9	0	0
CH_4	6.70	2.3	113.9	0	0
H_2	12.70	2.3	113.9	0	0
N_2	39.70	3.0	113.9	0	0
O_2	1.40	2.2	113.9	0	0
Tar					
Tar concentration, mg/L	27.40	3.0	113.9	0.0	
Tar, ultimate analysis (%)	0.08	0	114	0.1	0.01
HCN					
HCN, mg/L	2.30	0.1	113.9	0	0
Ammonia					
NH3, ppmv	5030.29	247.4	113.9	0	0
Miscellaneous					
Cp dry air, kJ/kg-K	1.03	0.02	113.9	0	0
Cp dry stack gas, kJ/kg-K	1.27	0.02	113.9	0	0
Cp moisture, kJ/kg-K	1.89	0.02	113.9	0	0
Run time, min	57	5	113.9	0	0
		Original Closure	113.9		

Absolute Uncertainty (%) **22.1**
Aluminum

Table A-7
ASF 1 Uncertainty
Power Balance

	Experimental Value	Error in same units	Closure with Error	Difference	Difference Squared
Air					
Air flow rate, L/min	21.45	5	72.1	2.4	5.8
Air moisture content, (% wb)	0.40	0.05	69.7	0.0	0.0
Air temperature, C	21.00	1	69.7	0.0	0.0
Air Density, g/L	1.34	0.1	70.4	0.7	0.5
Fuel					
Fuel flow rate, g/min	115.75	23.1	58.2	-11.6	133.4
Fuel moisture content, (% wb)	9.00	1	70.4	0.7	0.5
Fuel ultimate analysis (%)	36.27	1	69.7	0.0	0.0
Bed					
Bed In, g	866	1	69.7	0.0	0.0
Bed, HP and Cyclone Outputs					
Mass bed out, g	751.60	25	69.5	-0.2	0.0
Mass HP out, g	1730.50	50	70.0	0.3	0.1
Mass cyclone out, g	507.30	25	69.8	0.1	0.0
Bed out ultimate analysis, (%)	2.23	1	69.9	0.2	0.0
HP ultimate analysis, (%)	34.64	1	70.3	0.6	0.4
Cyclone ultimate analysis (%)	25.63	1	69.9	0.2	0.0
HHV Bed Out, MJ/kg	1.50	0.2	69.8	0.1	0.0
HHV HP Out, MJ/kg	14.14	0.2	70.0	0.3	0.1
HHV Cyclone Out, MJ/kg	10.63	0.2	69.8	0.1	0.0
Stack					
Stack Gas (%)					
CO	19.70	2.4	70.0	0.3	0.1
CO_2	19.80	2.4	69.2	-0.5	0.3
CH_4	6.70	2.3	74.1	4.4	19.4
H_2	12.70	2.3	71.8	2.1	4.4
N_2	39.70	3.0	68.8	-0.9	0.8
O_2	1.40	2.2	69.5	-0.2	0.0
Tar					
Tar concentration, mg/L	27.40	3.0	69.7	0.0	0.0
Tar, ultimate analysis (%)	68.43	1	69.7	0.0	0.0
HCN					
HCN, mg/L	2.30	0.1	69.7	0.0	0.0
Ammonia					
NH3, ppmv	5030.29	247.4	69.6	-0.1	0.0
Miscellaneous					
Cp dry air, kJ/kg-K	1.03	0.02	69.7	0.0	0.0
Cp dry stack gas, kJ/kg-K	1.27	0.02	69.7	0.0	0.0
Cp moisture, kJ/kg-K	1.89	0.02	69.7	0.0	0.0
Run time, min	57	5	70.0	0.3	0.1
		Original Closure	69.7		

Absolute Uncertainty (%) **12.9**
Power

Table A-8
SLF 2 Uncertainty
Carbon

	Experimental Value	Error in same units	Closure with Error	Difference	Difference Squared
Air					
Air flow rate, L/min	24.70	5	53.4	1.6	2.6
Air moisture content, (% wb)	0.40	0.05	51.8	0.0	0.0
Air temperature, C	326	1	51.8	0.0	0.0
Air Density, g/L	1.34	0.1	52.3	0.5	0.3
Fuel					
Fuel flow rate, g/min	124.82	25.0	43.1	-8.7	75.7
Fuel moisture content, (% wb)	8	1	52.3	0.5	0.3
Fuel ultimate analysis (%)	36.19	1	50.4	-1.4	2.0
Bed					
Bed In, g	1299	1	52.4	0.6	0.4
Bed, HP and Cyclone Outputs					
Mass bed out, g	2344.20	25	51.8	0.0	0.0
Mass HP out, g	1193.00	50	51.8	0.0	0.0
Mass cyclone out, g	113.20	25	51.8	0.0	0.0
Bed out ultimate analysis, (%)	20.88	1	52.3	0.5	0.3
HP ultimate analysis, (%)	18.70	1	52.0	0.2	0.0
Cyclone ultimate analysis (%)	18.58	1	51.8	0.0	0.0
HHV Bed Out, MJ/kg	8.77	0.2	51.8	0.0	0.0
HHV HP Out, MJ/kg	7.92	0.2	51.8	0.0	0.0
HHV Cyclone Out, MJ/kg	7.88	0.2	51.8	0.0	0.0
Stack					
Stack Gas (%)					
CO	11.60	2.3	54.3	2.5	6.3
CO_2	10.20	2.3	53.8	2.0	4.0
CH_4	5.70	2.3	54.5	2.7	7.3
H_2	15.00	2.4	52.4	0.6	0.4
N_2	53.00	3.5	50.8	-1.0	1.0
O_2	4.50	2.2	51.7	-0.1	0.0
Tar					
Tar concentration, mg/L	75.61	3.0	51.6	-0.2	0.0
Tar, ultimate analysis (%)	44.46	1	52.4	0.6	0.4
Ammonia					
NH3, ppmv	9948.72	381.4	51.8	0.0	0.0
Miscellaneous					
Cp dry air, kJ/kg-K	1.03	0.02	51.8	0.0	0.0
Cp dry stack gas, kJ/kg-K	1.27	0.02	51.8	0.0	0.0
Cp moisture, kJ/kg-K	1.87	0.02	51.8	0.0	0.0
Run time, min	102	5	51.8	0.0	0.0
		Original Closure	51.8		

All error values have been <u>added</u> to calculate the closure with error value

Absolute Uncertainty (%) **10.0**
Carbon

Table A-9
SLF 2 Uncertainty
Aluminum

	Experimental Value	Error in same units	Closure with Error	Difference	Difference Squared
Air					
Air flow rate, L/min	24.70	5	40.4	0.2	0.04
Air moisture content, (% wb)	0.40	0.05	40.2	0	0
Air temperature, C	326.39	1	40.2	0	0
Air Density, g/L	1.34	0.1	40.3	0.1	0.01
Fuel					
Fuel flow rate, g/min	124.82	25.0	35.9	-4.3	18.49
Fuel moisture content, (% wb)	8	1	40.5	0.3	0.09
Fuel ultimate analysis (%)	3.59	1	34.4	-5.8	33.64
Bed					
Bed In, g	1299	1	40.6	0.4	0.16
Bed, HP and Cyclone Outputs					
Mass bed out, g	2344.20	25	40.5	0.3	0.09
Mass HP out, g	1193.00	50	40.7	0.5	0.25
Mass cyclone out, g	113.20	25	40.4	0.2	0.04
Bed out ultimate analysis, (%)	7.83	1	43.3	3.1	9.61
HP ultimate analysis, (%)	7.48	1	41.8	1.6	2.56
Cyclone ultimate analysis (%)	6.26	1	40.4	0.2	0.04
HHV Bed Out, MJ/kg	8.77	0.2	40.2	0	0
HHV HP Out, MJ/kg	7.92	0.2	40.2	0	0
HHV Cyclone Out, MJ/kg	7.88	0.2	40.2	0	0
Stack					
Stack Gas (%)					
CO	11.60	2.3	40.2	0	0
CO_2	10.20	2.3	40.2	0	0
CH_4	5.70	2.3	40.3	0.1	0.01
H_2	15.00	2.4	40.3	0.1	0.01
N_2	53.00	3.5	40.1	-0.1	0.01
O_2	4.50	2.2	40.2	0	0
Tar					
Tar concentration, mg/L	75.61	3.0	40.2	0	0
Tar, ultimate analysis (%)	3.55	1	40.2	0	0
Ammonia					
NH3, ppmv	9948.72	381.4	40.2	0	0
Miscellaneous					
Cp dry air, kJ/kg-K	1.03	0.02	40.6	0.4	0.16
Cp dry stack gas, kJ/kg-K	1.27	0.02	40.6	0.4	0.16
Cp moisture, kJ/kg-K	1.87	0.02	40.6	0.4	0.16
Run time, min	102	5	40.2	0	0
		Original Closure	40.2		

Absolute Uncertainty (%) **8.1**
Aluminum

Table A-10
SLF 2 Uncertainty
Power

	Experimental Value	Error in same units	Closure with Error	Difference	Difference Squared
Air					
Air flow rate, L/min	24.70	5	90.0	4.9	24.0
Air moisture content, (% wb)	0.40	0.05	85.1	0.0	0.0
Air temperature, C	326.39	1	85.1	0.0	0.0
Air Density, g/L	1.34	0.1	86.8	1.7	2.9
Fuel					
Fuel flow rate, g/min	124.82	25.0	71.1	-14.0	196.0
Fuel moisture content, (% wb)	8	1	86.0	0.9	0.8
Fuel ultimate analysis (%)	36.19	1	85.1	0.0	0.0
Bed					
Bed In, g	1299	1	85.1	0.0	0.0
Bed, HP and Cyclone Outputs					
Mass bed out, g	2344.20	25	85.0	-0.1	0.0
Mass HP out, g	1193.00	50	84.9	-0.2	0.0
Mass cyclone out, g	113.20	25	85.0	-0.1	0.0
Bed out ultimate analysis, (%)	20.88	1	85.5	0.4	0.2
HP ultimate analysis, (%)	18.70	1	85.3	0.2	0.0
Cyclone ultimate analysis (%)	18.58	1	85.1	0.0	0.0
HHV Bed Out, MJ/kg	8.77	0.2	85.3	0.2	0.0
HHV HP Out, MJ/kg	7.92	0.2	85.2	0.1	0.0
HHV Cyclone Out, MJ/kg	7.88	0.2	85.1	0.0	0.0
Stack					
Stack Gas (%)					
CO	11.60	2.3	86.4	1.3	1.7
CO_2	10.20	2.3	84.1	-1.0	1.0
CH_4	5.70	2.3	90.1	5.0	25.0
H_2	15.00	2.4	88.7	3.6	13.0
N_2	53.00	3.5	81.9	-3.2	10.2
O_2	4.50	2.2	84.8	-0.3	0.1
Tar					
Tar concentration, mg/L	75.61	3.0	85.9	0.8	0.6
Tar, ultimate analysis (%)	44.46	1	85.0	-0.1	0.0
Ammonia					
NH3, ppmv	9948.72	381.4	85.1	0.0	0.0
Miscellaneous					
Cp dry air, kJ/kg-K	1.03	0.02	85.1	0.0	0.0
Cp dry stack gas, kJ/kg-K	1.27	0.02	85.1	0.0	0.0
Cp moisture, kJ/kg-K	1.87	0.02	85.1	0.0	0.0
Run time, min	102	5	85.1	0.0	0.0
			Original Closure	85.1	

Absolute Uncertainty (%) **16.6**
Power